AMORPHOUS SILICA BASED BIOMATERIALS FOR MUSCULOSKELETAL TISSUE REGENERATION APPLICATIONS

By-

KAMAL AWAD

DISSERTATION

Submitted in partial fulfillment of the requirements

For the degree of Doctor of Philosophy in

Materials Science and Engineering at The

University of Texas at Arlington

August 2021

Arlington, Texas

Supervising Committee:

Dr. Venu Varanasi, Supervising Professor
Dr. Efstathios "Stathis" I. Meletis, Committee Chair
Dr. Pranesh P. Aswath
Dr. Marco Brotto
Dr. Harry Tibbals
Dr. Kyungsuk Yum

ACKNOWLEDGMENTS

Firstly, I would like to express my deep appreciation and gratitude to Dr. Venu Varanasi, associate professor at the Bone-Muscle Research Center (BMRC) and the Department of Materials Science and Engineering at the University of Texas at Arlington (UTA) for his kind supervision, encouragement, and critical comments during the preparation of this dissertation. I would like to equally thank my co-mentors Dr. Pranesh B. Aswath, professor of Materials Science and Engineering at UTA, and Dr. Marco Brotto, Director of the BMRC-UTA for their advising and time spent with me and my research projects. Deep thanks are also extended to Dr. Efstathios “Stathis” I. Meletis, Dr. Harry Tibbals, and Dr. Kyungsuk Yum for being on my committee and being so encouraging and cordial.

Deep thanks to the BMRC family, Dr. Varanasi’s, and Dr. Brotto’s research groups and especially Dr. Leticia Brotto for their help and support during the research and dissertation preparation. I would like to thank the college of Nursing and Health Innovation (CONHI-UTA) for the support through the CRS pilot project grant and especially Dr. Paul Fadel and Mrs. Kim Doubrava for their help and support during my research at the BMRC.

I am also thankful to my colleagues Dr. Felipe Monte, Neelam Ahuja, Marian Awadalla, and Dr. Ami Shah for being supportive and sharing their knowledge throughout my research. My sincere acknowledgment to Dr Jeichao Jiang and David Yen for the all the support and training at the CCMB facility. My sincere acknowledgment to engineer Dennis Bueno at the clean room facilities at NRC-UTA. My deepest words of appreciation to Beth Robinson, Natalie Burden, and Lashonda Davis

for helping through all the official matters and for their good wishes through all five years of my graduate studies. Also, sincere acknowledgment to the National Research Centre in Egypt, especially Dr. Adel Girgis for his continuous support and encouragement.

Finally, my deep gratitude is due to my parents, my lovely wife, and my wonderful daughter and son for being very supportive and encouraging throughout my endeavor in the USA over the last five years.

DEDICATION

THIS DISSERTATION IS DEDICATED WITH LOVE AND AFFECTION TO MY

MY PARENTS

AND

MY LOVELY WIFE

“MARIAN AWADALLA”

“YOU ARE THE BEST PARTNER IN MY LIFE”

ABSTRACT

Amorphous Silica Based Biomaterials for Musculoskeletal Tissue Regeneration Applications

Kamal Awad, Ph.D.

The University of Texas at Arlington, 2021

Supervising Professor: Venu Varanasi

Musculoskeletal (MSK) injury includes any injuries that affect the bones, muscles, ligaments, tendons, or nerves. Open bone fracture is one of the common types of MSK traumatic injuries which results in not only bone fracture but also damage/loss of associated muscles, nerve, vasculature, endothelium, periosteum, fascia, and connective tissue. Surgical procedures and biological interventions are required to fix the broken bone, and muscle transfer is performed to compensate the skeletal muscle defects. Current treatments include fixative metal implants and regenerative biopolymer scaffolds, then muscle flap procedures to cover the bone. Yet, these treatments are inadequate because the used materials do not stimulate rapid tissue regeneration. Thus, novel materials that lead to stability and rapid healing are vital for rapid MSK tissue regeneration. The proposed research is a step towards developing new materials and hydrogels doped with nanoparticles (NPs) for MSK tissue regeneration. For this purpose, the investigator utilized silica-based biomaterials through the Si-O-N-P elements system to deliver specific chemistries at the injury vicinity to trigger preferable biological behaviors. Our central hypothesis is that amorphous silica-based biomaterials could promote rapid bone healing and functional muscle regeneration via osteokines, myokines, and antioxidant activity. Amorphous silica-based thin-film coatings were

prepared by Plasma Enhanced Chemical Vapor Deposition (PECVD) technique while novel chemical synthesis approach was tested and optimized to synthesize SiONx-NPs. 3D printing technology was used to print different biopolymer scaffolds doped with NPs with and without cell laden for tissue regeneration applications. XPS, XANES, SPM, HR-SEM, HR-TEM, and nano-indentation were employed to analyze and characterize the studied materials. Cell culture studies were performed to study the effect of the synthesized materials on the cellular behavior and tissue regeneration. As outcomes, this study presented new materials that enhance the osteogenesis and myogenesis for an optimal treatment and stability for MSK injuries.

Keywords: Tissue engineering; Bone; Muscles, Implants; Nanoparticles; Oxidative stress.

TABLE OF CONTENTS

LIST OF ILLUSTRATIONS

Chapter 2

Chapter 3

Chapter 4

Chapter 5

Chapter 6

Chapter 7

LIST OF TABLES

CHAPTER 1: GENERAL INTRODUCTION

1.1 INTRODUCTION

Sudden, onset, and severe physical injuries that require immediate medical attention to rescue life and limb are known as traumatic injuries. MSK conditions includes any injury that affects bones, muscles, ligaments, tendons, or nerves, and affects more than 2.3 billion people globally. In the US, nearly 30 M Americans suffer with some sort of MSK injury that requires medical attention, costing nearly $900 billion in associated medical care costs. Open bone fractures and concomitant severe muscle loss are common types of MSK injuries that leads to long-term disability. These injuries lead to broken bones, soft tissue damage including the nervous and vascular systems, and severe muscle loss. Acute muscle injury, resulting in a loss of 20% or more of the native muscle tissue, is known as volumetric muscle loss (VML). It is classified as significant damage to skeletal muscle compartments, concomitant with Type III open fractures, and it often results in the loss of extracellular matrix, vasculature, neural components, and chronic functional deficits, leading to long-term disability. Furthermore, the high level of reactive oxygen species (ROS) at the injury site critically affects the tissue regeneration. Thus, these injuries are beyond the normal physiologic repair and require extensive regenerative therapy.

The regeneration of bone and muscle tissue following musculoskeletal injuries is essential to restore function and prevent chronic musculoskeletal disorders related to physical inactivity. Recent regenerative musculoskeletal research suggests that the restoration of function and structure for normal physical activity is dependent on the synergy of regeneration processes found in bone and muscle tissue. Current treatment

modalities utilize metal implants (i.e., Ti fixative implants) to fix the broken bone, as well as muscle flap (i.e., autologous muscle transfer) procedures to overcome the lost tissue.

Despite the advances in bone tissue engineering, the implants used are still associated with complications, such as aseptic loosening and failure due to the lack of surface bioactivity, leading to poor osteointegration. In addition, autologous tissue transfers, which is considered the current treatment standard, still suffer from many limitations, such as donor site morbidity, significant tissue loss, and functional deficits due to impaired endogenous regeneration capacity. Thus, there is a crucial need to engineer biologically active materials that stabilize the fractured bones, compensate for the lost soft tissue, and upregulate the expression of biomarkers for rapid and functional tissue regeneration.

1.2 RESEARCH OBJECTIVES

The primary objective of the proposed research project is to develop new materials to stimulate bone and muscle regeneration for rapid MSK tissue healing. Amorphous silica-based biomaterials, coatings, and 3D printed hydrogels will be investigated in this project. In pursuit of this goal, the research will concentrate on the use of silicon-based biomaterials through the Si-O-N elements system due to their significant effect on tissue regeneration. Thin-film coatings of $SiON_x$ will be applied on silicon wafers and standard metal implants to study their effect on the regenerative capacity of MSK tissues, such as bone and muscles. A novel approach to synthesize $SiON_x$ nanoparticles will be tested and optimized towards creating the same chemistry of $SiON_x$-thin films that were prepared by the PECVD technique. These nanoparticles will be imbedded in GelMa-ALG hydrogels and 3D printed to study their effects on the

tissue's regenerative capacity. Extensive characterization for the synthesized materials will be performed through different advanced characterization tools to understand the materials' properties and their mechanical and biological effects. The findings from the proposed work will contribute to the field of biomaterials by developing promising and novel materials for speeding the MSK tissue healing process.

As a result of the significant increase in bone fractures and bone-loss injuries, there has been crucial demand for bioactive adequate bone grafting materials that can provide stability and enhance osteogenesis due to their surface bioactivity compared to bioinert metal implants. Bioactive bone substitutes can enhance osteogenesis via rapid bone mineral formation, such as deposition of calcium phosphate. Thus, different materials, coatings, and techniques have been used to enhance the bone implant's bioactivity. Bioactive implant materials (for load bearing applications) or 3D printed scaffolds (for non-load bearing applications) that can support the fractured bone and stimulate soft tissue regeneration are crucial for rapid MSK tissue healing. It is well-known that silicon has an essential role in bone biology and its deficiency produces defects in connective and skeletal tissues. Many studies have shown the significant effects of silicon on bone formation, regeneration, and vasculogenesis in both *in-vitro* and *in-vivo* models.

1.3 CENTRAL HYPOTHESIS

Our central hypothesis is that bioactive amorphous $SiON_x$/$SiONP_x$-based biomaterials will promote rapid bone healing by enhancing the implant's surface bioactivity and support functional muscle regeneration via antioxidant activity that mitigates the ROS level. The sustained release of bioactive ingredients such as Si-ions

will influence muscle and soft tissue that are in near proximity of the fractured bone. Furthermore, the design and creation of synthetic muscle constructs based on amorphous silica biomaterials that provide sustained release of Si-ions in the injury site will allow for accelerated healing and promoted tissue regeneration. Therefore, the research will focus on the following specific aims.

1.4 SPECIFIC AIMS

1.4.1 Determine Changes in Bone Chemical Structure Using XANES Technique

In this aim, the author will study and validate the use of X-ray Absorption Near Edge Structure (XANES) to identify characteristic changes in MSK tissue structure using x-ray absorbance in normal and disordered MSK tissues. XANES is a commonly used spectroscopic technique that studies the chemical structure/coordination, which yields insight into the types of present bond in the materials. It provides information on the oxidation state, coordination number of individual elements, as well as the chemical structure of the biomaterial. Here, XANES was used to evaluate the structural environment of Ca and P in the inorganic phase of bone, i.e., hydroxyapatite (HA), which is an integral component. Obtaining this information can reveal changes in the local environment of Ca and P ions in bone, thereby investigating the changes in bone nature and mineralization during remodeling and regeneration.

1.4.2 Study the Effect of Si-O-N-P Coatings on Surface Bioactivity *In-Vitro*.

In this aim, the investigator will study the effect of the bioactive amorphous $SiON_x$/$SiONP_x$-PECVD as potential surface coatings for Ti implants in bone applications in-vitro. This aim will focus on the surface coating's properties and interfacial adhesion between the amorphous silica based PECVD coating and Ti implants as the substrate.

Then, apatite formation (in cell free medium) will be used to study and compare the surface bioactivity of the modified Ti to the bare implants. This will be performed by immersing the samples in alternative simulated body fluid (SBF) media to allow mineral deposition. Then, comprehensive analysis will be performed to understand the effect of the surface coatings on the bone mineral formation.

1.4.3 Study Bacterial and Osteogenic Activity of Si-O-N System *In-Vivo*.

In this aim, the investigator will focus on *in-vitro* and *in-vivo* studies to investigate the effect of bioactive Si-O-N coating system on bone regeneration. *In-vitro* cytotoxicity, proliferation, and differentiation studies using Mesenchymal Stem Cells (MSCs) will be performed to test the initial cellular response and osteogenic activity of the coating's chemistry compared to Ti implants as standard bone implants. Next, 1000 nm layer of $SiON_x$ will be deposited on the Ti. Then, bare, and coated Ti-$SiON_x$ implants will be implanted into a critical size defect rabbit mandible model for *in-vivo* testing. Collected blood serum will be screened for biomarkers including antioxidants, oxidative stress, and osteogenic activity. Extracted bones will be extensively studied to investigate the rate and quality of the regenerated bones. Various characterization techniques will be used such as nano indentation (mechanical properties), XANES, X-ray imaging, and micro-CT (bone chemical structure and quality).

1.4.4 Study the Effect of Ionic Silicon on Skeletal Muscle *In-Vitro*.

In this aim, the investigator will study the effect of Si-ions on the skeletal muscles' activity. The author hypothesized that ionic silicon would promote myogenesis via antioxidant activity that mitigates oxidative stress and enhances muscle functionality for rapid muscle regeneration. This aim will concentrate on the effect of ionic silicon on

skeletal muscle cells' activity, such as proliferation, migration, differentiation, and myokines and myogenic biomarkers and genes expression. To achieve this goal, C2C12 skeletal muscle cells will be studied under normal and oxidative stress conditions that mimic the injury site conditions to gain insight on the effect of Si-ions on myogenesis during the early stage of muscle regeneration. Outcomes from this aim will provide a clear understanding about the effect of silicon-based biomaterials on skeletal muscles that have never been reported before. Furthermore, the results will be used to develop muscle grafts based on silicon-based biomaterials for successful muscle regeneration.

1.4.5 Synthesis and Characterization of Novel $SiO_2/SiON_x/SiONP_x$-Nanoparticles.

In this aim, the author will investigate and optimize a novel approach to synthesize SiO_2/SiONx/SiONPx-nanoparticles. A novel approach will be proposed and executed to synthesize amorphous SiO_2/SiONx/SiONPx-nanoparticles based on the hydrolysis of Tetraethyl Orthosilicates (TEOS, Si-precursor) and 3-Aminopropyl triethoxysilane (APTES, Si-precursor) in the presence of phosphoric acid (H_3PO_4) as the source of phosphorus and the use of glucose and imidazole as catalysts. This approach is based on mimicking the role of the active sites during the natural silicification process in sponges by using structurally similar chemicals such as imidazole and glucose in the presence of Si-precursors. Thus, the investigator will focus on synthesis, understanding the reaction mechanism, and characterization of these nanoparticles to better comprehend their properties for further application as loaded nanoparticles on 3D printed hydrogels for tissue regeneration. Successful completion of this aim will lead to novel amorphous $SiO_2/SiON_x/SiONP_x$-nanoparticles that can be used in composite

scaffolds for bone substitutes or embedded in hydrogels for soft tissue regeneration applications.

1.5 SIGNIFICANCE OF THE PROPOSED RESEARCH

In the proposed research, the author will investigate new techniques towards developing materials that target both bone and muscle for rapid and functional MSK tissue regeneration. For bone implants, the investigator will study the effects of amorphous $SiON_x$/$SiONP_x$-PECVD coatings as a potential coating for the Ti implants. A combination of Ti (substrate) and bioactive $SiON_x$/$SiONP_x$ (coating) will provide an optimal medical implant that has the unique properties of both metallic implants and bioceramics coatings. Mechanical and interface studies of Ti-$SiON_x$-bone will provide significant insights for potential clinical application of these materials. Then, the investigation of novel approach to synthesize novel nanoparticles with the same chemistry of $SiON_x$/$SiONP_x$-thin films will allow the use of these materials in soft tissue application, especially for 3D printed hydrogels-based for muscle grafts applications.

1.6 DISSERTATION STRUCTURE

In this section, an overview of this dissertation is provided. Moreover, the significance and contribution of each chapter to the central theme of the dissertation is highlighted.

Chapter 1, General Introduction: The author presented the general theme of the proposed research project with focus on the main idea, specific aims, and the significance in the field of musculoskeletal tissue regeneration.

Chapter 2, Background: This chapter provides the reader with a general understanding of the musculoskeletal system with focus on bone and skeletal muscle.

Then, a summary of the up-to-date materials that have been used for bone and muscle applications is given. The author focused on the metallic and ceramic materials as the most common bone implantable materials. Also, the recent advances in the field of muscle regenerative materials were discussed with focus on synthetic hydrogels as potential materials for muscle grafts applications.

Chapter 3: This chapter discusses XANES as a sensitive characterization technique to evaluate the chemical structure and quality of regenerated bones compared to control ones. The author has investigated various types of bones including diabetic, hypertensive, and treated bones to uncover the chemical changes in the inorganic phase during the bone remodeling process. This chapter assessed local calcium (Ca) and phosphorus (P) coordination of bone and concluded that the presence of soluble Ca and P, products of bone resorption, is an indicator for poorly developed bone due to unbalanced bone resorption and formation.

Chapter 4: This chapter investigates the potential use of amorphous silica-based coatings deposited by low temperature PECVD method on Ti implants to enhance its surface bioactivity for rapid bone healing. The investigator compared the commercially pure anodized Ti implants to SiONx/SiONPx coated Ti to reveal the effect of these bioactive coatings on the surface bioactivity and interfacial adhesion. Surface bioactivity was tested by comprehensive surface characterization (i.e., chemical composition, surface energy, morphology, and mechanical properties) and percentage area of apatite formation on each surface. This chapter concluded that improved surface bioactivity of Ti-SiON and Ti-SiONP coatings promotes their potential use as strongly adherent

bioactive surface coatings for Ti implants and role in acting as a substrate for future potential bone regeneration.

Chapter 5: This chapter investigates the cellular and antibacterial activity (*in-vitro)* and the effect on bone healing (*in-vivo*) of amorphous $SiON_x$ coatings. Mesenchymal stem cells (MSCs) and Methicillin-Resistant Staphylococcus Aureus (MRSA) bacteria will be used for the *in-vitro* studies and critical sized defects in the rabbit mandibular model will be used for the *in-vivo* studies. The investigator compared the commercially pure anodized Ti implants to $SiON_x$-coated Ti to reveal the effect of these bioactive coatings on the surface bioactivity, antibacterial activity, and bone healing rate. Comprehensive analysis will be conducted using HR-SEM, XANES, Micro-CT, X-ray imaging, and biomarker assays for cells activity and osteogenic effect. This chapter concluded that SiONx coatings exhibit antioxidant properties and bacteriostatic effect, reduce healing times, and enhance bone formation and osteointegration on the surface of implants.

Chapter 6: In this chapter, the author investigated, for the first-time, the effect of silicon on skeletal muscle cell's activity under normal and oxidative stress conditions to reveal its potential roles in muscle regeneration applications. *In vitro* studies using C2C12 skeletal muscle cells were performed under different conditions. C2C12 cell viability, proliferation, migration, and myotube formation were assessed and compared to a positive control. Myogenic genes and biomarkers expression were measured using Quantitative Real-Time Polymerase Chain Reaction (qRT-PCR) and ELISA kits, respectively. This chapter concluded that ionic silicon may have a potential effect in unfavorable situations where reactive oxygen species is predominant, affecting cell

viability, proliferation, migration, and differentiation. Furthermore, this study provides a guide for designing Si-containing biomaterials with desirable Si-ion release for skeletal muscle regeneration.

Chapter 7: In this chapter, the author investigated new reactions to synthesize SiO_x/$SiON_x$/$SiONP_x$ nanoparticles that will be used in soft tissue regeneration. After investigating the effects of $SiON_x$/$SiONP_x$-PECVD thin-film coatings and revealing their potential roles in bone and muscle regeneration, the author intended to create the same chemistry in the nanoparticles format to utilize 3D printing technology for soft tissue applications. The proposed reactions and mechanisms were discussed, as well as the characterization of the novel nanoparticles were performed. This chapter concluded that SiO_x/$SiON_x$/$SiONP_x$ nanoparticles can be synthesized using simple reactions under normal conditions.

Chapter 8, Conclusion: This chapter finalizes this dissertation and provides the link among all previous chapters, demonstrating the importance of this research and the significance of the results. Here, the author demonstrated how $SiON_x$- and $SiONP_x$-PECVD coatings can be beneficial for enhanced osteointegration and rapid bone regeneration via its antioxidant effect. Further, the author presented, new evidence revealing the significant roles of silicon containing biomaterials for muscle regeneration applications. Finally, the author proposed new reactions to synthesize amorphous silica-based nanoparticles with the same chemical structure of these potential PECVD thin films to allow their use in soft tissue applications.

CHAPTER 2: BACKGROUND

Bone and muscle are the two major components of the musculoskeletal (MSK) system [1]. They are mechanically and physically connected to provide locomotion ability for humans. The MSK system has primary functions that include supporting the body, providing stability, allowing motion, and protecting other vital organs [2]. All components of the MSK system work together to accomplish each function. Sudden, onset, and severe physical injuries that affect the MSK system are known as MSK traumatic injuries [3,4]. Open bone fracture and concomitant severe muscle loss are common types of MSK injuries that lead to continuous life disability [5]. These injures lead to broken bones, soft tissue damage, and severe muscle injuries that can result in more than 20% muscle loss which known as volumetric muscle loss (VML) [6,7]. Healing of fractured bone is significantly impaired in presence of extensive muscle injuries [8].

These MSK injuries afflict more than 2.3 billion people globally and ~30 million Americans leading to nearly one-trillion dollars in medical care costs [9,10]. Usually, treating an open bone fracture must follow three steps: surgically cleaning the bone, removing contaminated tissue, and stabilizing the fractured bone. Ti and its alloys have been used for bone fixation to assist defects stabilization and bone healing. Then, muscle flap procedures are used to cover the bone, followed by extensive physical rehabilitation [11,12]. Yet, fixative implants and muscle flap procedures are still inadequate for open fracture treatment. These procedures are inadequate because fixative metal implants and regenerative biopolymer scaffolds do not stimulate rapid bone formation once implanted. Titanium fixation plates provide structural support, but their bioinert surface (i.e., poor osseointegration) and no antioxidant effect cannot target rapid bone

healing [13,14]. Furthermore, vascularized free tissue transfer causes donor site morbidity and has low harvest volume [15]. In the next section, the author will give a brief overview on the MSK system and then summarize the literature to present state-of-the-art biomaterials that have been used as implants and grafts in tissue regeneration applications.

1. MUSCULOSKELETAL SYSTEM

The MSK system consists mostly of bones, skeletal muscles, and tendons [16]. Other vital parts of the MSK system include ligaments, cartilage, and other connective tissues. Tendons are dense, tough, and flexible fibrous connective tissues that connect muscles to bones [2]. Tendons assist the MSK system in complex mechanical functions that allow limb and joint motion. Tendons have viscoelastic properties that allow smoothness in joint motion and help resist abnormal joint displacement under pressure or high loads [17]. Tendons are made of 90 % collagen type I, proteoglycans, elastin, and lipids [16]. The type of cells found in tendons include fibroblasts and tendon surface cells. Cartilage is a firm, whitish, and flexible essential connective tissue that carries most of the load in a joint and protects the nearby bones [18]. Ligaments are equally dense white fibrous elastic tissues responsible for attaching bones together. Ligaments help to limit joint dislocation, and they prevent hyperextension and hyperflexion [2].

Skeletal muscles are an important part of the MSK system. They originate from dense connective tissues or bones and result in body movement and posture [16]. Skeletal muscles generate heat and are responsible for 40 to 50% of the total body weight [16]. Skeletal muscles have a remarkable ability to self-regenerate via a process with various stages known as myogenesis [19] (Figure 2.1). Myogenesis starts by the

activation of satellite cells that undergo the proliferation step to form myoblasts. Myoblasts are capable to differentiate to form myocytes, which is the basic unit of a skeletal muscle [19]. Myocytes are cylindrical and multinucleated cells with a diameter ranging between 50 and 150 μm [20]. Myocytes can specialize into cardiac, skeletal, and smooth muscles. Terminal differentiation “fusion” of myocytes leads to myotubes formation [19]. Collection of hundreds and even thousands of myocytes can be found in muscle fibers, causing the fibers to have lengths of up to 10 cm [16]. Skeletal muscles can be bound by connective tissues called epimysium to form individual muscles [16]. There are some connective tissues that separate individual muscle fibers and are called perimysium. Muscle cells are surrounded by connective tissues called endomysium. The combination of the collagenous membrane and the adjacent cell is called sarcolemma. If the connective tissues are intact, regeneration of the skeletal muscles after an injury is possible. Humans have two types of skeletal muscle fibers: type 1 and type 2 fibers. These fibers can be differentiated by their color. Type 1 fibers are red or darker due to the presence of myoglobin, can maintain sustained force, and have a weight-bearing capacity [16]. Type 2 fibers are white, have abundant glucose, contain a scant mitochondria, cannot maintain sustained activity because of lactic acid, and are important in sudden and rapid movements [16]. Muscles also contain specific proteins which have different responsibilities. These proteins include Myoglobin, Creatinine phosphokinase, and dystrophin. Myoglobin is responsible for oxygen buffering, Creatinine phosphokinase is an important part of energetic function, and dystrophin is essential to preserve cellular and cell membrane integrity [20].

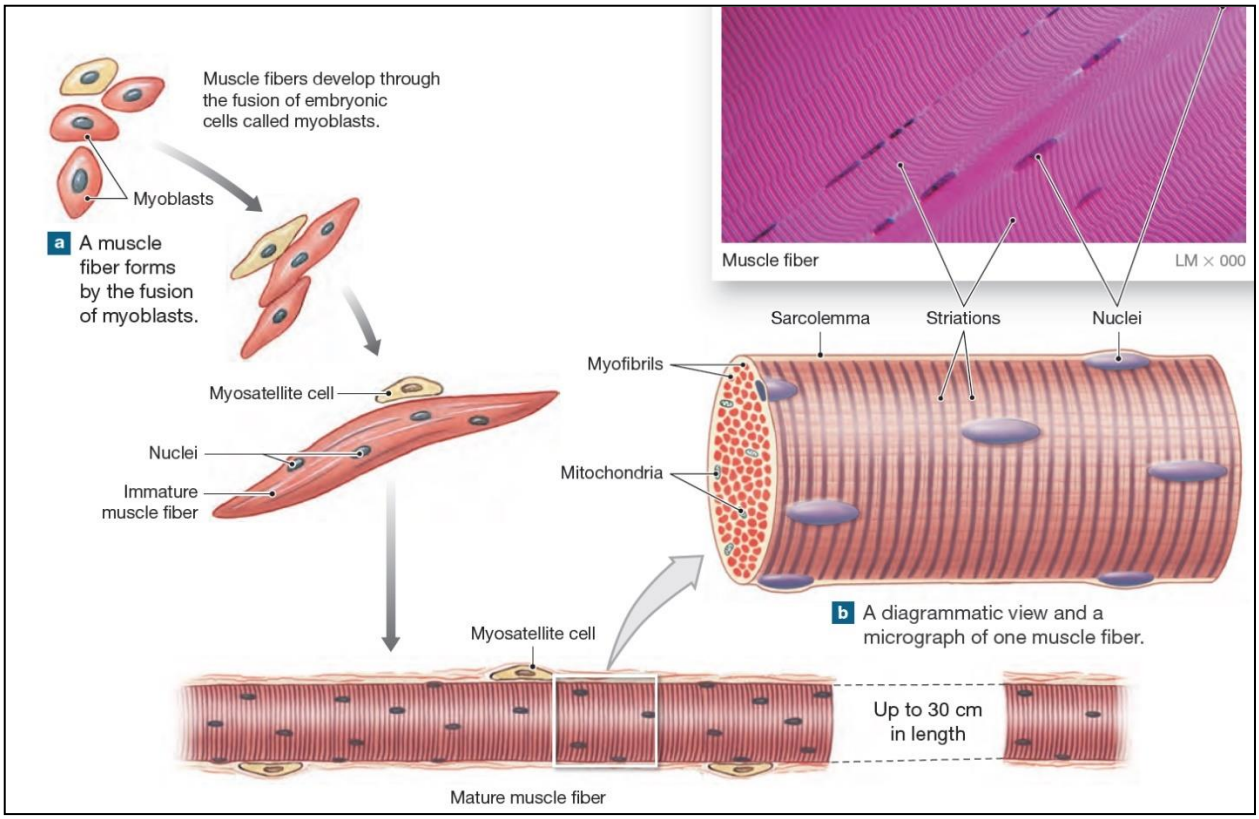

Figure 2. 2: Muscle development across various stages of myogenesis. Courtesy of pinterest.com [21].

Bone is a connective tissue made of cells and extracellular matrix, and the basic unit of bone is the mineralized collagen [22]. The cells that form an integral part of bone include osteoclasts, osteoblasts, and osteocytes, but the two main groups are osteoclasts and osteoblasts. Osteoclasts are responsible for bone resorption, while osteoblasts are responsible for bone formation and maturation into osteocytes. Osteoclasts are giant, multinucleated cells with nuclei ranging in number from two to several hundred. Osteoclasts originate in the hemopoietic stem cell system, but their differentiation, activity, and survival are regulated by the mesenchymal cells of the osteoblast lineage [23]. Osteoclasts absorb the mineral and matrix parts of the bones.

Osteoblasts are differentiated cells and lay down the organic matrix of a new bone. These cells make up four to six percent of the total cells in bone and are known

for their bone formation function [22]. The origin of osteoblasts varies based on the life stage and setting [24]. Skeletal Stem Cells (SSCs) are usually considered to be the origin for osteoblasts, but the term does not account for the challenging characteristics of mesenchyme-derived cell types [24]. To be more inclusive in the description of the origin of osteoblasts, the cells are said to originate from skeletal stem and progenitor cells (SSPCs) [24]. Some factors that contribute to the growth of osteoblasts include bone morphogenic proteins (BMPs), wingless (Wnt) proteins, and fibroblast growth factor (FGF) [22]. As osteoblasts mature, they become responsible for three main functions: bone marrow synthesis, osteoclastogenesis, and endocrine function.

Bone matrix synthesis is accomplished in two steps. The first step involves the secretion of collagen proteins, especially collagen type I, non-collagen proteins like osteocalcin, osteonectin, and osteopontin, and proteoglycans like decorin and biglycan [22]. This step is followed by the mineralization of the bone matrix where matrix vesicles secrete hydroxyapatite crystals which spread throughout the matrix [22]. The non-mineralized bone matrix is called the osteoid. When osteoblasts age, the cells can either undergo apoptosis, become osteocytes, or become bone-lining cells. Bone-lining cells lose the ability to synthesize the matrix because they are flattened cells with few organelles and a slender nuclei [23].

Osteocytes are the most mature stage of osteoblasts. Osteocytes make up 90% of the cells in a mature skeleton [22]. They form an extensive network of cell processes by having the ability to communicate with each other, lining cells, and surfacing osteoblasts [23]. This network of communication allows bone to determine the need for bone augmentation or reduction based on the detection of microdamage and in response to

mechanical demands [23]. Osteocytes play an important part in maintaining calcium and phosphorus levels in serum [16]. They are also capable of translating mechanical stimuli into biochemical stimuli. Additionally, the apoptosis of osteocytes has been linked with an increase in RANK ligand expression which promotes osteoclast formation [22].

Bones has two main phases: the organic and inorganic phase. The organic phase consists mostly of collagen. Collagen is not only the organic component of bone but is a part of ligament, tendons, skin, cornea, blood vessels, cartilage, and other extracellular tissues [25]. There are more than twenty human collagens and among all of those, type I collagen is the most abundant in bone [26]. The main inorganic crystal phase of bone is hydroxyapatite (HA). Apatite mineral contains impurities that cause bone mineral to contain more than just HA. The impurities substitute hydroxyl and phosphate groups with carbonate ions. Thus, in the presence of 4-6% carbonate concentrations, bone HA becomes poorly crystalline, calcium deficient, and carbonated [26].

Bone is considered the toughest tissue in the body, but it can suffer traumatic and nontraumatic injuries, which frequently occur in the musculoskeletal system. There has been a rise in musculoskeletal traumas in the United States [27]. Metabolic bone diseases have an impact on remodeling processes which disrupts skeletal functions, thus leading to bone fractures and an imbalance in the homeostasis of bone calcium and phosphorus [23]. Tendon disorders, along with ligament disorders, are a large subset of musculoskeletal injuries responsible for pain and disability in millions of individuals [17].

2. BONE IMPLANTS MATERIALS

The recent era has witnessed a dramatic increase in bone-muscle grafts and substitution procedures due to the massive increase in the number of road accidents,

wars, trauma cases, the rate of congenital facial deformities, and technological advancements [10]. Then, different types of implants were manufactured to replace or support the missing or damaged parts and restore the normal skeletal function of the body. Implants can be categorized based on the materials of which the implants are made such as metals, ceramics, and polymers.

2.1.1 Metallic Materials

Cobalt/chrome, stainless steel, and titanium are the most used metal implants, but titanium is considered the gold standard for metal implants [28]. Pure Ti-implants were first introduced as dental implants in 1965. Since then, Ti and its alloys have been used as biomaterials for medical applications such as orthopedics and dental implants [29,30]. Ti has unique properties such as its excellent biocompatibility, favorable response of tissues on its surface, the absence of allergic reaction, high corrosion resistance, and specific mechanical properties that make it a suitable metal for orthopedic and dental implants applications [31–33].

To provide superior structural materials with excellent chemical, mechanical, and biological biocompatibility, another approach that targets alloying elements has been introduced. Many Ti-alloys were developed including Titanium-6Aluminium-7Niobium (Ti6Al7Nb) and Titanium-6Aluminium-4Vanadium (Ti6Al4V). These alloys result in β- and β+α alloys that have higher strength and mechanical properties [30]. Specifically, the β-alloys offer the unique characteristic of low elastic modulus and superior corrosion resistance [34]. However, Ti and its alloys could not meet all clinical requirements and still suffer from many limitations [34–36]. One of the most common limitations of Ti-implants is aseptic loosening, which is known as the failure of the bond between the implants and

the bone in the absence of infection [35,36]. Metallic debris from Ti alloys induce aseptic loosening that results in severe osteolysis [36]. As a result, 75% of the implants' failures occur due to the aseptic loosening and impaired implant fixation [34–36]. On the other hand, oxidative stress, and the absence of antioxidant effects of Ti implants are common issues that these materials present. R. Tsaryk et al. reported that Ti6Al4V alloy induced permanent oxidative stress during the in vitro study of endothelial cells on the surface of Ti6Al4V alloy [14,37].

Using the findings from the previous studies, we can conclude that stress shielding effect [33,38], cytotoxicity of alloying elements [31], aseptic loosening [35,36,39], poor long-term stability, absence of antioxidant effects [14,37], and prolonged healing time remain critical issues for Ti implants. Thus, many researchers have concentrated on Ti surface modification to overcome these limitations. Various surface modification techniques have been introduced, such as mechanical treatment, thermal spraying, sol-gel, chemical/electrochemical treatment, and ion implantation [34]. Out of these strategies, deposition of bioactive materials such as silica, hydroxyapatite (HA), calcium silicates, and Al_2O_3 on the surface of Ti was of great interest due to the enhancement in the osteoconductivity and biocompatibility of the Ti surface. However, these coatings are still less than optimal due to poor interfacial bonding, thin film cracking, and delamination [40–43].

2.1.2 Ceramic Materials

Due to their excellent biocompatibility and biological surface activity, ceramic materials have become attractive materials for implants or coating materials. Compared to Ti implants, many studies on ceramic implants have shown low or weak inflammation

responses, better osseointegration, soft tissue attachment, and less to no bacterial adhesion [44–47]. Zirconium oxide (Zirconia), silicon oxide (Silica), hydroxyapatite (HA), aluminum oxide, calcium phosphates, and bioactive silicon nitride are the common ceramic materials that have been used in the implant industry. Zirconia has become a potential substitute for Ti-implants in dental implantology due to its excellent biocompatibility, tissue integration, low affinity to plaque, and favorable biomechanical properties [47]. Calcium phosphate compounds (such as HA and Tricalcium phosphate) are the common bioactive ceramic coatings that have been coated on metallic implants to accelerate bone formation [48,49]. Most importantly, silicon-based bioceramics have gained a great attention due to the significant role of silicon in the tissue regeneration process [50–52].

Sustained release of Si-ions stimulates the osteogenic cells proliferation, differentiation, and gene expression for rapid and successful bone tissue regeneration [50–53]. A recent study has shown that Si-ions can prevent the reduction in bone formation that occurs in diabetic patients due to the high glucose environments [53]. Furthermore, silicate bioceramics can regulate immune responses by altering the ionic microenvironment between the implants and the hosts [51]. Due to these properties, bioactive silicon nitride has been introduced as a novel biomaterial for orthopedic applications. In 2008, Si_3N_4 was cleared by FDA for its use in spinal fusion procedures to serve as intervertebral spacers for stabilization of cervical and thoracolumbar spine. On top of that, it is being developed for reconstructive applications, however it has not been cleared yet [54,55]. Most recent is the PECVD amorphous silicon oxynitride that has been developed by Varanasi et. al, as a potential new fracture healing biomaterial that

adheres well to the implant surface, releases Si^{+4} to enhance osteogenesis, and forms a surface hydroxyapatite for collagen mineral attachment [56].

PECVD coating has remarkable advantages compared to other coating methods [57]. This method requires a relatively low temperature (~200-400˚C) and prevents mismatches between the coating and the substrate materials. PECVD coating can efficiently form a stable coating layer of amorphous silica on an underlying metal surface. These new biomaterials enhance osteogenesis via antioxidant and osteogenic markers expression [56]. Furthermore, amorphous silicon oxynitrophosphide coatings enhanced the angiogenic activity of endothelial cells, and ionic silicon improved endothelial cell survival under toxic reactive oxygen species conditions via enhanced angiogenic marker expression and antioxidant activity [57,58]. Although these mentioned studies indicated the potential use of these novel developed PECVD SiONx coatings for Ti implants, comprehensive studies of the Ti-SiONx interface, HA nucleation, and nano-mechanical properties of the newly formed bones have yet to be performed.

3. MUSCLE REGENERATION MATERIALS

Skeletal muscle constitutes about 40% of total body mass and is responsible for movement of the human body [59]. Although skeletal muscle has remarkable endogenous regenerative capacity, acute severe traumatic tissue loss greater than 20% overwhelms this capacity [60,61]. The limitations of skeletal muscle to self-repair following severe injuries and the failure to regenerate healthy and functional muscle tissue have opened the door to the investigation of novel alternative approaches. Thus, many strategies that stimulate functional muscle regeneration have been proposed, including tissue engineering techniques, such as bioactive scaffolds, cell therapies, or cell laden

biomaterials [62–64]. These strategies aim to generate functional multinucleated myotubes through rapid differentiation of muscle progenitor myoblast cells, the key step in the regeneration process [65]. This process is initiated by the activation of satellite cells, or mononucleated muscle precursor cells, that undergo several proliferative cycles to finally differentiate to form multinucleated myotubes [66–68]. Various myogenic transcription factors are expressed within hours of satellite cell activation and regulate the myogenic differentiation process. These factors include myogenic determination protein (MyoD), myogenin (MyoG), and myogenic factor-5 (Myf-5) for cell cycle regulation, and muscle regulatory factor-4 (MRF4) for terminal differentiation. MyoD is a vital gene for myoblast progression and regulation during differentiation to form skeletal muscles [68,69]. The expression of the myogenic marker MyoG is an early indicator of myoblast commitment and differentiation [66,70]. In addition, myokines are molecules released by skeletal muscle and thought to function as hormone like-molecules, exerting endocrine and paracrine effects on other associated organs and muscle metabolic signaling pathways [71].

Skeletal Muscle Tissue Engineering (SMTE) aims to repair, replace, or restore the functionality in skeletal muscles that have been damaged or lost due to diseases, accidents, or severe traumatic injuries [72]. SMTE includes the culture of myogenic cells or stem cells, use of engineered scaffolds, and generation of functional skeletal muscle that can be transplanted into the patient's body [73]. The skeletal muscle tissue culture (*in vitro* and *ex vivo*) has been established for more than a century, and natural and synthetic materials have been extensively developed to generate functional muscle tissue *in vitro* [72]. Fibrin, alginate, and polycaprolactone based polymers are among the

first materials that have been used *in-vitro* for this application [74–76]. Besides the materials, the engineering of muscle fibers *in-vitro* requires a specific environment and architecture to assure the alignment of the myofibers and favor their fusion and myogenesis, which are still the main challenges [77]. Many strategies have been developed to induce the cell and myofiber alignments such as use of grooves/ridges, micro/nano-patterned substrates, nanofibers, hydrogel compaction, chemical surface printing, and mechanical and electrical stimulations [78,79]. Although these strategies aimed to mimic the structure and microenvironment of the skeletal muscles *in vivo* by providing the anisotropic surface that allows the muscle cell alignment and fusion, they still have limitations in inducing precise 3D spatial cell organization [72]. As a result, 3D bioprinting techniques aimed to overcome these limitations by providing high precision in scaffolds microenvironment design, cells and matrix deposition, and rapid fabrication of complex structures [80]. Since then, bioink became the most important factor for the successfulness of these new strategies. Bioinks should maintain specific properties such as ideally mimicking the extracellular matrix to support cell activities, and ideal rheological properties to allow printability and fidelity. GelMa, hyaluronic acid methacrylate, carboxymethyl, oxidized methacrylate alginate, and methacrylate alginate are a few examples of such bioinks [72]. Thus, the development of bioinks is an active research area and many natural and synthetic hydrogels have been tested for an optimal bioink.

In recent years, many bioactive materials have been introduced for MSK tissue engineering including silicon (Si) and silicon-based biomaterials [81,82]. As mentioned above, silicon-based biomaterials have been shown to promote osteoblast

differentiation, extracellular matrix deposition, and bone regeneration [57,83], but the effect of silicon and silicon-based biomaterials on skeletal muscles regeneration has not been uncovered yet. Recent evidence indicates that C2C12 myoblasts cells cultured on a silicon substrate maintained normal biological activities [84]. Research has shown that silica nanoparticles have a beneficial effect on myoblast fusion in C2C12 skeletal muscle cells [66]. Additionally, our preliminary data indicates that micro-patterned silicon oxynitride enhanced adhesion, growth, and myotube and axon alignment of muscle and nerve cells [85–87]. Yet, the effect of silicon on skeletal muscle cell activity, such as proliferation, migration, differentiation, and myogenic biomarker expression, has not been explored.

REFERENCES

1. Li, G. Bin *et al.* Muscle-bone crosstalk and potential therapies for sarco-osteoporosis. *J. Cell. Biochem.* **120**, 14262–14273 (2019).

2. Overview of the Musculoskeletal System. (2020).

3. Ahn, J., Nana, A. D., Mirick, G. & Anna N Miller. Traumatic Injuries. *Burd. Musculoskelet. Dis. United States* (2014).

4. Rosenbloom, B. N., Khan, S., Mccartney, C. & Katz, J. Systematic review of persistent pain and psychological outcomes following traumatic musculoskeletal injury. *J. Pain Res.* **6**, 39–51 (2013).

5. Griffin, M., Malahias, M., Hindocha, S. & Khan, W. Update on the management of compound lower limb fractures. *Open Orthop. J.* **6**, 518–524 (2012).

6. Pollot, B. E. & Corona, B. T. Volumetric muscle loss. *Methods Mol. Biol.* **1460**, 19–31 (2016).

7. Garg, K. *et al.* Volumetric muscle loss: persistent functional deficits beyond frank loss of tissue. *J. Orthop. Res.* **33**, 40–46 (2015).

8. Utvåg, S. E., Iversen, K. B., Grundnes, O. & Reikerås, O. Poor muscle coverage delays fracture healing in rats. *Acta Orthop. Scand.* **73**, 471–474 (2002).

9. Lawrence, R. C. *et al.* Estimates of the prevalence of arthritis and other rheumatic conditions in the United States: Part II. *Arthritis Rheum.* **58**, 26–35 (2008).

10. Jaimo Ahn, Nana, A. D., Mirick, G. & Miller, A. N. Cause of MSK Traumatic

Injuries. *Burd. Musculoskelet. Dis. United States* (2014).

11. Corona, B. T., Ward, C. L., Baker, H. B., Walters, T. J. & Christ, G. J. Implantation of in vitro tissue engineered muscle repair constructs and bladder acellular matrices partially restore in vivo skeletal muscle function in a rat model of volumetric muscle loss injury. *Tissue Eng. Part A* **20**, 705–715 (2014).

12. Greising, S. M., Dearth, C. L. & Corona, B. T. Regenerative and Rehabilitative Medicine: A Necessary Synergy for Functional Recovery from Volumetric Muscle Loss Injury. *Cells. Tissues. Organs* **202**, 237–249 (2016).

13. Goodacre, C. J., Bernal, G., Rungcharassaeng, K. & Kan, J. Y. K. Clinical complications with implants and implant prostheses. *J. Prosthet. Dent.* **90**, 121–132 (2003).

14. Iwai-Yoshida, M. *et al.* Antioxidant and osteogenic properties of anodically oxidized titanium. *J. Mech. Behav. Biomed. Mater.* **13**, 230–236 (2012).

15. Chatterjea, A., Meijer, G., van Blitterswijk, C. & de Boer, J. Clinical application of human mesenchymal stromal cells for bone tissue engineering. *Stem Cells Int.* **2010**, 215625 (2010).

16. Fedoruk, M. J. & Hong, S. Musculoskeletal System. in (ed. Wexler, P. B. T.-E. of T. (Third E.) 403–406 (Academic Press, 2014). doi:https://doi.org/10.1016/B978-0-12-386454-3.00063-4.

17. Miller, K., Hsu, J. E. & Soslowsky, L. J. 6.618 - Materials in Tendon and Ligament

Repair. in (ed. Ducheyne, P. B. T.-C. B.) 257–279 (Elsevier, 2011). doi:https://doi.org/10.1016/B978-0-08-055294-1.00218-X.

18. Messent, E. A., Ward, R. J., Tonkin, C. J. & Buckland-Wright, C. Osteophytes, juxta-articular radiolucencies and cancellous bone changes in the proximal tibia of patients with knee osteoarthritis. *Osteoarthr. Cartil.* **15**, 179–186 (2007).

19. Mukund, K. & Subramaniam, S. Skeletal muscle: A review of molecular structure and function, in health and disease. *Wiley Interdiscip. Rev. Syst. Biol. Med.* **12**, e1462 (2020).

20. Salvage, S. C., Jackson, A. P. & Huang, C. L.-H. Structure and Function of Skeletal Muscle. in (ed. Zaidi, M. B. T.-E. of B. B.) 247–269 (Academic Press, 2020). doi:https://doi.org/10.1016/B978-0-12-801238-3.11208-5.

21. Formation of a multinucleate skeletal muscle fiber. (2018) doi:https://www.pinterest.at/pin/41095415335625091/.

22. Black, J. D. J. & Tadros, B. J. Bone structure: from cortical to calcium. *Orthop. Trauma* **34**, 113–119 (2020).

23. Dunstan, C. R., Blair, J. M., Zhou, H. & Seibel, M. J. 6.21 - Bone, Mineral, Connective Tissue Metabolism. in (eds. Taylor, J. B. & Triggle, D. J. B. T.-C. M. C. I. I.) 495–520 (Elsevier, 2007). doi:https://doi.org/10.1016/B0-08-045044-X/00182-6.

24. Mesnieres, M. & Maes, C. Osteoblast Lineage Stem and Progenitor Cells. in (ed.

Zaidi, M. B. T.-E. of B. B.) 383–396 (Academic Press, 2020). doi:https://doi.org/10.1016/B978-0-12-801238-3.11177-8.

25. Wagermaier, W. & Fratzl, P. B. T.-R. M. in M. S. and M. E. Collagen. in (Elsevier, 2016). doi:https://doi.org/10.1016/B978-0-12-803581-8.01493-4.

26. Farbod, K., Nejadnik, M. R., Jansen, J. A. & Leeuwenburgh, S. C. G. Interactions between inorganic and organic phases in bone tissue as a source of inspiration for design of novel nanocomposites. *Tissue Eng. Part B. Rev.* **20**, 173–188 (2014).

27. Moran, M. E., Hodgson, J. L., Jensen, J. F. & Wood, T. L. Musculoskeletal injury survivors' resiliency: A systematic review. *Disabil. Health J.* **14**, 100987 (2021).

28. Teo, W. Z. W. & Schalock, P. C. Metal Hypersensitivity Reactions to Orthopedic Implants. *Dermatol. Ther. (Heidelb).* **7**, 53–64 (2017).

29. Dabrowski, B., Swieszkowski, W., Godlinski, D. & Kurzydlowski, K. J. Highly porous titanium scaffolds for orthopaedic applications. *J. Biomed. Mater. Res. Part B Appl. Biomater.* **95B**, 53–61 (2010).

30. Pohler, O. E. M. Unalloyed titanium for implants in bone surgery. *Injury* **31**, D7–D13 (2000).

31. Abdel-Hady Gepreel, M. & Niinomi, M. Biocompatibility of Ti-alloys for long-term implantation. *J. Mech. Behav. Biomed. Mater.* **20**, 407–415 (2013).

32. Takemoto, M. *et al.* Mechanical properties and osteoconductivity of porous

bioactive titanium. *Biomaterials* **26**, 6014–6023 (2005).

33. Oh, I.-H., Nomura, N., Masahashi, N. & Hanada, S. Mechanical properties of porous titanium compacts prepared by powder sintering. *Scr. Mater.* **49**, 1197–1202 (2003).

34. Liu, X., Chu, P. K. & Ding, C. Surface modification of titanium, titanium alloys, and related materials for biomedical applications. *Mater. Sci. Eng. R Reports* **47**, 49–121 (2004).

35. Apostu, D., Lucaciu, O., Berce, C., Lucaciu, D. & Cosma, D. Current methods of preventing aseptic loosening and improving osseointegration of titanium implants in cementless total hip arthroplasty: a review. *J. Int. Med. Res.* **46**, 2104–2119 (2018).

36. Lombardi, A. V. J., Mallory, T. H., Vaughn, B. K. & Drouillard, P. Aseptic loosening in total hip arthroplasty secondary to osteolysis induced by wear debris from titanium-alloy modular femoral heads. *J. Bone Joint Surg. Am.* **71**, 1337–1342 (1989).

37. Tsaryk, R. *et al.* Response of human endothelial cells to oxidative stress on Ti6Al4V alloy. *Biomaterials* **28**, 806–813 (2007).

38. Moyen, B. J., Lahey, P. J. J., Weinberg, E. H. & Harris, W. H. Effects on intact femora of dogs of the application and removal of metal plates. A metabolic and structural study comparing stiffer and more flexible plates. *J. Bone Joint Surg. Am.* **60**, 940–947 (1978).

39. Parvizi, J., Suh, D.-H., Jafari, S. M., Mullan, A. & Purtill, J. J. Aseptic loosening of total hip arthroplasty: infection always should be ruled out. *Clin. Orthop. Relat. Res.* **469**, 1401–1405 (2011).

40. Gredić, T., Zlatanović, M. & Münz, W.-D. Plasma nitriding of Ti and Ti-Al coatings. *Surf. Coatings Technol.* **61**, 338–345 (1993).

41. Zheng, J.-H., Kato, M. & Nakasa, K. Effect of intermediate layer on wear-delamination life of low-frictional SiC-2.6mass%Ti film sputter-deposited on titanium substrate. *Surf. Coatings Technol.* **205**, 2532–2537 (2010).

42. Otsuka, Y., Kojima, D. & Mutoh, Y. Prediction of cyclic delamination lives of plasma-sprayed hydroxyapatite coating on Ti–6Al–4V substrates with considering wear and dissolutions. *J. Mech. Behav. Biomed. Mater.* **64**, 113–124 (2016).

43. Chung, Y.-Y. *et al.* High revision rate of hydroxyapatite-coated ABG-I prosthesis. *J. Orthop. Sci.* **14**, 543–547 (2009).

44. Pieralli, S., Kohal, R. J., Jung, R. E., Vach, K. & Spies, B. C. Clinical Outcomes of Zirconia Dental Implants: A Systematic Review. *J. Dent. Res.* **96**, 38–46 (2017).

45. Cionca, N., Hashim, D., Cancela, J., Giannopoulou, C. & Mombelli, A. Pro-inflammatory cytokines at zirconia implants and teeth. A cross-sectional assessment. *Clin. Oral Investig.* **20**, 2285–2291 (2016).

46. Scarano, A., Piattelli, M., Caputi, S., Favero, G. A. & Piattelli, A. Bacterial adhesion on commercially pure titanium and zirconium oxide disks: an in vivo

human study. *J. Periodontol.* **75**, 292–296 (2004).

47. Cionca, N., Hashim, D. & Mombelli, A. Zirconia dental implants: where are we now, and where are we heading? *Periodontol. 2000* **73**, 241–258 (2017).

48. Kuroda, K. & Okido, M. Hydroxyapatite coating of titanium implants using hydroprocessing and evaluation of their osteoconductivity. *Bioinorg. Chem. Appl.* **2012**, 730693 (2012).

49. Huang, C. H. & Yoshimura, M. Direct ceramic coating of calcium phosphate doped with strontium via reactive growing integration layer method on α-Ti alloy. *Sci. Rep.* **10**, 10602 (2020).

50. Wu, C. T. & Chang, J. Silicate bioceramics for bone tissue regeneration. *Wuji Cailiao Xuebao/Journal Inorg. Mater.* **28**, 29–39 (2013).

51. Huang, Y., Wu, C., Zhang, X., Chang, J. & Dai, K. Regulation of immune response by bioactive ions released from silicate bioceramics for bone regeneration. *Acta Biomater.* **66**, 81–92 (2018).

52. Wang, C. *et al.* Preparation of laponite bioceramics for potential bone tissue engineering applications. *PLoS One* **9**, e99585–e99585 (2014).

53. Dong, X. *et al.* Inhibition of the negative effect of high glucose on osteogenic differentiation of bone marrow stromal cells by silicon ions from calcium silicate bioceramics. *Regen. Biomater.* **7**, 9–17 (2020).

54. McEntire, B. J. & Lakshminarayanan, R. Processing and Characterization of

Silicon Nitride Bioceramics. *Bioceram. Dev. Appl.* **6**, 1–9 (2016).

55. Awad, K. R. *et al.* Silicon nitride enhances osteoprogenitor cell growth and differentiation via increased surface energy and formation of amide and nanocrystalline HA for craniofacial reconstruction. *Med. DEVICES SENSORS* **2**, e10032 (2019).

56. Ilyas, A. *et al.* Amorphous Silica: A New Antioxidant Role for Rapid Critical-Sized Bone Defect Healing. *Adv. Healthc. Mater.* **5**, 2199–2213 (2016).

57. Monte, F. A. do *et al.* Amorphous Silicon Oxynitrophosphide-Coated Implants Boost Angiogenic Activity of Endothelial Cells. *Tissue Eng. Part A* **26**, 15–27 (2019).

58. Monte, F. *et al.* Ionic silicon improves endothelial cells' survival under toxic oxidative stress by overexpressing angiogenic markers and antioxidant enzymes. *J. Tissue Eng. Regen. Med.* **12**, 2203–2220 (2018).

59. Nakayama, K. H. *et al.* Treatment of volumetric muscle loss in mice using nanofibrillar scaffolds enhances vascular organization and integration. *Commun. Biol.* **2**, 170 (2019).

60. Goldman, S. M., Henderson, B. E. P., Walters, T. J. & Corona, B. T. Co-delivery of a laminin-111 supplemented hyaluronic acid based hydrogel with minced muscle graft in the treatment of volumetric muscle loss injury. *PLoS One* **13**, e0191245 (2018).

61. Kasukonis, B. *et al.* Codelivery of Infusion Decellularized Skeletal Muscle with Minced Muscle Autografts Improved Recovery from Volumetric Muscle Loss Injury in a Rat Model. *Tissue Eng. Part A* **22**, 1151–1163 (2016).

62. Quintero, A. J., Wright, V. J., Fu, F. H. & Huard, J. Stem cells for the treatment of skeletal muscle injury. *Clin. Sports Med.* **28**, 1–11 (2009).

63. Stilhano, R. S., Martins, L., Ingham, S. J. M., Pesquero, J. B. & Huard, J. Gene and cell therapy for muscle regeneration. *Curr. Rev. Musculoskelet. Med.* **8**, 182–187 (2015).

64. Rizzi, R. *et al.* Tissue engineering for skeletal muscle regeneration. *Muscles. Ligaments Tendons J.* **2**, 230–234 (2012).

65. Patel, A. *et al.* Carbon-based hierarchical scaffolds for myoblast differentiation: Synergy between nano-functionalization and alignment. *Acta Biomater.* **32**, 77–88 (2016).

66. Poussard, S. *et al.* Internalization and fate of silica nanoparticles in C2C12 skeletal muscle cells: Evidence of a beneficial effect on myoblast fusion. *Int. J. Nanomedicine* **10**, 1479–1492 (2015).

67. Quiroga, H. P. O., Goto, K. & Zammit, P. S. Skeletal Muscle Regeneration in the Mouse. *Methods Mol. Biol.* **1460**, 85–100 (2016).

68. Gurevich, D., Siegel, A. & Currie, P. D. Vertebrate Myogenesis. *Results Probl. Cell Differ.* **56**, 191–213 (2015).

69. Shintaku, J. *et al.* MyoD Regulates Skeletal Muscle Oxidative Metabolism Cooperatively with Alternative NF-κB. *Cell Rep.* **17**, 514–526 (2016).

70. Han, X. H., Jin, Y.-R., Seto, M. & Yoon, J. K. A WNT/beta-catenin signaling activator, R-spondin, plays positive regulatory roles during skeletal myogenesis. *J. Biol. Chem.* **286**, 10649–10659 (2011).

71. Pedersen, B. K. Muscles and their myokines. *J. Exp. Biol.* **214**, 337–346 (2011).

72. Ostrovidov, S. *et al.* 3D Bioprinting in Skeletal Muscle Tissue Engineering. *Small* **15**, 1–14 (2019).

73. Ostrovidov, S. *et al.* Stem Cell Differentiation Toward the Myogenic Lineage for Muscle Tissue Regeneration: A Focus on Muscular Dystrophy. *Stem cell Rev. reports* **11**, 866–884 (2015).

74. Asadi, N., Del Bakhshayesh, A. R., Davaran, S. & Akbarzadeh, A. Common Biocompatible Polymeric Materials for Tissue Engineering and Regenerative Medicine. *Mater. Chem. Phys.* 122528 (2019) doi:https://doi.org/10.1016/j.matchemphys.2019.122528.

75. Rinaudo, M. Biomaterials based on a natural polysaccharide: alginate. *TIP* **17**, 92–96 (2014).

76. Hosseini, V. *et al.* Engineered contractile skeletal muscle tissue on a microgrooved methacrylated gelatin substrate. *Tissue Eng. Part A* **18**, 2453–2465 (2012).

77. Jana, S., Levengood, S. K. L. & Zhang, M. Anisotropic Materials for Skeletal-Muscle-Tissue Engineering. *Adv. Mater.* **28**, 10588–10612 (2016).

78. Memic, A. *et al.* Nanofibrous Silver-Coated Polymeric Scaffolds with Tunable Electrical Properties. *Nanomater. (Basel, Switzerland)* **7**, (2017).

79. Shi, X. *et al.* Microfluidic Spinning of Cell-Responsive Grooved Microfibers. *Adv. Funct. Mater.* **25**, 2250–2259 (2015).

80. X, C., G, G. & Y, Q. Accelerated myotube formation using bioprinting technology for biosensor applications. *Biotechnology Letters* vol. 35 315–321.

81. Henstock, J. R., Canham, L. T. & Anderson, S. I. Silicon: The evolution of its use in biomaterials. *Acta Biomater.* **11**, 17–26 (2015).

82. Gaharwar, A. K. *et al.* Bioactive silicate nanoplatelets for osteogenic differentiation of human mesenchymal stem cells. *Adv. Mater.* **25**, 3329–3336 (2013).

83. Ilyas, A., Lavrik, N. V, Kim, H. K. W., Aswath, P. B. & Varanasi, V. G. Enhanced Interfacial Adhesion and Osteogenesis for Rapid “Bone-like” Biomineralization by PECVD-Based Silicon Oxynitride Overlays. *ACS Appl. Mater. Interfaces* **7**, 15368–15379 (2015).

84. Bhuyan, M. K., Rodriguez-Devora, J. I., Fraser, K. & Tseng, T. L. B. Silicon substrate as a novel cell culture device for myoblast cells. *J. Biomed. Sci.* **21**, 4–8 (2014).

85. AWAD, K. R. *et al.* Micro-patterned Bioactive Amorphous Silicon Oxynitride

Enhances Adhesion, Growth, and Myotubes and Axon Alignment in Muscle and Nerve Cells. *FASEB J.* **34**, 1 (2020).

86. Ahuja, N. *et al.* Preliminary study of in-situ 3D bioprinted nano-silicate biopolymer scaffolds for muscle repair in VML defects. *FASEB J.* **34**, 1 (2020).

87. Awad, K. R. *et al.* Patterned Silicon Oxynitride (SiONx) Scaffolds Enhance Alignment and Myogenic Differentiation of C2C12 Muscle Cells. *FASEB J.* **33**, 539.5-539.5 (2019).

CHAPTER 3: HEPATOCYTE GROWTH FACTOR ADMINISTRATION INCREASES BONE SOLUBLE PHOSPHATE AND ALTERS BONE CHEMICAL STRUCTURE IN DIABETIC HYPERTENSIVE RATS

Kamal Awad[a,b,c], Natasha G Boyes[d], Ramlah Iqbal[d,e], Mohamed Ahmed[e], Adel Mohamed[e], Pranesh Aswath[a], Corey R. Tomczak[d], Venu Varanasi[a,b,*]

a. Department of Materials Science and Engineering, College of Engineering, University of Texas at Arlington, Texas 76019, USA.
b. Bone-Muscle Research Center, College of Nursing & Health Innovation, University of Texas at Arlington, Texas 76019, USA.
c. Department of Ceramics and Building materials, National Research Center, Dokki, Cairo, Egypt, 12622.
d. College of Kinesiology, University of Saskatchewan, Saskatoon, SK, Canada.
e. Departments of Anatomy, Physiology, and Pharmacology, College of Medicine, University of Saskatchewan, Saskatoon, SK, Canada.

Corresponding author

Dr. Venu Varanasi, PhD

Associate Professor, Bone Muscle Research Center

College of Nursing and Health Innovation

University of Texas at Arlington

Address: 655 W. Mitchell St., Box 19410, Arlington, TX 76019

Email: Venu.varanasi@uta.edu

Phone: 817-272-1743

ABSTRACT

Hepatocyte growth factor (HGF) is a novel potential therapy for improving bone health in patients with type II diabetes and hypertension, but its effect on the bone molecular structure has not been revealed yet. Here, X-ray absorption near edge structure (XANES) spectroscopy was used to explore the effects elicited by HGF on the bone's chemical structure. This study assessed local calcium (Ca) and phosphorus (P) coordination of diabetic hypertensive rat bones, each with and without HGF treatment. Results revealed that HGF has significant effects on Ca and P coordination chemistry as confirmed by presence of more soluble phosphates in the HGT treated groups. Data indicated that treated bones have a poorly developed phosphate structure as proved by a drastic drop in post-edge shoulder in P $L_{2,3}$-edge compared to diabetic-hypertensive and diabetic-control bone. The presence of soluble Ca and P and the products of bone resorption with HGF treatment suggests unbalanced bone resorption and formation.

Keywords: Bone; Fracture; Chemical composition; Tissue; biomedical; XANES; HGF.

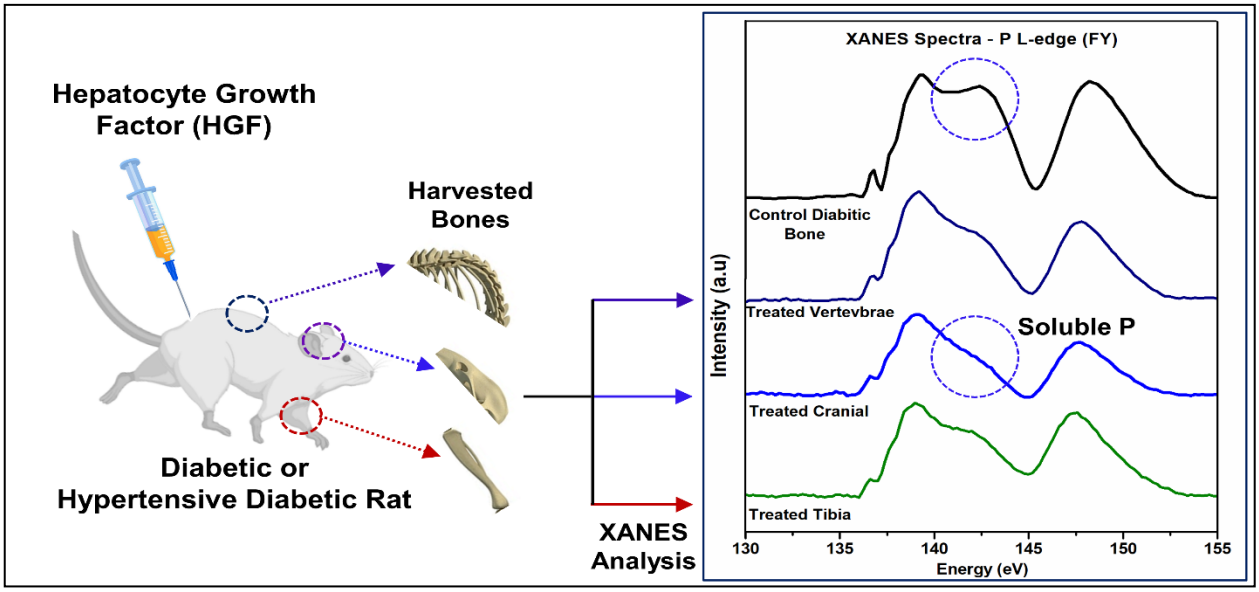

Figure 3.0: Graphical abstract: XANES analysis of extracted rat bones.

1. INTRODUCTION

Patients with type II diabetes mellitus have insulin deficiency and peripheral insulin resistance [1]. Diabetes is associated with increased morbidity, mortality, and economic cost [1,2]. The relationship between diabetes and bone health is complex, type dependent [3], and bilateral, such that (a) bone tissue helps regulate glucose metabolism, and (b) insulin levels affect bone formation and bone resorption [4]. Patients with type II diabetes have normal-to-increased areal bone mineral density [4–6], most likely caused by the decreased bone turnover because of excess circulating insulin levels, which occurs because of insulin resistance [4,7]. Simultaneously, patients with type II diabetes exhibit increased cortical porosity or other deficits in bone microarchitecture or chemical structure [8–11] that contribute to bone fragility [4]. Indeed, despite possessing higher bone mineral density, patients with type II diabetes have a higher fracture risk for vertebral, hip, and other nonvertebral bones [12,13], even after adjusting for bone mineral density [6,14]. Anti-diabetic medications (e.g., insulin, metformin) have mixed evidence on their relationship with bone fracture incidence [15,16], but insulin treatment may increase risk of fractures [16]. Despite a clear relationship between type II diabetes and bone fragility and health, the mechanisms and pathogenesis of this complex relationship remain unclear, and treatment options targeting bone fragility are lacking.

Type II diabetes and hypertension are often found together and thus share pathophysiological mechanisms [17–20]. Indeed, 50-85% of patients with type II diabetes also live with hypertension, and 50% of hypertensive patients exhibit glucose intolerance, insulin resistance, or type II diabetes [17,21–23]. Hypertension is associated with lower bone mineral density [24], higher bone loss [25], and greater fracture risk [26],

independent of bone mineral density in women [27]. Mechanistically, chronic hypertension can increase calcium loss in the urine [28], which may impact bone remodeling [27] and lower bone mineral density [24]. Effects of cardiovascular medications on bone fracture risk in hypertensive patients has mixed evidence; thiazide diuretics seem to exhibit a moderately protective effect based on a randomized clinical trial [29], while it appears that beta-blockers, calcium channel blockers, and renin-angiotensin system blockade may each have mild, but not clinically significant, protective effects [29]. The role that medications play in mitigating fracture risk in combined diabetes and hypertension is, to our knowledge, understudied and unknown. An effective treatment that addresses the combined negative impact of diabetes and hypertension on bone has not been studied.

Hepatocyte growth factor (HGF) is a soluble cytokine previously known as scatter factor, secreted from differentiated mesenchymal stem cells [30,31]. HGF is implicated in osteogenesis, bone repair, and bone remodeling [30]. HGF has been found to reverse the fibrogenic process, inhibit the extra cellular matrix (ECM) deposition, suppress collagen synthesis, and reduce the amount of pre-existing extracellular matrix including fibrillar collagen [32–34]. HGF enhances metalloproteinase-1 (MMP-1) production which in turn moves to the susceptible sites in collagen and then unwinds the triple helix structure of collagen [35]. The consequential effect of breaking the hydrogen bonds linking in the center of triple helix (i.e., N-H of glycine with C=O of adjacent polypeptide) and removal of collagen C-terminus is the exposing of the scissile bond en-route to the digestion of the outer layer of monomers in the collagen fibril [35,36]. However, little is known on the effect of HGF on the chemical structure of the bone mineral phase. Understanding these changes are vital as they have implications in overall bone health.

HGF interacts with its cognate receptor, c-Met, found in osteoblasts, osteoclasts, and epithelial and endothelial cells of multiple tissues, including bone marrow [30,31]. HGF-to-c-Met binding causes a signaling cascade with multiple downstream effects, including increased osteoclast migration, spread area [37], osteoclast activity at the bone site [38], consequent bone resorption by osteoclasts (mediated by osteoblasts) [37], and osteoblast cell cycle progression [38]. HGF can support the survival and proliferation of osteoclast precursors and can replace other stimulating factors (e.g., M-CSF) to support osteoclast differentiation in human cells [39]. Using in vitro human mesenchymal stem cells, HGF promoted osteogenic differentiation via expression and transcription of osteogenic markers (i.e., osteocalcin, osterix, osteoprotegerin) and was thus deemed necessary for osteoblast mineralization [40]. Furthermore, in an application of a drug delivery model in vitro, blocking endogenous HGF signaling in MSCs disrupted osteogenesis in a dose-dependent manner [40]. HGF increased differentiation of mesenchymal stem cells into osteoblasts and displayed evidence of femoral head tissue repair in rabbits, an effect that was HGF concentration dependent [41]. An HGF treatment enhanced osteoblast differentiation when used as a bone implant coating on hydroxyapatite surfaces to enhance implant-to-bone integration [42]. Finally, in an in vivo rabbit tibial osteotomy model, HGF administration increased bone healing (i.e., bone mineralization, angiogenesis, new bone formation, and absorption of applied β-tricalcium phosphate) and mechanical bone strength, particularly in the early phase of healing following the tibial osteotomy [43]. On the other hand, HGF was embedded in a biodegradable gelatin hydrogel for continuous release for a period of 2 weeks to enhance the in vivo regenerative effect of HGF [44]. Thus, for HGF to have potential use

in drug delivery in bone tissue regeneration, further studies on its effects on bone mineral chemistry and structure are necessary.

Interestingly, osteoclasts secrete HGF, suggesting that HGF activity operates in an autocrine-paracrine regulation feedback loop of bone remodeling [38]. HGF may be a coupling factor between osteoblasts and osteoclasts, such that HGF stimulates osteoclast bone resorption, which in turn stimulates osteoblast new bone formation [38]. It may be possible that the presence of localized soluble Ca and P with the HGF treatment could suggest unbalanced bone resorption and formation, however, no study has detected such an effect to this day. The stimulation of both osteoclasts and osteoblasts by HGF allows bone resorption and deposition to be tightly coupled for sophisticated bone remodeling [38] and may thus be an optimal targeted treatment for bone fragility in patients with type II diabetes and hypertension. However, there is no in-vivo data regarding the effect of HGF treatment on bone health in type II diabetes and hypertension. To explore this literature gap, knowledge of the chemical coordination of diabetic and hypertensive bone could help understand the pathophysiology of these combined comorbidities and thereby improve therapies.

X-ray Absorption Near Edge Structure (XANES) is a commonly used spectroscopic technique to study the chemical structure/coordination that yield insight into the types of present bond in the materials. XANES spectroscopy provides information on the oxidation state, coordination number of individual elements as well as the chemical structure of biomaterial. As reported, analyses of apatite-group minerals indicate that XANES spectral patterns are not strongly affected by crystallinity [45]. Thus, XANES is used to evaluate the structural environment of Ca and P in the inorganic

phase of bone (i.e., hydroxyapatite), which is an integral component of bone [46–49]. Obtaining this information could reveal changes in the local environment of Ca and P ions in bone, thereby investigating changes in bone nature and mineralization because of diabetes and hypertension, as well as the subsequent potential treatment of HGF.

Thus, the purpose of this study was to assess the local Ca and P coordination of combined diabetic and hypertensive cranial, vertebral, and tibial rat bones, each with and without HGF treatment. We hypothesized that HGF will increase the rate of bone remodeling, such that levels of soluble Ca and P will be greater in the bones treated with HGF compared to both untreated combined diabetic and hypertensive rat bones, and untreated diabetic control rat bones.

2. MATERIALS AND METHODS

2.1. Animals and Materials

Twenty-four male Zucker diabetic fatty (ZDF) rats (9-11 weeks old) were purchased from Charles River as part of a larger ZDF rat study. Three of these ZDF rats were subsequently used for the current XANES protocol and analysis. All protocols were approved by the Animal Research Ethics Board at the University of Saskatchewan (#20170030; approval granted on April 24, 2019) and followed the guidelines of the Canadian Council on Animal Care. ZDF rats were acclimatized for one week in the animal care facility with free access to food and water. Rats were subcutaneously given long-acting insulin (Glargine; Sanofi-Aventis, Frankfurt -Höchst, Germany) to maintain a fasting plasma glucose at ~30 mmol/L. Daily injection of insulin was given to prevent uncontrolled hyperglycemia. Body weight and fasting blood glucose (glucometer) were monitored weekly. ZDF rats exhibit obesity with diabetes and are widely used in the

study of type II diabetes [50]. They develop insulin resistance and glucose intolerance at the age of 3-8 weeks and become overtly diabetic between 8-10 weeks of age [50]. However, ZDF rats do not develop hypertension, therefore, the current study initiated and established hypertension via deoxycorticosterone acetate (DOCA)-salt treatment. ZDF rats were then divided into 1 of 3 conditions: (1) control diabetic; (2) hypertensive diabetic; and (3) treated hypertensive diabetic. To serve as a control diabetic condition, 1 ZDF rat was injected subcutaneously with a 1mL mixture of 50% propylene glycol and 50% 0.9 saline twice weekly for 4 weeks. To serve as a hypertensive diabetic condition, 1 ZDF rat was injected subcutaneously with DOCA (Sigma Aldrich, Canada) and 1mL mixture of 50% propylene glycol and 50% 0.9 saline twice weekly and was given 1% NaCl in their daily drinking water for 4 weeks [51]. To serve as a treated hypertensive diabetic condition, 1 ZDF rat was treated with HGF subcutaneous injections (500 µg/kg body weight) [52], was given DOCA with 50% propylene glycol and 50% 0.9 saline twice weekly and received 1% NaCl in their daily drinking water for 4 weeks.

2.2. Bone Collection

Rats were euthanized after 8 weeks following study initiation. Bone samples were excised immediately after euthanasia. Cranial, vertebral, and tibial bones were collected from each subject and refrigerated (4-6˚C) in formaldehyde (separate tube per subject) until sample preparation prior to XANES analysis.

2.3. Sample Preparation

Bone samples were cleaned of tissue and cut into approximately 2 mm × 2 mm pieces. Samples were then sequentially dehydrated in ethanol and placed in a vacuum chamber for 72+ hours to allow for complete dehydration of the samples. Cranial bone

samples consisted of outer and inner cortical layers and a middle trabecular layer. Vertebral samples consisted of both outer cortical bone and a layer of inner trabecular bone. Tibial samples consisted of outer cortical bone and a layer of inner trabecular bone, harvested at the tibial proximal epiphysis.

2.4. XANES Analysis

XANES utilizes the white radiation (X-ray) generated from a synchrotron [49,53] which generates an intense electromagnetic beam by accelerating charged particles at near-light speeds [54]. This electromagnetic radiation (i.e., X-ray) has sufficient energy to excite a core electron of an atom to an empty hole below the ionization threshold, “excitonic state”, or above the ionization threshold, “continuum state” [55]. When a core electron absorbs an X-ray photon with energy matched to its distinct binding energy, it will be ejected from its core thereby leaving a core hole. These extremely energetic core holes have an average life span of 1 femtosecond due to their unstable nature, so it decays rapidly through Auger electron ejection or X-ray emission [56]. The typical XANES spectra consist of three different zones: a pre-edge, an absorption main edge, and a post-edge. The ‘edge’ means that each spectrum is taken around an element-specific core-electron excitation energy, for example the K- and L-energy level led to K- and $L_{2,3}$-edge spectra, respectively [57]. The absorption edge is a phenomenon that corresponds to absorption of the X-ray photon by a specific type of core electron and appears as an abrupt increase in the absorption. It is used to determine the oxidation state and it can be shifted up to 5 eV per one-unit change. The pre-edge structures appear as a weak transition below the absorption edge, and it can be used to investigate the local geometry around an absorption atom. The post-edge appears because of the scattering

of photoelectrons at low kinetic energy and provides information about the atomic position of the neighbor atoms. The absorption can be measured through the current or total electron yield (TEY) or the fluorescence yield (FY) of the materials during absorption [57,58].

In this study, P $L_{2,3}$-edge, P K-edge, Ca $L_{2,3}$-edge, Ca K-edge, and O K-edge were used to characterize the chemical structure of the three study groups: untreated diabetic control, untreated diabetic hypertensive, and HGF treated diabetic hypertensive rat bones. Data were obtained at the Canadian Light Source (CLS), Saskatoon, Canada, using three different beam lines [59]. The beam lines include the Variable Line Spacing Plane Grating Monochromator (VLS-PGM-11ID-2) for the P $L_{2,3}$-edge fluorescence yield XANES spectra, the High-Resolution Spherical Grating Monochromator (SGM-11ID-1) for the Ca $L_{2,3}$-edge and O K-edge in total electron yield XANES spectra, and The Soft X-ray Microcharacterization Beamline (SXRMB, 06B1-1) was for the P K-edge and Ca K-edge spectra. The energy range, specific edges, resolution, and spot size for each beamline are listed in Supplementary Information 1. To characterize the chemical structure of each bone by type and group, powdered model compounds of known chemical compositions were analyzed to compare with our spectra obtained from regions of the cranial, tibial, and vertebral bones. These model compounds include alpha tricalcium phosphate (α-$Ca_3(PO_4)_2$; α-TCP), beta tricalcium phosphate (β-$Ca_3(PO_4)_2$; β-TCP), Ca carbonate ($CaCO_3$), Ca oxide (CaO), monetite or Ca monohydrogen phosphate ($CaHPO_4$), Ca pyrophosphate ($Ca_2P_2O_7$), and hydroxyapatite ($Ca_{10}(PO_4)_6(OH)_2$; HA). The model compounds were studied to compare distinct features that can be shared with XANES spectra of different regions of bone

(i.e., cranium, tibia, vertebrae). Prior any bone sample testing, complete set of standards model compounds were investigated to account for any beam shift in guidance of the standard reported literature. Longitudinal sections of each tested bone were placed on the specific beamline holder for consistent analysis. Ten consecutive scans were recorded each time for each sample, the spectra were averaged and used for analysis. The incident beam (I_0) was measured simultaneously using ion chambers for SXRMB beamline, or from the current emitted from nickel mesh (for VLS PGM beamline) and gold mesh (for SGM beamline) located just before the KB focusing mirrors which is the last optical elements of the beamline. The sample's stage is set at 45° to both the incident beam and detector for all used beamlines. All spectra were normalized to the intensity of the (I_0), followed by background subtraction, and Lorentzians multiple peaks fitting using origin pro software. The background correction was performed by subtracting an extrapolated linear curve between the starting point of the first pre-edge feature and the first data point to ensure a consistent data treatment.

3. RESULTS AND DISCUSSION

XANES spectroscopy was used to study the changes in the chemical coordination of the different types of bone (diabetic control, diabetic hypertensive, and HGF treated diabetic hypertensive). XANES spectra showed the contribution of Ca, P, and O in the chemical structure of the studied bones that were compared to the standard model compounds used in this study. In this section, we will present the results of P L- & K-edge, Ca L- & K-edge, and O K-edge for the standard model compounds and the bone samples.

3.1 Phosphorus L2,3-edge fluorescence yield (FY) XANES spectra of standard model compounds:

P $L_{2,3}$-edge is ideally used to distinguish between different phosphate compounds bonded with Ca in bone samples [46,47,49]. Thus, all the examined model compounds were mainly coordinated with Ca. Figure 1 shows the P $L_{2,3}$-edge FY XANES spectra of six standard model compounds: HA, nano-HA, $CaHPO_4$, $Ca_2P_2O_7$, β-TCP, and α-TCP. P $L_{2,3}$-edge spectra for all standards were in an agreement with the P $L_{2,3}$-edge XANES reference compounds reported by the CLS researchers [60]. All standard model compounds show the first pre-edge peaks, “a”, appearing initially at 135.5 eV for α-TCP and β-TCP, followed by pre-edge peaks for HA, $Ca_2P_2O_7$, and $CaHPO_4$ occurring at 136.5 eV. The second pre-edge peaks, “b”, appear at 137.5 eV for HA, nano-HA, and $Ca_2P_2O_7$, and clearly appeared as a shoulder in $CaHPO_4$, while α-TCP and β-TCP show a second pre-edge peak at 137.0 eV. The second pre-edge peak of α-TCP was clearly identified as a weak shoulder while β-TCP presented a distinctive feature that makes it unique compared to other model compounds, a presence of a third

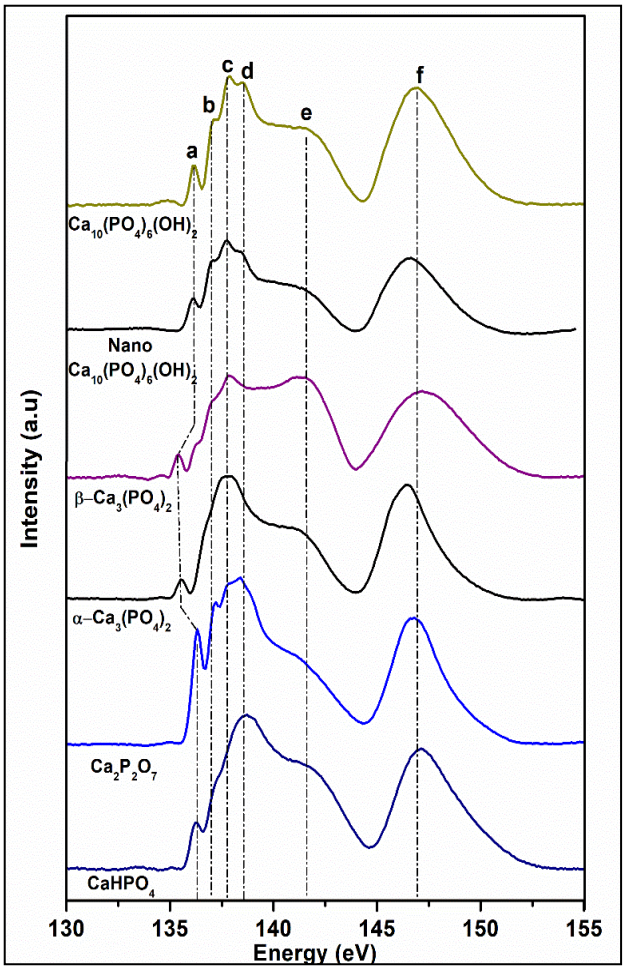

Figure 3.1: Phosphorus $L_{2,3}$-edge FY XANES spectra of the model compounds.

pre-edge peak at 136.6 eV. The first and second pre-edge peaks are typically separated by 1 eV and arise from the spin-orbital splitting of 2p electrons into $2p_{1/2}$ and $2p_{3/2}$ levels that represents L_3 and L_2 edges, respectively [49,60]. The main $L_{2,3}$-edge peak, “c”, for HA, α-TCP, β-TCP, and $Ca_2P_2O_7$ appears at 137.9 eV, while the main edge peak for $CaHPO_4$ arises at 138.5 eV. The main edge peaks arise due to the electron transition to 3p orbitals that exist in the presence of other elements such as O and cationic species such as Ca. A unique post-edge peak, “d”, for HA and $Ca_2P_2O_7$ occurs at 138.6 eV that is absent in the other model compounds. For HA and β-TCP, a flat line shoulder “e” parallel to the X-axis was observed between 139.0 eV and 142.0 eV. This flat shoulder is a prominent feature for the less soluble phosphate compounds [49,60]. Thus, the remaining model compounds have more soluble phosphates as indicated by the drooping in the post-edge shoulder. The secondary peak “f” that appears at 147.2 eV for β-TCP and at 146.7 eV for the other model compounds is attributed to the transition from the 2p to the 3d orbital in P. Based on our results from P $L_{2,3}$-edge FY data, the model compounds are consistent with the previously reported data [46,47,49,60]. A third pre-edge peak at 136.3 eV is a unique feature for the β-TCP, and the post-edge peak at 138.6 eV can be used to distinguish HA from all other model compounds.

3.2 Phosphorus $L_{2,3}$-edge FY XANES spectra of the bone samples:

P $L_{2,3}$-edge FY data were collected to compare the HGF treated diabetic hypertensive rat bones to the untreated diabetic hypertensive bones and the diabetic control bones as shown at Figure 2. Key distinctive differences arose between the standard model compound results and the three bone sample group results. All bone samples showed a first pre-edge peak, “a”, at 135.5 eV, a second pre-edge peak, “b”, at

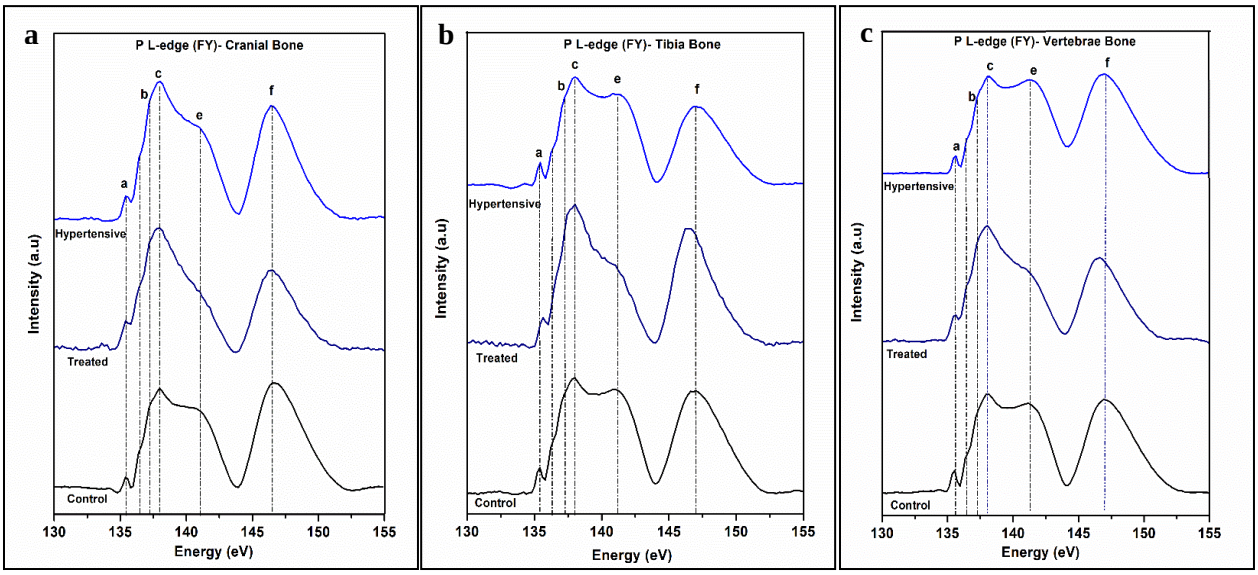

Figure 3.2: Phosphorus $L_{2,3}$-edge FY XANES spectra of the a) Control, treated, and hypertensive cranial bone, b) Control, treated, and hypertensive tibial bone, and c) Control, treated, and hypertensive vertebral bone.

137.0 eV, and a third pre-edge shoulder at 136.3 eV. The main edge peak “c” appears at 137.9 eV for the three groups (Figure 2-a-c). A flat line shoulder “e” is parallel to the X-axis and extends from 139.0 to 142.0 eV in the diabetic control and diabetic hypertensive samples of the cranial, tibial, and vertebral bones. Although the diabetic hypertensive cranial, tibial, and vertebral bones all showed a flat line shoulder, the intensity of these shoulders were reduced compared to the diabetic control bones which in turn presented a high intensity shoulder post-edge peak. Interestingly, the treated diabetic hypertensive cranial, tibial, and vertebral bones showed a drooping in the post-edge shoulder indicating more soluble phosphates compared to the untreated diabetic hypertensive and diabetic control bones. Finally, wide secondary peaks, “f”, appeared at 147.3 eV for untreated diabetic control bone samples while the treated bones and diabetic hypertensive spectra were shifted to a lower energy at 146.5 eV. The examined bone sample chemical structure can be explained by comparing their spectra to those of

the standard model compounds resulted in section 3.1. Cranial, tibial, and vertebral bone samples from all three groups exhibited a third pre-edge peak at 136.3 eV which is identical with the third pre-edge peak of the standard β-TCP. Furthermore, the secondary peaks that appeared at 147.3 eV in all three groups are identical with the secondary peak of β-TCP model compound. Thus, the chemical structure of the tested bone approximates the chemical structure of β-TCP more closely than the remaining model compounds. Only the HGF treated diabetic hypertensive tibial and vertebral bones showed a secondary peak at 146.5 eV which is closer to the secondary peak of the HA model compound and indicates the presence of HA along with the β-TCP in this group only. As mentioned above, all HGF treated cranial, tibial, and vertebral bones showed a drop in the intensity of the post-edge shoulder which confirms the presence of more soluble phosphates that may be attributed to the effect of the HGF treatment. The HGF treated bones appear to have poorly developed phosphate structure as evidenced by the sloping shoulder of the cranial, tibial, and vertebral bones. Although the untreated diabetic hypertensive bones presented a decrease in the post-edge shoulder intensity compared to the diabetic control bones, the HGF treated bones showed a drastic drop in the post-edge shoulder compared to the untreated diabetic hypertensive and diabetic control bones, confirming the presence of more soluble phosphates and poorly developed phosphate structure in the HGF treated samples. It is also important to note the difference in P coordination between the cranial, tibial and vertebral bones; the cranial bone has the smallest proportion of insoluble phosphates (β-TCP and HA), the vertebral bone has the highest proportion of β-TCP and HA, and the tibial bone P coordination is between the two but closer to the vertebral bone than the cranial bone.

Mechanistically, the difference in bone type P coordination may be due to the mechanical loading of the vertebrae and tibia, which may help in the mineralization process resulting in the formation of insoluble phosphates of Ca.

3.3 Phosphorus K-edge FY XANES spectra of the standard model compounds:

P K-edge FY analysis investigates the core shell "1s" electrons and the associated transitions in phosphate-containing compounds to differentiate between the different potential P coordination variations. Figure 3 illustrates the FY spectra of P K-edge of various Ca-P standard model compounds. All model compounds show the main absorption of P K-edge peak, "a", at 2152.3 eV and two post-edge peaks at 2162.8 eV and 2169.5 eV labeled respectively as "b" and "c", which are related to Ca-P and O oscillation, respectively [61]. Notably, β-TCP has the highest intensity peak, "b", while α-TCP, $Ca_2P_2O_7$, and $CaHPO_4$ show very low intensity for the same peak. Another post-edge peak, "d", was present for pure and nano HA at 2155.3 eV that was observed as a post-edge shoulder for the other model compounds, except $CaHPO_4$.

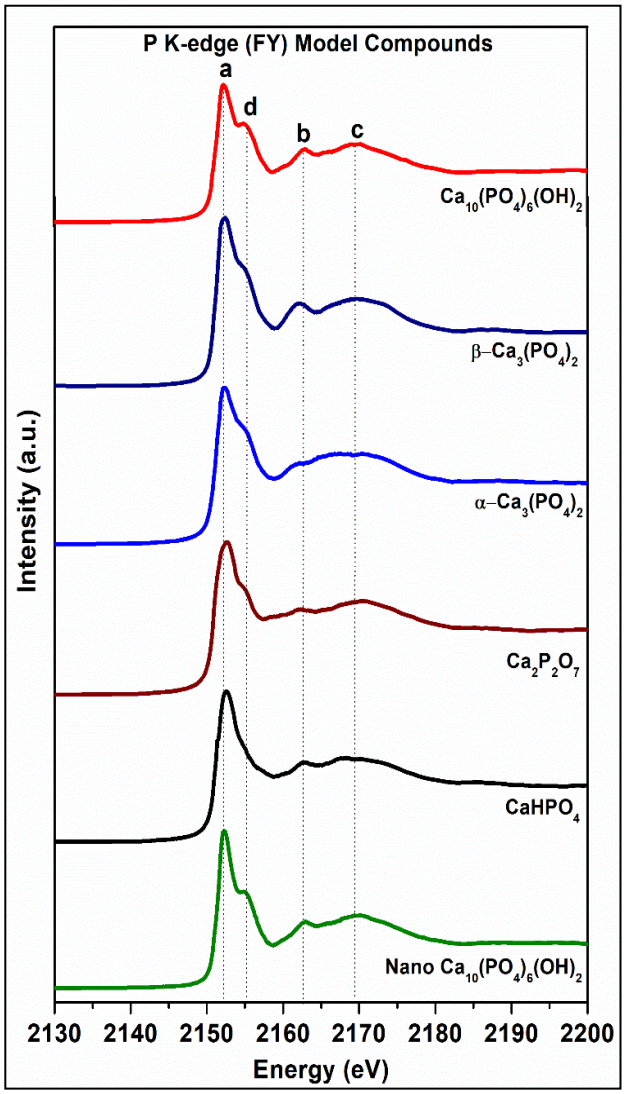

Figure 3.3: Phosphorus K-edge FY XANES spectra of the model compounds.

This shoulder is attributed to a transition of 1s P electrons to the 3d Ca orbital. The presence of a post-edge peak, “d”, is unique to HA and there are no other distinctive features that differentiate HA from the remaining model compounds on the P K-edge spectra. A close observation of this post-edge peak/shoulder at 2155.3 eV reveals that this shoulder is more defined for Ca phosphate compounds, like HA and β-TCP, with decreasing solubility and increasing thermodynamic stability. Based on the intensity of this shoulder, the solubility of the standard compounds can be ordered from less soluble to high soluble as follows: HA, β-TCP, α-TCP, $Ca_2P_2O_7$, and $CaHPO_4$. On the other hand, this shoulder tends to disappear in the more soluble Ca phosphate compounds like $CaHPO_4$. This behavior indicates that certain spectral features, such as this post-edge shoulder, become more distinct with increasing stability of the Ca phosphate phase. Spectra of P K-edge of various Ca phosphate standard model compounds are in excellent agreement with previously reported data [46,49,62].

3.4 Phosphorus K-edge FY XANES spectra of the bone samples:

Figure 4 presents the P K-edge FY spectra of the studied bone samples. All bone samples were generally similar with the spectra of the standard model compounds. All bone samples indicated the presence of the main absorption peak “a” of P K-edge followed by two post-edge peaks, “b” and “c”. The shoulder, “d”, was similar to the β-TCP standard for cranial and vertebral bones of all three groups. A slight decrease in the shoulder intensity can be observed by comparing the diabetic control bones to the untreated diabetic hypertensive and HGF treated diabetic hypertensive bones. This decrease in the shoulder intensity was further confirmed from the relative area under the peak which was extracted after multiple peaks fitting using Lorentzians function as

shown in the Supplementary Information 2 and 3. A low intensity peak, “d”, was observed at 2154.88 eV which suggests that the diabetic control tibial bone is more like HA than other model compounds. The broad resonance peak “c” of the control tibial bone was splitted into two peaks at 2166.76 and 2172.28 eV and could be attributed to O oscillation [63], indicating changes in the bone chemical coordination of the diabetic control tibial bone sample. Similar broad peak was observed for the untreated diabetic hypertensive vertebral bone sample, while the intensity of the main P K-edge was predominant. The P K-edge results are similar to the P $L_{2,3}$-edge data that also indicated the presence of more soluble phosphates in the HGF treated bone samples.

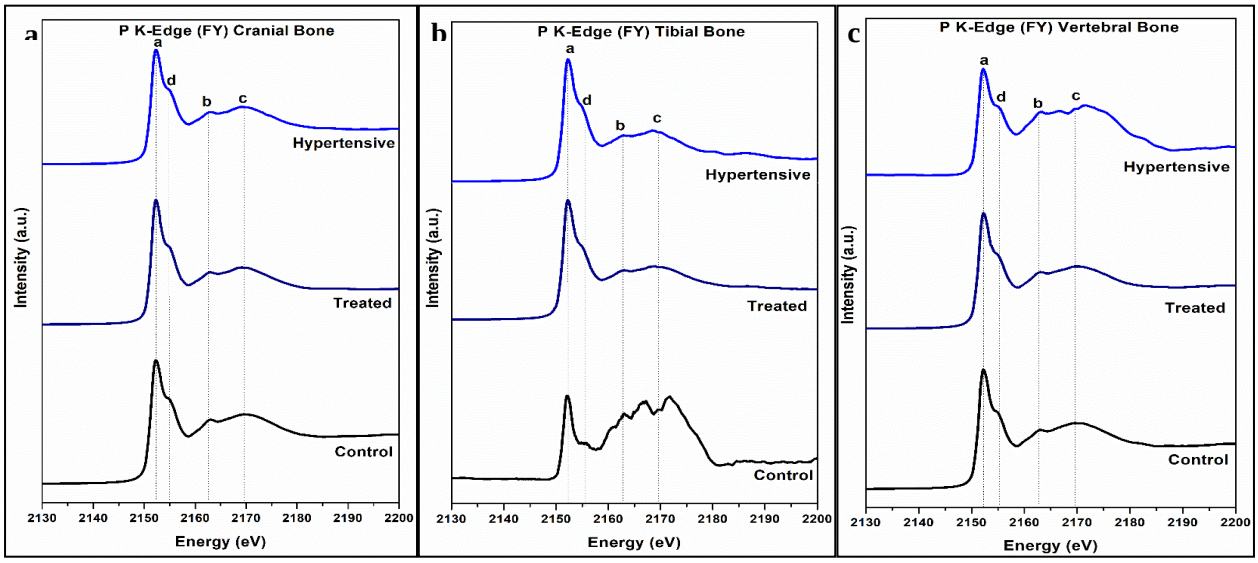

Figure 3.4: Phosphorus K-edge FY XANES spectra of the a) Control, treated, and hypertensive cranial bone, b) Control, treated, and hypertensive tibial bone, and c) Control, treated, and hypertensive vertebral bone.

3.5 Calcium $L_{2,3}$-edge TEY XANES spectra of the standard model compounds:

In vertebrates, HA, carbonated HA, $CaCO_3$, and Ca-P compounds are the most dominant biomineral found [64]. Thus, Ca phosphate biomaterials are researched extensively in the field of orthopedic medicine applications. Ca itself has a significant

role in the biological functions of living organisms, particularly in the interactions of Ca^{2+} ions with proteins [64,65]. Therefore, Ca $L_{2,3}$-edge XANES spectra have been studied for naturally occurring and synthetic Ca-based minerals. Since Ca^{2+} cations have no electrons existing in the 3d orbitals, the 2p absorption is determined by the electrons transitioning from $2p^63d^0$ to $2p^53d^1$. The Ca $L_{2,3}$-edge spectra consist of two main spin-orbital related peaks, L_3 and L_2, usually termed peak a2 and b2, and appear at 350.5 eV and 353.8 eV, respectively. There are other pre-edge peaks that appear to precede the L_3- and L_2-edge main peaks; a1 pre-edge peak appears at 349.2 eV and b1 at 352.5 eV. The main reason for this multiple-peak pattern of Ca $L_{2,3}$-edge is the crystal field arising from the symmetry of the atoms surrounding the Ca^{2+} ions where Ca^{2+} is in octahedral coordination [64,65]. Here, we used six standard Ca-based model compounds to study and compare the nature of the Ca that exists in the tested bone groups. Figure 5 shows the Ca $L_{2,3}$-edge TEY XANES spectra of α-TCP, β-TCP, $CaCO_3$, $CaHPO_4$, HA, and nano HA model compounds. All model compounds showed the L_3, "a1" and "a2", and L_2, "b1" and "b2", main peaks. The

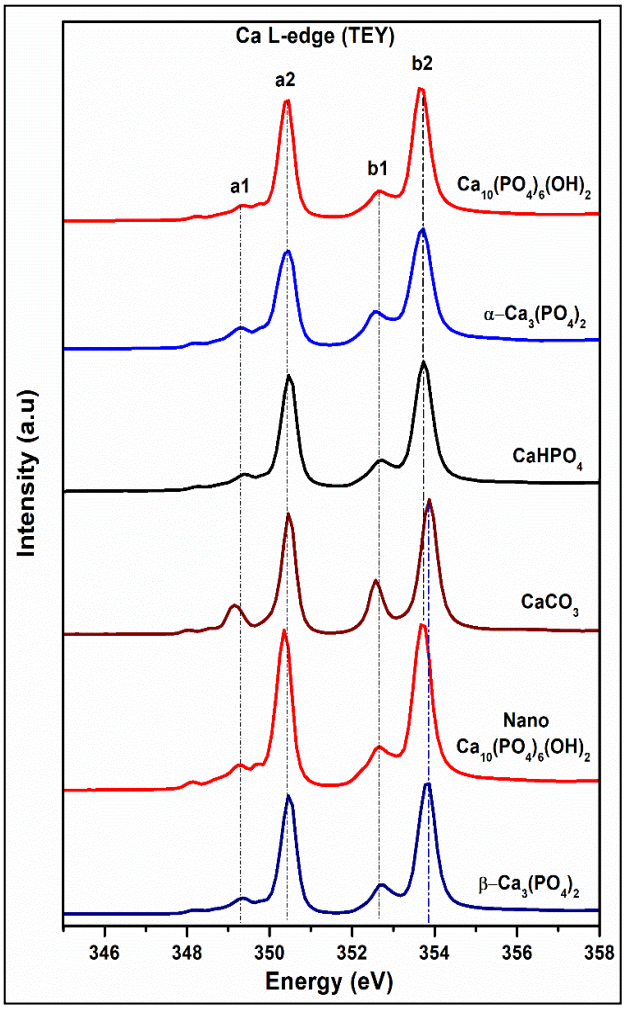

Figure 3.5: Calcium $L_{2,3}$-edge TEY XANES spectra of the model compounds.

main L_3-edge peak, “a2”, appeared at 350.3 eV for all model compounds. The pre-edge peak, “a1”, for all model compounds occurred at 349.3 eV except $CaCO_3$, which showed a high intensity pre-edge peak at 349.1 eV. The main L_2-edge peak, “b2”, appeared at 353.7 eV for all compounds except $CaCO_3$ and β-TCP that appeared at 353.8 eV. Also, the pre-edge b1 peak appeared at 352.6 eV for all model compounds except $CaCO_3$, which showed a high intensity peak at 352.5 eV. All model compounds showed that the L_2 peak at 353.7 eV is more dominant than the L_3 peak at 350.4 eV, given the slightly higher intensity of the L_2 peak. Nanocrystalline HA presented peaks broadening compared to the standard HA, as confirmed by wider and higher-relative peaks’ area as extracted from the multiple peaks fitting (Supplementary Information 4). The model compounds in this study are identical with the previously reported data by Fleet et al., and Naftel et al. [64,65]. The a2 and b2 main edge peaks appeared at 350.3 eV and 353.7 eV, respectively, with a peak-to-peak (b2-a2) separation of 3.4 eV; this precisely matches previously reported data by Fleet et al. [64]. Finally, pre-edge peaks a1 (349.3 eV) and b1 (352.6 eV) appeared at same position as previously reported with a peak-to-peak separation (b1-a1) of 3.3 eV [64]. Peak’s fitting revealed that b1/b2 ratio (i.e., ratio of the area under the curve of peak b1 divided by peak b2) is 0.29 for both HA and TCP, 0.31 for $CaHPO_4$, 0.35 for nano-HA, and 0.39 for $CaCO_3$ as shown in Supplementary Information 5.

3.6 Calcium $L_{2,3}$-edge TEY XANES spectra of the bone samples:

Figure 6 shows the Ca $L_{2,3}$-edge TEY spectra for the cranial, tibial, and vertebral bone samples of the diabetic control, untreated diabetic hypertensive, and HGF treated diabetic hypertensive rats. Figure 6-a shows that the cranial bones in all three groups

have the pre-edge a1 and b1 peaks at 349.3 eV and 352.6 eV, respectively, that exactly match the pre-edge peaks of all model compounds except $CaCO_3$. The main L_3 and L_2 main edge peaks of the cranial bones appeared at 350.4 eV and 353.8 eV, respectively, which exactly match the main edge peak for β-TCP and carbonate standard model compounds. It could be noticed that the HGF treated cranial bones showed lower peak intensity compared to both the untreated diabetic hypertensive and control cranial bone groups. Also, the spectra of the treated cranial bone were closely matching to the $CaHPO_4$ standard that was further confirmed from the same b1/b2 ratio of 0.31. Spectra of the tibial bones of all three groups is presented in Figure 6-b that showed pre-edge peaks, “a1” and “b1” at 349.3 eV and 352.6 eV, respectively. Diabetic control tibial bone appeared to have $L_{2,3}$ main edge peaks at 350.3 eV and 353.7 eV. It can be noticed that the control bones of cranial and tibia are closely matching the spectra of the nano-HA standard as further reveled from the b1/b2 ratio of 0.35. On the other hand, the diabetic

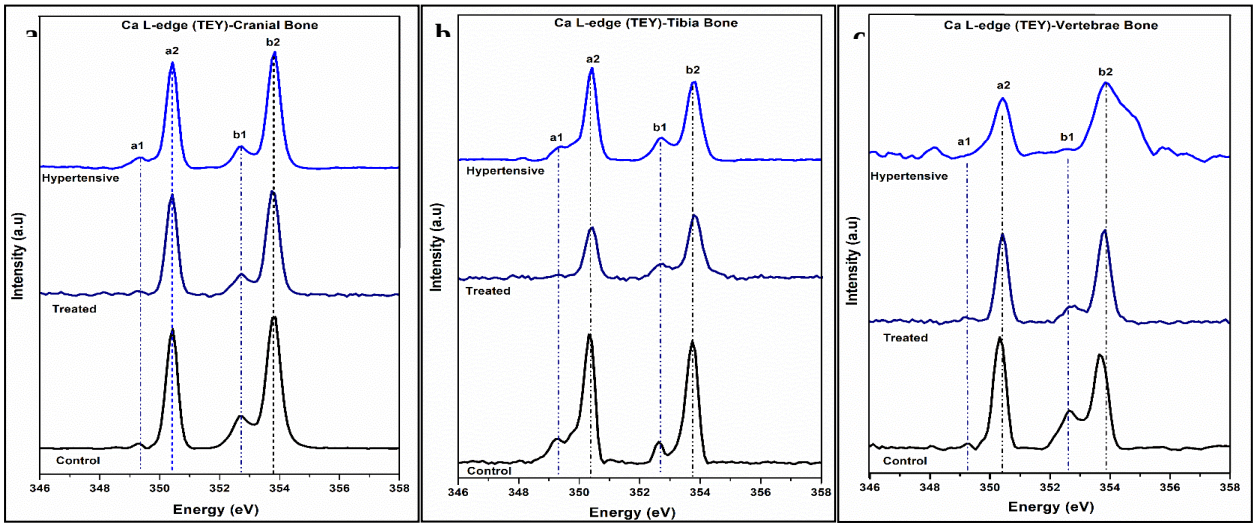

Figure 3.6: Calcium $L_{2,3}$-edge TEY XANES spectra of the a) Control, treated, and hypertensive cranial bone, b) Control, treated, and hypertensive tibial bone, and c) Control, treated, and hypertensive vertebral bone.

hypertensive bones appeared to have more β-TCP and HA as confirmed by $L_{2,3}$ main edge peaks at 350.4 eV and 353.8 eV. The vertebral bone spectra shown in Figure 6-c indicates that the diabetic control bone has an HA-like structure (b1/b2 0.31), however, the L_3 peak at 350.3 eV was more dominant than L_2 peak at 353.7 eV. Treated vertebral bone appeared to have a dominant L_2 peak at 353.8 eV and an L_3 at 350.4 eV, which matches more with the β-TCP and carbonate structures as further revealed from the b1/b2 ratio of 0.30. Diabetic hypertensive vertebral bone exhibited low intensity $L_{2,3}$ peaks at 350.4 eV and 353.8 eV that also matches with the β-TCP structure. Also unexplained broadening in the b2 peak in diabetic hypertensive vertebral bone was observed. All vertebral bone samples exhibited a1 and b1 pre-edge peaks at 349.3 eV and 352.6 eV, respectively. Thus, it can be concluded that for all cranial, tibia, and vertebrate bones, the control diabetic bones have HA or nano HA like structure, the hypertensive bones predominate more β-TCP structure, while the treated bone show more $CaHPO_4$. On the other hand, peak a1 is almost missing in all treated samples. This can be attributed to the charging effect of the bones that can also explain the low quality of the TEY spectra of the texted bone specimens. It is very common for insulating materials to have a problem of sample charging that can affect a range of characterization techniques such as X-ray photoemission spectroscopy (XPS) and Auger electron spectroscopy (AES) where the charging affects the energies of electrons and causes major shifts of features [66,67]. However, in XANES, the energy is defined by the incident radiation and no shift in the features can be introduced and the only effect is the reduced intensity of the collected TEY spectra [68].

From the bone samples spectra, it may be suggested that the HGF treatment has an effect on the Ca-phosphate structure of the bone. The treated cranial and tibial bones exhibited a different behavior compared to the untreated diabetic control. The untreated diabetic control bone of cranium, tibia, and vertebrae displayed a more HA-like bone structure compared to the untreated diabetic hypertensive and HGF treated bones that match more with carbonate and β-TCP, thereby confirming a more carbonated Ca-phosphate structure in the HGF treated groups. A valid explanation for this may be found in a previous study which showed that ionic CO_3^{2-} can be present in two structural positions: either in the apatite channel replacing the OH^- or in replacing the phosphate group in the carbonate apatite [69–71]. In the current study, since the P $L_{2,3}$-edge FY spectra showed that the HGF treated bone samples have more soluble phosphates, it is acceptable that the carbonate ions replaced the phosphate group leading to carbonated apatite in the HGF treated bones. The Ca $L_{2,3}$ main edge spectra confirmed this by showing the identical match of $L_{2,3}$ peaks of the untreated diabetic hypertensive and HGF treated bones with the β-TCP and $CaCO_3$ model compounds, while the untreated diabetic control bones exactly match with the HA and nano-HA standard model compound.

3.7 Calcium K-edge FY XANES spectra of the standard model compounds:

Figure 7 presents the stacked Ca K-edge FY spectra of CaO, $CaCO_3$, and some Ca phosphate standard model compounds. All Ca phosphate compounds presented a unique pre-edge peak, “a”, at 4040.4 eV that can be used to differentiate Ca-P from Ca carbonate or oxides. This peak arises in Ca-P compounds due to the dipole forbidden 1s→3d transition [72]. This usually happens due to the hybridization between Ca 3d and

the p orbitals of the ligand. On the other hand, $CaCO_3$ presented a unique dominant post-edge peak, “d”, at 4060.50 eV that is the characteristic feature of the carbonate spectrum. This feature presents weakly in all other model compounds, including CaO. Another well-defined pre-edge peak, “b”, appeared at 4045.3 eV for HA and both TCPs and at 4044.73 eV for CaO and $CaCO_3$. Pre-edge peak, “b”, was observed as a shoulder at 4045.0 eV for the other model compounds, $Ca_2P_2O_7$ and $CaHPO_4$. The main edge peak, “c”, of Ca K-edge due to 1s→np transitions appeared at 4050.0 eV for all model compounds. HA and $CaCO_3$ have a main edge peak split that was absent in all other model compounds, and this doublet can be attributed to 1s→4p transitions [72]. Our reported spectra of the standard model compounds agree with the previously reported data [46,49,61,72].

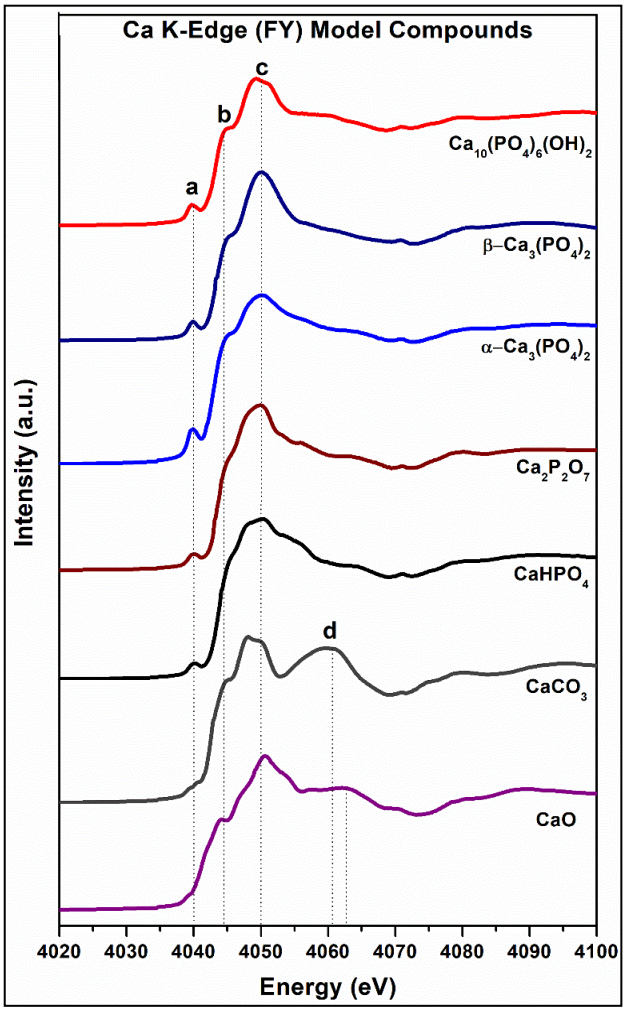

Figure 3.7: Calcium K-edge FY XANES spectra of the model compounds.

3.8 Calcium K-edge FY XANES spectra of the bone samples:

Figure 8 presents the stacked Ca K-edge FY XANES spectra of Ca K-edge of the HGF treated diabetic hypertensive, untreated diabetic hypertensive, and untreated diabetic control bone samples. Spectra are similar to the reported standard model

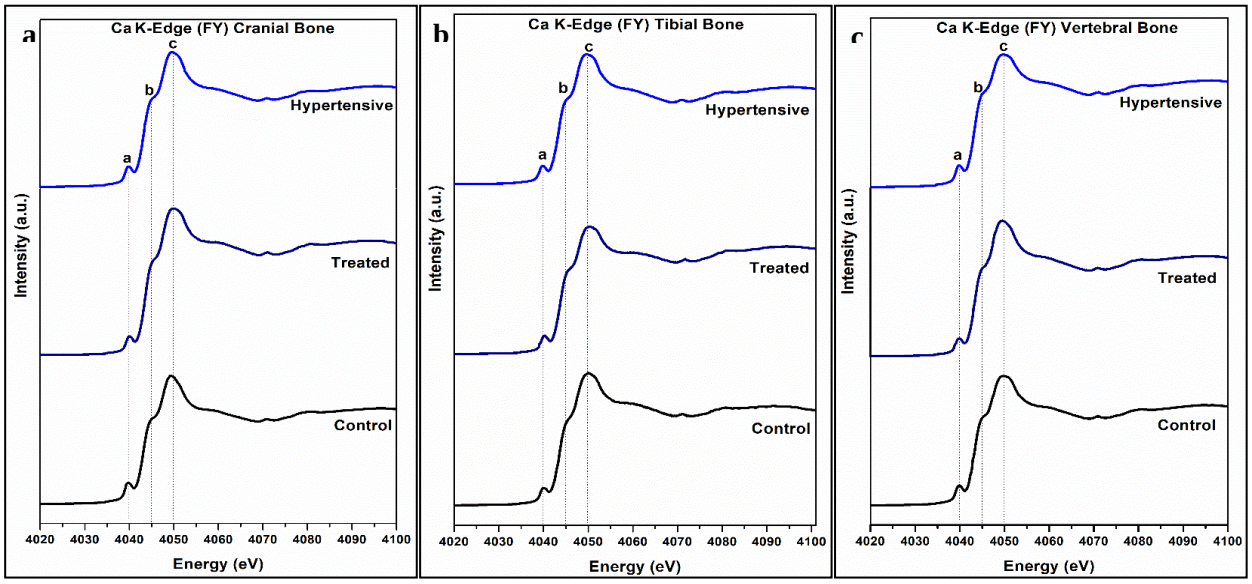

Figure 3.8: Calcium K-edge FY XANES spectra of the a) Control, treated, and hypertensive cranial bone, b) Control, treated, and hypertensive tibial bone, and c) Control, treated, and hypertensive vertebral bone.

compounds. All samples showed the two pre-edge peaks, “a” and “b”, at 4040.4 eV and 4045.3 eV, respectively. Although all bone samples indicated the presence of the Ca K main edge peak, “c”, at 4050.0 eV, the spectra were closer to the β-TCP standard due to the absence of the unique doublet feature of HA. None of the studied bone samples displayed the post-edge “d” that is a unique feature in $CaCO_3$ and CaO, indicating that CaO and $CaCO_3$ are not present in the studied bone samples. Although Ca $L_{2,3}$-edge revealed some changes in the HGF treated and untreated diabetic hypertensive bone structures compared to the untreated diabetic control bone structure, the Ca K-edge did not provide enough differences between the tested groups for meaningful interpretation. This could be possibly attributed to the poor energy resolution of the K-edge caused by the short lifetime of the 1s core hole compared to the better resolution of the L-edge that provide a direct probe of the covalency in transition metal coordination complexes [73].

3.9 Oxygen K-edge XANES spectra of the standard model compounds:

The O K-edge TEY XANES spectra are usually used to distinguish between carbonate and phosphate compounds and identify the local coordination of O[47]. Figure 9 shows the O K-edge TEY XANES spectra of HA, $CaHPO_4$, β-TCP, α-TCP, $CaCO_3$, and nano HA. HA and $CaHPO_4$ show high intensity pre-edge peak “a” at 536.6 eV, while both TCP compounds exhibited their pre-edge peaks at 536.9 eV. On the other hand, $CaCO_3$ showed a very high intensity primary peak at 538.1 eV which is a unique feature that can be used to distinguish the carbonates from the phosphate compounds. Nano HA, HA, and β-TCP compounds exhibited the main edge peak “c” and the post-edge peak “d” at 540.8 eV and 543.9 eV, respectively, which can be used to distinguish the phosphates from carbonates. Due to its nanocrystalline nature, the nano HA exhibited unique features compared to the HA. Nano HA presented low intensity with peak broadening of the pre-edge peak “a” that can be obviously noticed compared to the high intensity sharp pre-edge peak of the HA. However, the main edge peak for α-TCP was observed at a lower energy of 540.3 eV. $CaHPO_4$

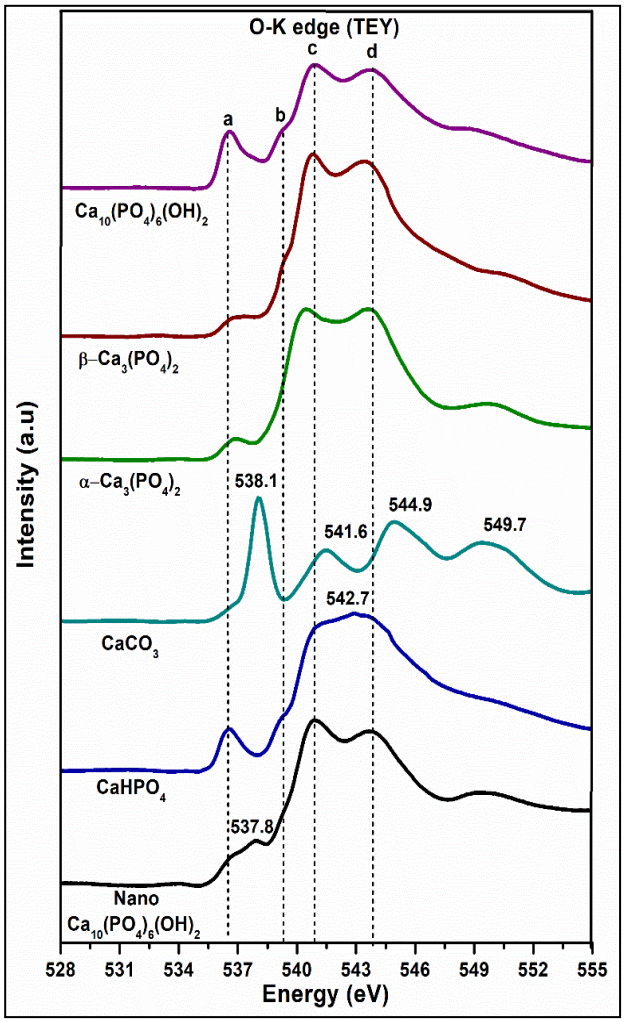

Figure 3.9: Oxygen K-edge TEY XANES spectra of the model compounds.

exhibited a broad peak ranging from 541.0 to 544.4 eV, while $CaCO_3$ appeared to have two unique peaks at 541.6 eV and 544.9 eV that clearly differentiates the $CaCO_3$ spectrum from the other standard model compounds. All model compounds except $CaHPO_4$ have a secondary peak at approximately 549.7 eV. HAs, $CaHPO_4$, and β-TCP also have a pre-edge shoulder “b” at 539.4 eV which is absent in the other model compounds. Although the presented spectra of O K-edge are shifted by 2.7 eV compared to the O K-edge data reported by Rajendran et al. in 2013 [49], our data remain in agreement with the HA O K-edge spectra that was reported by Charpentier et al. in 2014 [74]. By comparing the O K-edge model compounds, the peak at 540.8 eV arises due to the presence of phosphates and the unique peak at 538.1 eV is only observed for the carbonate structure. Finally, the high intensity pre-edge peak at 536.6 eV can be used to distinguish the HA and $CaHPO_4$ from the other phosphate model compounds.

3.10 Oxygen K-edge XANES spectra of the bone samples:

Figure 10 presents the O K-edge TEY XANES spectra of the studied bone samples. Most bone samples showed very high intensity peak “a” at 536.6 eV and 539.4 eV, which matched with the low intensity pre-edge peak at 536.6 eV and the shoulder “b” at 539.4 of the HA and $CaHPO_4$ model compounds. This significant increase in the peak’s intensity can be attributed to the presence/overlap of the first and second peaks of carbonate but shifted to a lower energy state. The carbonate peaks present at 538.1 and 541.6 eV in $CaCO_3$ are shifted to lower energy 536.6 eV and 539.4 eV, respectively, in all bone samples. All bone samples exhibited the main phosphate peak “c” at 540.8 eV and a higher intensity post-edge peak “d” at 543.9 eV, which matched the phosphate model compounds’ main peaks. Both HGF treated and

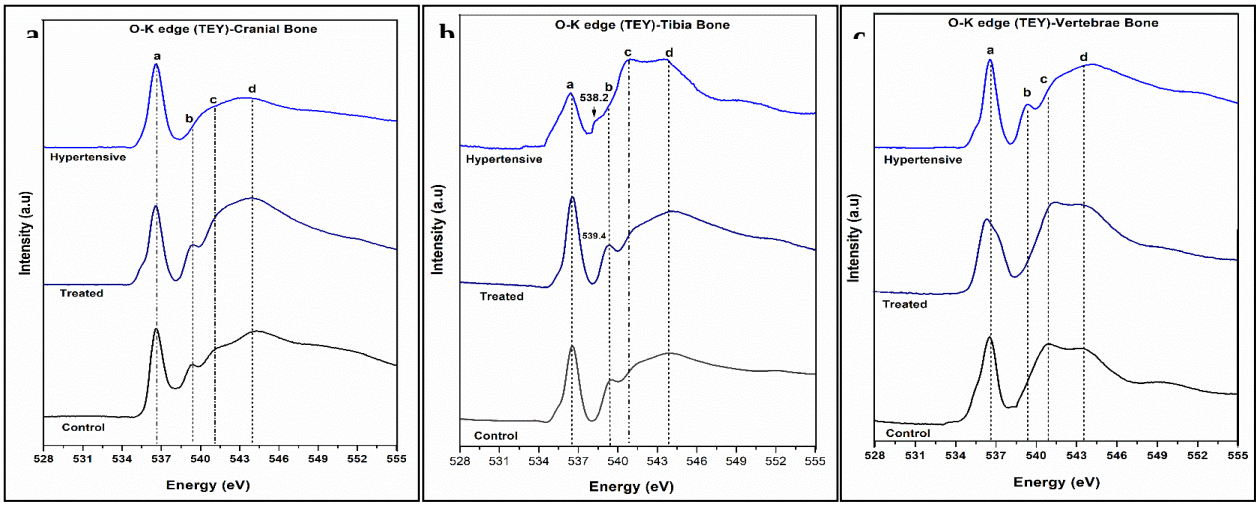

Figure 3.10: Oxygen K-edge TEY XANES spectra of the a) Control, treated, and hypertensive cranial bone, b) Control, treated, and hypertensive tibia bone, and c) Control, treated, and hypertensive vertebrae bone.

untreated diabetic hypertensive cranial bones exhibited a broad high intensity peak ranging from 541.03 eV to 543.9 eV that exactly matched the $CaHPO_4$ model compound. Both untreated diabetic control and HGF treated diabetic hypertensive tibial bones showed high intensity peaks at 536.6 and 539.4 eV, indicating a greater carbonate to phosphate ratio. However, the hypertensive tibial bone sample showed a shifted low intensity peak at 538.2 eV and a high intensity broad phosphate peak ranging from 540.7 to 543.8 eV, also indicating a greater phosphate to carbonate ratio. The untreated diabetic hypertensive vertebral bone showed the high intensity peak at 536.6 eV and the pre-edge peak at 539.4 eV, indicating predominance of carbonates in the untreated diabetic hypertensive group while phosphates tended to dominate in the HGF treated and untreated diabetic control groups.

We explained the studied bone samples and correlated them to the examined standard model compounds. Although all bone samples showed the presence of a pre-edge peak at 536.6 eV that perfectly matched with HA and $CaHPO_4$, the high intensity of this peak can be explained by the formation of a carbonated phosphate complex. In

the studied bone samples, the CO_3^{2-} is likely replacing the PO_4^{3-} anion in the phosphates thereby yielding a carbonated phosphate complex. This results in the peaks associated with the carbonate in the bone samples to be shifted to lower energy; such shifts in the peak position are very common and can be attributed to the differences in the local coordination of O in $CaCO_3$ and the carbonate in a carbonate-phosphate complex [49]. The presence of broad peaks ranging from 540.7 eV to 543.8 eV for most bone samples indicates that the examined bone samples are closer to the $CaHPO_4$ soluble phosphate structure. Finally, the O K-edge clearly showed a predominance of carbonates in the cranial and tibial bone samples, while phosphates tended to dominate in the vertebral bone samples. More importantly, the HGF treated animals clearly indicated the development of a higher phosphate-to-carbonate ratio in the cranial and vertebral bones. However, the tibia shows higher carbonate content compared to phosphate, thus, the location of HGF treatment and/or XANES measurement appears to effect on bone chemical structure as well. Although collagen present in a high concentration (typically ~20 wt.%) in bones as the predominant organic phase, previous studies by Rajendran et al., on dried and calcined bones at 400 °C and 700 °C indicated that dried bones could preserve the collagen while 700 °C drive-off all the collagen content in the bone samples [49]. Rajendran et al., reported a significant difference in the oxygen K-edge XANES spectra of dried bones compared to the calcined ones, but they attributed these changes to the predominant of phosphate in the dried bone verses mixture of carbonate and phosphate in the calcined bones [49]. Another study by Aruwajoye et al., attributed the changes in oxygen K-edge XANES spectra in necrotic and normal trabecular bone to the carbonate presence and its substitution with phosphates in the

bone structure [47]. Although previous studies related the changes in the oxygen K-edge only to the inorganic phase of the bone, it is possible that the organic phase “collagen” could attribute to the changes in the oxygen K-edge. Thus, it is recommended to utilize the scanning transmission X-ray microscopy STXM/XANES technique that allows the detection of CO_3^{2-} groups in apatites even within the organic matrix of the bone [75].

Finally, it is important to reiterate that bone remodeling involves sequential osteoclast-mediated bone resorption and osteoblast-mediated bone formation at the same location [76]. This process occurs in five consequence stages which are osteoclast activation, bone resorption, reversal "osteoblast activation", bone formation, and quiescence [76,77]. For healthy new bone formation, the osteoclast and osteoblast activation should be balanced or coupled. If this condition is not met, the bone balance of the newly formed bone could be negative (i.e., less bone formed relative to the amount of bone resorbed), or positive (i.e., more bone formed relative to the amount of bone resorbed) rather than a healthy, desirably net neutral. On the other hand, HGF is expected to stimulate osteoclast bone resorption which in turn stimulates osteoblast new bone formation. The presence of soluble Ca and P, both products of bone resorption, with the HGF treatment suggests unbalanced bone resorption and formation. This can be possibly attributed to the effect of HGF that stimulates the osteoclast activity without balanced osteoblast activation. These findings reveal the potential effects of HGF on the bone remodeling process. Furthermore, the presence of soluble Ca and P due to HGF treatment appears coincident with prior reported fibrillar collagen loss due to HGF treatment, suggesting a potential dual role of HGF on collagen and mineral chemical changes.

4. CONCLUSION

In this study, a comprehensive XANES analysis was performed to test the effect of HGF treatment on diabetic hypertensive compared to untreated diabetic hypertensive and diabetic control bone structures. Based on the above presented data from the phosphorus $L_{2,3}$-edge FY spectra, K-edge FY spectra, calcium $L_{2,3}$-edge TEY spectra, and O K-edge TEY XANES spectra, it can be concluded that the HGF treatment has some effects on the calcium phosphate structure of bone. The phosphorus $L_{2,3}$-edge FY and K-edge FY data indicated the presence of more soluble phosphates in the bone samples treated with HGF. The phosphorus $L_{2,3}$-edge data indicated that the treated bones have a poorly developed phosphate structure as evidenced by the drastic drop in the post-edge shoulder compared to the diabetic hypertensive and diabetic control bone (i.e., cranium, tibia, vertebrae). Furthermore, Ca $L_{2,3}$-edge TEY and O K-edge TEY spectra showed that the diabetic hypertensive and treated bones matched more with the calcium carbonate and β-TCP structures, confirming more carbonated calcium phosphate structure due to the substitution of either the OH^- or PO_4^{3-} in the apatite structure with the CO_3^{2-} ion. Finally, the O K-edge data indicated a predominance of carbonates in the cases of cranial and tibial bones while phosphates tended to dominate in the vertebral bones, which suggests that the location of treatment/measurement appears to have an effect on the bone structure. In conclusion, the HGF treatment increased soluble phosphates in Zucker diabetic hypertensive fatty rats compared to untreated diabetic hypertensive and untreated diabetic control rats; thus, HGF treatment may have pushed diabetic hypertensive bones into a remodeling

phase to counteract the deleterious effects of diabetes and hypertension on bone health.

Acknowledgements

The authors would like to thank Dr. Kimaya Vyavhare for her help and support during the sample's analysis. Also, the authors would like to thank the Canadian Light Source team (Drs. Tom Regier, Zachary Arthur, Lucia Zuin, David Wang, and Mohsen Shakouri) for their great support and assistance during collection and interpretation of this data. All XANES experiments were conducted at the Canadian Light Source, Saskatoon, Saskatchewan, Canada that is supported by NSERC, NRC, CIHR, and the University of Saskatchewan.

Declarations

Funding: The authors want to thank the National Institutes of Health (NIH), the University of Texas at Arlington (UTA), and the UTA College of Nursing & Health Innovation Bone-Muscle Research Center (UTA-CONHI-BMRC) for their generous support for this study. The following NIH Grants supported KA and VV: (Grant Number 1R03DE023872-01, 1R56DE027964-01A1-01, NIH S10OD025230). Also, we thank the UTA-CONHI for their generous support for the first author KA via the CRS Pilot Grant.

Conflicts of interest/Competing interests: The authors declare no Conflict-of-interest for this study.

Availability of data and material: Not Applicable.

Code availability: Not Applicable.

5. SUPPLEMENTARY INFORMATION (SI)

SI 1: Experimental setup for spectral acquisition at respective beamlines (CLS Beamline).

Beamline	Energy range (eV)	Edges	Resolution (eV)	Spot size
SGM	250-2000	Ca $L_{2,3}$-edge, O K-edge	0.2	1000 µm x 100 µm
VLS-PGM	5.5-250	P $L_{2,3}$-edge	0.1	500 µm x 500 µm
SXRMB	1,700-10,000	P K-edge, Ca K-edge	0.5	300 x 300 µm

SI 2: P K-edge peak fitting using Lorentzians function of the studied bone samples.

Samples		Peak	Position	Area	Error (±)	Goodness-of-fit (R^2)
Cranial Bone	Control Bone	a	2152.31	69.93	5.93	0.96
		b	2162.39	78.05	23.04	
		c	2170.17	154.69	28.59	
		d	2154.91	82.58	10.95	
	Hypertensive Bone	a	2152.32	66.53	4.98	0.97
		b	2162.19	61.29	17.86	
		c	2169.70	108.08	20.62	
		d	2154.86	74.95	9.24	
	Treated Bone	a	2152.33	64.09	4.34	0.975
		b	2162.25	57.38	16.8	
		c	2169.81	118.40	20.89	
		d	2154.83	70.44	7.95	
Tibial Bone	Control Bone	a	2152.23	1.478	0.20	0.85
		b	2162.2	1.815	0.83	
		c	2166.76	1.296	1.1	
			2172.28	2.458	0.66	
		d	2154.88	0.7045	0.36	
	Hypertensive Bone	a	2152.31	15.79	1.06	0.98
		b	2162.08	13.48	4.51	
		c	2169.35	33.41	5.54	
		d	2154.76	17.52	1.95	
	Treated Bone	a	2152.30	25.66	1.87	0.977
		b	2162.01	24.89	8.34	
		c	2169.71	50.67	9.67	
		d	2154.82	28.39	3.7	
		a	2152.30	17.89	1.6	0.98

Vertebral Bone	Control Bone	b	2162.34	15.79	5.9	
		c	2170.36	59.70	6.4	
		d	2154.81	33.99	2.3	
	Hypertensive Bone	a	2152.27	13.35	3.1	0.96
		b	2163.19	27.31	10.1	
		c	2172.49	55.42	9.68	
		d	2154.90	22.27	4.67	
	Treated Bone	a	2152.16	10.28	2.44	0.95
		b	2161.55	58.73	3.4	
		c	2170.00	94.41	7.3	
		d	2154.38	18.65	3.3	

SI 3: Peak's fitting of Phosphorus K-edge FY XANES spectra of the a) Control, treated, and hypertensive cranial bone, b) Control, treated, and hypertensive tibial bone, and c) Control, treated, and hypertensive vertebral bone. Fitting was performed using Lorentzians function.

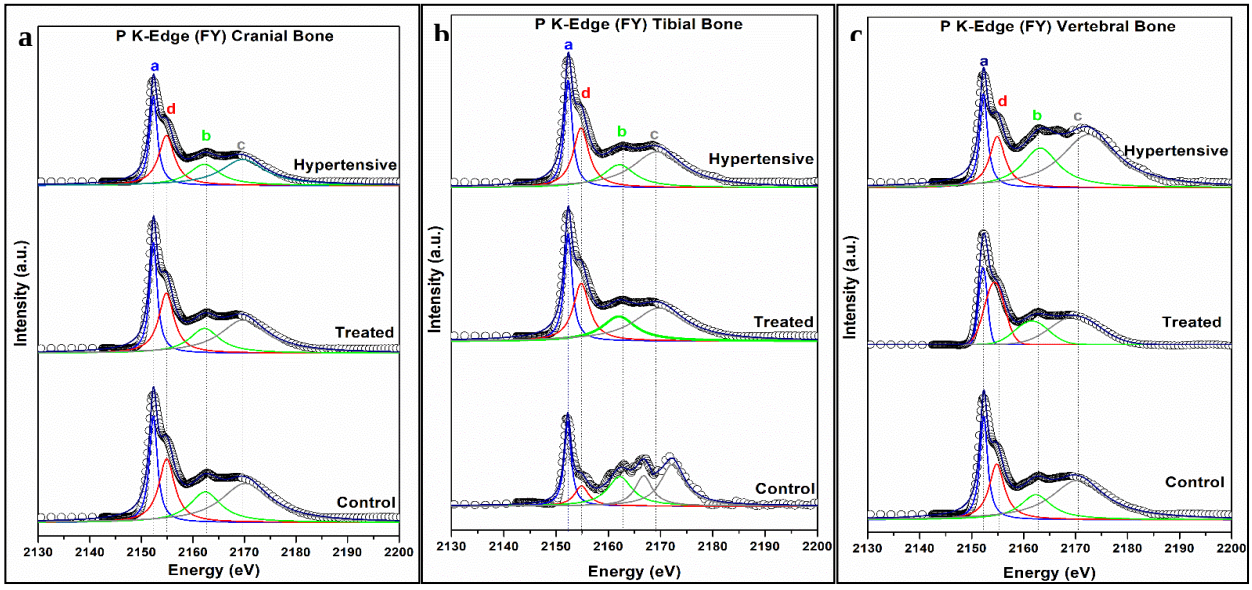

SI 4: Peak's fitting of Ca L-edge of the standards model compounds.

Sample/Area	a2	a1	b2	b1
HA	1.29±0.07	0.34±0.04	0.66±0.023	0.46±0.025
Nano-HA	1.35±0.04	0.35±0.028	0.70±0.02	0.48±0.026

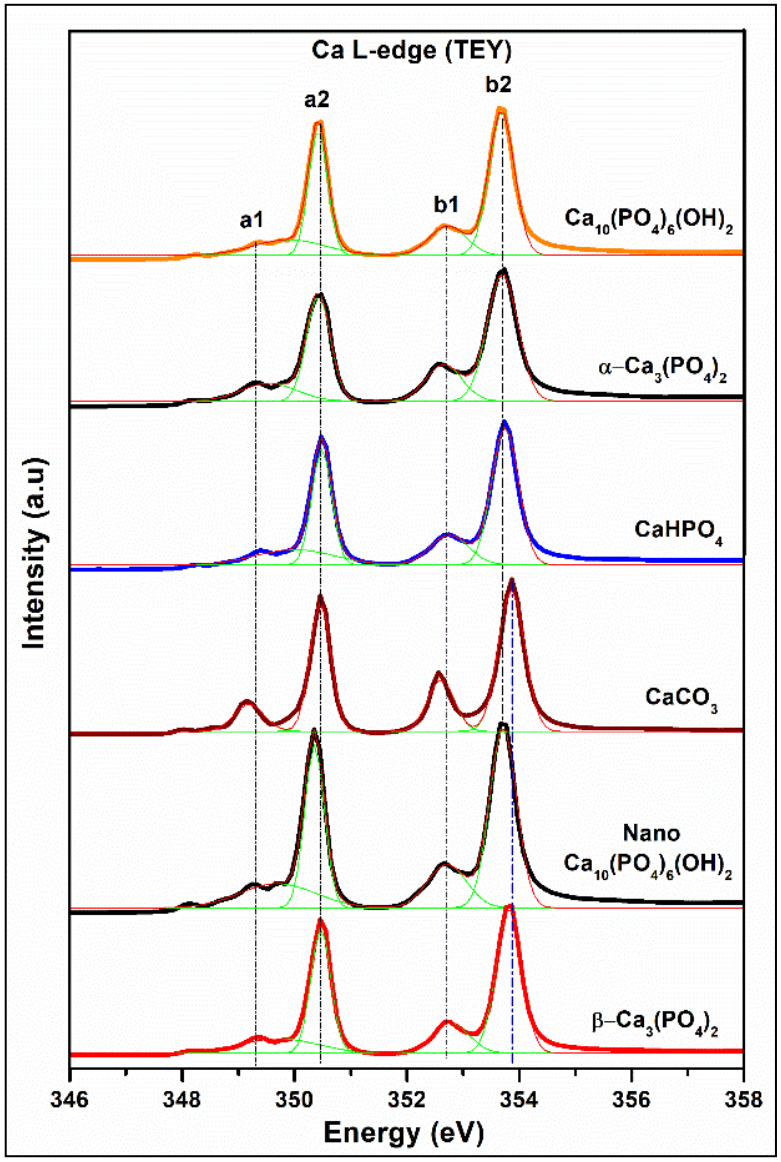

SI 5: Peak's fitting of Ca L-edge of the tested bone samples with b1/b2 peak ratio.

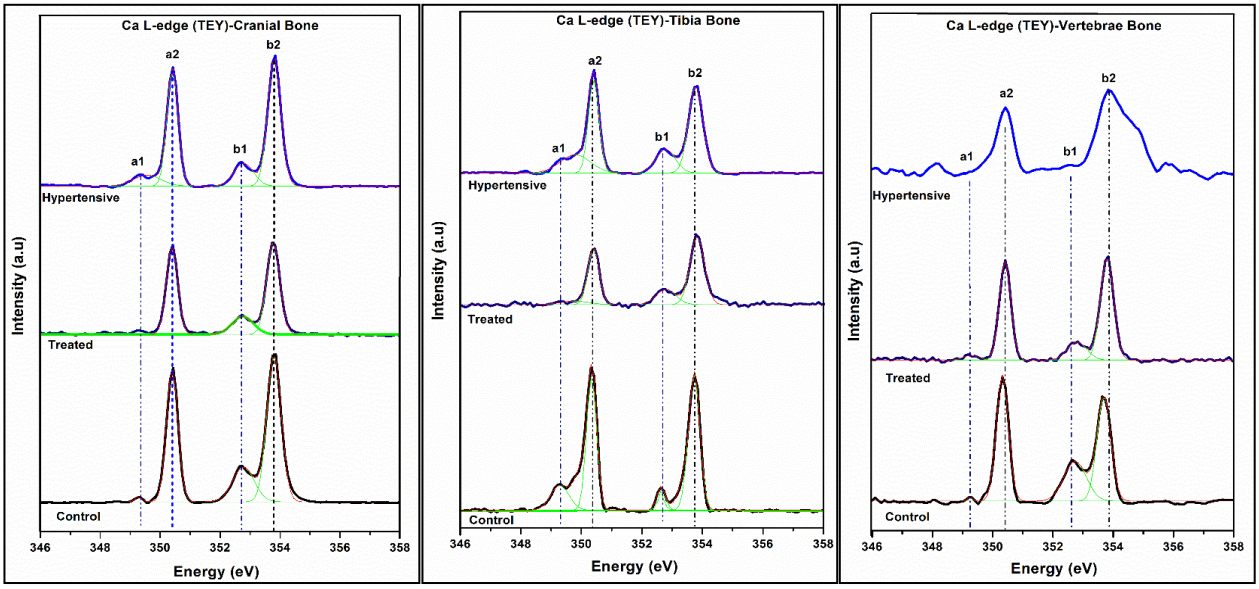

Sample	b1/b2 ratio	Cranial Bone	b1/b2 ratio
HA	0.29±0.01	**Control**	0.36±0.001
Nano-HA	0.35±0.025	**Hypertensive**	0.26±0.002
B-TCP	0.29±0.015	**Treated**	0.31±0.012
$CaCO_3$	0.39±0.021		
$CaHPO_4$	0.31±0.003		

Tibia Bone	b1/b2 ratio	Vertebrate Bone	b1/b2 ratio
Control	0.35±0.011	**Control**	0.31±0.001
Hypertensive	0.28±0.017	**Hypertensive**	---
Treated	0.28±0.002	**Treated**	0.30±0.01

HA – represents stoichiometric healthy bone.

Nano-HA – nanocrystalline HA representing multiple crystallites in the HA mineral. During remodeling there will be increased presence of nano-HA vs HA.

Beta-TCP – indicative of remodeling since b-TCP is precursor for stochiometric HA.

$CaHPO_4$ – soluble Ca or O or P that indicates remodeling where soluble mineral can be present. This soluble mineral be used to use reform the bone layer but represents an intermediate step prior to b-TCP formation.

REFERENCES

1. American Diabetes Association. Classification and Diagnosis of Diabetes: Standards of Medical Care in Diabetes - 2018. Diabetes Care **41**, S13–S27 (2018).
2. Yang, W. et al. Economic costs of diabetes in the U.S. in 2017. Diabetes Care **41**, 917–928 (2018).
3. Napoli, N. et al. The alliance of mesenchymal stem cells, bone, and diabetes. Int. J. Endocrinol. **2014**, (2014).
4. Conte, C., Epstein, S. & Napoli, N. Insulin resistance and bone: a biological partnership. Acta Diabetol. **55**, 305–314 (2018).
5. Strotmeyer, E. S. et al. Diabetes is associated independently of body composition with BMD and bone volume in older white and black men and women: The health, aging, and body composition study. J. Bone Miner. Res. **19**, 1084–1091 (2004).
6. Ma, L. et al. Association between bone mineral density and type 2 diabetes mellitus: A meta-Analysis of observational studies. Eur. J. Epidemiol. **27**, 319–332 (2012).
7. Tonks, K. T., White, C. P., Center, J. R., Samocha-Bonet, D. & Greenfield, J. R. Bone turnover is suppressed in insulin resistance, independent of adiposity. J. Clin. Endocrinol. Metab. **102**, 1112–1121 (2017).
8. Burghardt, A. J. et al. High-resolution peripheral quantitative computed tomographic imaging of cortical and trabecular bone microarchitecture in patients with type 2 diabetes mellitus. J. Clin. Endocrinol. Metab. **95**, 5045–5055 (2010).
9. Patsch, J. M. et al. Increased cortical porosity in type 2 diabetic postmenopausal

women with fragility fractures. J. Bone Miner. Res. **28**, 313–324 (2013).

10. Yu, E. W. et al. Defects in cortical microarchitecture among African-American women with type 2 diabetes. Osteoporos. Int. **26**, 673–679 (2015).
11. de Waard, E. A. C. et al. The association between diabetes status, HbA1c, diabetes duration, microvascular disease, and bone quality of the distal radius and tibia as measured with high-resolution peripheral quantitative computed tomography—The Maastricht Study. Osteoporos. Int. **29**, 2725–2738 (2018).
12. Poiana, C. & Capatina, C. Fracture Risk Assessment in Patients With Diabetes Mellitus. J. Clin. Densitom. **20**, 432–443 (2017).
13. Vestergaard, P. Discrepancies in bone mineral density and fracture risk in patients with type 1 and type 2 diabetes - A meta-analysis. Osteoporos. Int. **18**, 427–444 (2007).
14. Strotmeyer, E. S. et al. Nontraumatic fracture risk with diabetes mellitus and impaired fasting glucose in older white and black adults: The health, aging, and body composition study. Arch. Intern. Med. **165**, 1612–1617 (2005).
15. Pscherer, S., Kostev, K., Dippel, F. W. & Rathmann, W. Fracture risk in patients with type 2 diabetes under different antidiabetic treatment regimens: A retrospective database analysis in primary care. Diabetes, Metab. Syndr. Obes. Targets Ther. **9**, 17–23 (2016).
16. Monami, M. et al. Bone fractures and hypoglycemic treatment in type 2 diabetic patients: A case-control study. Diabetes Care **31**, 199–203 (2008).
17. Petrie, J. R., Guzik, T. J. & Touyz, R. M. Diabetes, Hypertension, and Cardiovascular Disease: Clinical Insights and Vascular Mechanisms. Can. J.

Cardiol. **34**, 575–584 (2018).

18. Libianto, R., Batu, D., MacIsaac, R. J., Cooper, M. E. & Ekinci, E. I. Pathophysiological Links Between Diabetes and Blood Pressure. Can. J. Cardiol. **34**, 585–594 (2018).
19. Ferrannini, E. & Cushman, W. C. Diabetes and hypertension: The bad companions. Lancet **380**, 601–610 (2012).
20. Mills, K. T. et al. Global disparities of hypertension prevalence and control: a systematic analysis of population-based studies from 90 countries. Circulation **134**, 441–450 (2016).
21. Mitchell, B. D., Stern, M. P., Haffner, S. M., Hazuda, H. P. & Patterson, J. K. Risk factors for cardiovascular mortality in Mexican Americans and non-Hispanic whites. Am. J. Epidemiol. **131**, 423–33 (1990).
22. Lastra, G., Syed, S., Kurukulasuriya, L. R., Manrique, C. & Sowers, J. R. Type 2 diabetes mellitus and hypertension: An update. Endocrinol. Metab. Clin. North Am. **43**, 103–122 (2014).
23. Lima, N. K. C., Abbasi, F., Lamendola, C. & Reaven, G. M. Prevalence of insulin resistance and related risk factors for cardiovascular disease in patients with essential hypertension. Am. J. Hypertens. **22**, 106–111 (2009).
24. Tsuda, K., Nishio, I. & Masuyama, Y. Bone Mineral Density in Women with Essential Hypertension. Am. J. Hypertens. **14**, 704–707 (2001).
25. Cappuccio, F. P., Meilahn, E., Zmuda, J. M. & Cauley, J. A. High blood pressure and bone-mineral loss in elderly white women: A prospective study. Lancet **354**, 971–975 (1999).

26. Vestergaard, P., Rejnmark, L. & Mosekilde, L. Hypertension is a risk factor for fractures. Calcif. Tissue Int. **84**, 103–111 (2009).

27. Yang, S., Nguyen, N. D., Center, J. R., Eisman, J. A. & Nguyen, T. V. Association between hypertension and fragility fracture: A longitudinal study. Osteoporos. Int. **25**, 97–103 (2014).

28. MacGregor, G. A. & Cappuccio, F. P. The kidney and essential hypertension: A link to osteoporosis? Journal of Hypertension vol. 11 781–785 (1993).

29. Barzilay, J. I. et al. The Impact of Antihypertensive Medications on Bone Mineral Density and Fracture Risk. Curr. Cardiol. Rep. **19**, (2017).

30. Frisch, R. N., Curtis, K. M., Aenlle, K. K. & Howard, G. A. Hepatocyte growth factor and alternative splice variants - expression, regulation and implications in osteogenesis and bone health and repair. Expert Opin. Ther. Targets **20**, 1087–1098 (2016).

31. Whang, Y. M., Jung, S. P., Kim, M. K., Chang, I. H. & Park, S. I. Targeting the hepatocyte growth factor and c-met signaling axis in bone metastases. Int. J. Mol. Sci. **20**, (2019).

32. Matsuda, Y., Matsumoto, K., Nakamura, T. & Ichida, T. Hepatocyte Growth Factor Suppresses the Onset of Liver Cirrhosis and Abrogates Lethal Hepatic Dysfunction in Rats1. J. Biochem. **118**, 643–649 (1995).

33. Sherriff-Tadano, R. et al. Antifibrotic effects of hepatocyte growth factor on scleroderma fibroblasts and analysis of its mechanism. Mod. Rheumatol. **16**, 364 (2006).

34. Jinnin, M. et al. Effects of Hepatocyte Growth Factor on the Expression of Type I

Collagen and Matrix Metalloproteinase-1 in Normal and Scleroderma Dermal Fibroblasts. J. Invest. Dermatol. **124**, 324–330 (2005).

35. Van Doren, S. R. Matrix metalloproteinase interactions with collagen and elastin. Matrix Biol. **44**–**46**, 224–231 (2015).
36. Lodish, H. et al. Collagen: The Fibrous Proteins of the Matrix. (2000).
37. Fuller, K., Owens, J. & Chambers, T. J. The effect of hepatocyte growth factor on the behavior of osteoclasts. Biochemical and Biophysical Research Communications vol. 212 334–340 (1995).
38. Grano, M. et al. Hepatocyte growth factor is a coupling factor for osteoclasts and osteoblasts in vitro. Proc. Natl. Acad. Sci. U. S. A. **93**, 7644–7648 (1996).
39. Adamopoulos, I. E., Xia, Z., Lau, Y. S. & Athanasou, N. A. Hepatocyte growth factor can substitute for M-CSF to support osteoclastogenesis. Biochem. Biophys. Res. Commun. **350**, 478–483 (2006).
40. Aenlle, K. K., Curtis, K. M., Roos, B. A. & Howard, G. A. Hepatocyte growth factor and p38 promote osteogenic differentiation of human mesenchymal stem cells. Mol. Endocrinol. **28**, 722–730 (2014).
41. Wen, Q. et al. Change in hepatocyte growth factor concentration promote mesenchymal stem cell-mediated osteogenic regeneration. J. Cell. Mol. Med. **16**, 1260–1273 (2012).
42. Hossain, M., Irwin, R., Baumann, M. J. & McCabe, L. R. Hepatocyte growth factor (HGF) adsorption kinetics and enhancement of osteoblast differentiation on hydroxyapatite surfaces. Biomaterials **26**, 2595–2602 (2005).
43. Goshima, K., Nakase, J., Xu, Q., Matsumoto, K. & Tsuchiya, H. Repair of

segmental bone defects in rabbit tibia promoted by a complex of β-tricalcium phosphate and hepatocyte growth factor. J. Orthop. Sci. **17**, 639–648 (2012).

44. Ohno, T. et al. Drug Delivery System of Hepatocyte Growth Factor for the Treatment of Vocal Fold Scarring in a Canine Model. Ann. Otol. Rhinol. Laryngol. **116**, 762–769 (2007).

45. Ingall, E. D. et al. Phosphorus K-edge XANES spectroscopy of mineral standards. J. Synchrotron Radiat. **18**, 189–197 (2011).

46. Demirkiran, H., Hu, Y., Zuin, L., Appathurai, N. & Aswath, P. B. XANES analysis of calcium and sodium phosphates and silicates and hydroxyapatite–Bioglass®45S5 co-sintered bioceramics. Mater. Sci. Eng. C **31**, 134–143 (2011).

47. Aruwajoye, O. O., Kim, H. K. W. & Aswath, P. B. Bone Apatite Composition of Necrotic Trabecular Bone in the Femoral Head of Immature Piglets. Calcif. Tissue Int. **96**, 324–334 (2015).

48. Sindhupakorn, B., Thienpratharn, S. & Kidkhunthod, P. A structural study of bone changes in knee osteoarthritis by synchrotron-based X-ray fluorescence and X-ray absorption spectroscopy techniques. J. Mol. Struct. **1146**, 254–258 (2017).

49. Rajendran, J., Gialanella, S. & Aswath, P. B. XANES analysis of dried and calcined bones. Mater. Sci. Eng. C **33**, 3968–3979 (2013).

50. Kitada, M., Ogura, Y. & Koya, D. Rodent models of diabetic nephropathy: Their utility and limitations. Int. J. Nephrol. Renovasc. Dis. **9**, 279–290 (2016).

51. Janssen, U., Riley, S. G., Vassiliadou, A., Floege, J. & Phillips, A. O. Hypertension superimposed on type II diabetes in Goto Kakizaki rats induces progressive nephropathy. Kidney Int. **63**, 2162–2170 (2003).

52. Ren, X. et al. Synergistic effects of combining anti-midkine and hepatocyte growth factor therapies against diabetic nephropathy in rats. Am. J. Med. Sci. **350**, 47–54 (2015).

53. Bovenkamp, G. L., Zanzen, U., Krishna, K. S., Hormes, J. & Prange, A. X-ray absorption near-edge structure (XANES) spectroscopy study of the interaction of silver ions with Staphylococcus aureus, Listeria monocytogenes, and Escherichia coli. Appl. Environ. Microbiol. **79**, 6385–6390 (2013).

54. Hulbert, S. L. & Williams, G. P. 1 - SYNCHROTRON RADIATION SOURCES. in (eds. Samson, J. A. R. & Ederer, D. L. B. T.-V. U. S.) 1–25 (Academic Press, 2000). doi:https://doi.org/10.1016/B978-012617560-8/50002-5.

55. Bonnelle, C. Chapter 7. X-Ray spectroscopy. Annu. Reports Sect. 'C' (Physical Chem. **84**, 201–272 (1987).

56. Berrah, N. et al. Double-core-hole spectroscopy for chemical analysis with an intense X-ray femtosecond laser. Proc. Natl. Acad. Sci. U. S. A. **108**, 16912–16915 (2011).

57. Gurman, S. J. Amorphous Materials: X-ray Absorption Spectroscopy. in (eds. Buschow, K. H. J. et al.) 256–259 (Elsevier, 2001). doi:https://doi.org/10.1016/B0-08-043152-6/00055-3.

58. Achkar, A. J., Regier, T. Z., Monkman, E. J., Shen, K. M. & Hawthorn, D. G. Determination of total x-ray absorption coefficient using non-resonant x-ray emission. Sci. Rep. **1**, 182 (2011).

59. Hu, Y. F. et al. Commissioning and performance of the variable line spacing plane grating monochromator beamline at the Canadian Light Source. Rev. Sci.

Instrum. **78**, 83109 (2007).

60. Kruse, J. et al. Phosphorus L2,3-edge XANES: overview of reference compounds. J. Synchrotron Radiat. **16**, 247–259 (2009).

61. Sato, S., Neves, E. G., Solomon, D., Liang, B. & Lehmann, J. Biogenic calcium phosphate transformation in soils over millennial time scales. J. Soils Sediments **9**, 194–205 (2009).

62. Liu, J., Hu, Y., Yang, J., Abdi, D. & Cade-Menun, B. J. Investigation of Soil Legacy Phosphorus Transformation in Long-Term Agricultural Fields Using Sequential Fractionation, P K-edge XANES and Solution P NMR Spectroscopy. Environ. Sci. Technol. **49**, 168–176 (2015).

63. Güngör, K., Jürgensen, A. & Karthikeyan, K. G. Determination of Phosphorus Speciation in Dairy Manure using XRD and XANES Spectroscopy. J. Environ. Qual. **36**, 1856–1863 (2007).

64. Fleet, M. E. & Liu, X. Calcium L2,3-edge XANES of carbonates, carbonate apatite, and oldhamite (CaS). Am. Mineral. **94**, 1235–1241 (2009).

65. Naftel, S. J., Sham, T. K., Yiu, Y. M. & Yates, B. W. Calcium L-edge XANES study of some calcium compounds. J. Synchrotron Radiat. **8**, 255–257 (2001).

66. Seah, M. P. & Spencer, S. J. AES of bulk insulators – control and characterisation of the surface charge. J. Electron Spectros. Relat. Phenomena **109**, 291–308 (2000).

67. Cros, A. Charging effects in X-ray photoelectron spectroscopy. J. Electron Spectros. Relat. Phenomena **59**, 1–14 (1992).

68. Gilbert, B. et al. Charging phenomena in PEEM imaging and spectroscopy.

Ultramicroscopy **83**, 129–139 (2000).

69. Fleet, M. E. & Liu, X. Coupled substitution of type A and B carbonate in sodium-bearing apatite. Biomaterials **28**, 916–926 (2007).

70. Fleet, M. E. & Liu, X. Location of type B carbonate ion in type A–B carbonate apatite synthesized at high pressure. J. Solid State Chem. **177**, 3174–3182 (2004).

71. Fleet, M. E., Liu, X. & King, P. L. Accommodation of the carbonate ion in apatite: An FTIR and X-ray structure study of crystals synthesized at 2–4 GPa. Am. Mineral. **89**, 1422–1432 (2004).

72. Li, W., Liu, X.-M. & Hu, Y. Potassium and Calcium K-Edge XANES in Chemical Compounds and Minerals: Implications for Geological Phase Identification. Geostand. Geoanalytical Res. **44**, 805–819 (2020).

73. Baker, M. L. et al. K- and L-edge X-ray absorption spectroscopy (XAS) and resonant inelastic X-ray scattering (RIXS) determination of differential orbital covalency (DOC) of transition metal sites. Coord. Chem. Rev. **345**, 182–208 (2017).

74. Salarian, M., Xu, W. Z., Wang, Z., Sham, T.-K. & Charpentier, P. A. Hydroxyapatite–TiO2-based Nanocomposites Synthesized in Supercritical CO2 for Bone Tissue Engineering: Physical and Mechanical Properties. ACS Appl. Mater. Interfaces **6**, 16918–16931 (2014).

75. Cosmidis, J., Benzerara, K., Nassif, N., Tyliszczak, T. & Bourdelle, F. Characterization of Ca-phosphate biological materials by scanning transmission X-ray microscopy (STXM) at the Ca L2,3-, P L2,3- and C K-edges. Acta Biomater.

12, 260–269 (2015).

76. Väänänen, K. Mechanism of osteoclast mediated bone resorption--rationale for the design of new therapeutics. Adv. Drug Deliv. Rev. **57**, 959–971 (2005).

77. Boyle, W. J., Simonet, W. S. & Lacey, D. L. Osteoclast differentiation and activation. Nature **423**, 337–342 (2003).

CHAPTER 4: INTERFACIAL ADHESION AND SURFACE BIOACTIVITY OF ANODIZED TITANIUM MODIFIED WITH SION AND SIONP SURFACE COATINGS

Kamal Awad[1, 2, 3], Simon Young[4], Pranesh Aswath[1], Venu Varanasi[1, 2, *]

[1]Department of Materials Science and Engineering, College of Engineering, The University of Texas at Arlington, Arlington, TX 76019, USA.

[2]Bone-Muscle Research Center, College of Nursing & Health Innovation, The University of Texas at Arlington, Arlington, TX 76019, USA.

[3]Refractories, Ceramics and Building Materials Department, National Research Centre, Dokki, Cairo 12622, Egypt.

[4]Department of Oral and Maxillofacial Surgery, the University of Texas Health Science Center at Houston, School of Dentistry, Houston, Texas 77054, USA

*Corresponding Author, (venu.varanasi@uta.edu)

Dr. Venu Varanasi, PhD

Associate Professor, Bone Muscle Research Center

College of Nursing and Health Innovation

University of Texas at Arlington

Address: 655 W. Mitchell St., Box 19410, Arlington, TX 76019

Email: Venu.varanasi@uta.edu

Phone: 817-272-1743

Fax: 817-272-1360

ABSTRACT:

Titanium (Ti) surface modification via coating technologies (plasma spraying, electron-beam deposition) has been used to enhance bone-implant bonding by increasing the rate of hydroxyapatite (HA) formation, a property known as bioactivity. Yet, these methods involve fabrication at high temperature (> 600 ^{0}C) that reduces coating-implant adhesion due to thermal expansion mismatch and reduces bioactivity due to increased crystallinity in the coating. Thus, amorphous surface coatings with strong Ti substrate adhesion that can be fabricated at relatively low temperatures are crucially needed for enhanced osseointegration. Therefore, this study is aimed to enhance the Ti surface bioactivity via strongly adherent bioactive thin film coatings deposited by low temperature (< 400 ^{0}C) plasma enhanced chemical vapor deposition technique on nanopore anodized Ti surface. Two groups of coatings (silicon oxynitride (SiON) and silicon oxynitrophosphide (SiONP)) were deposited on anodized Ti and tested for interfacial adhesion and surface bioactivity. TEM and XPS were used to investigate the interfacial composition while interfacial adhesion was tested using nano-indentation tests which indicated a strong interfacial adhesion between the coatings and the anodized Ti substrate. Surface bioactivity of the modified Ti was tested by comprehensive surface characterization (i.e., chemical composition, surface energy, morphology, and mechanical properties) and apatite formation on each surface. The SiONP coating significantly enhanced the Ti surface bioactivity that presented the highest surface coverage of carbonated hydroxyapatite (HCA, ~ 40%) with a Ca/P ratio (~ 1.65) close to the stoichiometric hydroxyapatite (~ 1.67) found in bone biomineral. The HCA structure and morphology were confirmed by HR-TEM/SAED, XRD, FT-IR,

and HR-SEM/EDX. This study concluded that the improved surface bioactivity of Ti-SiON and Ti-SiONP coatings suggests their potential use as strongly adherent bioactive surface coatings for Ti implants.

KEYWORDS: Titanium; Surface modification; Silica Coatings; Bioactivity; Implants.

Highlights

1. PECVD SiON and SiONP coatings significantly enhanced CP-Ti surface bioactivity.
2. Strong interfacial adhesion between SiON/SiONP coatings and the Ti substrate.
3. SiONP coating increase surface coverage of carbonated hydroxyapatite (~ 40%).
4. SiON and SiONP are promising as bioactive surface coatings for Ti implants.

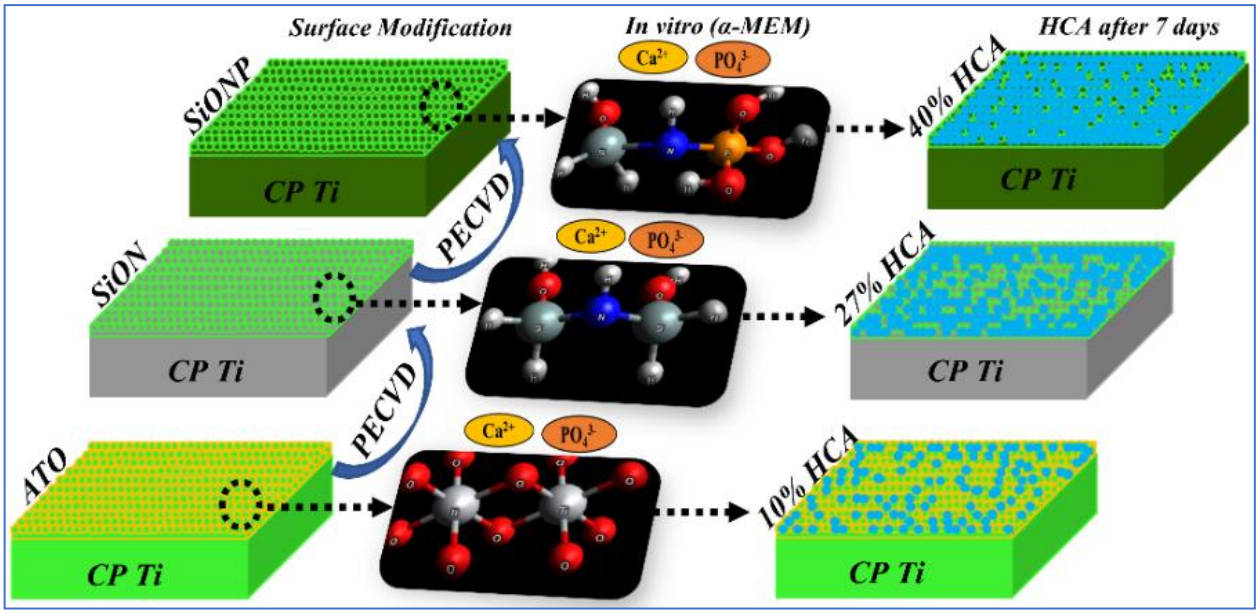

Figure 4.0: Graphical abstract shows the chemical structure and percentage of HA coverage.

1. INTRODUCTION

Commercially pure Ti (CP-Ti) was first introduced as an implant in 1965. Since then, Ti and its alloys have been adopted broadly for orthopaedic, dental, and craniofacial applications [1,2] Ti has unique properties such as biocompatibility, favorable response of tissues on its surface, absence of allergic reaction, high corrosion resistance, and specific mechanical properties that make it a suitable metal for use as a bone implant [3–5]. But Ti implants under normal manufacturing steps lead to an oxidized, contaminated, stressed, plastically deformed, and non-uniformed surface native oxide layer which introduce many limitations and require further surface modification. One of the most common limitations of Ti-implants is aseptic loosening which is the failed bonding between the implants and the bone due to poor osteointegration [6–8]. Also, metallic debris from Ti alloys induce aseptic loosening that results in severe osteolysis [8]. As a result, 75% of implant failures occur because of aseptic loosening and impaired implant fixation. Thus, various surface modification techniques have been applied to the biological, chemical, and mechanical properties to improve bone-implant bonding. These techniques include mechanical treatment (e.g., sand blasting), surface coatings (e.g., thermal spraying, sol-gel, plasma deposition, and ion beam-assisted deposition), chemical treatment (e.g., acid etching), and electrochemical treatment (e.g., anodic oxidation) [9–11]. Anodic oxidation (anodization) of the CP-Ti is one of the most successful surface treatments over the last few decades [12]. It allows the formation of an anodic titanium oxide (ATO) layer with interconnected nanopore structure on the surface. This controlled growth layer is much thicker than the natively formed oxide layer on the Ti surface that can enhance corrosion resistance and biocompatibility [13]. All these surface

modification techniques depend on the understanding that the implant surface plays an extremely important role in the onset biological reactions between the artificial material surface and the biological environment. Improving implant bioactivity significantly improved the osseointegration with enhanced bone-implant contact and mineralization leading to rapid bone regeneration [14]. Thus, there is a crucial need for optimal surface modification that results in bioactive surface with rapid and uniform surface apatite nucleation for good bone formability on the implant's surface.

Deposition of bioactive materials on the surface of Ti is of great interest due to the potential to improve implant bioactivity and bone-implant bonding. In this regard, calcium phosphate or HA based coatings have proven an elevated potential to enhance the Ti surface activity and bone regeneration capability. However, these coatings suffer from poor interfacial adhesion with the metal substrate due to the lack of miscible interface between the ionic Ti/TiO2 and the covalent structure of calcium phosphate layer [15–18]. Most recent is the plasma enhanced chemical vapor deposition (PECVD) of amorphous silica-based coatings (Si-O-N-P system) that has been developed by Varanasi and colleagues as potential bioactive coatings that adheres well to the implant surface, releases Si^{+4} to enhance osteogenesis, and forms surface HCA for collagen mineral attachment [15,19–21]. Our previous studies on these PECVD coatings indicated that Si-O-N-P system chemistry can be described according to a random mixing model (RMM) or random bonding model (RBM) depending on the oxygen and nitrogen content in each coating [21,22]. In the RBM, oxygen and nitrogen are incorporated in the silica tetrahedral network to form nonstoichiometric $Si_wO_xN_y$. Thus, oxygen-rich films were found to exhibit random bonding of nonstoichiometric $Si_wO_xN_y$ when (x+y=4) and

$Si_wO_xN_yP_z$ when (x+y+z=4) for SiON and SiONP systems, respectively [22]. On the other hand, nitrogen-rich films exhibited random mixing of $[Si{-}Si]_w{-}[Si{-}O]_x{-}[Si{-}N]_y$ for $Si_wO_xN_y$ and $[Si{-}Si]_w{-}[Si{-}O]_x{-}[Si{-}N]_y{-}[O\text{-}P]_z$ for $Si_wO_xN_yP_z$ system [15,19,23]. The RMM coatings allow hydrogen bonding on the surface such as Si-H, N-H, and Si-O-H which is favorable for enhanced bioactivity. PECVD coatings have remarkable advantages compared to other coating methods [20]. This method requires a relatively low temperature (~250-400˚C) that prevents mismatch between the coating and the substrate materials. PECVD coating can efficiently form a stable amorphous layer on an underlying metal surface. These new biomaterial coatings enhance osteogenesis via antioxidant and osteogenic marker expression [19]. The unique chemical structure of these amorphous PECVD SiON or SiONP is supposed to provide a hydrophilic surface with high surface free energy and readily available functional groups (e.g., Si-H, N-H, and Si-OH) once immersed/implanted in a physiological environment [20,24]. The presence of such a surface with its unique chemical structure could initiate the formation of apatite-like bone structure leading to rapid bone healing by supporting both osteoconductivity and osseointegration. However, we have not fully understood the nature of the coating-implant interface and affect these coatings have on HA formation verses bare Ti implants to gain improved understanding on how these coatings can potentially improve implant bioactivity and interfacial adhesion.

Thus, the aim of this study is to characterize the interfacial adhesion and surface activity of anodized titanium modified with SiON and SiONP PECVD surface coatings. SiON and SiONP coated anodized CP Ti will be comprehensively analyzed and compared to clinically relevant anodized Ti fixation devices. Interfacial composition and

adhesion between the coatings and Ti substrate as well as the modified surface bioactivity via rapid and uniform HA nucleation will be tested. The goal of this study is to show that SiON and SiONP coatings enhance the surface bioactivity verses bare implant surface while providing strong adhesion to the underlying Ti/ TiO_2 surface. The deposited thin films in this study are RMM type and will be abbreviated as SiON and SiONP for simplicity.

2. MATERIALS AND METHODS

2.1 Study Design

This study was performed in two consecutive sections to investigate our proposed hypothesis. The anodized CP-Ti surface was modified by depositing 300 nm thick bioactive amorphous SiON and SiONP thin film coatings. Then, surface topography, chemical structure, interfacial composition and adhesion, wettability and surface energy, and mechanical properties of the SiON- and SiONP-CP-Ti modified surfaces were compared to an anodized CP-Ti surface. Second, cell-free *in-vitro* studies (i.e., only cell culture medium without cells) were performed to test the surface activity and hydroxyapatite formation on SiON- and SiONP-CP-Ti modified surfaces compared to CP-Ti. This step was performed by immersion of all samples in alpha modified essential medium (α-MEM) for 12 hours and 7 days. After each time-point, samples were removed and dried for comprehensive analysis using high resolution-scanning electron microscopy (HR-SEM) coupled with energy dispersive X-ray (EDX) analysis, optical profilometer scanning, FT-IR analysis, and transmission electron microscopy. Many of the methods below are brief summaries of detailed methods given in our prior work [21,25–27]. We provide added detail below relevant to this manuscript.

2.2 SiON and SiONP Thin Films Deposition

CP-Ti plates (grade II, ASTM F67) were provided by KLS Martin Group (Mühlheim/Donau, Germany). According to the manufacturer, the surface of the provided CP-Ti plates was processed by vibration grinding and glass bead blasting, and finally finished by anodic oxidation. In this study, anodized CP-Ti plates were used as substrate materials and controls. SiON and SiONP were deposited as thin film coatings on anodized CP-Ti surfaces following our prior published protocol [20,28]. A low temperature PECVD technique was used to deposit a 300 nm thin film of either SiON or SiONP coatings on the anodized CP-Ti substrate. CP-Ti plates' surfaces were cleaned using oxygen plasma cleaning through March PX-500 Plasma Asher (March Plasma Systems Inc., California, USA). The cleaned CP-Ti samples were loaded into a TRION ORION II PECVD System (TRION Technology, Florida, USA) to deposit 300 nm of SiON or SiONP thin film on the CP-Ti as substrates. The deposition was performed in four sequential steps: first, the chamber was purged with argon gas at a flow rate of 250 sccm for 30 seconds to ensure adequate chamber cleaning and removal of any possible dust on the sample's surface. Second, a conditioning step was performed in which all required gases being used for deposition were run for 30 seconds to stabilize the gas flow rate and prepare the chamber for specific thin film chemistry. Third, a deposition step was performed in which all required gases were run at a specific flow rate (Table 1) with ICP power of 75 W and RIE power of 30 W. Finally, a cleaning step was carried out using argon of 250 sccm for 180 seconds to prepare the chamber for the next run. Before the process, the lower electrode was uniformly heated to 400 °C. The chamber pressure was held at 900 mTorr and the excitation frequency was 13.56 MHz during all

processing steps. Silane (SiH_4) and phosphine (PH_3) gases were used as sources of silicon and phosphorus, respectively, and both were diluted in argon (Ar) (15%SiH_4/ 2% PH_3/ 85%Ar). Nitrous oxide (N_2O) was used as the source for oxygen and ammonia gas was used as the source for nitrogen. The exact flow rates of each gas in sccm, the deposition rate of SiON and SiONP, and the refractive index are reported in Table 4.1.

Table 4. 1. Gas Flow Rates, deposition rate, and refractive index for Silicon Oxynitride (Si-O-N) and Silicon Oxynitrophosphide (Si-O-N-P) Layers Deposited by PECVD.

Sample	Gas flow rate (sccm)				Deposition Rate (nm/min)	Refractive index (n)
	$SiH_4/PH_3/Ar$	N_2O	N_2	NH_3		
SiON	24	3	225	50	41.0	1.82
SiONP	24	16	225	50	38.5	1.68

2.3 Surface Characterization

Surface morphology and chemical composition: Scanning electron microscopy (SEM, S-3000N, Hitachi, Japan) coupled with energy dispersive X-ray spectroscopy (EDS) was used to study the surface microstructure, morphology, and chemical composition before and after surface modification. SEM working distance was set to 15 mm with accelerating voltage of 20 kV and various SEM images were captured at different magnifications to compare the surface morphology before and after the addition of thin film coatings. Ultra HR-SEM (Hitachi S-4800 II FE SEM; Hitachi) was used to capture the nanostructure of the surfaces before and after coating. Images were acquired at a working distance of 10 mm under 20 kV at different magnifications. For the EDX analysis, the accelerating voltage was held constant at 15 kV and areas of interest were scanned for composition analysis. FT-IR was also used to reveal the surface chemical structure and indicate the surface functional groups after surface

modification with SiON and SiONP compared to uncoated anodized CP-Ti. The interfacial analysis of Ti-SiONx coatings was performed using X-ray photoelectron spectroscopy (Thermo Scientific K-Alpha XPS, MA, USA) and transmission electron microscopy (TEM, Hitachi HF-3300, Japan) at the Center for Nanophase Materials Sciences (CNMS) at Oak Ridge National Laboratory, Oak Ridge, TN (ORNL). Monochromatic Al-K alpha source with an energy of 1486.6 eV and Ar^+ beam sputtering operated at an energy of 4.2 keV was used for XPS analysis. Samples were prepared using a Hitachi NB5000 dual-beam SEM focused ion beam (SEM-FIB) onto Cu grids prior to imaging by TEM.

Surface roughness: An optical profilometer (Wyko NT9100, Veeco Instruments Inc., USA) was used to capture the surface topography and measure the surface roughness parameters. A large area (310 μm * 232.5 μm) of the samples' surface was scanned via non-contact mapping in three dimensions and six images per each sample were captured for analysis. Roughness parameters such as roughness average (Ra) and root mean-square roughness (Rq) were estimated for all samples. Ra represents the arithmetic average of the absolute values of the profile heights over the evaluation length, while the Rq indicates the root mean square average of the profile heights over the evaluation length [29,30]. Surface roughness parameters were used to compare the CP-Ti surface before and after modification with SiON and SiONP coatings as well as after HA deposition at 12 hours and 7 days in α-MEM.

Wettability and Surface Energy: Surface wettability was assessed using contact angle measurements. Surface contact angles were measured using 250-U4 Goniometer/Tensiometer with a super speed German-made camera and DROP-image

Advanced software (Ramé-hart instrument co., NJ, USA). The sessile drop technique was used to measure the surface contact angle of all samples. Deionized water and diiodomethane (99% purity, Sigma-Aldrich Co., St. Louis, MO, USA) were used as probing liquids to measure the contact angle of each sample at 25 °C. For each coating, three samples were tested with 3 repetitive drops of DI water and diiodomethane on each sample for a total reading of nine measurements per coated sample as well as anodized CP-Ti samples. Contact angle images were captured on each surface using a high-resolution camera within 10 seconds of droplet seeding. Using the contact angle results, the free surface energy of each sample was calculated using the Owens-Wendt-Kaelble (OWK) equation [31]. The OWK equation (1) relates the contact angle (Ɵ) of a solid surface to its total surface free energy, broken into its polar and dispersive components [31].

$$\gamma_{LV}(1+\cos\theta) = 2\left(\sqrt{\gamma_L^d \gamma_s^d} + \sqrt{\gamma_L^p \gamma_s^p}\right) \qquad (Eq.1)$$

Where γ_{LV} represents the total surface free energy of a solid surface, and S and L represent the solid and liquid phases, respectively. γ^d and γ^p refer to the dispersive and polar surface tension components. The values of surface energy and its corresponding dispersive and polar components of deionized water and diiodomethane were previously reported [31] as shown in Table 4.2. These values were used in our calculations.

Table 4.2. Surface energy and surface tension components of water and diiodomethane.

Liquid	γ_L^d (mJ/m2)	γ_L^p (mJ/m2)	γ_{LV} (mJ/m2)
Water	21.8±0.7	51.0	72.8
Diiodomethane	49.5	1.3	50.8

Mechanical properties: Vickers hardness and nanoindentation tests were performed to investigate any changes in the mechanical properties of the CP-Ti compared to the SiON and SiONP modified surfaces. Vickers microhardness was measured using a LECO LM 300 AT Micro Hardness Tester (LECO Co., MI, USA) operated at a load of 500g for 10 seconds and 50x objective was used to visualize the indent after each indentation. After Vickers hardness testing, the samples surfaces were scanned using HR-SEM to capture the indentation dents on each surface. The two diagonals (d1 and d2) of the diamond shaped indentation were measured and the hardness (H_V) was determined using the following equation [32]:

$$H_V = 0.1891 * F / d^2 \qquad (Eq. 2)$$

where F is the applied load, and d is the average of indentation diagonals. The H_V is given in kg/mm^2 which can be converted into GPa by multiplying the previous equation by 0.009806. For nanoindentation, a 3600 µm^2 surface area was scanned using scanning probe microscopy (SPM) and the area of interest was indented with a Berkovich tip using a Hysitron Ubi-1 Nanoindenter (Hysitron, Minneapolis, MN). For each sample, 12 nanoindentations were performed on the selected area according to the following loading function: ramped up to 10 mN at a rate of 250 µN/s, held for 10 seconds, and then unloaded at 250 µN/s. The unloading slope of the load-displacement curve was used to calculate the reduced elastic modulus (E_r) and the hardness (H) based on the Oliver-Pharr method [33,34]. E_r can be defined as the elastic modulus that contains the elastic contributions of the specimen and the diamond indenter tip according to the following equation [35]:

$$\frac{1}{E_r} = \frac{1 - v_s^2}{E_s} + \frac{1 - v_i^2}{E_i} \qquad (Eq.3)$$

here, E_S and E_i indicate the elastic modulus of the sample and the indenter tip, while v_S and v_i represent the Poisson's ratio of the sample and the indenter tip, respectively. Then, the E_r can be calculated using the slope of the linear part of the unloading curve (S) and the projected contact area of the Berkovich tip (A_c) according to equation (4) [33,34]. The projected contact area of the indenter tip was determined by calibrating the tip at various indentation depths with fused quartz.

$$E_r = \frac{\sqrt{\pi}}{2} \frac{s}{\sqrt{A_C}} \qquad (Eq.4)$$

Then, the hardness can be defined as the maximum applied load (P_{Max}) divided by the projected contact area of the indenter tip (A_c) as follows [33]:

$$H = P_{Max}/A_c \qquad (Eq.5)$$

Nano-scratch tests were performed to investigate the interfacial adhesion strength of PECVD thin film coatings on the anodized CP-Ti surface. Briefly, the indenter tip was dragged horizontally on the surface while the vertical force is increased simultaneously. This coupled motion can detach the thin film coatings from the substrate if the adhesion strength of the films was exceeded. The nano-scratch tests left behind a scratch mark on the surface that could be visualized using scanning probe microscopy (SPM). A Hysitron Ubi-1 Nanoindenter (Hysitron, Minneapolis, MN) was used to perform nano-scratch tests on the PECVD coatings. Load controlled nano-scratch tests were performed on the surface using the following load function: the normal load started from 0 mN and gradually increased until load peak of 10 mN over 4 µm horizontal displacement for 30 seconds. SPM topographical 2D post scratch images

were captured to ensure successful scratches. Lateral force versus normal force, lateral displacement verses normal force and lateral forces, and normal displacement versus time curves were extracted and analyzed to investigate film adhesion.

2.4 In-vitro Cell Free Studies "Surface Apatite formation"

To compare the bioactivity of the SiON and SiONP- CP-Ti coatings to the CP-Ti, *in-vitro* cell free studies were performed at two time-points (12 hours and 7 days). For each time-point, three samples of each group (i.e., CP-Ti as a control, SiON-Ti, and SiONP-Ti) were cleaned in 100 % pure ethanol followed by two rinses with phosphate buffered saline (PBS-1x) and finally immersed in α-MEM in sterile tissue culture plates. Then, samples were incubated in 37°C for 12 hours and 7 days. At each time-point, samples were washed twice with PBS-1x and dried overnight at 37°C. Then samples were used for comprehensive analysis. It is important to mention that α-MEM is commonly used in cell culture studies and its composition is more similar to the concentration of salts in human blood plasma, which makes the α-MEM a more suitable solution compared to the SBF solution [36]. As well as α-MEM is an important source for passive ion exchange with the bioactive material surfaces, thus it can be used to investigate the biomaterials response to the blood plasma and the cell culture media environment.

The HA and mineral deposition on the surfaces were confirmed and studied using various techniques, including SEM/EDX followed by ImageJ software analysis, high resolution transmission electron microscopy (HR-TEM), X-ray diffraction, optical profilometer, and FT-IR analysis. SEM/EDX analysis was used to scan the surface morphology after HA formation on the surface for 12 hours and 7 days in α-MEM. EDX

data was used to investigate the chemical composition and calculate the calcium to phosphate ratio (Ca/P) to compare the formed HA on each sample to the Ca/P ratio of the standard hydroxyapatite. SEM images were further used to quantitively investigate the HA surface area coverage using ImageJ software [37]. The HA formation was further confirmed by FT-IR analysis. HR-TEM (H-9500 HR-TEM, Hitachi, Japan) with selected area electron diffraction (SAED) was used to image the HA crystal planes and diffraction patterns. This diffraction pattern from HR-TEM was further confirmed by XRD analysis.

2.5 Statistical analysis

OriginPro 8.5 software was used for all graphs and statistical analysis, bar graphs display group means and standard deviations. A one-way ANOVA followed by Tukey's post hoc was used for between group comparisons. For significance level, $P < 0.05$ was considered as statistically significant, with * representing $p < 0.05$, ** representing $p < 0.01$, and *** representing $p < 0.001$. For *in-vitro* studies, a minimum of three replicates at two separate time points were used for each experiment per each group of samples according to ISO10993-5.

3. RESULTS AND DISCUSSION

3.1 Surface Modification and Characterization

After surface modification, comprehensive surface analysis was performed to study the effect of PECVD coatings on the micro- and nanostructures, surface functional groups, surface wettability and surface energy, surface roughness, and micro- and nano-mechanical properties compared to the anodized CP-Ti. The physical appearance and microstructure of medical grade anodized CP-Ti locking plates, as

received, and after surface modification with SiON- and SiONP-coatings, are shown in Figure 4.1. Due to the importance of visual identification of Ti plates and screws for orthopedic surgeons in the medical field, it was important to visually differentiate the anodized CP-Ti plates and the PECVD coated plates based on their colors. The anodized CP-Ti plates have a green color (Figure 4.1-A), while SiON-Ti plates have a gray color (Figure 4.1-B), and SiONP-Ti plates are dark green (Figure 4.1-C). The microstructure of each sample, as scanned by SEM at different magnifications, is shown in Figure 1(D-I). Low and high magnification SEM imaging of the coated plates revealed that SiON and SiONP PECVD coatings have no effect on the surface topography or morphology. Figure 4.1 (G-I) clearly shows the microstructure and surface roughness profile that can be attributed to the glass bead blasting prior to anodic oxidation of the surface as mentioned by the manufacturer. Glass bead blasting is an effective technique for increasing surface roughness and enhancing the coating-substrate interaction by reducing the native oxide layer on the substrate surface [38]. This effect was further confirmed by surface roughness measurements as reported by scanning a large surface area of each sample using an optical profilometer as shown in Figure 4.1 (J-L). Comparison of the surface roughness parameters of CP-Ti (*Ra* = 459 ± 21 and *Rq* = 615 ± 43) to the SiON surface (*Ra* = 487 ± 22 and *Rq* = 653 ± 30) and SiONP (*Ra* = 487 ± 22 and *Rq* = 653 ± 30) indicated that there was no significant difference in surface roughness after the PECVD coatings.

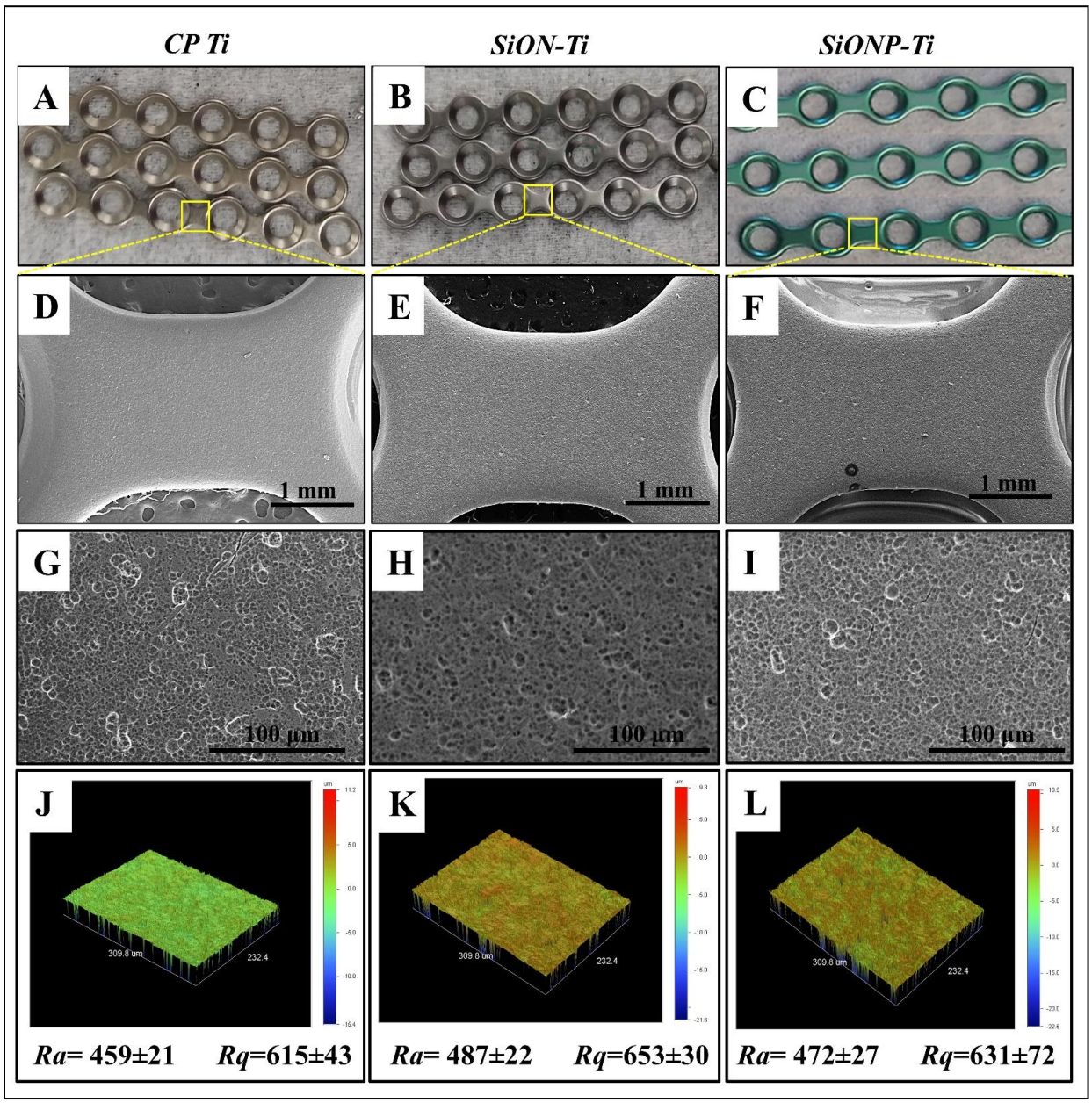

Figure 4.1: Visual identification (A-C) and HR-SEM images (D-I) compare the bare anodized CP-Ti to the SiONx and SiONPx PECVD coated plates. Microstructure confirms no topography changes after the coating. J-L) Optical profilometer 3D images show the surface roughness of the bare anodized CP-Ti (J) compared to the coated surfaces (K & L).

Ultra HR-SEM images in Figure 4.2 present the microstructure and surface topography of the anodized CP-Ti compared to the SiON and SiONP PECVD coatings at different magnifications. The anodized CP-Ti surface indicates the presence of an

ATO layer with nanopore structure on the surface as shown at Figure 4.2 (A & D) and confirmed by EDX (Figure 4.2-G). This ATO layer was developed during the surface anodization and displays diversification of nanopores with sizes from 150 to 350 nm. This layer enables specific advantages on the Ti surface such as increasing surface area, large pore volume, and uniform pore size distribution [39]. Previous studies have also indicated that the formation of an active ATO layer on the surface of Ti improves the biocompatibility [40], enhances the HA formation, and strengthens the interfacial strength between Ti substrate and surface coatings [41]. Here, the microstructure investigation of the SiON (Figure 4.2-B &E) and SiONP (Figure 4.2-C &F) PECVD films on the anodized CP-Ti revealed the formation of thin film coatings with cell-like surface features. The formation of cell-like features of the deposited thin films indicates that the ATO layer nanopores could work as anchors and deposition sites to support thin film adhesion on the Ti substrate. Furthermore, these nanoporous features of ATO could facilitate the deposition and adhesion of thin films by working as pinholes, ensuring mechanical interlocking between the Ti substrate and the deposited thin films. This behavior has been confirmed in previous studies by Jin et al. [42] and Zhou et al. [39] which indicated that nanopores, with 200 nm pore diameters, were effective as bonding pinholes for nanostructured grain growth with strong interfacial adhesion. The chemical composition of each sample was investigated using EDX composition analysis (Figure 4.2 G-I) and the atomic percentage (at%) of each sample is reported at Table 4.3. The CP-Ti compositional analysis revealed the presence of oxygen as well as phosphorus (P) at low % of 0.512±0.07 which can be attributed to the anodic oxidation of the surface. On the other hand, SiON and SiONP PECVD coated samples indicated the

presence of Si, O, and N on both surfaces plus P with a % of 3.47±0.36 on the SiONP surface.

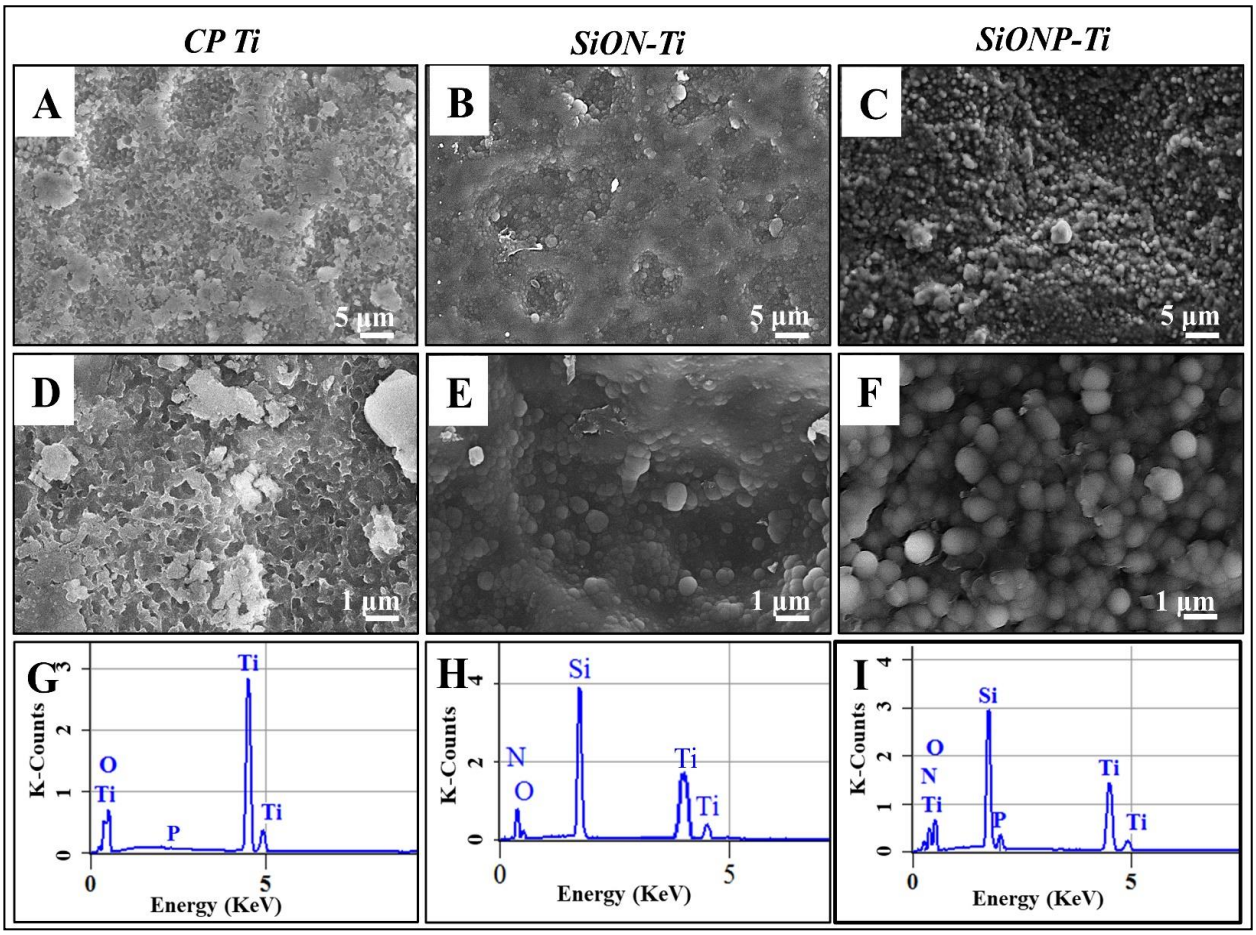

Figure 4.2: Ultra HR-SEM images (A-F) compare the anodized CP-Ti to the SiONx and SiONPx PECVD coated plates. A&D) Confirm the presence of an anodic titanium oxide (ATO) layer with nanopore structure. B-F) Show the cell-like nanostructure after the SiONx and SiONPx deposition on the anodized CP-Ti. G-I) EDX compositional analysis spectra showing the exact chemical composition of each surface.

Table 4. 3. Atomic percentage (At%) shows the elemental composition of CP-Ti, SiON-Ti, and SiONP-Ti as reported from EDX analysis.

at (%)	N	O	Si	P	Ti
Pure-Ti	-----	21.7±1.9	----	0.512±0.07	77.04±2.8
SiON	19.1±3	9.9±1.38	41.1±2	---	29.9±2
SiONP	14.48±1.8	6.035±2	43.59±2.5	3.47±0.36	32.41±2

The surface of anodized CP-Ti, SiON-Ti, and SiONP-Ti was further investigated to study the surface functional groups that are revealed from the FT-IR spectra (Figure 4.3). The CP-Ti spectra indicate the presence of a broad strong band in range 550-900 cm^{-1}, which can be attributed to the vibrational modes of the Ti-O bond from the ATO surface layer [43,44]. For SiON-CP-Ti and SiONP-CP-Ti, the peaks near 800 cm^{-1} represent the Si-O-Si [45], while the modes at 950 cm^{-1} can be attributed to the Ti-O-Si vibration [46]. Bands at 842 cm^{-1} represent the Si-N stretching mode [47], while bands at 1175 and 3330 cm^{-1} are attributed to the bending and stretching vibration modes of N-H, respectively [48]. Bands at 953 cm^{-1} on PECVD SiON-CP-Ti and SiONP-CP-Ti surfaces are attributed to the presence of Si-OH stretching modes [49]. These bands were observed on the surface of PECVD coatings due to the readily available silanol groups on the oxide surface, which are commonly observed for low temperature PECVD [28]. It is important to mention that deposition of amorphous silica based thin films brings the unique surface properties of Si_3N_4, SiON, and SiONP to the surface of reconstructive fixative materials (e.g., titanium plates). These bioactive amorphous coatings with surface multi-functional

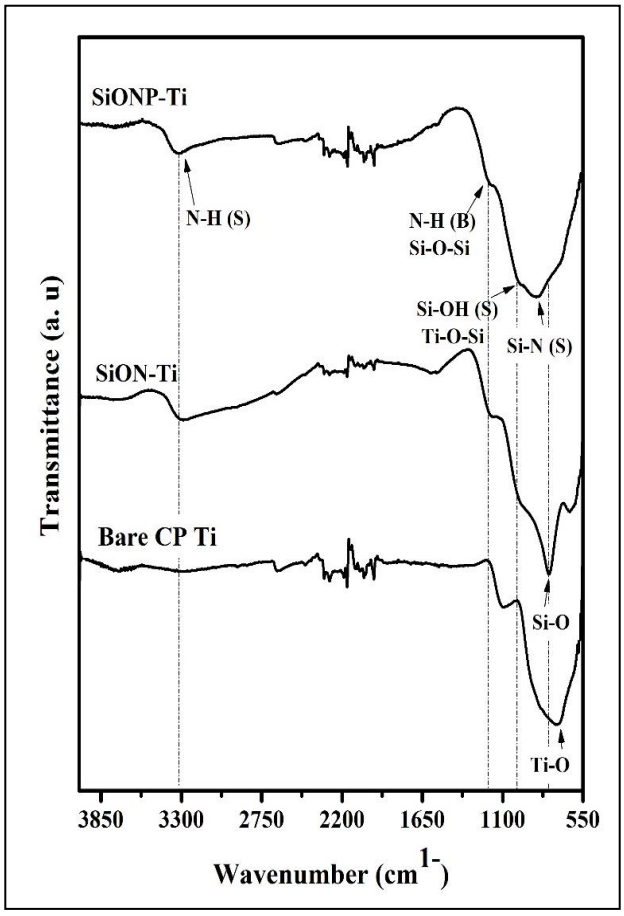

Figure 4.3: FT-IR spectra of the anodized CP-Ti compared to SiONx-Ti and SiONPx-Ti coatings.

groups (i.e. Si-O, Si-N, Si-H, and N-H) are partially soluble under physiological conditions because N-H and Si-H bonding allow immediate dissolution/degradation *in-vitro* [19–21,26,28]. As a result, these bioactive surfaces enhance cell adhesion, protein adsorption, and rapid mineralization leading to early bone regeneration on the implant surface [15,19,23]. Furthermore, these coatings also promoted sustainable release of Si^{+4} for enhancing osteogenesis, angiogenesis, and myogenesis [15,20,23,25,50,51].

Compositional analysis of the SiON layer and the Ti-TiO_2-SiON interface was performed using HR-TEM and XPS by milling through the thickness of the surface coatings (100 nm) reaching the Ti substrate. Figure 4.4-a presents the cross-section micrographs of the interface which indicated amorphous SiON layer on the top of the TiO_2 layer and the crystalline Ti substrate. The elemental composition of the coating as a function of the deposition depth is presented in Figure 4.4-b. This identifies the composition in all layers including regions A (amorphous SiON layer), region B (TiO_2 layer), and region C (Ti crystalline substrate). Binding energy spectra of the individual elements present in these regions is presented in Figure 4.4-c. Si 2p analysis indicated the predominate of Si-O bonding at the coating layer (region A), N 1s analysis indicated the presence of N-H and Si-N in the coating layer. The O 1s analysis indicated the presence of both O-Ti and O-Si bonding at the interfacial layer (region B). Also, Ti 2p indicated the presence of Ti-O bonding at region B while Ti-Ti predominant at region C. These results indicate the presence of SiO_2 and TiO_2 at the interface layer providing cross-bonding between the coating and the substrate as presented in Rxn 4. This interfacial bonding leads to strong adherent coatings which agrees with previously

published data [21,28]. These results also agree with the SEM/EDX, and FT-IR data presented above.

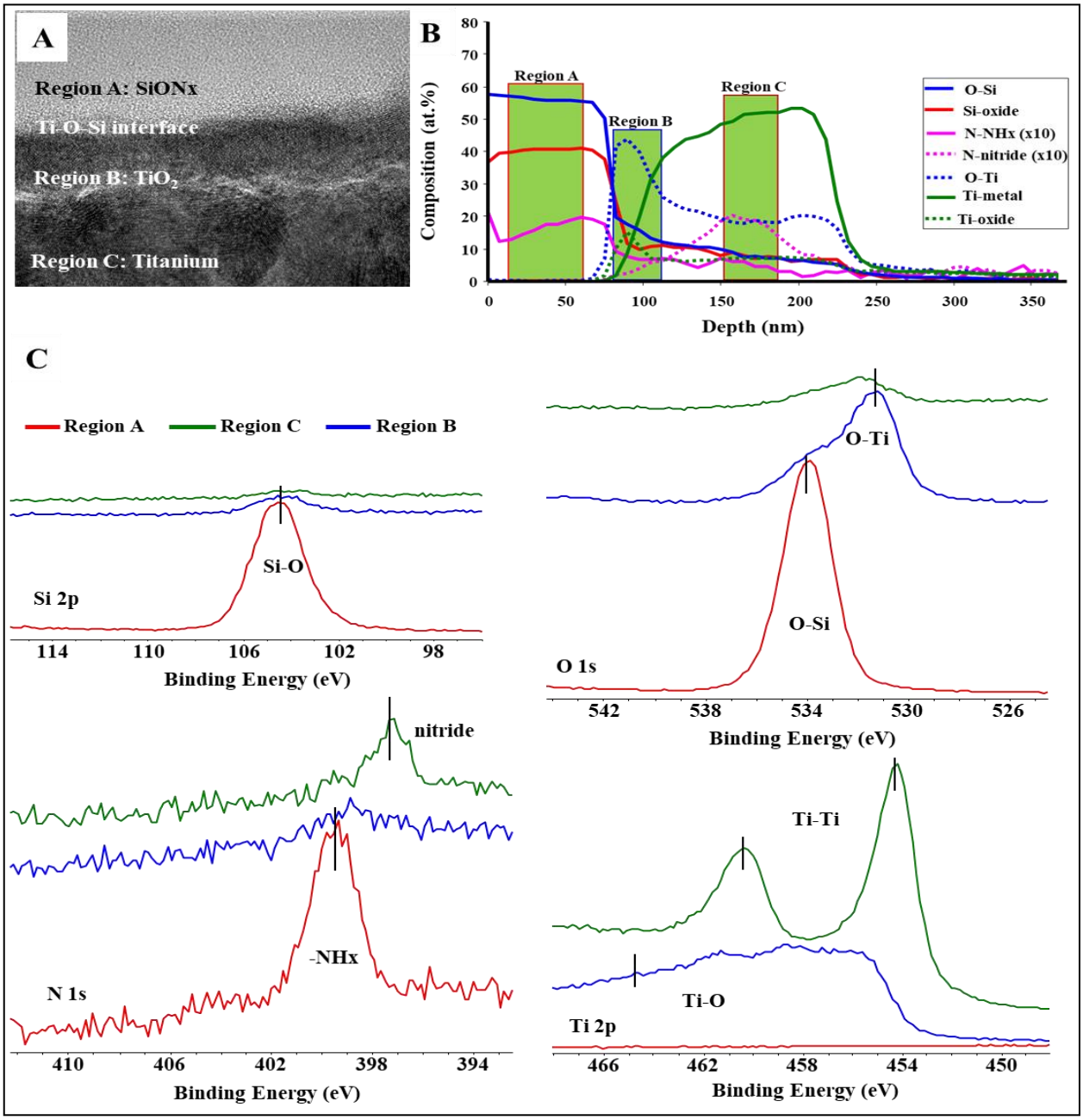

Figure 4.4: TEM and XPS analysis of the Ti-SiONx coating interface. A) TEM micrographs magnify the Ti-TiO_2-SiONx interface. B) XPS depth scale determined by sputter rate of 15 nm/min, sputter cycles were 30 sec and shaded areas show region that had different chemical signals. (C) Individual XPS spectra from these regions are compared for Si, O, N, and Ti. Note that N 1s signal are magnified by a factor of 10.

Surface mechanical properties of the modified surfaces were evaluated to study any change after the SiON and SiONP thin films deposition compared to the CP-Ti surface. Figure 4.5 and Table 4.4 present the micro- and nano-mechanical properties as determined by Vickers and nanoindentation tests, respectively. Based on the Vickers test, hardness of the anodized CP-Ti was 198.1±6.8 HV (~1.92±0.07 GPa), which was close to the hardness value (1.97±0.4 GPa) as estimated from load-displacement curves after nanoindentation testing (Figure 5-B). Vickers indents "diamond-like shape" as scanned by HR-SEM after the indentation test is shown in Figure 4.5-A. The Vickers hardness did not reveal any significant changes after SiON and SiONP deposition, while the nano-hardness of SiONP (6.7±0.99 GPa) was significantly higher compared to both CP-Ti (1.97±0.4 GPa) and SiON (3.05±1.1 GPa) with a significance level of ***$p<0.001$. The difference in micro- and nano-hardness values is attributed to the indentation depth that exceeds the thin film depth and reaches the substrate with Vickers test compared to the nanoindentation that did not exceed the thin films thickness. The reduced elasticity modulus, calculated from load-displacement curves, of CP-Ti was 139.7±26 GPa which slightly increased after SiON and SiONP thin films deposition to 147±15 and 160±24 GPa, respectively, with no significant difference compared to the CP-Ti. The maximum indentation/penetration depth (h_{Max}) of each surface can be seen from the load-displacement curves in Figure 4.5-B and is reported in Table 4. 4, which is in a reasonable correlation with the hardness of each material. The reported H and E_r values in this study are in a reasonable agreement with previously reported values [33,52–54].

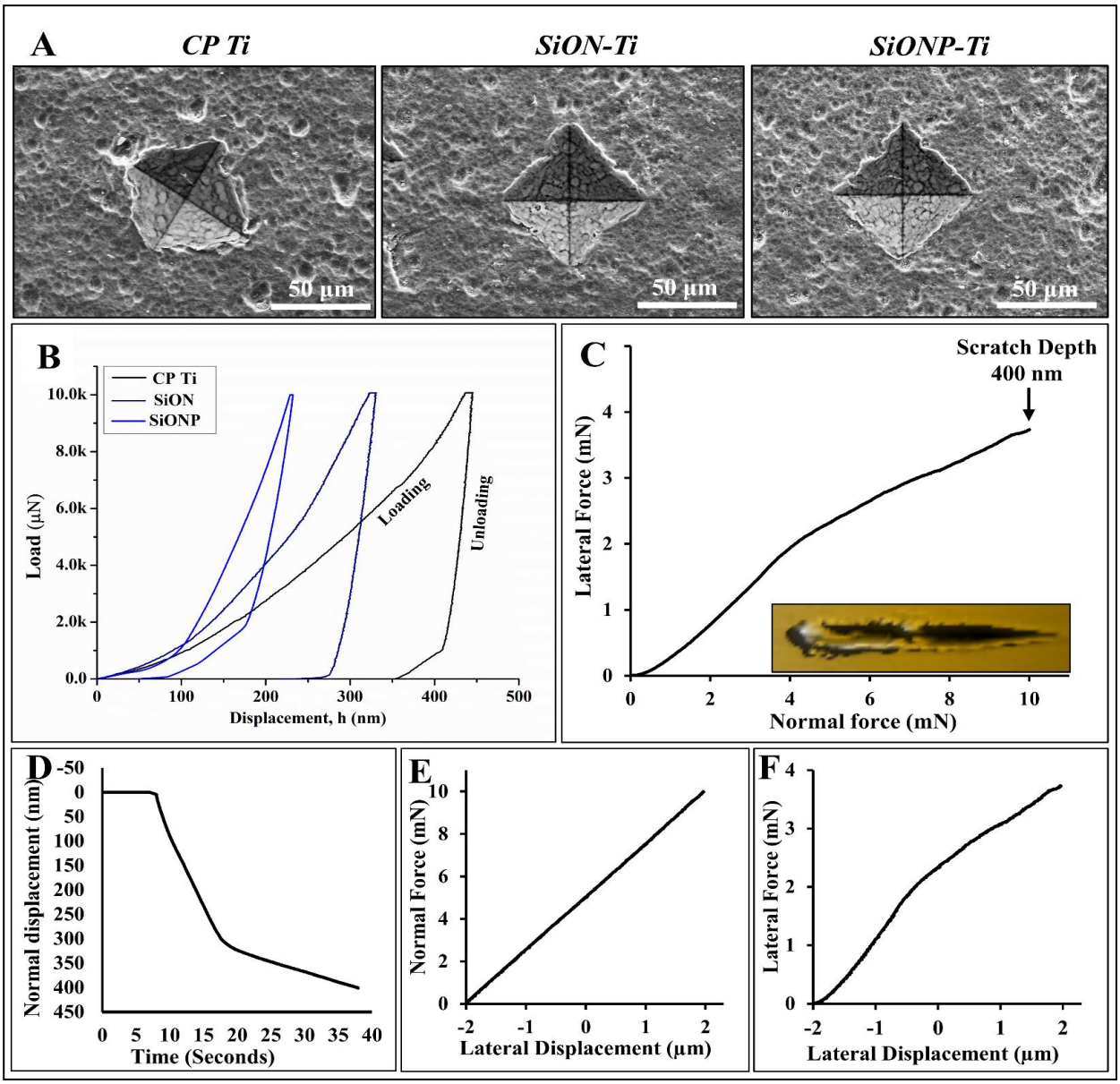

Figure 4.5: Mechanical properties of the anodized CP-Ti compared to SiONx-Ti and SiONPx-Ti coatings. A) HR-SEM images show the Vickers indents "diamond-like shape" after the indentation test. B) Load-displacement curves of nanoindentation for the anodized CP-Ti compared to PECVD coatings. C-F) Nano-scratch test analysis for 300 nm PECVD thin-film on the anodized CP-Ti surface. C) Lateral vs. normal forces curve with maximum scratch depth of 400 nm, image insert shows the 2D SPM topography after the scratch test. D) Normal displacement vs. time. Lateral displacement vs. normal force (E) and vs. lateral force (F).

Table 4. 4. Mechanical properties of CP-Ti, SiON-Ti, and SiONP-Ti as calculated from the Vickers hardness and nano-indentation tests.

	Vickers hardness		Nano-indentation		
	Hardness (HV)	**Hardness (GPa)**	**Reduced modulus (GPa)**	**Hardness (GPa)**	**hMax (nm)**
CP-Ti	198.1±6.8	1.92±0.07	139.7±26	1.97±0.4	440±31
SiON-CP-Ti	199.9±4.9	1.95±0.05	147±15	3.05±1.1	302±43
SiONP-CP-Ti	206.1±4.2	2.01±0.04	160±24	6.7±0.99	224±30

Nano-scratch test results are shown in Figure 4.5 (C-F). In the load-controlled scratch tests, the normal force is gradually increased to the maximum applied load. Thus, at low force at the beginning, the deformation is considered elastic, which then turns to plastic deformation at the applied high force. This significant increase in the applied force may result in thin film cracking and delamination. Normal force versus lateral force or lateral displacement curves are usually used to investigate thin films interfacial adhesion, cracking, fracture, and delamination [39,55]. Here, there was no significant change in resistant “lateral force” with increasing vertical load or lateral displacement which confirms strong PECVD thin films adhesion with the underlying anodized CP-Ti as shown in Figure 4.5-C & F. The slight change in the resistance (Figure 4.5-C) can be attributed to the hardness change within the layers. This was further confirmed by normal displacement versus time curves that indicated slope changes without significant reductions in normal displacement, indicating no breakthrough of the thin films. The change around 300 nm can be explained by the indenter tip resistance present while transitioning from the thin film to the substrate. Also, the slope of the normal force-lateral displacement curve did not indicate any sudden change which means no cracking or significant fracture was observed as shown

in Figure 4.5-E. The results from the nano-scratch tests indicate a strong interfacial adhesion between PECVD thin films and the CP-Ti substrate which can be attributed to the ATO layer nanopores that work as anchors and deposition sites to support thin film adhesion on the Ti substrate. Moreover, the advantages of using low temperature PECVD to deposit thin films without thermal expansion mismatch and well-adherent layers are demonstrated by these results [28].

Activation of the Ti surface by deposition of such bioactive coatings with its multi-surface functional groups is hypothesized to enhance the surface wettability and increase the surface free energy. Thus, surface wettability of the modified surfaces was tested by contact angle measurements followed by surface energy calculations. Figure 6 presents the contact angle and the corresponding surface free energy of each coating compared to the anodized CP-Ti. The water contact angle on the CP-Ti surface was found to be 65.65 ± 3.6°, which agrees with previously reported data [11,56,57]. Deposition of SiON/SiONP thin films on the CP-Ti surface significantly enhances the surface wettability as indicated by the significant decrease in the water contact angle compared to the CP-Ti (***$p<0.001$). The water contact angle was found to be 43.45 ± 0.7° and 41.65 ± 0.95° for SiON and SiONP, respectively. The contact angle of the diiodomethane displayed the same behavior as DI water (Figure 6- A & B). The surface free energy of each coating as calculated according to OWK equation (1) broken into its polar and dispersive components is shown in Figure 4.6-C. The anodized CP-Ti surface energy was 37.92 mJ/m^2 which significantly increased after SiON and SiONP deposition to be 56.01 and 57.78 mJ/m^2, respectively. Surface wettability is a crucial aspect for all medical implants,implants with enhanced hydrophilicity and low contact angles (<90°),

will present high surface energy leading to rapid and improved cell adhesion and protein adsorption within the first 6 hours of cell culture *in-vitro* [20,58]. Furthermore, increasing surface free energy enhances the calcium phosphate deposition leading to faster HA nucleation in SBF [59], enhanced osteoprogenitor cell adhesion, and increased collagen and extracellular matrix production [60].

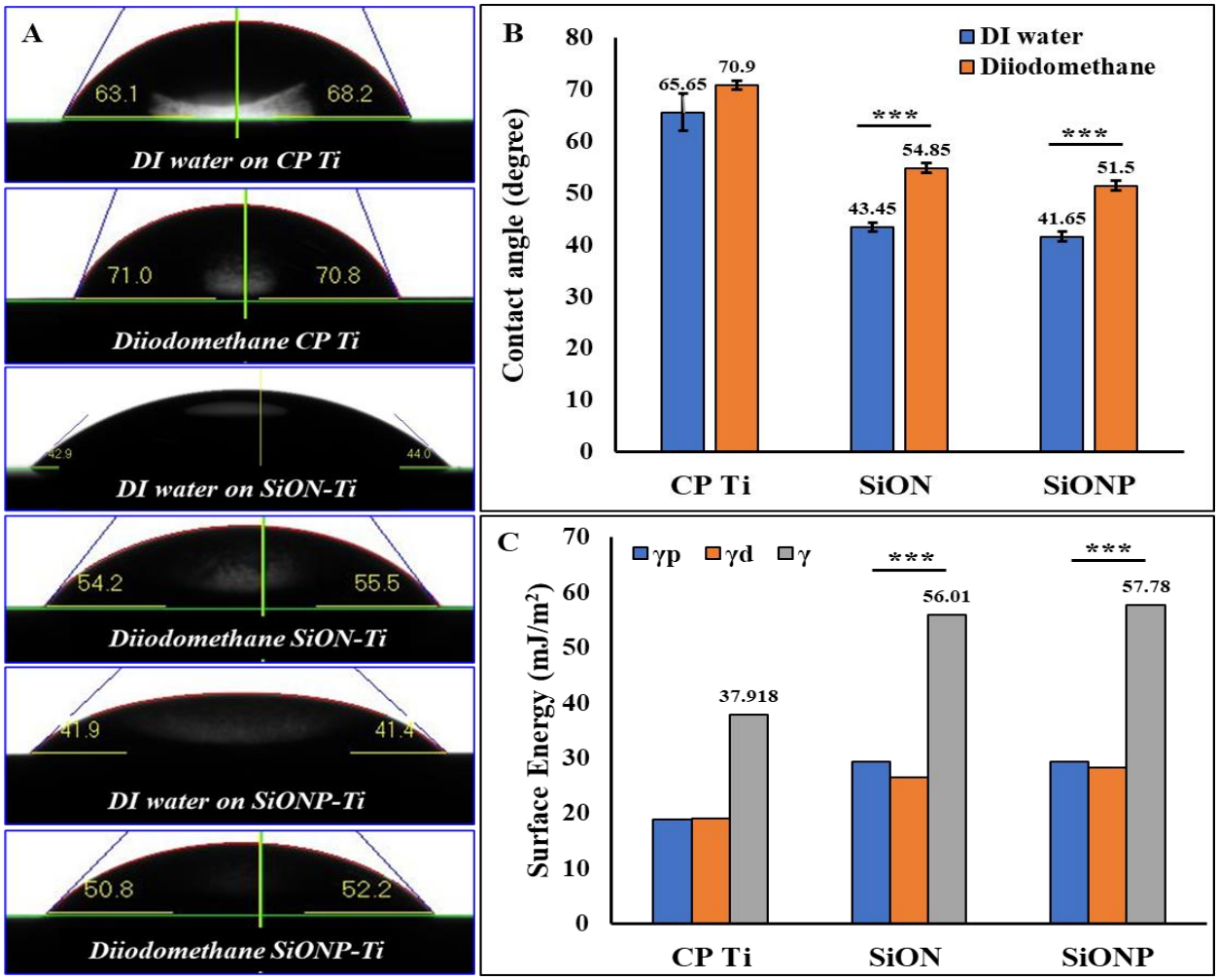

Figure 4.6: Surface wettability and energy of the anodized CP-Ti compared to SiONx-Ti and SiONPx-Ti coatings. A) Shows the droplet spreading on each surface as captured within 10 seconds. B) Shows the average values of the contact angles with standard deviations. C) The calculated surface free energy broken into its dispersive and polar components. (***) presents significant level when $p<0.001$ compared to Ti.

3.2 In-vitro Cell Free "Surface Apatite formation"

Formation of bone-like apatite, CaP layer on the surface of the implantable materials, is a vital requirement for successful bone growth on synthetic materials *in vivo*. This apatite layer adsorbs and activates signaling proteins and cells responsible for bone formation [61]. This *in vivo* interaction can be predicted by testing the formation of CaP on the implant's surface *in-vitro*. In this section, the surface bioactivity and its effect on CaP/HA formation was investigated by sample immersion for 12 hours and 7 days in α-MEM, with similar ionic composition to human blood plasma. Then, the effect of the SiON- and SiONP-CP-Ti modified surfaces on calcium phosphate deposition and CaP/HA formation compared to the anodized CP-Ti was comprehensively studied.

HR-SEM was used to capture the CaP formation on the tested samples after 12 hours (Figure 4.7) and 7 days (Figure 4.8) of immersion in the α-MEM. By comparing the SiON- and SiONP-CP-Ti treated surfaces to the anodized CP-Ti, it is revealed that the treated surfaces have significantly higher surface coverage of CaP deposition as early as 12 hours after 7 days. The bright deposition on the samples' surfaces, as shown from the SEM images Figure 4.7 & 4.8 (A-F), present the CaP deposition as confirmed from the EDX compositional analysis Figure 7 & 8 (J-L). Samples' surface was again scanned by an optical profilometer after 12 hours and 7 days of immersion to reveal any surface profile changes as shown in Figures 4.7 & 4.8 (G-I). Comparing each surface to its bare surface "before immersion" revealed that the surface topography/profile had significantly changed on the SiON- and SiONP-CP-Ti modified surfaces as confirmed from the Ra and Rq values. This significant change in the surfaces' profile is attributed to the CaP deposition on each surface. The SEM images

were further used for semi-quantitative analysis of the CaP/HA surface area coverage (%) on each sample after 12 hours and 7 days (Figure 4.8). Figure 4.8(A-F) presents the SEM images after ImageJ analysis to calculate CaP/HA surface area coverage, black color represents the background surface of each sample, and the white color indicates the HA deposition. The mean values with standard deviation of the calculated HA (%) are presented in Figure 4.8 (G). The modified surfaces of SiON-CP-Ti and SiONP-CP-Ti significantly increased the CaP/HA nucleation as early as 12 hour after immersion when compared to the anodized CP-Ti with a significant level of ***$p<0.001$. Furthermore, the SiONP-CP-Ti modified surface displayed the highest HA surface coverage (~40 %) compared to the anodized CP-Ti (~10 %) and the SiON-CP-Ti (~27 %) after 7 days as shown in Figure 4.8 (G). The Ca/P ratio of the formed CaP/HA was calculated from the EXD analysis and is shown in Figure 4.9 (H). The anodized CP-Ti presented Ca/P of 1.55±0.23 compared to 1.54±0.03 and 1.63±0.02 for the SiON- and SiONP-CP-Ti, respectively, after 12 hours. These Ca/P ratios were increased to 1.6±0.03, 1.62±0.08, and 1.65±0.09 for CP-Ti, SiON-, and SiONP-CP-Ti, respectively, after 7 days of immersion. For both CP-Ti and SiON-CP-Ti, the Ca/P ratios at early stage of immersion, 12 hours, are close to the CaP ratio of the stoichiometric tricalcium phosphate (TCP, stoichiometric Ca/P ratio = 1.50), this Ca/P ratio increased after 7 days to fit more with the Ca/P ratio of stoichiometric HA. Most important is that SiONP-CP-Ti surface indicated CaP formation with Ca/P ratio closer to the stoichiometric HA even at the early immersion time of 12 hours (1.63±0.02) and increased to (1.65±0.09) at 7 days as shown in Figure 9 (H).

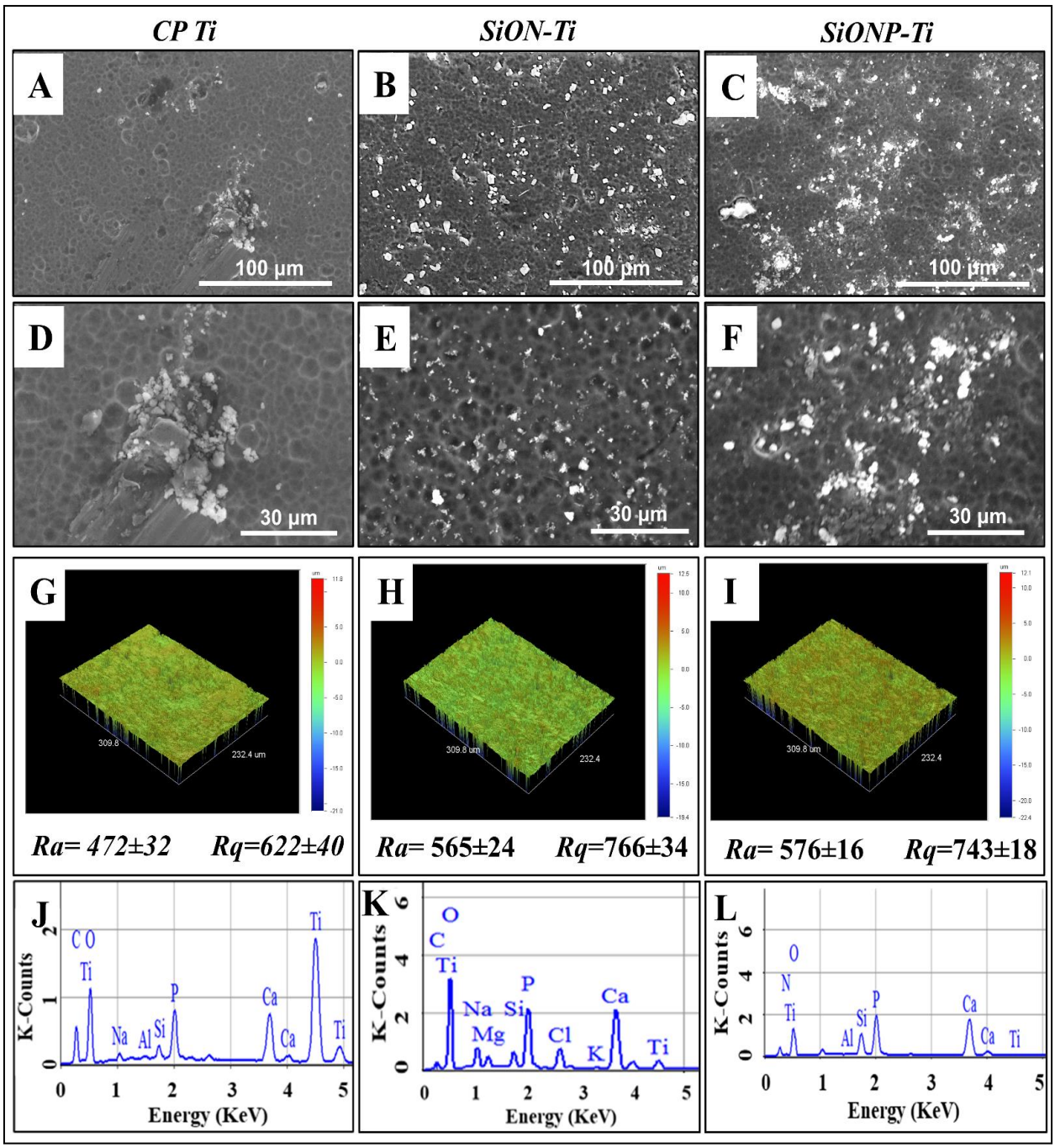

Figure 4.7: Calcium-phosphate/hydroxyapatite formation on the surfaces after 12 hours of immersion in α-MEM. A-F) HR-SEM images show the HA formation on the anodized CP-Ti (A&D), SiONx-CP-Ti (B & E), and SiONPx-CP-Ti (C & F) at different magnifications. G-I) Surface profile and roughness as scanned by an optical profilometer after 12 hours of immersion. J-L) EDX spectra indicating the compositional analysis of the HA formed on each surface, respectively.

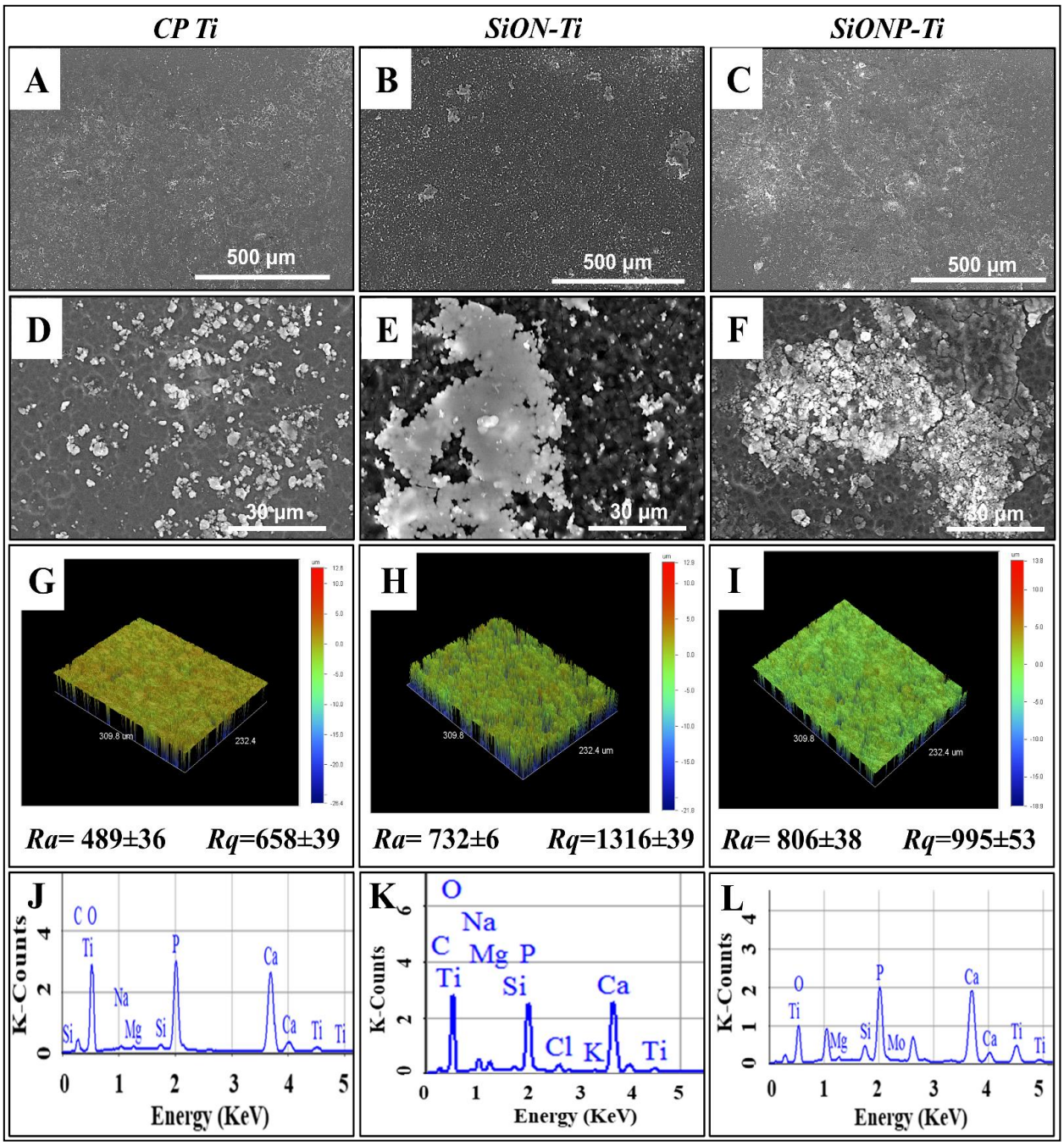

Figure 4.:. Hydroxyapatite formation on the surfaces after 7 days of immersion in α-MEM. A-F) HR-SEM images show the HA formation on the anodized CP-Ti (A&D), SiONx-CP-Ti (B & E), and SiONPx-CP-Ti (C & F) at different magnifications. G-I) Surface profile and roughness as scanned by an optical profilometer after 7 days of immersion. J-L) EDX spectra indicating the compositional analysis of the HA formed on each surface, respectively.

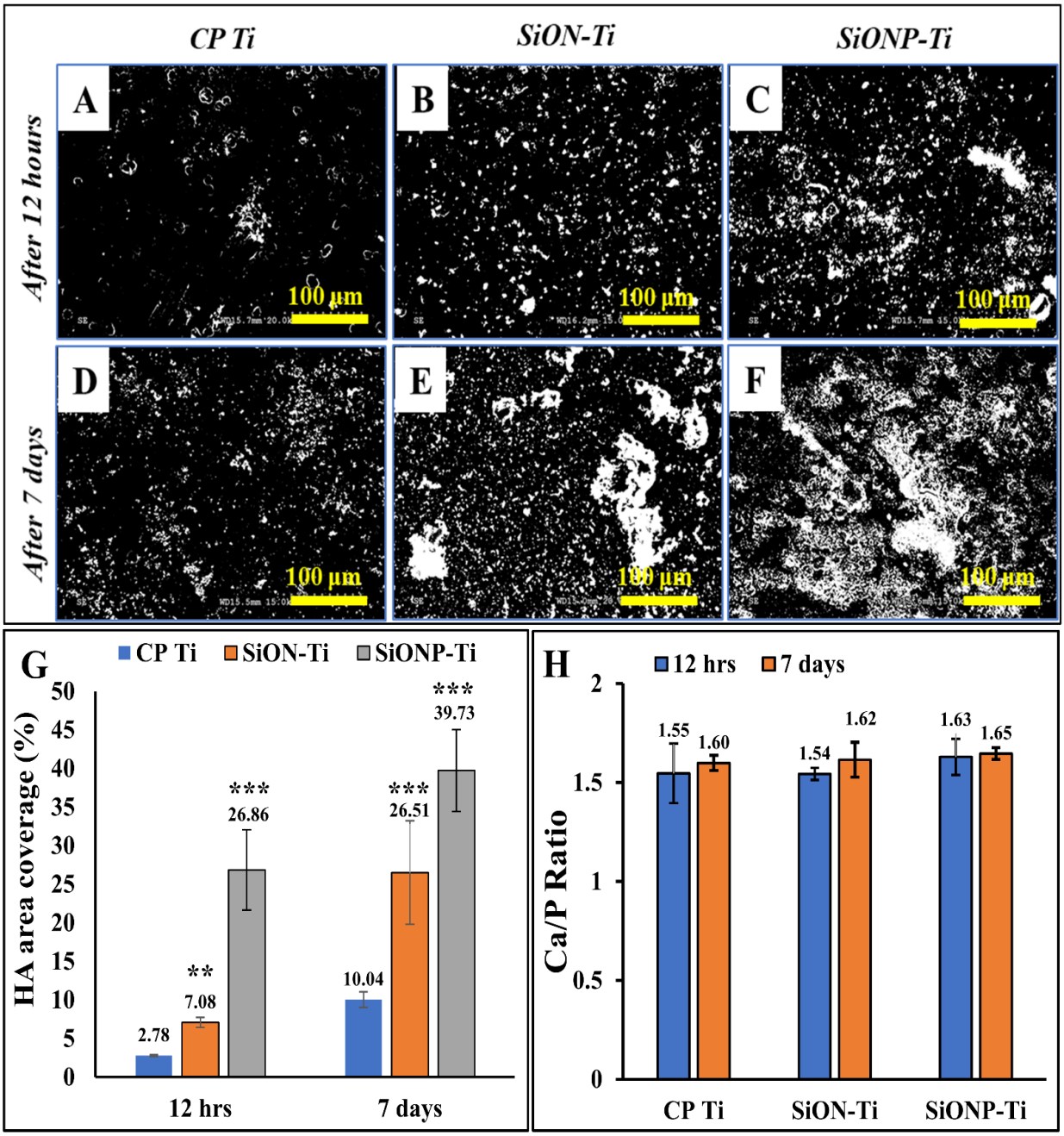

Figure 4.9: Hydroxyapatite coverage and Ca/P ratio after 12 hours and 7 days of immersion in α-MEM. A-F) ImageJ processed HR-SEM images show the HA formation on the anodized CP-Ti (A&D), SiONx-CP-Ti (B & E), and SiONPx-CP-Ti (C & F) at different magnifications, blue presents the background, and the white presents the HA deposition. G) Surface area coverage of HA (%) on each surface as calculated from the SEM images. H) Ca/P ratio as calculated from the EDX compositional analysis data.

The results of SiONP-CP-Ti had pronounced and revealed unique surface chemistry that significantly increased the HA surface coverage with highest Ca/P ratio closest to the stiochiometric HA at early time points. The CP-Ti and SiON-CP-Ti results are in reasonable agreement with results reported previously at early stages of *in-vitro* immersion [26] and *in vivo* implantation [62,63]. At early *in-vitro* and *in-vivo* stages, the thermodynamically metastable phase TCP is kinetically favorable and tends to form HA as immersion time increases. Previous studies indicated apatite formation with Ca/P ratio range from 1.28 to 1.46 after Ti surface immersion in SBF [64–66]. The higher Ca/P ratios reported here indicating rapid apatite nucleation is expected to lead to a faster osseointegration of the modified Ti implants.

The enhanced CaP coverage with higher Ca/P ratio on the modified PECVD SiON/SiONP-CP-Ti surfaces can be attributed to the enhanced surface activity (i.e., wettability and surface energy) with readily available silanol groups on the silica based-PECVD thin films surfaces. In physiological environment (i.e., *in-vitro* or *in-vivo*) these silanol groups are immediately available for dissolution, polymerization, and reprecipitation to form a silica gel network for early carbonated HA formation [28]. The enhanced HA area coverage on SiONP compared to the SiON can be attributed to the incorporation of phosphorus in the structure. This phosphorus is presumed to be rapidly dissolved from the amorphous SiONP coatings concomitant with Si-ion release, leading to a relatively open structure layer of silica gel. This environment allows for ion exchange and formation of Ca-PO_4 within 6 hours, which becomes a more stable carbonated hydroxyapatite structure by consuming the Ca and P from the media/solution within 18 hours [36].

The structure of the formed CaP or hydroxycarbonate-apatite (HCA) was further investigated using FT-IR analysis as shown in Figure 4.10. FT-IR spectra indicate the presence of phosphate groups (PO_4^{3-}) on the samples surface appeared as vibration mode at 603 cm^{-1} and strong stretching band range from 1050-1100 cm^{-1}. Weak carbonate absorption (*v3* CO_3^{2-}) bands appeared at range of 1400-1550 cm^{-1}. A water absorption band was observed around 1650 cm^{-1}, while the broad band extended from 2500-3700 cm^{-1} was assigned to the OH^- absorption bands. The strong peak around 870 cm^{-1} appeared on the SiON-CP-Ti surface can be attributed to the joint contribution of carbonate and HPO_4^{2-}ions, this peak was significantly weaker on the other surfaces. These FT-IR spectra are in a reasonable agreement with previously reported data [67,68] of HCA formation on $CaSiO_3$ surfaces immersed in simulated body fluid solution [68].

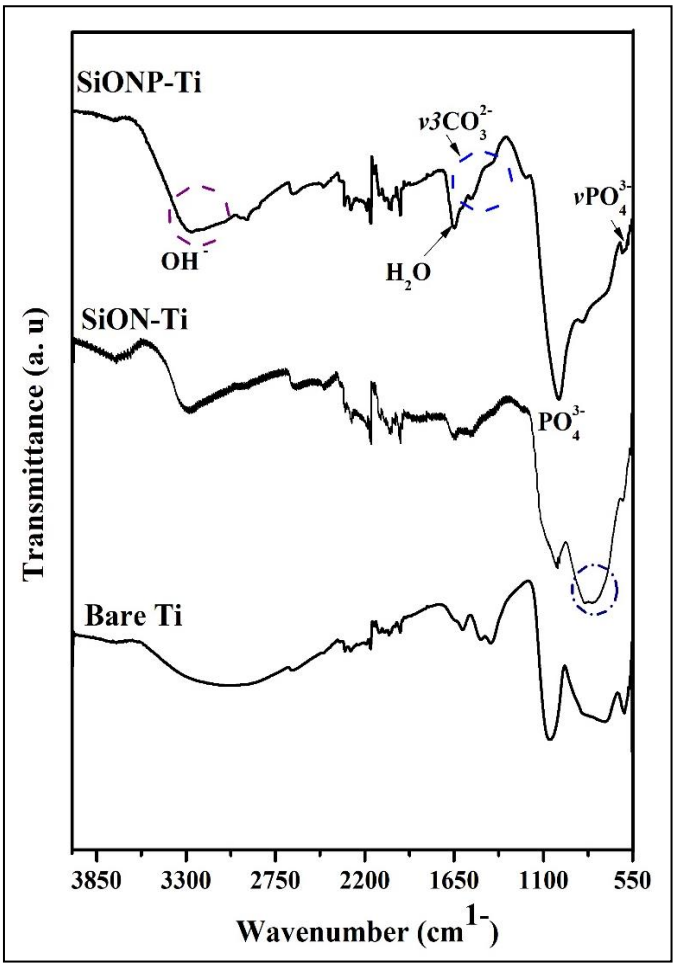

Figure 4.10: FT-IR spectra of HCA formation on the anodized CP-Ti compared to SiONx-Ti and SiONPx-Ti coatings after 7 days of immersion.

HR-TEM coupled with SAED was used to further investigate the crystal structure of the formed HCA on the surfaces after 7 days of immersion in α-MEM. Figure 4.11 illustrates the HR-SEM and HR-TEM images with SAED diffraction patterns as well as XRD patterns. The TEM micrographs revealed a high degree of aggregation of the HCA particles as shown in Figure 4.11 (B). High magnification HR-TEM images (Figure 4.11-C) revealed the polycrystalline nature of the formed HCA as indicated by linear lattices arranged in random directions. This was further confirmed by the analysis of regions D, E, and F that show the (002), (211), and (222) planes marked with the corresponding d-spacing. The SAED pattern (Figure 4.11-G) shows the Debey rings which indicates a polycrystal HCA with irregularly shaped polycrystals in an isotropic orientation. The interplanar spacing of the presented Debey rings are in a reasonable agreement with the characteristic spacing of apatite-like structure [69–72]. This results were further confirmed with XRD analysis that presented exact agreement as shown in Figure 11-H. The XRD patterns indicate the presence of (002), (211), and (222) crystal planes at 2Θ = 25.5°,31.77°, and 45.5°, respectively, which exactly matches the nanocrystalline HA planes (JCPDS #09-0432) [73,74]. These presented data from the HR-TEM coupled with SAED and XRD analysis confirmed the formation of a nanocrystalline HCA on the surface of the studied materials in this study. These results confirm and clarify what has been reported by our group in previous studies. Prior studies on a PECVD Ti/TiO_2-SiON revealed the formation of hydroxycarbonate apatite within 6 hours as confirmed by XPS and XANES analysis, and SiON surface chemistry induced osteogenic gene expression of human periosteal cells and led to a rapid bone-like biomineral formation within 4 weeks [21,28].

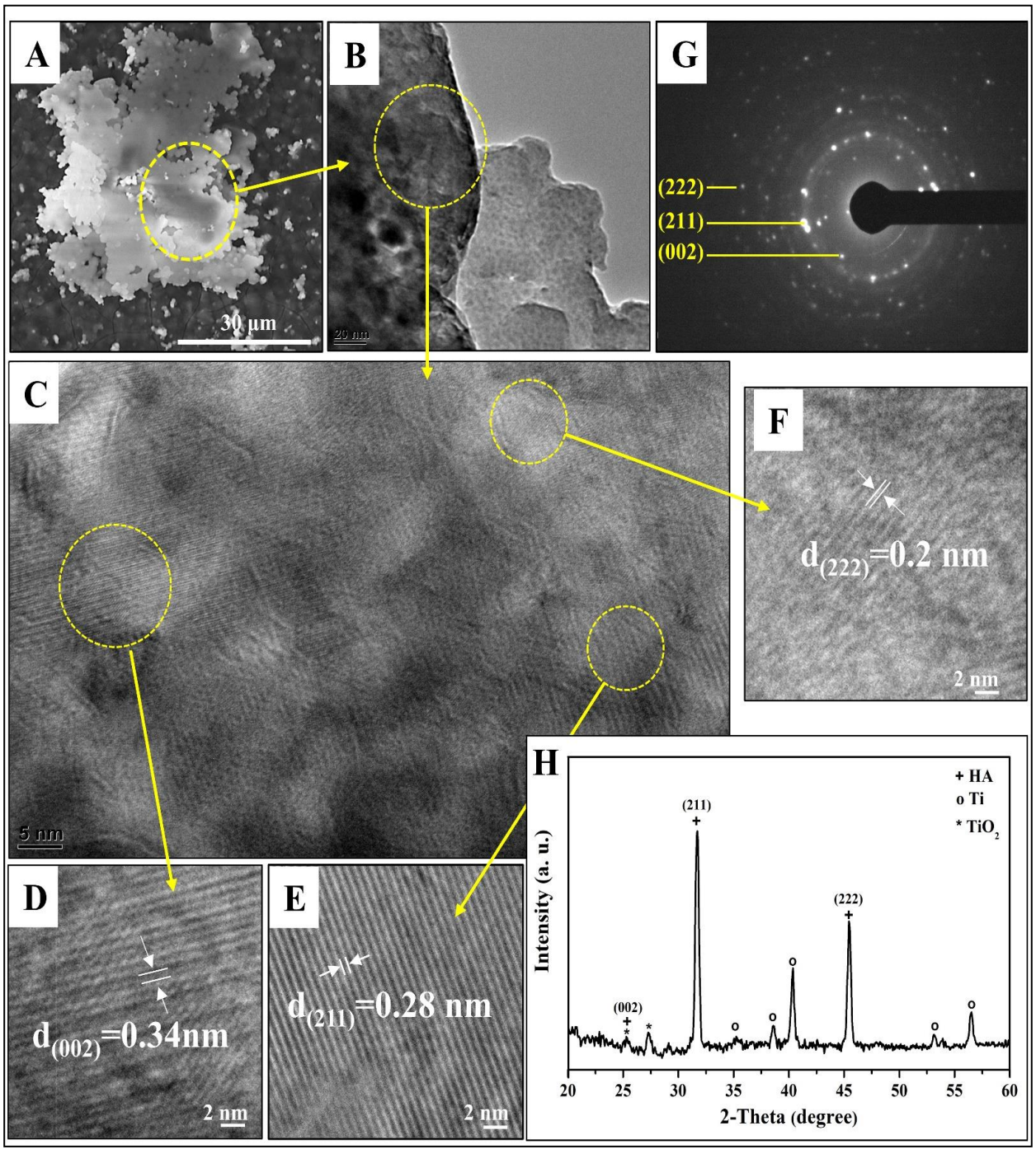

Figure 4.11: Crystal structure analysis of the HCA. A) HR-SEM image shows the HCA nucleation after 7 days of immersion. B-F) HR-TEM images at different magnifications show the crystallographic planes of HCA. G) SAED analysis indicating Debye rings of the polycrystalline HCA confirmed with and XRD (H).

Finally, this study aimed to uncover the interfacial adhesion and surface bioactivity of anodized titanium modified with SiON and SiONP PECVD surface coating. This study indicated that a strongly adherent thin film coatings can be successfully deposited on any medical device or implantable material that can fit in the reactor geometry. PECVD is a well-known method that has been used in the semiconductor industries for decades. Using the PECVD reactor allows for uniform plasma deposition of various thin film coatings such as silicon dioxide [19], silicon nitride [75], silicon oxynitride [21], phosphosilicate glass [20,23], and borophosphsilicate glass at low temperatures from 250-400 °C. Thus, the PECVD reactions (Rxn) can be summarized as presented below (Rxn 1-3). The N liberated from the NH_3 works as a network former to substitute the O in the silica network, while the P from PH_3 works as a network modifier in a small percent (i.e., < 4%) in the silica structure.

$$O\text{-}Ti\text{-}O + wSiH_4 + xN_2O \rightarrow O\text{-}Ti\text{-}O\text{-}Si_wO_x + 2wH_2 + xN_2 \quad \textit{(Rxn. 1)}$$

$$O\text{-}Ti\text{-}O + wSiH_4 + xN_2O + yNH_3 \rightarrow O\text{-}Ti\text{-}O\text{-}Si_wO_xN_y + (2w+1.5y)\,H_2 + xN_2 \quad \textit{(Rxn. 2)}$$

$$O\text{-}Ti\text{-}O + wSiH_4 + xN_2O + yNH_3 + zPH_3 \rightarrow O\text{-}Ti\text{-}O\text{-}Si_wO_xN_yP_z + (2w+1.5y+1.5z)\,H_2 + xN_2 \quad \textit{(Rxn. 3)}$$

The PECVD layer in the above reactions assume RBM, for the RMM interpretation of the PECVD films, the final films structure will be $[Si\text{-}Si]_w{-}[Si\text{-}O]_x$ for amorphous silica, $[Si{-}Si]_w{-}[Si{-}O]_x{-}[Si{-}N]_y$ for amorphous SiON, and $[Si{-}Si]_w{-}[Si{-}O]_x{-}[Si{-}N]_y{-}[O\text{-}P]_z$ for amorphous SiONP.

The surface characterization revealed that deposition of PECVD thin films do not alter the surface topography or microstructure of the substrate while enhancing its surface bioactivity. Mechanical properties as studied by Vickers hardness and nano-indentation/scratch tests indicate a strong interfacial adhesion between the PECVD thin films and the anodized CP-Ti substrate due to the chemical bonding between the

coating layer and Ti-O that anchors and supports the thin films on the surface as indicated in the reactions above. Deposition of an amorphous layer of SiON or SiONP prevents the mismatching at the interfacial layer and provide a hydrophilic surface with high surface free energy and readily available functional groups (e.g., Si-H, N-H, Si-OH, and P-OH) once immersed/implanted in a physiological environment. The presence of such a surface with its unique chemical structure will initiate the formation of apatite-like bone structure (HCA) according to the mechanism known for bioactive bioglass-bone formation [76,77], but with a faster rate due to the availability of the surface silanol groups from the PECVD coatings. The bioactive bioglass bonds with bone through the formation of an HCA layer as proposed by Hench et al., [77]. Here, HCA formation was confirmed on the surface as shown from the HR-TEM with SAED, XRD patterns, FT-IR, and SEM/EDX that indicated Ca/P ratio in the range of 1.5-1.6 that exactly matches the poly crystalline carbonate-substituted apatite [76]. As presented above, the SiONP showed a significant enhancement of HCA formation as confirmed by the highest surface coverage and Ca/P ratio compared to the SiON and the anodized CP-Ti. This pronounced effect on the SiONP surface can be attributed to the presence of phosphorus in the structure which rapidly dissolve leading to a relatively open structure layer of silica gel with Si-ions release. This environment allows for ion exchange and formation of Ca-PO_4 within 6 hours, which becomes a more stable HCA structure at a faster rate than other surfaces. These findings confirm the previously proposed role of phosphate which is lowering the energy barrier to appetite nucleation on the bioglass surface [78,79]. Furthermore, the release of Si-ions from these coatings serves a vital role to enhance osteoblast markers *in-vitro* [80], endothelial cell angiogenic properties [20], and

enhance antioxidant expression, angiogenic marker expression, and reduce ROS levels needed for accelerating vascular tissue regeneration [15,19,20,23,24,81]. Our future studies will concentrate on the osteogenic effects and the complete healing process in-vivo.

4. CONCLUSIONS

The present study investigated the potential application of SiON and SiONP as bioactive amorphous thin film coatings for medical devices compared to the anodized CP-Ti surface. The surface characterization revealed that low temperature PECVD thin film coatings enhance the surface activity through increasing the wettability and surface energy, and the surface bioactivity by providing surface functional groups that work as nucleation sites for HCA formation at a faster rate and higher surface coverage compared to the anodized CP-Ti. Analysis of mechanical properties indicated no change in the microhardness while enhancing the nanohardness with SiON and SiONP coatings. SiON and SiONP thin films slightly increased the reduced elasticity modulus of the anodized CP-Ti, but no significant difference was observed. Nano-scratch tests indicated that PECVD coatings have a strong interfacial adhesion with the CP-Ti substrate due to the chemical bonding between the coating layer and the nanoporous ATO structure that anchors and supports the thin films on the surface. *In-vitro*-cell free-studies performed only in cell culture media indicated the formation of HCA on the surface after 12 hours of immersion. The SiONP-CP-Ti surface presented the highest surface coverage of HCA after 7 days of immersion with a Ca/P ratio close to the stoichiometric HA. The HCA structure and crystallinity were confirmed using various techniques such as HR-TEM, XRD, FT-IR, and HR-SEM/EDX. In conclusion, this study presents evidence for the surface bioactivity of the SiON and SiONP amorphous silica-

based PECVD coatings as strongly adherent potential coatings for rapid HA formation on medical grade CP-Ti implants.

Acknowledgements

The authors would like to thank the Varanasi's laboratory members, Neelam Ahuja and Sara Peper, at the Bone-Muscle Research Center for their assistance towards this manuscript. The authors would like to thank Dr. Jiechao Jiang and Mr. David Yan at the Characterization Center for Materials and Biology (CCMB) at the University of Texas at Arlington (UTA) for their help during the materials characterization. The authors want to thank Dr. Panagiotis Danoglidis and Mr. Michail Margas at the Center of Advanced Construction Materials at UTA. The authors want to thank Dr. Tobias Wolfram and Zeke Raiser from KLS Martin for their help and support for this study.

Funding

The authors want to thank the National Institutes of Health (NIH), the Osteo Science Foundation, the University of Texas at Arlington (UTA), and the UTA College of Nursing & Health Innovation Bone-Muscle Research Center (UTA-CONHI-BMRC) for their generous support for this study. The following NIH Grants supported KA and VV: (Grant Number 1R03DE023872-01, 1R56DE027964-01A1-01, NIH S10OD025230). Also, we thank the UTA-CONHI for their generous support for the first author KA via the CRS Pilot Grant.

Conflicts of Interest: The authors declare no conflict of interest.

REFERENCES

1. Dabrowski, B., Swieszkowski, W., Godlinski, D. & Kurzydlowski, K. J. Highly porous titanium scaffolds for orthopaedic applications. *J. Biomed. Mater. Res. Part B Appl. Biomater.* **95B**, 53–61 (2010).
2. Pohler, O. E. M. Unalloyed titanium for implants in bone surgery. *Injury* **31**, D7–D13 (2000).
3. Abdel-Hady Gepreel, M. & Niinomi, M. Biocompatibility of Ti-alloys for long-term implantation. *J. Mech. Behav. Biomed. Mater.* **20**, 407–415 (2013).
4. Takemoto, M. *et al.* Mechanical properties and osteoconductivity of porous bioactive titanium. *Biomaterials* **26**, 6014–6023 (2005).
5. Oh, I.-H., Nomura, N., Masahashi, N. & Hanada, S. Mechanical properties of porous titanium compacts prepared by powder sintering. *Scr. Mater.* **49**, 1197–1202 (2003).
6. Liu, X., Chu, P. K. & Ding, C. Surface modification of titanium, titanium alloys, and related materials for biomedical applications. *Mater. Sci. Eng. R Reports* **47**, 49–121 (2004).
7. Apostu, D., Lucaciu, O., Berce, C., Lucaciu, D. & Cosma, D. Current methods of preventing aseptic loosening and improving osseointegration of titanium implants in cementless total hip arthroplasty: a review. *J. Int. Med. Res.* **46**, 2104–2119 (2018).
8. Lombardi, A. V. J., Mallory, T. H., Vaughn, B. K. & Drouillard, P. Aseptic loosening in total hip arthroplasty secondary to osteolysis induced by wear debris from titanium-alloy modular femoral heads. *J. Bone Joint Surg. Am.* **71**, 1337–1342

(1989).

9. Rocha, R. C., Galdino, A. G. de S., Silva, S. N. da & Machado, M. L. P. Surface, microstructural, and adhesion strength investigations of a bioactive hydroxyapatite-titanium oxide ceramic coating applied to Ti-6Al-4V alloys by plasma thermal spraying. *Mater. Res.* **21**, 11–14 (2018).
10. S. Rupprecht. Brunette DM, Tengvall P, Textor M, Thomson P (Hrsg): Titanium in medicine: materialscience, surface science, engineering, biological responses and medical applications. *Mund-, Kiefer- und Gesichtschirurgie* **6**, 203 (2002).
11. Sharma, A. *et al.* Spark anodization of titanium–zirconium alloy: surface characterization and bioactivity assessment. *J. Mater. Sci. Mater. Med.* **26**, 221 (2015).
12. Sawase, T. & Watanabe, I. Surface Modification of Titanium and Its Alloy by Anodic Oxidation for Dental Implant BT - Implant Surfaces and their Biological and Clinical Impact. in (eds. Wennerberg, A., Albrektsson, T. & Jimbo, R.) 65–76 (Springer Berlin Heidelberg, 2015). doi:10.1007/978-3-662-45379-7_7.
13. Oh, H.-J., Lee, J.-H., Jeong, Y., Kim, Y.-J. & Chi, C.-S. Microstructural characterization of biomedical titanium oxide film fabricated by electrochemical method. *Surf. Coatings Technol.* **198**, 247–252 (2005).
14. Zhou, R. *et al.* Enhanced Osseointegration of Hierarchically Structured Ti Implant with Electrically Bioactive SnO2–TiO2 Bilayered Surface. *ACS Appl. Mater. Interfaces* **10**, 30191–30200 (2018).
15. Ilyas, A. *et al.* Rapid Regeneration of Vascularized Bone by Nanofabricated Amorphous Silicon Oxynitrophosphide (SiONP) Overlays. *J. Biomed.*

Nanotechnol. **15**, 1241–1255 (2019).

16. Ma, Q., Liao, J., Tian, T., Zhang, Q. & Cai, X. A potential flower-like coating consisting of calcium-phosphate nanosheets on titanium surface. *Chinese Chem. Lett.* **28**, 1893–1896 (2017).
17. Surmenev, R. A., Surmeneva, M. A. & Ivanova, A. A. Significance of calcium phosphate coatings for the enhancement of new bone osteogenesis – A review. *Acta Biomater.* **10**, 557–579 (2014).
18. Kim, H.-W., Kim, H.-E. & Knowles, J. C. Fluor-hydroxyapatite sol–gel coating on titanium substrate for hard tissue implants. *Biomaterials* **25**, 3351–3358 (2004).
19. Ilyas, A. *et al.* Amorphous Silica: A New Antioxidant Role for Rapid Critical-Sized Bone Defect Healing. *Adv. Healthc. Mater.* **5**, 2199–2213 (2016).
20. Monte, F. A. do *et al.* Amorphous Silicon Oxynitrophosphide-Coated Implants Boost Angiogenic Activity of Endothelial Cells. *Tissue Eng. Part A* **26**, 15–27 (2019).
21. Varanasi, V. G. *et al.* Role of Hydrogen and Nitrogen on the Surface Chemical Structure of Bioactive Amorphous Silicon Oxynitride Films. *J. Phys. Chem. B* **121**, 8991–9005 (2017).
22. Maginot, M. Chemical changes in DMP1-null murine bone & silica based pecvd coatings for titanium implant osseoapplications. *Ph.D. Thesis* (2014).
23. do Monte, F. A. *et al.* Silicon Oxynitrophosphide Nanoscale-Coating Enhances Antioxidant Marker -Induced Angiogenesis During In Vivo Cranial Bone Defect Healing. *JBMR Plus* **n/a**, e10425 (2020).
24. Monte, F. *et al.* Ionic silicon improves endothelial cells' survival under toxic

oxidative stress by overexpressing angiogenic markers and antioxidant enzymes. *J. Tissue Eng. Regen. Med.* **12**, 2203–2220 (2018).

25. Awad, K. *et al.* Ionic Silicon Protects Oxidative Damage and Promotes Skeletal Muscle Cell Regeneration. *International Journal of Molecular Sciences* vol. 22 (2021).
26. Awad, K. R. *et al.* Silicon nitride enhances osteoprogenitor cell growth and differentiation via increased surface energy and formation of amide and nanocrystalline HA for craniofacial reconstruction. *Med. DEVICES SENSORS* **2**, e10032 (2019).
27. Boonrawd, W., Awad, K. R., Varanasi, V. & Meletis, E. I. Wettability and In-Vitro study of titanium surface profiling prepared by electrolytic plasma processing. *Surf. Coatings Technol.* **414**, 127119 (2021).
28. Ilyas, A., Lavrik, N. V, Kim, H. K. W., Aswath, P. B. & Varanasi, V. G. Enhanced Interfacial Adhesion and Osteogenesis for Rapid “Bone-like” Biomineralization by PECVD-Based Silicon Oxynitride Overlays. *ACS Appl. Mater. Interfaces* **7**, 15368–15379 (2015).
29. Gadelmawla, E. S., Koura, M. M., Maksoud, T. M. A., Elewa, I. M. & Soliman, H. H. Roughness parameters. *J. Mater. Process. Technol.* **123**, 133–145 (2002).
30. Gurau, L., Mansfield-Williams, H. & Irle, M. Processing roughness of sanded wood surfaces. *Holz als Roh- und Werkst.* **63**, 43–52 (2005).
31. Owens, D. K. & Wendt, R. C. Estimation of the surface free energy of polymers. *J. Appl. Polym. Sci.* **13**, 1741–1747 (1969).
32. Pelleg, J. Chapter Five - Deformation in AM and traditional manufacturing: A

comparison. in (ed. Pelleg, J. B. T.-A. and T. M. C.) 225–288 (Elsevier, 2020). doi:https://doi.org/10.1016/B978-0-12-821918-8.00005-X.

33. Oliver, W. C. & Pharr, G. M. An improved technique for determining hardness and elastic modulus using load and displacement sensing indentation experiments. *J. Mater. Res.* **7**, 1564–1583 (1992).

34. Aruwajoye, O. O. *et al.* Microcrack density and nanomechanical properties in the subchondral region of the immature piglet femoral head following ischemic osteonecrosis. *Bone* **52**, 632–639 (2013).

35. Ehtemam-Haghighi, S., Cao, G. & Zhang, L.-C. Nanoindentation study of mechanical properties of Ti based alloys with Fe and Ta additions. *J. Alloys Compd.* **692**, 892–897 (2017).

36. Varanasi, V. G. *et al.* Chapter 9 - Surface Modifications and Surface Characterization of Biomaterials Used in Bone Healing. in (eds. Bose, S. & Bandyopadhyay, A. B. T.-M. for B. D.) 405–452 (Academic Press, 2017). doi:https://doi.org/10.1016/B978-0-12-802792-9.00009-4.

37. Schneider, C. A., Rasband, W. S. & Eliceiri, K. W. NIH Image to ImageJ: 25 years of image analysis. *Nat. Methods* **9**, 671–675 (2012).

38. Ziemian, C. W., Sharma, M. M., Bouffard, B. D., Nissley, T. & Eden, T. J. Effect of substrate surface roughening and cold spray coating on the fatigue life of AA2024 specimens. *Mater. Des.* **54**, 212–221 (2014).

39. Zhou, X. & Ouyang, C. Anodized porous titanium coated with Ni-CeO2 deposits for enhancing surface toughness and wear resistance. *Appl. Surf. Sci.* **405**, 476–488 (2017).

40. Manjaiah, M. & Laubscher, R. F. Effect of anodizing on surface integrity of Grade 4 titanium for biomedical applications. *Surf. Coatings Technol.* **310**, 263–272 (2017).

41. Abdelrahim, R., Badr, N. & Baroudi, K. Effect of anodization and alkali-heat treatment on the bioactivity of titanium implant material (an in vitro study). *J. Int. Soc. Prev. Community Dent.* 189 OP-195 VO–6 doi:10.4103/2231-0762.183107.

42. Jin, M., Yao, S., Wang, L.-N., Qiao, Y. & Volinsky, A. A. Enhanced bond strength and bioactivity of interconnected 3D TiO2 nanoporous layer on titanium implants. *Surf. Coatings Technol.* **304**, 459–467 (2016).

43. Arun Kumar, D., Merline Shyla, J. & Xavier, F. P. Synthesis and characterization of TiO2/SiO2 nano composites for solar cell applications. *Appl. Nanosci.* **2**, 429–436 (2012).

44. Praveen, P., Viruthagiri, G., Mugundan, S. & Shanmugam, N. Structural, optical and morphological analyses of pristine titanium di-oxide nanoparticles – Synthesized via sol–gel route. *Spectrochim. Acta Part A Mol. Biomol. Spectrosc.* **117**, 622–629 (2014).

45. Zhang, H.-X., He, X.-D. & He, F. Microstructural characterization and properties of ambient-dried SiO2 matrix aerogel doped with opacified TiO2 powder. *J. Alloys Compd.* **469**, 366–369 (2009).

46. Dihingia, P. J. & Rai, S. Synthesis of TiO2 nanoparticles and spectroscopic upconversion luminescence of Nd3+-doped TiO2–SiO2 composite glass. *J. Lumin.* **132**, 1243–1251 (2012).

47. Pandey, R. K. *et al.* Growth and characterization of SiON thin films by using

thermal-CVD machine. *Opt. Mater. (Amst).* **25**, 1–7 (2004).

48. Bugaev, K. O., Zelenina, A. A. & Volodin, V. A. Vibrational Spectroscopy of Chemical Species in Silicon and Silicon-Rich Nitride Thin Films. *Int. J. Spectrosc.* **2012**, 281851 (2012).
49. Ahmadi, A., Ramezanzadeh, B. & Mahdavian, M. Hybrid silane coating reinforced with silanized graphene oxide nanosheets with improved corrosion protective performance. *RSC Adv.* **6**, 54102–54112 (2016).
50. Ahuja, N. *et al.* Preliminary study of in-situ 3D bioprinted nano-silicate biopolymer scaffolds for muscle repair in VML defects. *FASEB J.* **34**, 1 (2020).
51. AWAD, K. R. *et al.* Micro-patterned Bioactive Amorphous Silicon Oxynitride Enhances Adhesion, Growth, and Myotubes and Axon Alignment in Muscle and Nerve Cells. *FASEB J.* **34**, 1 (2020).
52. Luz, A. R., Lepienski, C. M., Henke, S. L., Grandini, C. R. & Kuromoto, N. K. Effect of microstructure on the nanotube growth by anodic oxidation on Ti-10Nb alloy. *Mater. Res. Express* **4**, 76408 (2017).
53. Jung, Y.-G., Lawn, B. R., Martyniuk, M., Huang, H. & Hu, X. Z. Evaluation of elastic modulus and hardness of thin films by nanoindentation. *J. Mater. Res.* **19**, 3076–3080 (2004).
54. Beck, U., Smith, D. T., Reiners, G. & Dapkunas, S. J. Mechanical properties of SiO2 and Si3N4 coatings: a BAM/NIST co-operative project. *Thin Solid Films* **332**, 164–171 (1998).
55. Geetha, D., Joice Sophia, P., Radhika, R. & Arivuoli, D. Evaluation of nanoindentation and nanoscratch characteristics of GaN/InGaN epilayers. *Mater.*

Sci. Eng. A **683**, 64–69 (2017).

56. Takebe, J., Itoh, S., Okada, J. & Ishibashi, K. Anodic oxidation and hydrothermal treatment of titanium results in a surface that causes increased attachment and altered cytoskeletal morphology of rat bone marrow stromal cells in vitro. *J. Biomed. Mater. Res.* **51**, 398–407 (2000).

57. Kim, K., Lee, B.-A., Piao, X.-H., Chung, H.-J. & Kim, Y.-J. Surface characteristics and bioactivity of an anodized titanium surface. *J Periodontal Implant Sci* **43**, 198–205 (2013).

58. Arima, Y. & Iwata, H. Effect of wettability and surface functional groups on protein adsorption and cell adhesion using well-defined mixed self-assembled monolayers. *Biomaterials* **28**, 3074–3082 (2007).

59. Ho, Y.-H. *et al.* In-vitro biomineralization and biocompatibility of friction stir additively manufactured AZ31B magnesium alloy-hydroxyapatite composites. *Bioact. Mater.* **5**, 891–901 (2020).

60. Lim, J. Y. *et al.* Surface energy effects on osteoblast spatial growth and mineralization. *Biomaterials* **29**, 1776–1784 (2008).

61. Kokubo, T. & Takadama, H. How useful is SBF in predicting in vivo bone bioactivity? *Biomaterials* **27**, 2907–2915 (2006).

62. Porter, A. E., Hobbs, L. W., Rosen, V. B. & Spector, M. The ultrastructure of the plasma-sprayed hydroxyapatite–bone interface predisposing to bone bonding. *Biomaterials* **23**, 725–733 (2002).

63. Wang, H. *et al.* Early bone apposition in vivo on plasma-sprayed and electrochemically deposited hydroxyapatite coatings on titanium alloy.

Biomaterials **27**, 4192–4203 (2006).

64. Zhang, Y. & Santos, J. D. Microstructural characterization and in vitro apatite formation in CaO–P2O5–TiO2–MgO–Na2O glass-ceramics. *J. Eur. Ceram. Soc.* **21**, 169–175 (2001).

65. Cao, J., Lian, R., Jiang, X. & Liu, X. Formation of Porous Apatite Layer after Immersion in SBF of Fluorine-Hydroxyapatite Coatings by Pulsed Laser Deposition Improved in Vitro Cell Proliferation. *ACS Appl. Bio Mater.* **3**, 3698–3706 (2020).

66. Yoshida, E. & Hayakawa, T. Quantitative Analysis of Apatite Formation on Titanium and Zirconia in a Simulated Body Fluid Solution Using the Quartz Crystal Microbalance Method. *Adv. Mater. Sci. Eng.* **2017**, 7928379 (2017).

67. Liu, X., Ding, C. & Wang, Z. Apatite formed on the surface of plasma-sprayed wollastonite coating immersed in simulated body fluid. *Biomaterials* **22**, 2007–2012 (2001).

68. Ślósarczyk, A., Paszkiewicz, Z. & Paluszkiewicz, C. FTIR and XRD evaluation of carbonated hydroxyapatite powders synthesized by wet methods. *J. Mol. Struct.* **744–747**, 657–661 (2005).

69. Puvvada, N., Panigrahi, P. K. & Pathak, A. Room temperature synthesis of highly hemocompatible hydroxyapatite, study of their physical properties and spectroscopic correlation of particle size. *Nanoscale* **2**, 2631–2638 (2010).

70. Zhang, Q. *et al.* Facile and controllable synthesis of hydroxyapatite/graphene hybrid materials with enhanced sensing performance towards ammonia. *Analyst* **140**, 5235–5242 (2015).

71. Nosrati, H., Sarraf Mamoory, R., Svend Le, D. Q. & Bünger, C. E. Fabrication of gelatin/hydroxyapatite/3D-graphene scaffolds by a hydrogel 3D-printing method. *Mater. Chem. Phys.* **239**, 122305 (2020).

72. Aizawa, M., Matsuura, T. & Zhuang, Z. Syntheses of Single-Crystal Apatite Particles with Preferred Orientation to the *a*- and *c*-Axes as Models of Hard Tissue and Their Applications. *Biol. Pharm. Bull.* **36**, 1654–1661 (2013).

73. Brundavanam, R. K., Eddy, G., Poinern, J. & Fawcett, D. Modelling the Crystal Structure of a 30 nm Sized Particle based Hydroxyapatite Powder Synthesised under the Influence of Ultrasound Irradiation from X-ray powder Diffraction Data. **3**, 84–90 (2013).

74. Cengiz, B., Gokce, Y., Yildiz, N., Aktas, Z. & Calimli, A. Synthesis and characterization of hydroxyapatite nanoparticles. *Colloids Surfaces A Physicochem. Eng. Asp.* **322**, 29–33 (2008).

75. Song, J., Ma, X., Zui, W., Wei, C. & Chen, Z. Fabrication of Si_3N_4 Nanocrystals and Nanowires Using PECVD. *Adv. Mater. Sci. Eng.* **2010**, 892792 (2010).

76. Andersson, Ö. H. & Kangasniemi, I. Calcium phosphate formation at the surface of bioactive glass in vitro. *J. Biomed. Mater. Res.* **25**, 1019–1030 (1991).

77. Hench, L. L., Splinter, R. J., Allen, W. C. & Greenlee, T. K. Bonding mechanisms at the interface of ceramic prosthetic materials. *J. Biomed. Mater. Res.* **5**, 117–141 (1971).

78. Hench, L. L. & Kokubo, T. Properties of bioactive glasses and glass-ceramics BT - Handbook of Biomaterial Properties. in (eds. Black, J. & Hastings, G.) 355–363 (Springer US, 1998). doi:10.1007/978-1-4615-5801-9_22.

79. Wang, L., Ruiz-Agudo, E., Putnis, C. V, Menneken, M. & Putnis, A. Kinetics of Calcium Phosphate Nucleation and Growth on Calcite: Implications for Predicting the Fate of Dissolved Phosphate Species in Alkaline Soils. *Environ. Sci. Technol.* **46**, 834–842 (2012).

80. Varanasi, V. G. *et al.* The ionic products of bioactive glass particle dissolution enhance periodontal ligament fibroblast osteocalcin expression and enhance early mineralized tissue development. *J. Biomed. Mater. Res. Part A* **98A**, 177–184 (2011).

81. Cebe, T. *et al.* Novel 3D-printed methacrylated chitosan-laponite nanosilicate composite scaffolds enhance cell growth and biomineral formation in MC3T3 pre-osteoblasts. *J. Mater. Res.* **35**, 58–75 (2020).

CHAPTER 5: BACTERIOSTATIC SILICON OXYNITRIDE COATING ENHANCES BONE HEALING VIA ANTIOXIDANT ACTIVITY IN RABBIT MANDIBULAR BONE DEFECTS

Kamal Awad[1, 2, 3], Neelam Ahuja[2], Lindsay Wilson[4], Su[5], He Dong[5], Marco Brotto[2], Pranesh Aswath[1], Simon Young[4], Venu Varanasi[1, 2, *]

[1]Department of Materials Science and Engineering, College of Engineering, The University of Texas at Arlington, Arlington, TX 76019, USA.

[2]Bone-Muscle Research Center, College of Nursing & Health Innovation, The University of Texas at Arlington, Arlington, TX 76019, USA.

[3]Refractories, Ceramics and Building Materials Department, National Research Centre, Dokki, Cairo 12622, Egypt.

[4]Department of Oral and Maxillofacial Surgery, the University of Texas Health Science Center at Houston, School of Dentistry, Houston, Texas 77054, USA

[5]Department of Chemistry and Biochemistry, College of Science, The University of Texas at Arlington, Arlington, TX 76019, USA.

*Corresponding Author, (venu.varanasi@uta.edu)

Dr. Venu Varanasi, PhD

Associate Professor, Bone Muscle Research Center

College of Nursing and Health Innovation

University of Texas at Arlington

Address: 655 W. Mitchell St., Box 19410, Arlington, TX 76019

Email: Venu.varanasi@uta.edu

ABSTRACT

Mandibular fractures are one of the most common injuries to the facial skeleton and their treatment requires optimization of the functional and cosmetic outcomes. Although, titanium (Ti) implants are used to fixate bone fragments, complications can occur such as, prolonged healing time and delayed return to function. Furthermore, implant-related-infection is still one of the major complications in musculoskeletal trauma surgery. Here, we propose a new coating material, amorphous silicon oxynitride (SiONx), to enhance the healing rate of bone defects through mineral nucleation and the formation of a direct bond to bone, inducing the expression of antioxidant biomarkers, as well as, reducing both the reactive oxygen species and the infection rate due to its bacteriostatic effect. A Si-O-N amorphous coating of 1000 nm was deposited via a plasma enhanced chemical vapor deposition (PECVD) process on silicon wafers (for *in-vitro* studies) and prefabricated titanium plates and screws (for *in-vivo* studies). *In-vitro* studies, using mesenchymal stem cells (MSCs), were performed to test the surface bioactivity and cytotoxicity. Bacterial studies were performed using Methicillin-Resistant Staphylococcus Aureus (MRSA) bacteria. *In-vivo* studies were then performed on coated Ti plates and screws implanted in a rabbit mandibular critical size defect model to study the bone healing against the uncoated implant. Statistical analysis was conducted using T-test and one-way ANOVA along with post hoc analysis. *In-vitro* cytotoxicity studies using MSCs indicated normal cell adhesion and morphology on the modified surfaces without any cytotoxic effects. Micro-CT images of the healing rabbit mandibular defects revealed rapid bone regeneration for SiONx-coated implants as compared to uncoated implants after 8 weeks. The coated implants showed bone

growth on the surface of the implants as compared to uncoated implants which did not show bone growth on the surface. Serum analysis using ELISA showed significantly higher concentration of SOD1 at week 4 and week 8 and significantly lower lipid peroxidation (4HNE) at weeks 2, 4 and 8 for the coated implants. These results suggest that SiONx coatings exhibit antioxidant properties, bacteriostatic effect, reduced healing times, enhanced bone formation and osteointegration on the surface of implants.

Keywords: Critical bone defects; Titanium; Surface modifications; Bone healing; Alkaline phosphatase.

1. INTRODUCTION:

Due to the excellent physical and chemical properties and high biocompatibility with host tissue, Ti implants have been considered as the gold standard in the orthopedic and dental implant applications [1–3]. However, prolonged healing time, delayed return time to function, and possible implant-related infections are still the main complications for Ti implants due to the limited surface bioactivity [4]. The surface bioactivity is commonly defined as the ability of specific material to form a chemical bond with bone under *in-vivo* conditions [5]. The ability of Ti to spontaneously form a native thin oxide layer on the surface once exposed to air, allows the surface to tolerate and integrate into bone tissue [5]. However, Ti implants under normal manufacturing steps lead to an oxidized, contaminated, stressed, plastically deformed, and non-uniformed surface native oxide layer which introduces many limitations and poor surface bioactivity [6]. This poor bioactivity weakens the bone-implant bond which leads to poor osseointegration and implant failure. Thus, there is room for continued improvement of Ti bioactivity via surface modifications.

On the other hand, implant-related-infections are still one of the major complications in musculoskeletal trauma surgery [3]. A previous study has reported that infection preventions is of paramount importance in fracture stability and successful implantation [7]. In physiological environment, Ti implants are exposed to microbial adhesion and biofilm formation which ultimately can trigger local inflammation in the surrounding tissues and end with implant infection and failure [8–10]. These biofilms are challenging to treat due to their microbial composition complexity and tridimensional structure [9,11]. Implant's surface properties are the main player that directly controls the

biological responses and microbial adhesion on the surface [11,12]. Adsorption of protein on the surface of implant is the first biological response that directly mediates subsequent cellular events such as cell adhesion, microbial adhesion, and the overall osseointegration process [11,12]. Thus, tailoring the implant's surface for selective biological response that enhances cell's adhesion and reduce bacteria's attachment (i.e., bacteriostatic effect) is crucial for successful implantation.

In this regard, various surface modification techniques have been applied to Ti-implants to improve its biological properties for improved bone-implant integration and prevent infection. Some of the proposed surface modifications, including sand blasting, large grit, and acid-etching treatments, have enhanced implant primary stability and osseointegration process compared to machined implants [13]. However, the increased surface roughness obtained by this type of treatment also favors biofilm accumulation and results in enhanced bacterial growth [14]. Thus, Ti surface coatings were introduced to enhance its surface bioactivity without affecting the surface topography or roughness. This approach has been investigated using different coating techniques such as glow discharge, electrolytic plasma, and photocatalytic materials [15]. Although these surface modification techniques resulted in bioactive surfaces with antimicrobial properties, cell cytotoxicity and short-term efficiency are the currently main limitations for all coatings developed for Ti surfaces so far [15–17].

In this study, we tested our newly developed plasma enhanced chemical vapor deposition (PECVD) coatings as potential surface coatings for Ti implants. SiONx-PECVD coatings were deposited on silicon wafer and used for in-vitro bacterial and cells studies. Then, 1000 nm of SiONx-PECVD coating was deposited on Ti

implants and screws, which was then used for *in-vivo* testing using rabbit mandibular critical sized defect. *In-vitro* cytotoxicity studies using MSCs indicated normal cell adhesion and morphology on the modified surfaces without any cytotoxic effects. MRSA bacterial studies indicated that SiONx coating has a bacteriostatic effect compared to the bare Ti implants. *In-vivo* results revealed rapid bone regeneration for SiONx-coated implants as compared to uncoated implants. The coated implants showed bone growth on the surface of the implants as compared to the uncoated implants. Serum analysis using ELISA showed significantly higher concentration of SOD1 at week 4 and week 8 and significant decrease in 4HNE concentration for the coated implants. We concluded that SiONx coatings exhibit antioxidant properties, bacteriostatic effect, reduce healing times, and enhance bone formation and osteointegration on the surface of implants.

2. MATERIALS AND METHODS

2.1 Deposition of SiONx Surface Coatings

SiONx thin film coating was fabricated according to our previously published protocol [18–20]. Briefly, surface cleaning prior PECVD coating was performed using piranha solution (mixture of sulfuric acid, water, and hydrogen peroxide). Then, low temperature PECVD reactor was used to deposit a 1000 nm thin film coating of SiONx on silicon wafer as well as anodized commercially pure Ti (CP-Ti) substrate. Increasing the N_2O gas flow rate will increase the oxygen incorporation in the coatings over nitrogen content. Thus, five different chemistries of SiONx were fabricated based on changing the N_2O flow rate. The refractive index (n) of the deposited coatings were measured and used to distinguish the coatings in this study. Refractive index values

ranged from n=2 for N_2O = 0 sccm to n=1.45 for N_2O = 160 sccm. Exact flow rate and refractive index of each coating is provided in Table 5.1.

Table 5.1. Gas Flow Rates, deposition rate, and refractive index for Silicon Oxynitride (Si-O-N) and Silicon Oxynitrophosphide (Si-O-N) Layers Deposited by PECVD.

Sample	Gas flow rate (sccm)				Deposition Rate (nm/min)	Refractive index (n)
	15%SiH_4/Ar	N_2O	N_2	NH_3		
1	24	160	225	50	62.5	1.45
2	24	155	225	50	59.5	1.57
3	24	16	225	50	44.5	1.65
4	24	3	225	50	41.0	1.82
5	24	0	225	50	36.5	2.0

2.2 In-Vitro Studies

In-vitro cytotoxicity studies were performed according to ISO 10993-5 “biological evaluation of medical devices-part 5: tests for in-vitro cytotoxicity”. MSCs *in-vitro* cell culture studies were used to investigate the surface effect on cellular adhesion, cytotoxicity, and proliferation. Male human bone marrow MSCs was obtained from Lonza (Lonza Walkersville Inc., MD, USA). According to the provider, all cells are authenticated, performance assayed, and tested negative for mycoplasma. Cells were allowed to grow, and viability and morphology were measured after recovery from cryopreservation. For each experiment, cells were cultured in MSCGM BulletKitTM (Lonza, PT-3238 & PT-4105) specific growth medium. Cells were maintained at 37°C and 5% CO_2 in a completely humidified incubator. Cells were seeded and allowed to grow on the SiON-modified surfaces as well as the CP Ti surface as a control with n=3 samples for each group.

Cytotoxicity tests were performed after 24 and 48 hours of cell seeding. The MTS-CellTiter 96® Aqueous One Solution Cell Proliferation Assay, (Promega, Madison,

WI, USA) was used for quantitative analysis of cell growth and proliferation. A LIVE/DEAD™ Viability/Cytotoxicity Stain Kit was purchased from Thermo Fischer Scientific Inc. (Waltham, MA, USA) and used for qualitative analysis of cytotoxicity on the tested surfaces. All cell culture studies and assays were performed according to our previously published protocols [21]. The colorimetric absorbance of the MTS assay was determined using a microplate reader (SpectraMax® i3, Molecular Devices, CA) at 490 nm. Live/dead fluorescent images were then taken using a DMi8 inverted Leica microscope (Leica Microsystems Inc., IL, USA), with green staining for live cells and red staining for dead cells.

To study the effect of SiONx on osteogenic differentiation of MSCs, Alkaline Phosphatase (ALP) Kit (Colorimetric) was used to quantify the ALP activity in the differentiated MSCs after 1 and 4 days. MSCs were seeded on the SiONx surfaces and allowed to grow for 24 hours in normal growth media (MSCGM BulletKitTM). After 24 hours, growth media was removed, cells were washed with PBS, and fresh differentiation media was added. Differentiation media was collected at day 1 and 4 for ALP analysis.

Bacterial assays were conducted using MRSA bacteria. A single colony from the inoculation plate was used for each experiment. Mueller Hinton Broth (MHB) was used as the medium. A total of 105 colony-forming unit/mL (CFU/mL) were seeded onto the material surface with an inoculation loop. The samples were allowed to dry until there is no obvious liquid layer on the surface. Then the samples were incubated at 37 °C. Upon 12, 24, or 48 hrs of incubation, the bacterial on sample surface was stained with the live/dead bacteria assay kit solution at room temperature for 15 min. Finally, bacteria

were washed with phosphate buffer saline (PBS) for three times. Images were captured with EVOS M5000 Imaging System and analyzed with ImageJ software.

2.3 In-Vivo Studies

All animal studies were performed at Dr. Simon Young laboratory at the department of oral and maxillofacial surgery, University of Texas Health Science Center at Houston. All studies were performed on an easily accessible and reproducible, nonhealing alveolar bone defect in the rabbit mandible model (Figure 5.1) established and previously published by the Young's laboratory[22]. Briefly, mandibular critical size defects (CSDs) were introduced in adult male New Zealand white rabbits (Myrtle's Rabbitry, Thompson Station, TN) by creating 10-mm diameter and full thickness defect with both cortical plates removed the rabbit mandible. Then, bare and SiONx-Ti (n=1.82) coated fixation plate were secured with two screws on each side of the defect. Subsequently, the muscle and subcutaneous layers were closed with continuous resorbable 4-0 Vicryl sutures (Ethicon, Somerville, NJ) and the skin closed with interrupted 4-0 Vicryl sutures. After 8 weeks, the hemimandibles and surrounding tissues were harvested with the aid of bone shears and placed in 10% neutral buffered formalin for 48 h, rinsed thoroughly with phosphate buffered saline (PBS), and placed in 70% (v/v) ethanol solution for further analysis.

The collected serum at 2, 4, and 8 weeks was tested for antioxidant and reactive oxygen species (ROS) concentrations. Superoxide dismutase (SOD1) and 4-Hydroxynonenal (4HNE) levels in the blood serum were measured to reveal the antioxidant and ROS levels, respectively. Enzyme-linked immunosorbent assay (ELISA) kits (Cell Biolabs, Inc., San Diego, CA) were used to measure the SOD1 and 4HNE

concentrations in serum. The harvested mandibular bone defects fixed with bare and coated implants were investigated using a 45-Micro-Computer Tomograph 3D imager (µ-CT, Scanco Medical AG, Switzerland), and X-ray imaging to visualize the newly formed bone on the bare Ti compared to the coated implants. Then, X-ray Absorbance Near Edge Structure (XANES) analysis coupled with X-ray Fluorescence mapping was used to study the inorganic phase in the bone. Nano-indentation using Hysitron Ubi-1 Nanoindenter (Hysitron, Minneapolis, MN) was performed to study the mechanical properties of the surrounding and regenerated bones. Bone samples were polished using different grits size and surface was finished with 2000 grit. Then, 3600 µm2 surface area was scanned using scanning probe microscopy (SPM) and the area of interest was indented with a Berkovich tip. For each sample, 20 nanoindentations were performed on the selected area according to the following loading function: ramped up to 10 mN at a rate of 250 µN/s, held for 10 seconds, and then unloaded at 250 µN/s. The unloading slope of the load-displacement curve was used to calculate the reduced elastic modulus (E_r) and the hardness (H) based on the Oliver-Pharr method [23,24].

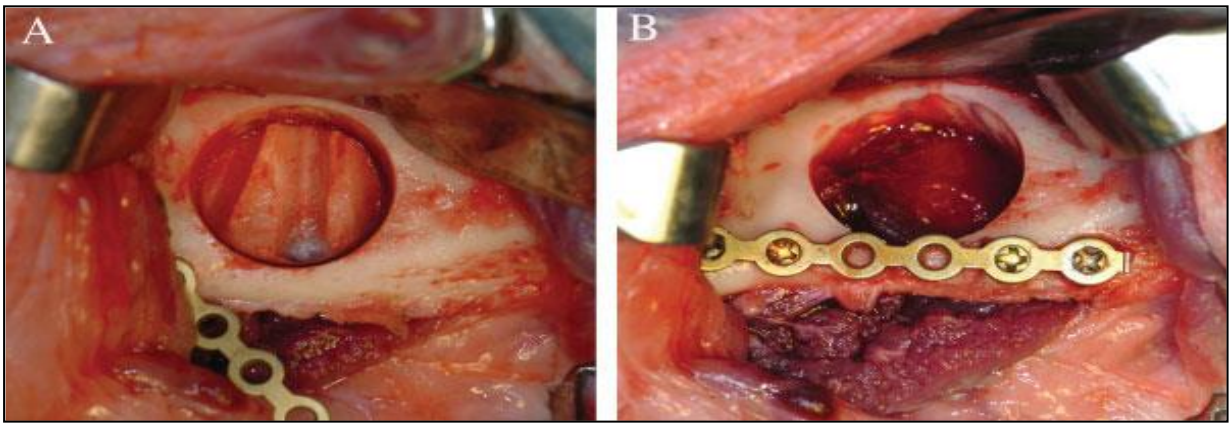

Figure 5.1: Intraoperative photos of the rabbit mandibular alveolar bone defects. A: Partial thickness defect showing intact lingual cortex and titanium fixation plate about to be secured in place. B: Full thickness defect with both cortical plates removed, and titanium fixation plate secured with two screws on each side of the defect.

2.4 Statistical analysis

OriginPro 8.5 software was used for all graphs and statistical analysis. A one-way ANOVA followed by Tukey's post hoc was used for between group comparisons. For significance level, $P < 0.05$ was considered as statistically significant, with * representing $p < 0.05$, ** representing $p < 0.01$, and *** representing $p < 0.001$. For *in-vitro* studies, a minimum of three replicates at two separate time points were used for each experiment per each group of samples according to ISO10993-5.

3. RESULTS AND DISCUSSION

3.1 *In-vitro studies*:

After SiONx thin film deposition on the silicon wafers and the anodized CP Ti mandibular implants (Figure 5.2), surface characterization (refractive index, chemical composition, and film thickness) was performed to confirm the chemistry of each

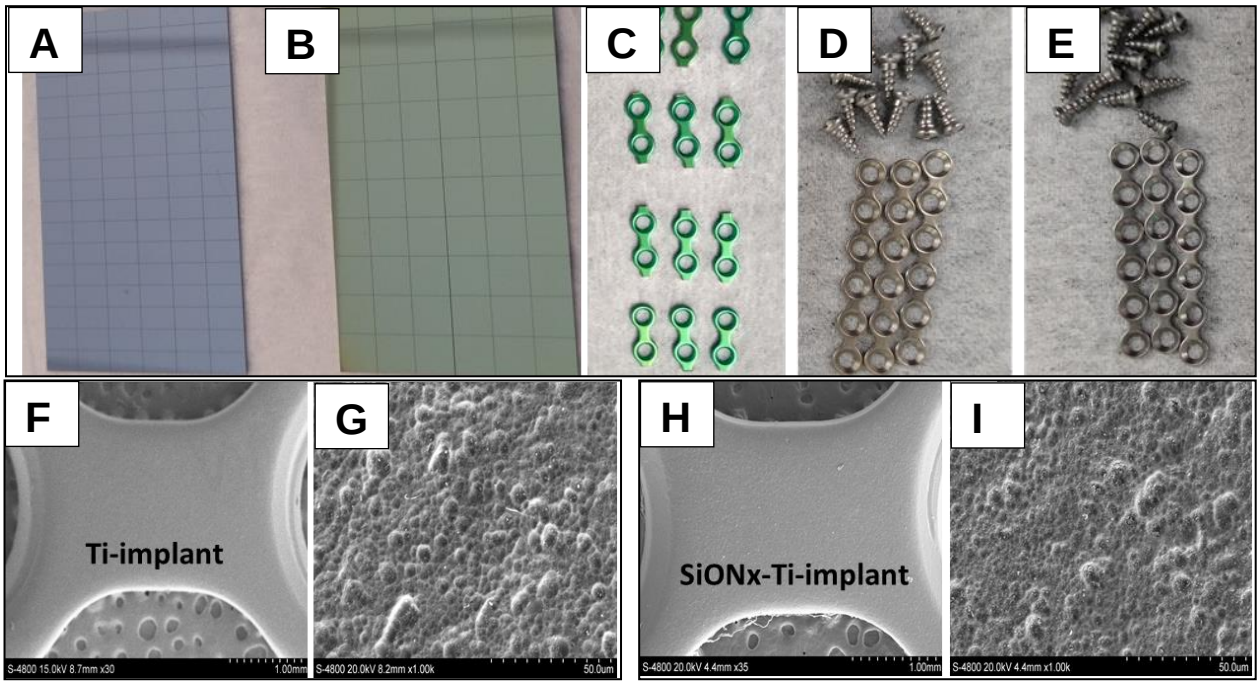

Figure 5.2: Implants images before and after PECVD coatings indicated no surface topography change. Image's show (a) bare Si wafer, (b) SiONx (n=1.82) coating on a Si-wafer, (c&d) bare Ti implants for *in-vitro* and *in-vivo* study, and (e) coated implants Ti-SiONx. (F-I) HR-SEM images indicate no microstructure change after coatings.

coating. Surface characterization results were in a good agreement with previously published data [25]. Sample 1 ($SiON_x$, n = 1.45) exhibited pure SiO_x structure with zero N incorporated and the highest oxygen content compared to other $SiON_x$ coatings. Sample 5 ($SiON_x$, n = 2.0) exhibited Si_3N_4 like structure with the lowest oxygen content and the highest nitrogen content compared to other samples. High resolution scanning electron microscopy indicated no change in the surface topography and microstructure of the Ti implants after deposition of 1000 nm layer thickness of SiONx (Figure 5.2 F-I).

In-vitro studies using MSCs were used to study the effect of SiONx surface coatings on the cellular behavior (i.e., cytotoxicity, cell viability, and proliferation). Cell viability was assessed by live/dead staining (qualitative cytotoxicity assay) while cells proliferation was further quantified by an MTS assay (quantitative cytotoxicity assay). Figures 5.3 and 5.4 illustrate the MSCs viability and proliferation after 1 and 4 days of culture on the different SiONx-surface coatings compared to tissue culture plate (TCP) as a positive control. Fluorescence images show the live cells (green) and dead cells (red) on the different tested surfaces which indicated good cell adhesion and spread on the surfaces. Almost no red stained cells were observed meaning no cytotoxic effect on the modified surfaces as well as the TCP control. This was further quantified using the cell proliferation MTS assay as indicated in Figures 5.3-B and 5.4-B. MTS cell viability results confirmed that $SiON_x$-coatings have optical density (OD) values comparable to the TCP control indicating good cell viability/proliferation at both time points, but no significant difference was observed. Only sample 1 (SiONx, n= 1.45) indicated less cells adhesion at day 1, that became slightly higher than TCP at day 4, but no significant difference was observed.

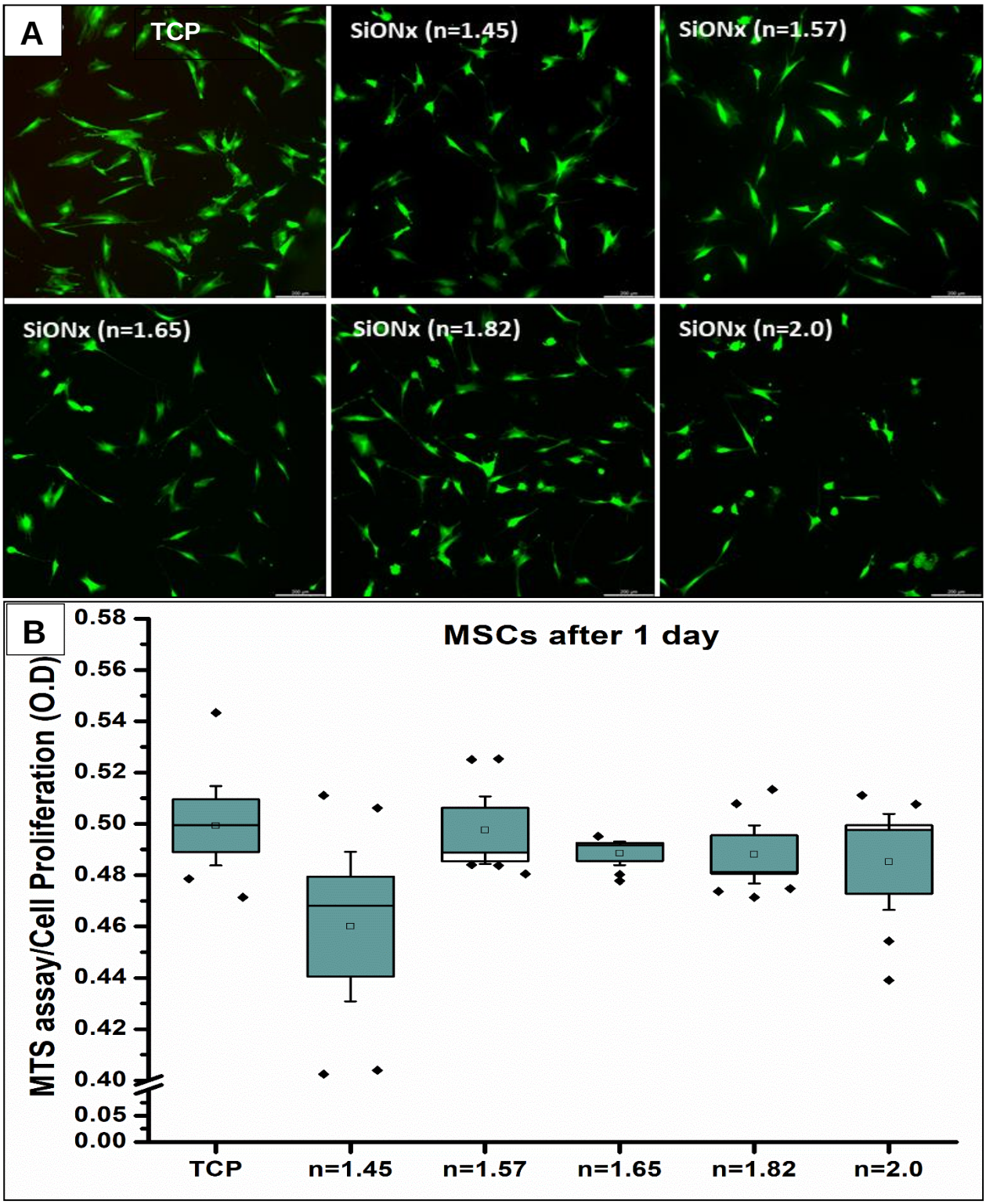

Figure 5.3: MSCs cell proliferation and viability on different SiONx coatings after 1 day. A) Fluorescence images show the live (green) and dead (red) cells. B) MTS assay presents the cells proliferation in optical density (OD) after 24 hours of cell's seeding.

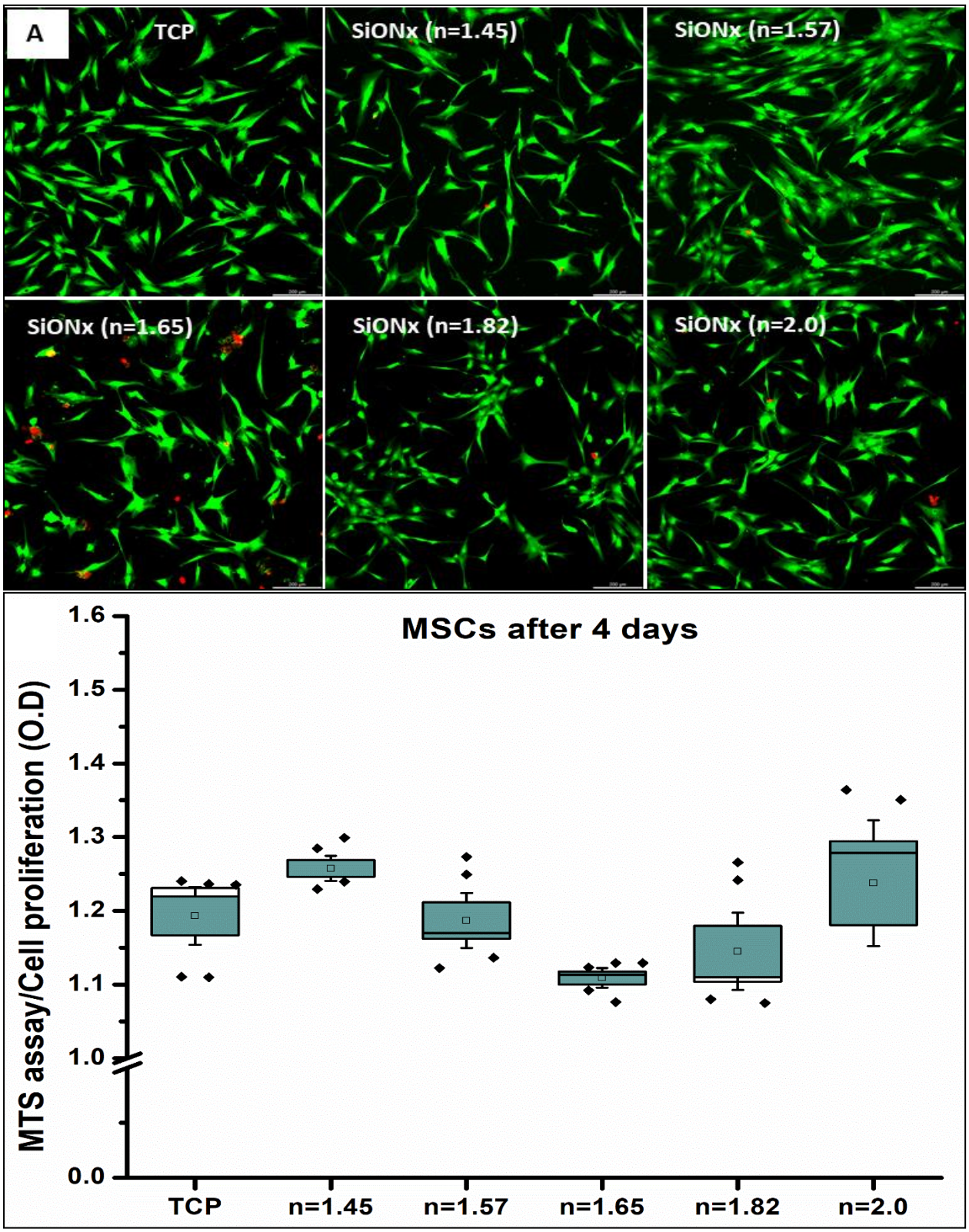

Figure 5.4: MSCs cell proliferation and viability on different SiONx coatings after 4 days. A) Fluorescence images show the live (green) and dead (red) cells. B) MTS assay presents the cells proliferation in optical density (OD) after 4 days of cell's seeding.

These data add an evidence for the surface bioactivity and biocompatibility of the amorphous silica-based PECVD coatings without any cytotoxic effect as tested using one of the most efficient cell source for tissue-engineering applications. MSCs are considered the main cell source for tissue-engineering applications due to their ability for self-renewal, differentiation into different cell lineages, and immunomodulatory properties[26]. MSCs are capable of proliferation, then differentiation to produce bone [27,28], ligament[29], adipose[30], cartilage[31,32], and muscle[33] tissues based on the type of conditioned cell culture media being used. MSCs have shown proven osteogenic differentiation when co-cultured with osteoblast cells[34] or directly seeded within porous scaffolds implanted in an animal model for bone defect repair[35,36].

ALP is involved in the process of calcification in various mineralizing tissues and is one of the most reliable osteogenic differentiation markers since it is produced by osteogenic cells such as osteoblasts [37–39]. Here, the effect of SiONx on the osteogenic differentiation of MSCs was studied through measuring ALP activity at day 1 and 4 of differentiation. Figure 5.5 shows the ALP activity in the differentiation media expressed in nmol/min/ml. High oxygen content SiONx samples (n=1.45 to n=1.65) presented lower ALP activity compared to TCP as a control, while high nitrogen content SiONx samples (n=1.82 and n=2.0) presented higher ALP activity compared to other samples and the TCP control at day 1 of differentiation. After 4 days of differentiation, high oxygen content samples presented a significant decrease in the ALP activity while the high nitrogen samples (n=2.0) presented ALP activity higher than the TCP control without significant difference.

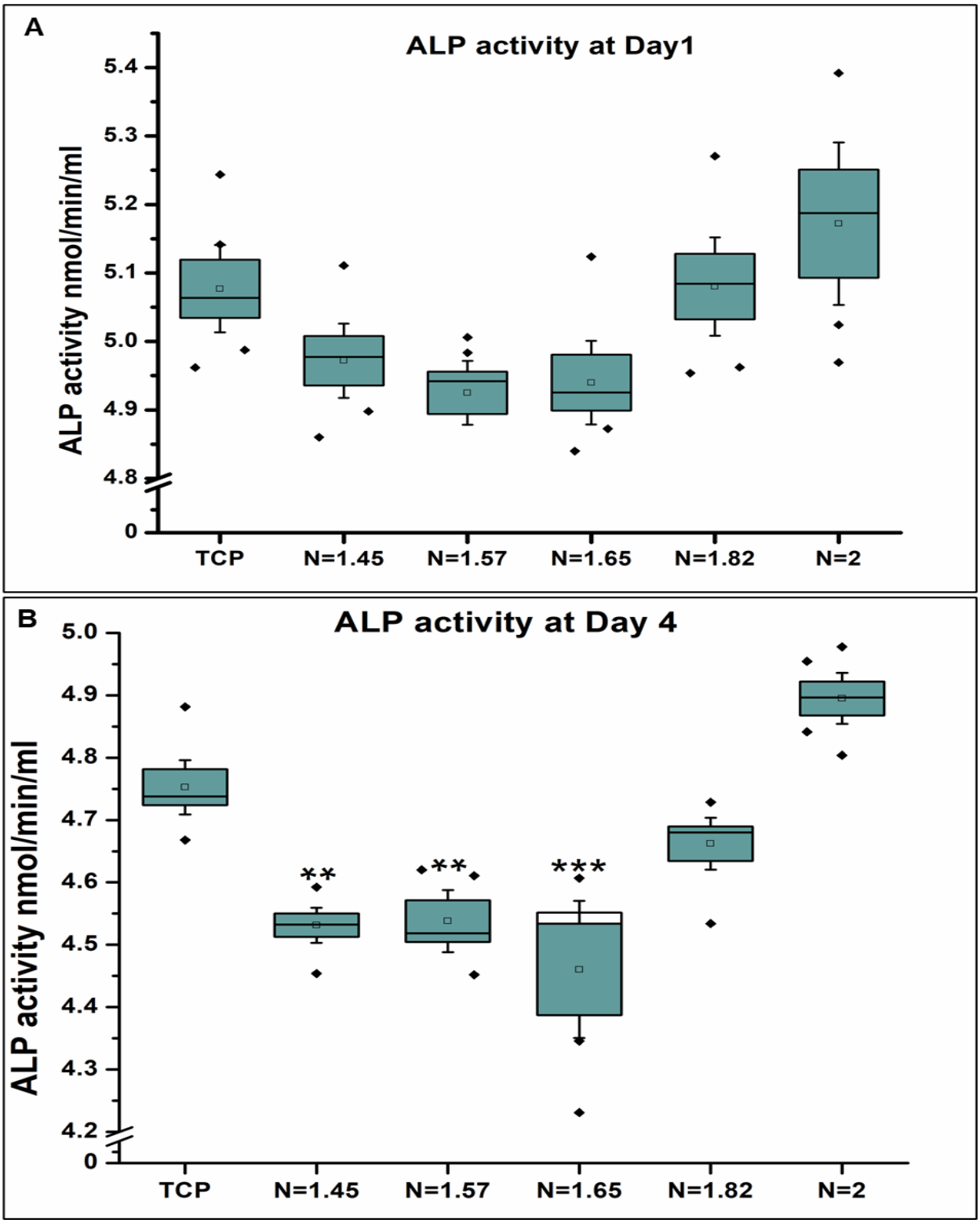

Figure 5.5: ALP activity on different SiONx coatings after 1 day (A) and 4 days (B) of differentiation. Only sample n=1.82 and n=2.0 showed higher ALP at day 1. ALP activity decreased at day 4 for all samples and control while n=1.82 and n=2.0 presented no significant difference compared to the control, (** $p<0.01$, *** $p<0.001$).

The enhancement in ALP activity could be attributed to the presence of nitrogen within the high nitrogen content samples while the decrease in ALP activity can be related to the higher oxygen content of the silica-like samples. These results agree with previous study reported that inorganic nitrogen released from nitrates enhances the ALP activity in bacterial [40]. Another study by Nausch indicated that bacterial ALP activity in marine ecosystems can be stimulated by both inorganic and organic nitrogen compounds [41].

MRSA is known as one of the most successful modern pathogens and a leading cause of bone and joint infections, skin and soft tissue infections, and hospitals - acquired infections [42,43]. Thus, this study intended to investigate the effect of SiONx coatings on MRSA compared to the bare Ti implants at 3 time-points as presented in Figures 5.6 - 5.9. Figure 5.7 - 5.9 presents the live/dead fluorescent images of MRSA on SiONx compared to Ti implants after 12, 24, and 48 hrs. All SiONx samples presented a significant decrease in the total number of bacteria at all time points. This can be seen from the decrease in the green stain (live bacteria) and the increase in red stain (dead bacteria). This was further quantified by counting the total number of live bacteria (Figure 5.6) on each sample using the green fluorescence images and ImageJ software. SiONx (n=1.82) presented the lowest bacterial counts at early time-point (12 hrs). SiONx (n=2.0) presented a significant decrease in bacterial counts at 12 hrs and the lowest bacterial counts at other time-points. This pronounced effect of SiONx suggest that SiONx has a bacteriostatic effect that inhibit the bacterial growth and proliferation compared to the Ti implants. The effect of SiONx chemistry can be attributed to the ability of these amorphous coatings to dissolve in the physiological

environment and release Si, N, and O ions. The surface of SiONx coatings mainly consist of Si-O_x, Si-OH, and Si-NH which undergoes the physiological environment tends to form Si-O^-, ΞSi-$O^•$, Si-$O_2^{-•}$, and Si-NH^+_3. As the cleavage of Si-bonds could possibly lead to some active species such as superoxide radicals (ΞSi-$O^•$ and Si-$O_2^{-•}$), as previously reported [44,45]. Presence of these radicals in high nitrogen content environment leads to formation of highly oxidative protonated radicals active in bacterial inactivation. This can explain the pronounced effect of high nitrogen content SiONx coatings that inhibited the bacterial growth compared to the Ti surface. Similar mechanism was proposed by Pezzotti et al., for silicon nitride that presented antibacterial activity against gram-negative phylum bacteroidetes [45]. Thus, the presented data suggest a possible antibacterial/bacteriostatic effect of SiONx coatings compared to the Ti implants that showed a massive bacterial growth on its surface.

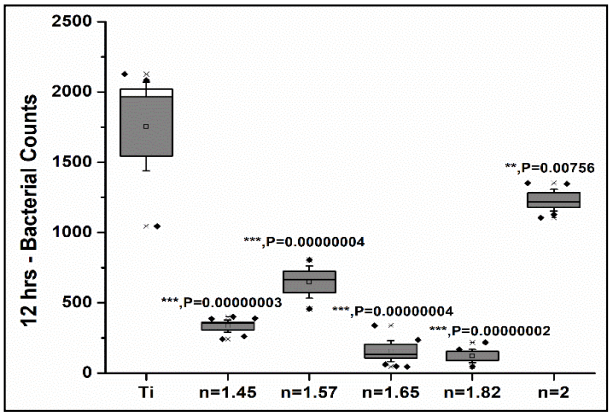

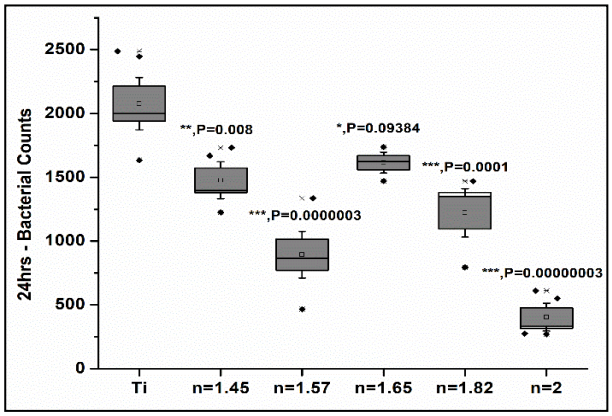

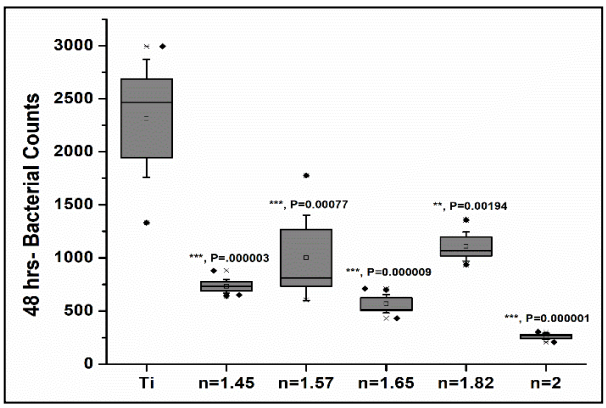

Figure 5.6: Bacteriostatic effect of SiONx verse Ti. Total MRSA counts on each sample after 12, 24, and 48 hours. All SiONx samples presented a significant decrease in the total number of bacteria at all time-points. SiONx (n=1.82) presented the lowest bacterial counts early at 12 hrs. SiONx (n=2.0) significantly decreased bacterial counts at 12 hrs.

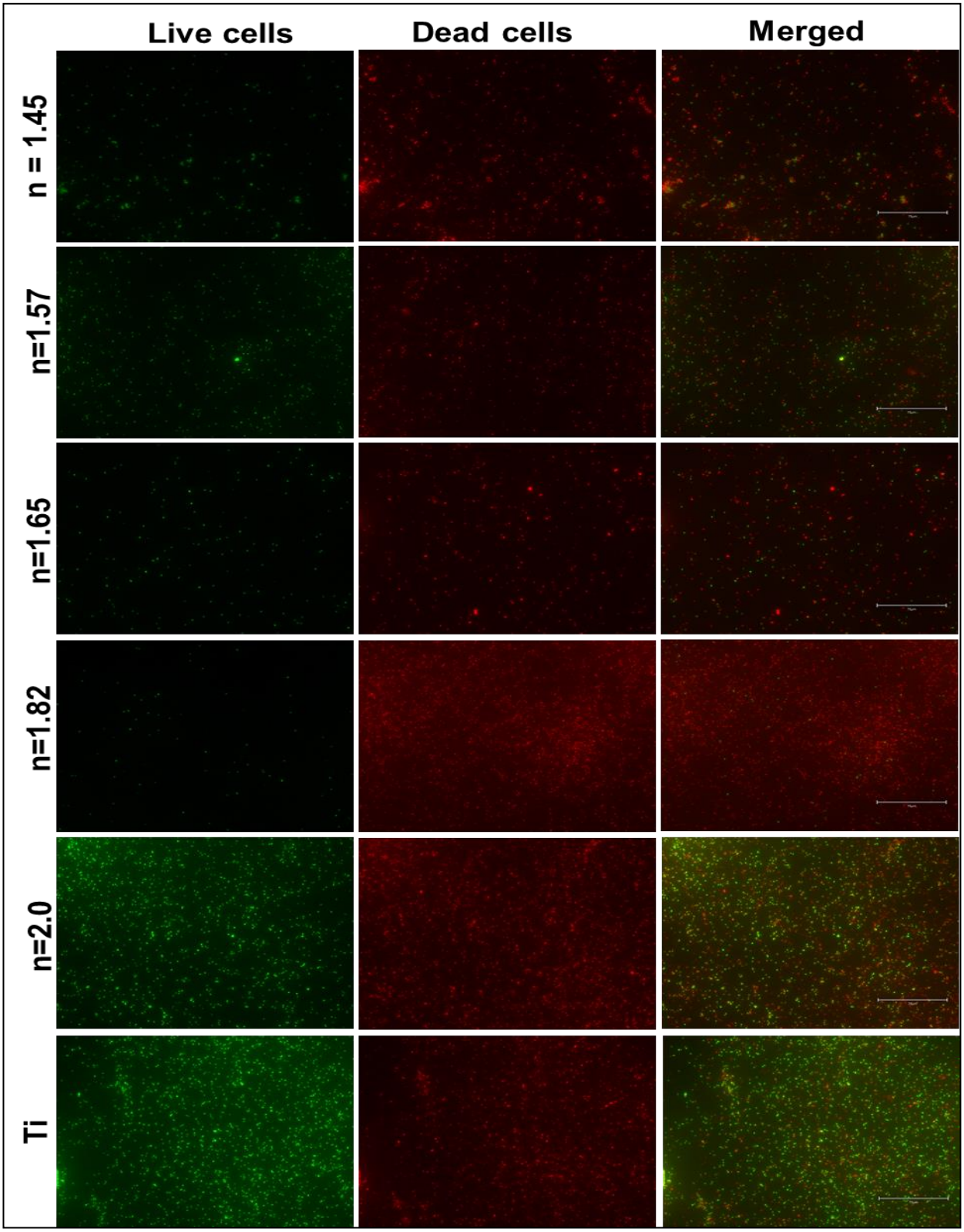

Figure 5.7: Bacteriostatic effect of SiONx coatings verse Ti implants. Fluorescence images show the live (green) and dead bacteria (red) on the different SiONx surfaces compared to Ti implant after 12 hours.

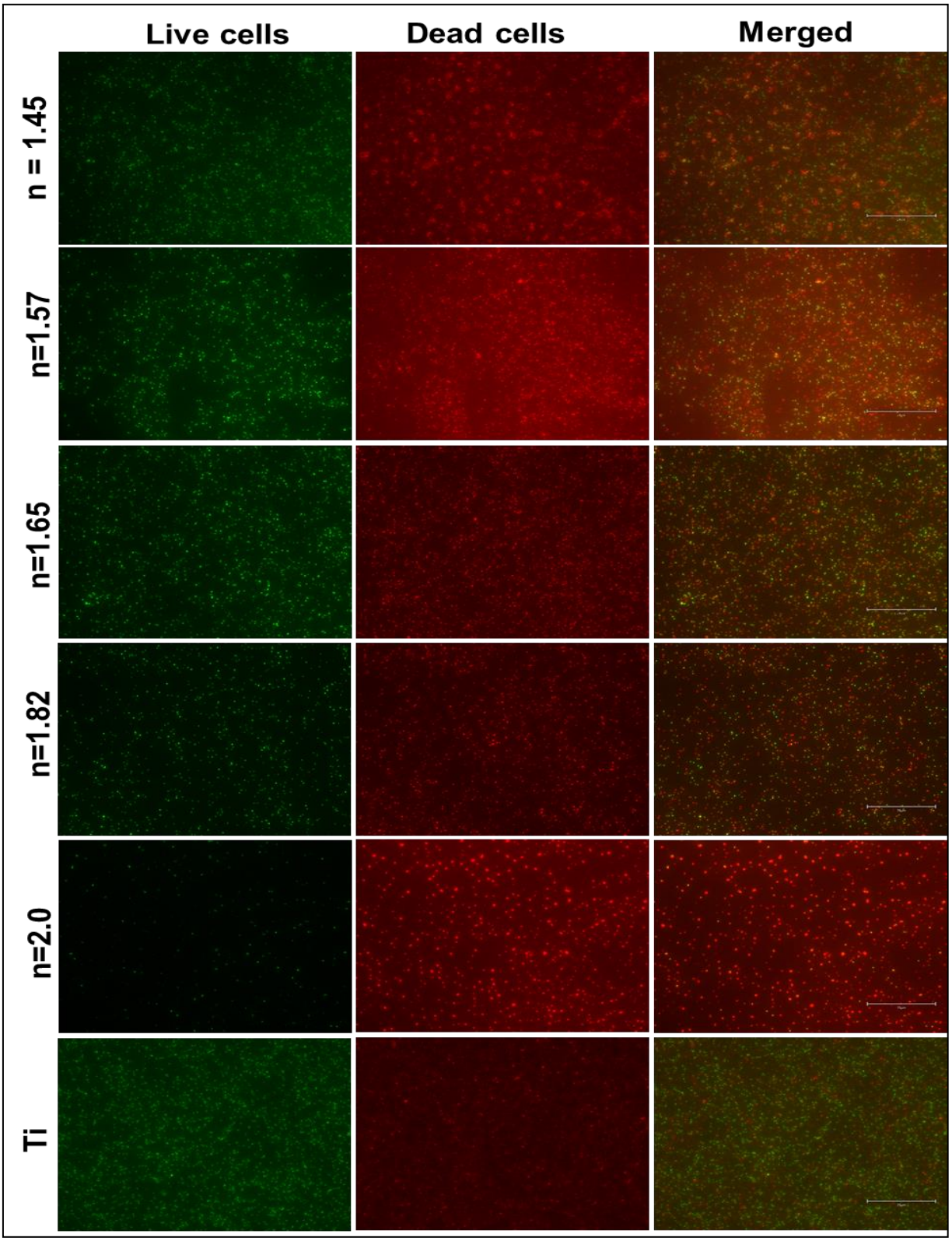

Figure 5.8: Bacteriostatic effect of SiONx coatings verse Ti implants. Fluorescence images show the live (green) and dead bacteria (red) on the different SiONx surfaces compared to Ti implant after 24 hours.

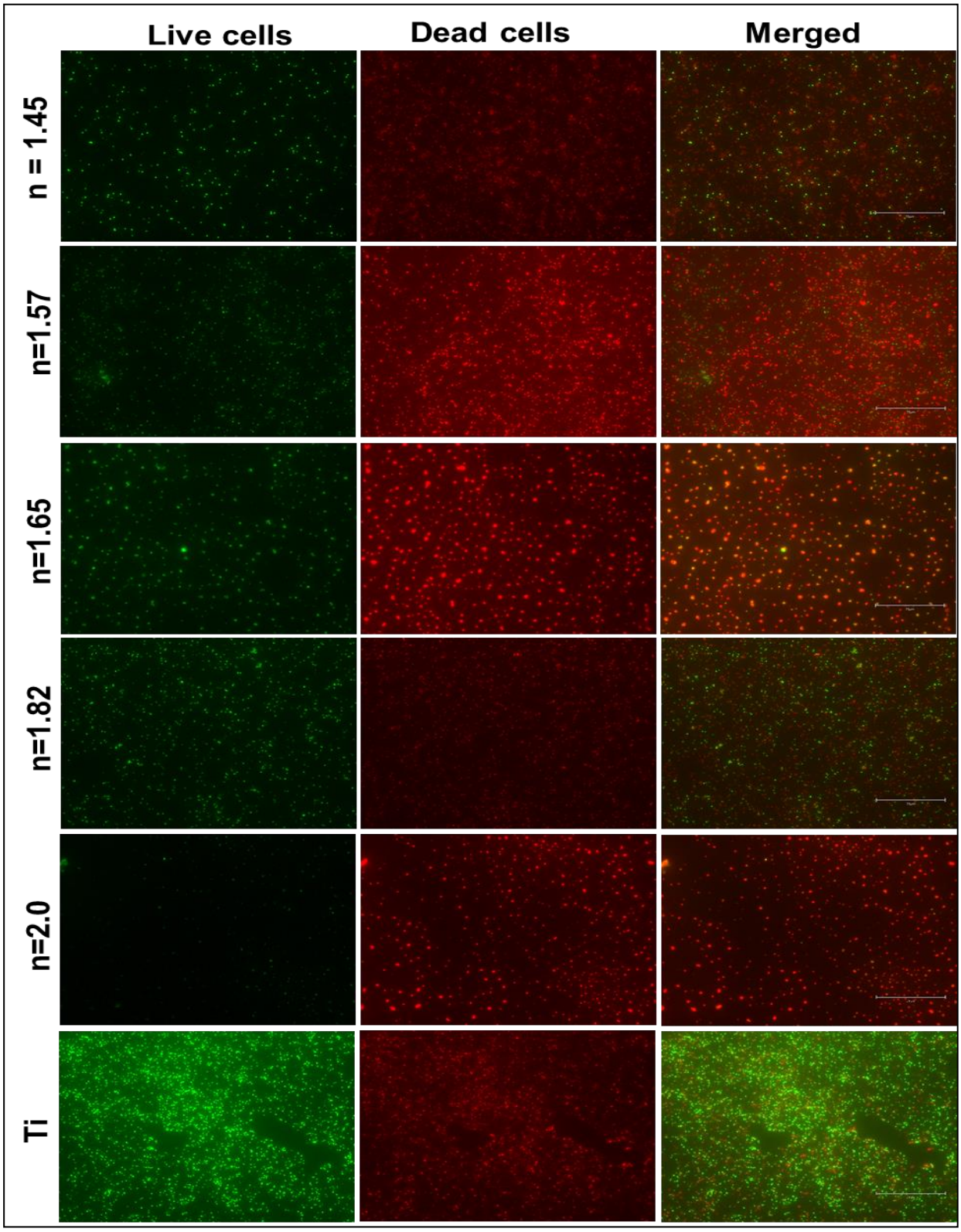

Figure 5.9: Bacteriostatic effect of SiONx coatings verse Ti implants. Fluorescence images show the live (green) and dead bacteria (red) on the different SiONx surfaces compared to Ti implant after 48 hours.

3.2 In-Vivo studies:

The collected blood serum was screened for different bone biomarkers and antioxidant activity. Figure 5.10 presents the SOD1 (Antioxidant), 4HNE (ROS marker), and ALP (Osteogenic marker) concentrations and activity in the collected rabbit serum after 1, 2, 4, and 8 weeks of the mandibular defect surgery. SOD 1 concentration was found to be elevated for the coated SiONx implants at all time points and a significant increase was observed at week 4 (**p<0.01) and week 8 (*p<0.05) as compared to the bare uncoated Ti implants. On the other hand, the 4HNE concentration decreased with

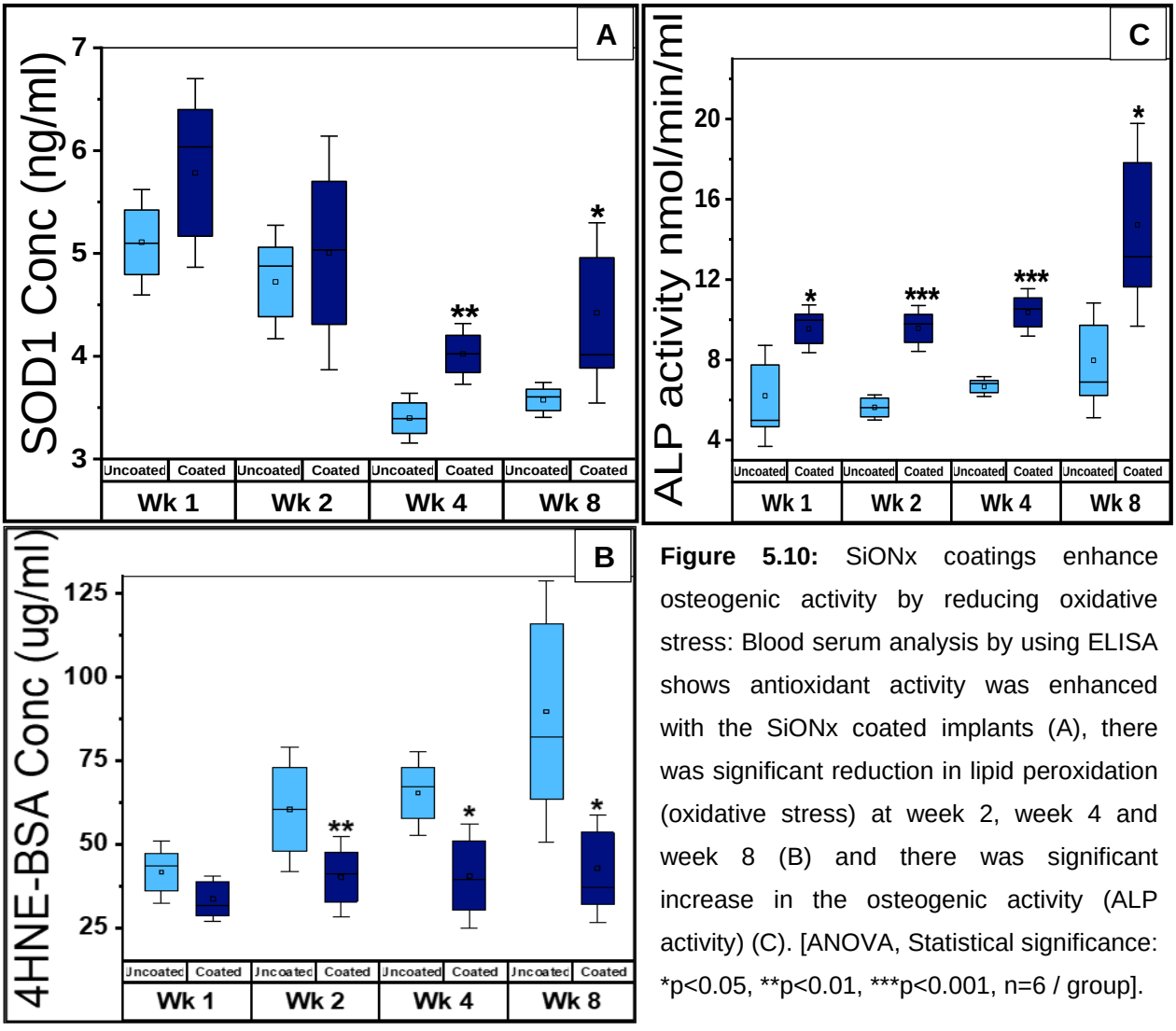

Figure 5.10: SiONx coatings enhance osteogenic activity by reducing oxidative stress: Blood serum analysis by using ELISA shows antioxidant activity was enhanced with the SiONx coated implants (A), there was significant reduction in lipid peroxidation (oxidative stress) at week 2, week 4 and week 8 (B) and there was significant increase in the osteogenic activity (ALP activity) (C). [ANOVA, Statistical significance: *p<0.05, **p<0.01, ***p<0.001, n=6 / group].

SiONx coated implants with significant decrease observed at weeks 2, 4, and 8 as compared to the bare Ti implants (Figure 5.10-B). Furthermore, the ALP activity in SiONx implants was significantly higher at all time points with high level of significance (***$p<0.001$) at weeks 2 and 4 compared to the bare Ti-implants. The pronounced effect SiONx in reducing the oxidative stress (4HNE) and enhancing the osteogenic markers (ALP) can be explained based on the antioxidant effect of the amorphous SiONx coatings. Release of Si-ions with higher valance state (+4) increase the charge transfer to antioxidant and enhance the overall antioxidant production[46]. The well-know SOD1 reaction with transition metals (i.e., Cu, Zn, and Mn) produces only one molecule of hydrogen peroxide (H_2O_2) according to equation 1. Then, via Fenton reaction and presence of catalase[47,48], the H_2O_2 is converted to one-water and half-oxygen molecule as in equation 2. In the case of Si^{+4}, the first reaction produces three molecules of H_2O_2 (Equation 3) which is three times higher compared to the normal reaction with transition metals (Equation 1). Then, via Fenton reaction and catalase reduction[47,48], $3H_2O_2$ is converted to $3H_2O$ and one and half-oxygen molecules which is 3-folds compared to the normal reaction. This pronounced antioxidant activity of Si-ions plays an important role in mitigating the effects of excessive ROS, which was confirmed by the significant reduction is 4HNE concentration. Thus, the enhancement of SOD1 (via Si-ions) reduces oxidative stress (4HNE) and accordingly improve biocompatibility, osteogenic activity, and osseointegration[49], as shown by the significant enhancement in ALP activity.

$$M^{2+}/SOD1 + O_2^{-}\ 2H^{+} = M^{2+}/SOD1 + H_2O_2 \qquad \textbf{(Eq. 1)}$$

$$Si^{4+}/SOD1 + 3O_2^{-}\ 6H^{+} = Si^{4+}/SOD1 + 3H_2O_2 \qquad \textbf{(Eq. 2)}$$

$$Fe^{3+}/CAT + H_2O_2 = Fe^{3+}/CAT + H_2O + \tfrac{1}{2}\ O_2 \qquad \textbf{(Eq. 3)}$$

$$Fe^{3+}/CAT + 3H_2O_2 = Fe^{3+}/CAT + 3H_2O + 1.5\ O_2 \qquad \textbf{(Eq. 4)}$$

The harvested rabbit bones were comprehensively studied to compare the effects of SiONx coated implants to the medically grade Ti impants. Figure 5.11 shows the extracted mandible with the bare Ti implants (Top) and the mandible with SiONx coated Ti (bottom). Visualization of the extracted bones revealed that the coated Ti implant are covered with newely formed bones and the defect size was smaller compared to the unocted Ti implant. Furthermore, the surrounding bone to uncoated Ti seemed to have very poor quality and the defect size was not much different compared to the original defect size. These observations were further confirmed by micro-CT and X-ray imaging as shown in Figure 5.12.

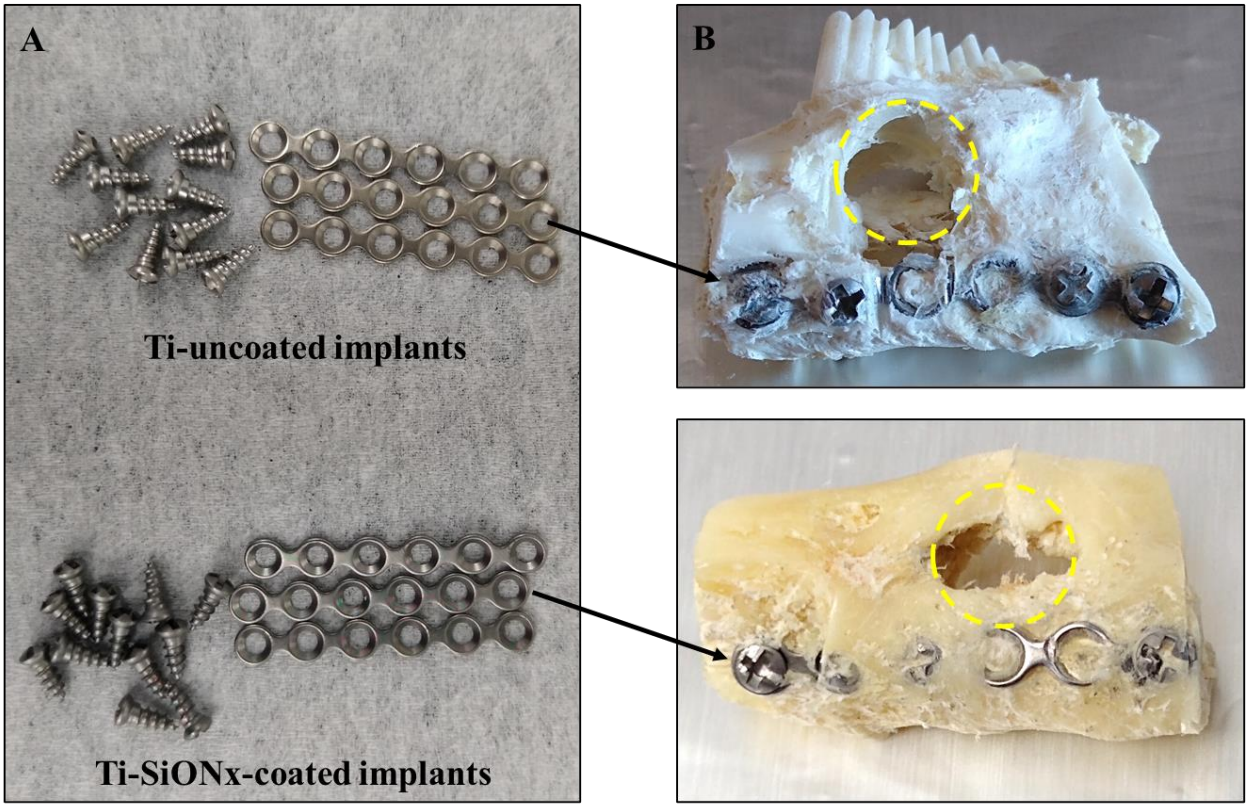

Figure 5.11: Ti-SiONx coated implants enhance the bone healing rate. A) Ti uncoated implants and screws (top) compared to coated implants (bottom) prior implantation. B) Extracted bone-implants after 8 weeks of surgery indicated higher bone healing rate on the coated implants (bottom) compared to the bare Ti implant (top).

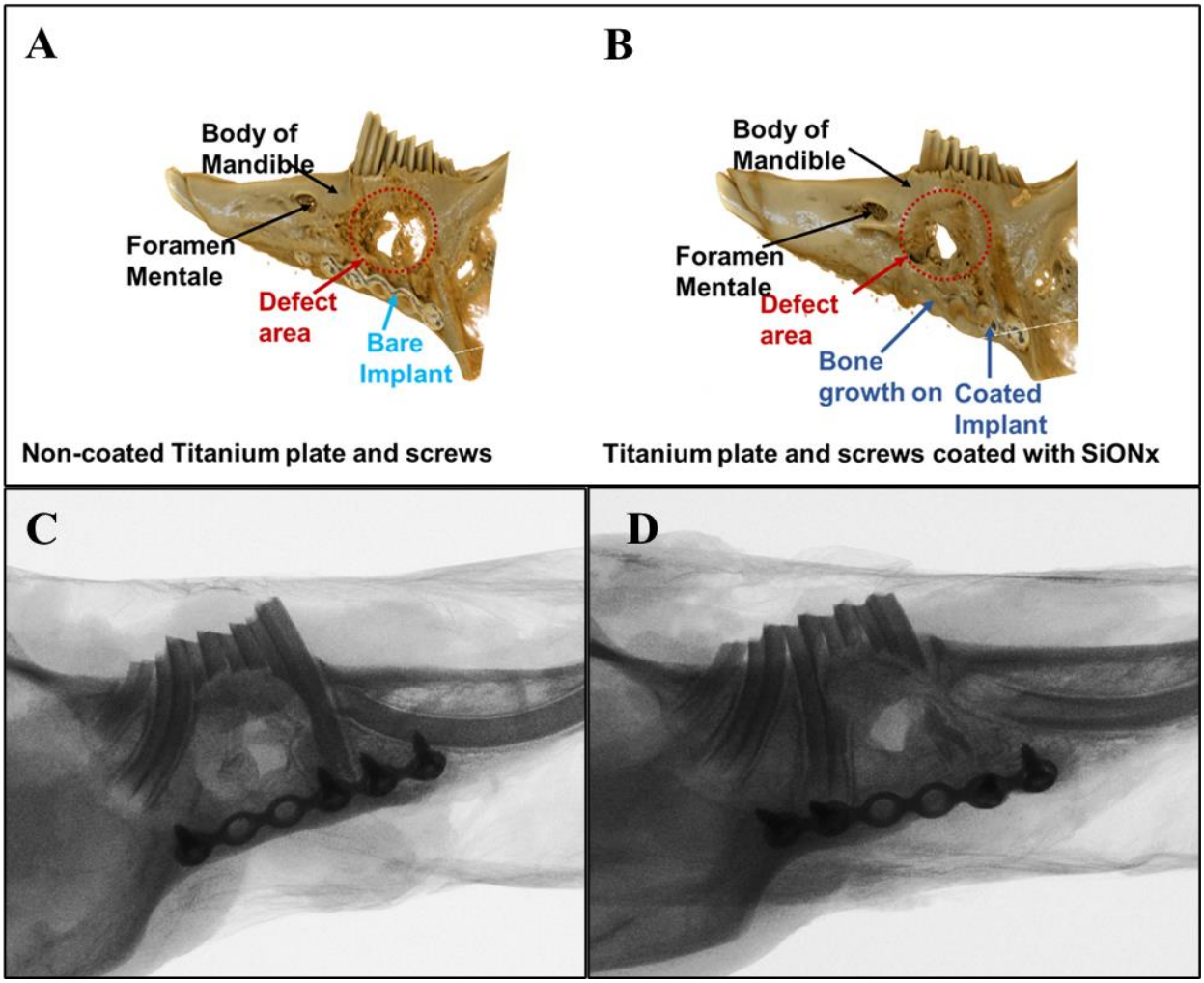

Figure 5.12: Micro-CT and X-ray imaging of the healing rabbit mandibular defects revealed rapid bone regeneration for SiONx-coated implants as compared to uncoated implants after 8 weeks. A) Micro-CT of bare implant that show uncovered implant with large area of the defect still exist. B) Micro-CT of bone growth on surface of the coated implant with higher bone regeneration, the defect is almost closed, and very small area is existing. X-ray images of the rabbit mandible after 8 weeks of surgery with non-coated (C) and coated implants (D) confirming the formation of dense regenerated bone on the coated implant compared to less dense formed bone near the bare implant as can be seen from

The micro-CT images of SiONx-coated implants confirmed the grwoth of newly formed bone on the surface of the implants indicated implant-bone bonding and enhanced osseointegration. The defect was almost closed with the coated implants which showed less than 30% defect size compared to more than 40% on uncoated implant after 8 weeks. The quality of regenerated bone was enhanced on the coated

implant as confirmed from the X-ray images, while regnerated bone near the uncoated implants had a poor quality with low density bone as confirmed from X-ray (Figure 5.12).

The chemical structure of the regenerated bones was further studied using the XANES analysis. Figure 5.13 show the Ca L edge XANES spectra some standard model compounds and the spectra of the bones. All studied bones indicated the presence of two main spin-orbital related peaks a2 and b2 which appeared at 350.5 and 353.8 eV, respectively. The pre-edge peaks a1 and b1 were located at 349.2 eV and 352.5 eV, respectively, which exactly match the standard model compounds. The surrounding and newely formed bone on the coated implants is simillar to the standard

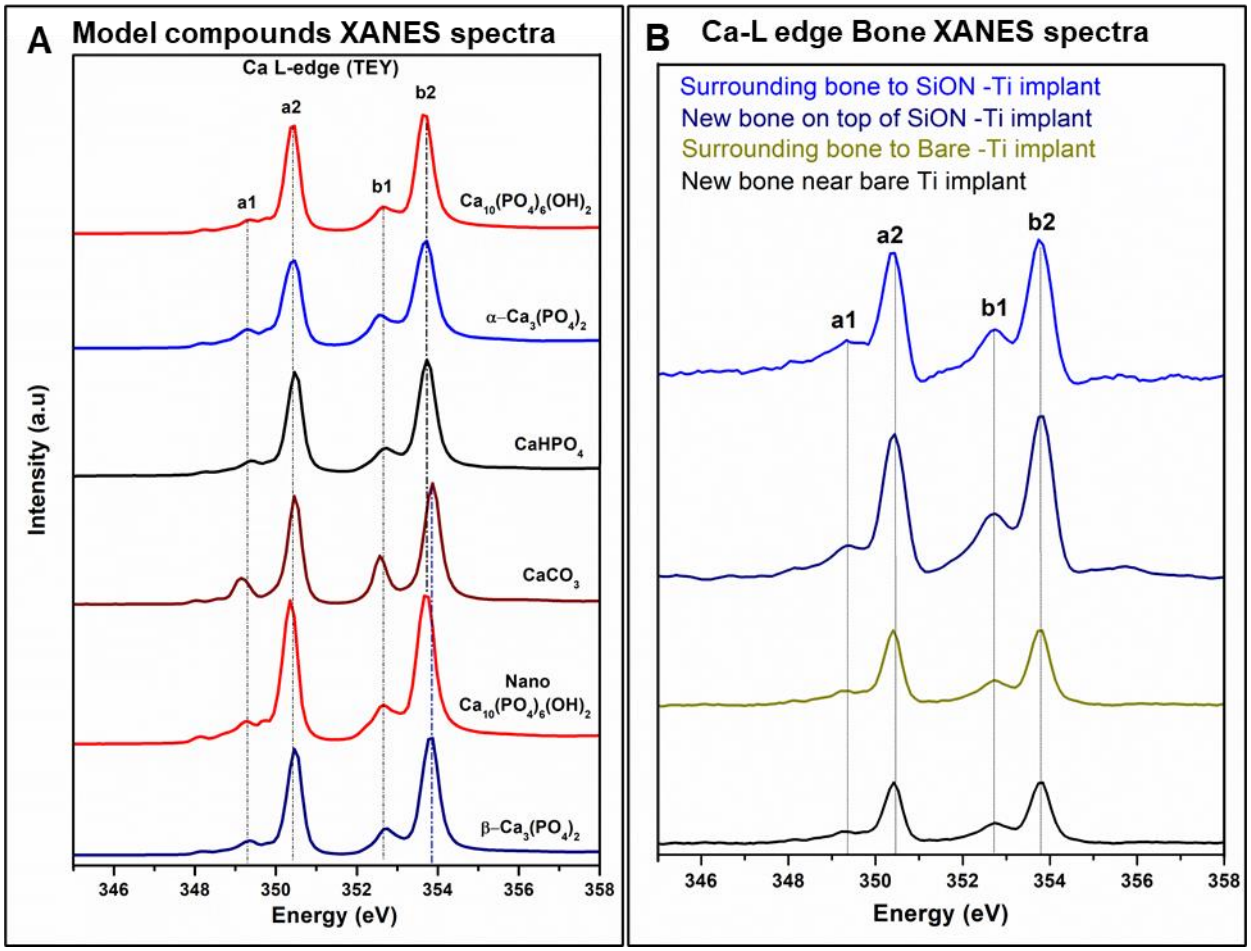

Figure 5.13: Ca L edge TEY XANES spectra of model compounds (A) and extracted mandibular bones after 8 weeks of surgery.

nano-hydroxyapatite (Nano-HA) spectra as shwon from the b1 peak and the broadening in the spectra. On the other hand, bone surrounding the uncoated Ti implants revealed low intensity with $CaHPO_4$-simillar spectra as can seen from the low intensity pre-edge peak a1. The P L edge spectra was also collected for the studied bones compared to standard model compounds as shown in Figure 5.14. The P L edge spectra revealed that all bones have β-tri calcium phosphate (β-TCP)-like structure that is confirmed from the third pre-edge peak appeared at 136.6 eV. This third pre-edge peak is a unique feature for the β-TCP and can be used to distinguish it from other bones. Also, the new formed and surrounding bones to the uncoated Ti implants presented intensity drop in

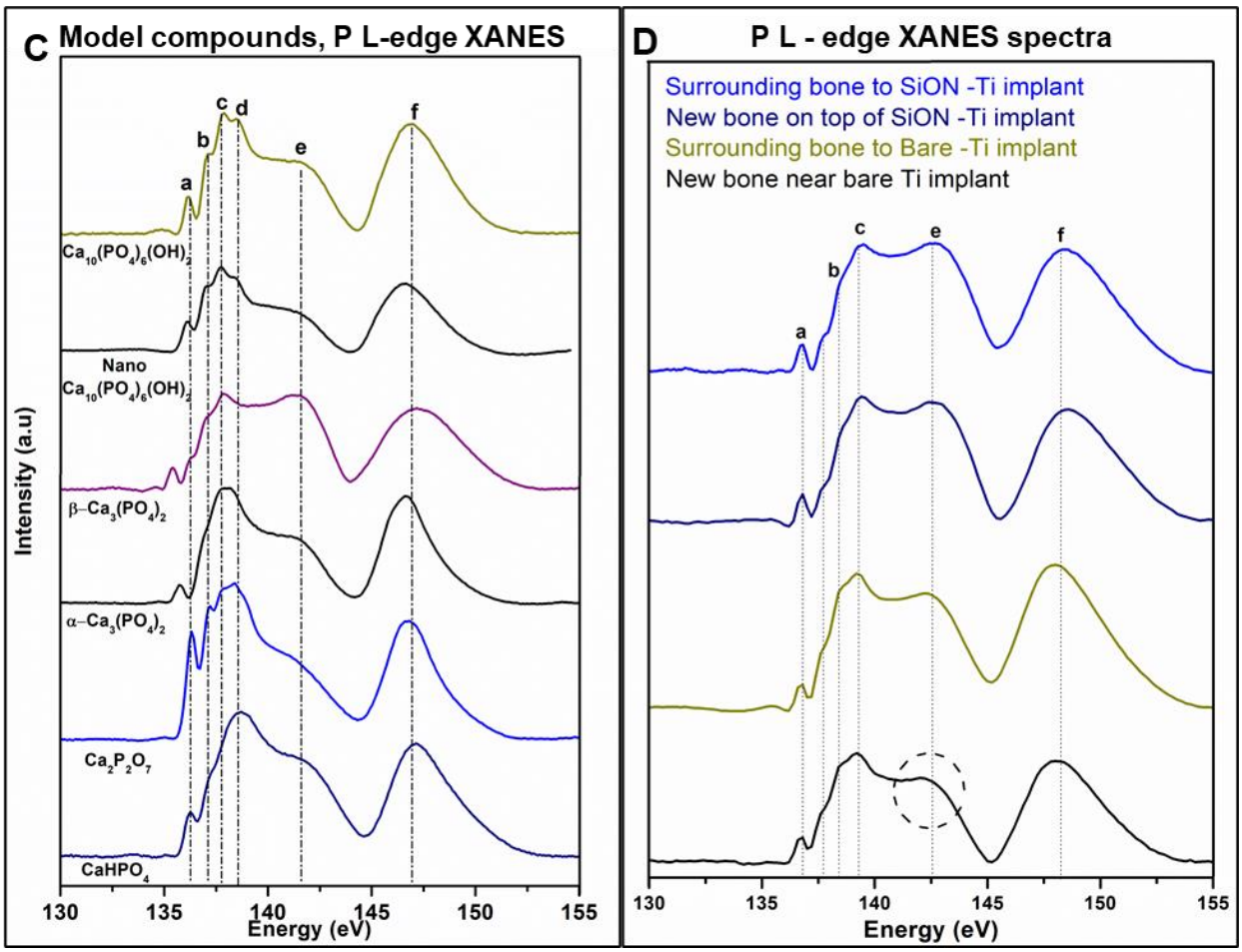

Figure 5.14: P L edge FY XANES spectra of model compounds (A) and extracted mandibular bones after 8 weeks of surgery.

the post edge shoulder appeared between 139.0 to 142.0 eV that indicating presence of more soluble phosphate in these bones. The P L edge spectra suggests that the chemical structure of regenerated and surrounding bone to uncoated implants is closer to the $CaHPO_4$ with presence of soluble phosphate. While the regenerated and surrounding bone to SiONx coated implant appeared to be closer to the β-TCP structure. Combining the Ca L edge and P L edge XANES spectra concluded that regenerated bone on uncoated implant have more soluble phosphate while regenerated bone on and near coated implants have HA and β-TCP structure. Furthermore, line scan and X-ray fluorescence mapping of Ca L edge was performed on the bone and coated implant as shown in Figure 5.15. Line scan allows to collect XANES spectra in a straight line for preset points. Here, 80 points were scanned to detect the changes in Ca L-edge in a line. Scan started from surrounding bone (before defect), crossed the regenerated bone, then the defect area, reaching the other side of the defect with regenerated bone again and stop at the surrounding bone after the defect. Line scan indicated no Ca exist in the defect area, low Ca spectra intensity in the new regenerated bone area, gradual increase in the Ca spectra intensity as passing from the regenerated bone towards the surrounding bone area. Furthermore, X-ray mapping for the bone and coated implant before and after the Ca L edge indicated the higher density and distribution of Ca in the regenerated bone even on the top of the coated implant confirming the bone growth on the coated implant. These results combined with the micro-CT and X-ray imaging confirmed the enhanced bone quality and osseointegration on the SiONx coated implants. As indicated by higher healing rate (small defect size left compared to larger defect size on uncoated implant, micro-CT) and enhanced bone

quality (no soluble phosphate, XANES), it can be concluded that SiONx coated Ti implants provide a faster bone healing and enhanced osseointegration.

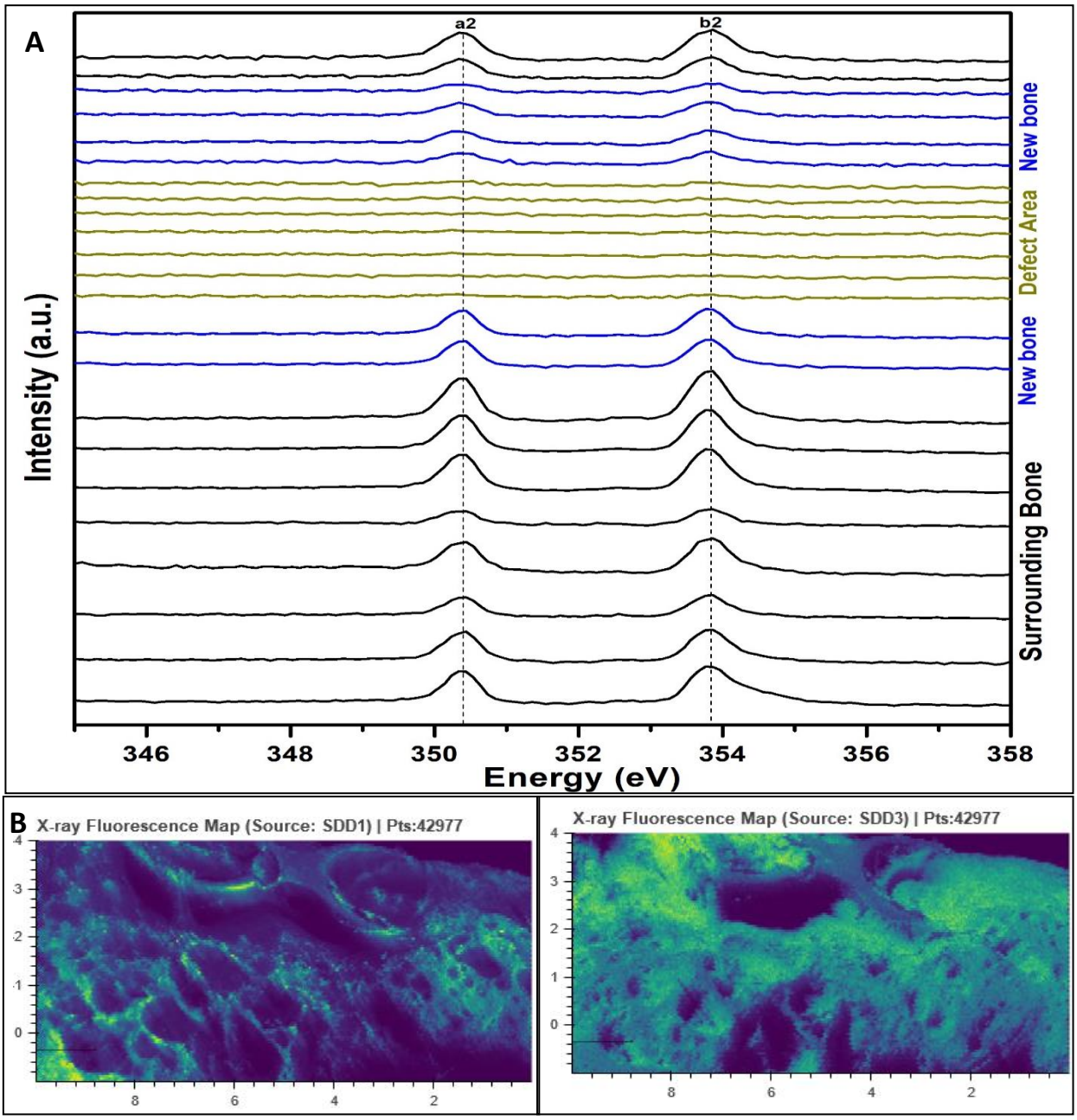

Figure 5.15: Line scan Ca L-edge XANES spectra of the regenerated bone surrounding the coated implant and the defect. From Top, spectra show the presence of the Ca in the surrounding bone (black), developed Ca in newly formed bone (blue), no Ca in the defect area (red), Ca in newly bone past defect area (blue), and Ca in surrounding bone after the defect area (black). X-ray Fluorescence mapping of the extracted rabbit bone on the coated implant before (B) and after (C) Ca L edge shows no Ca distribution before the edge, while presence of Ca (green color) after the edge energy.

The mechanical properties of the regenerated bone were evaluated by nano-indentation measurements. Figure 5.16 shows the load displacement curve of newly formed bone on top of SiONx-Ti coated implant, surrounding bone to coated implant, and surrounding bone to uncoated implant. Reduced elasticity modulus (Er) and hardness (H) were calculated from the nano-indentation data according to the Oliver-Pharr method [23,24]. The newly formed bone on coated implant found to have Er = 17.7 ± 1.6 GPa and H = 689 ± 99 MPa, while the surrounding bone to the SiONx coated Ti have Er = 24.1 ± 2.7 GPa and H=929±169 MPa, and surrounding bone to uncoated Ti presented Er = 22.6 ± 2.7 GPa and H = 918 ± 177 MPa.

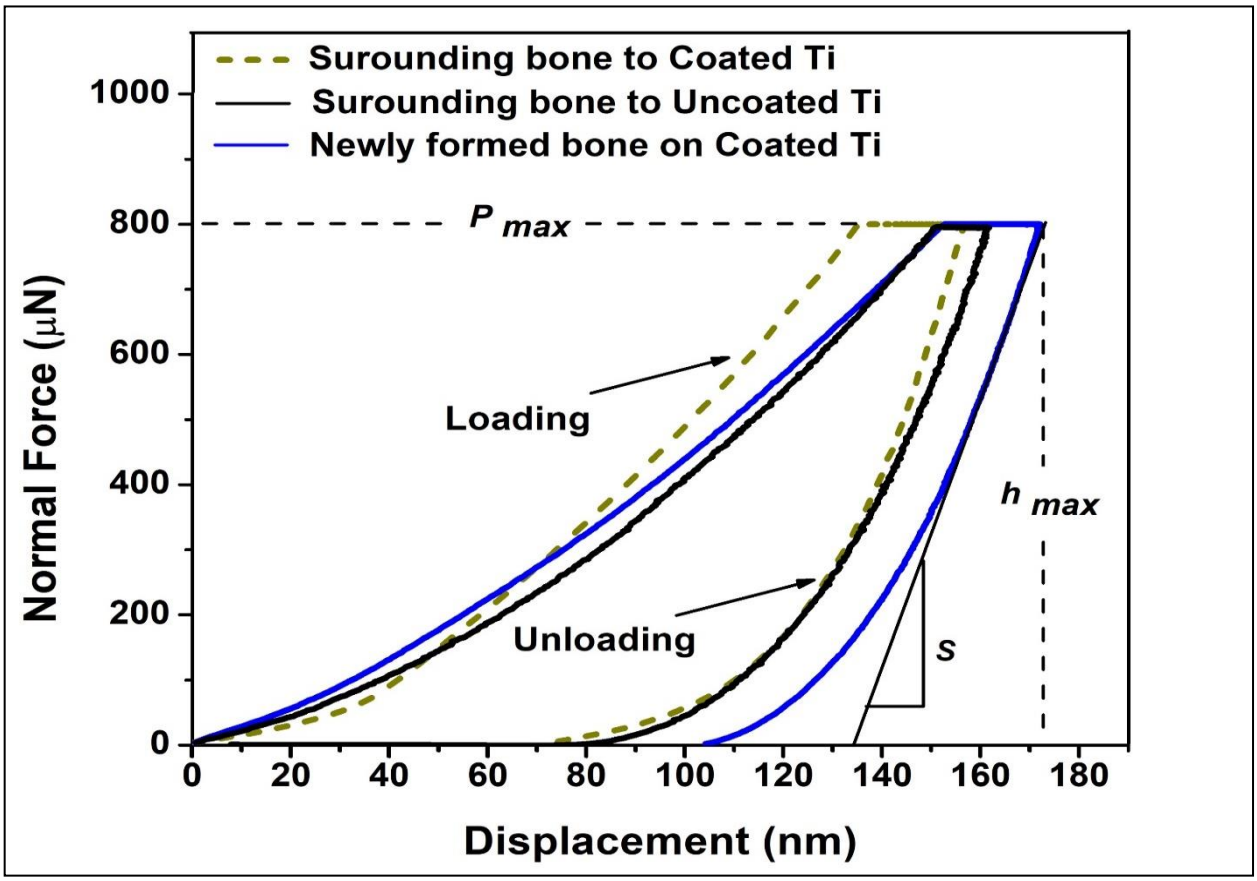

Figure 5.16: Load displacement curve comparing newly formed bone on Ti-implant (Er=17.7±1.6 GPa and H=689±99 MPa) to surrounding bone to coated Ti (Er=24.1±2.7 GPa and H=929±169 MPa) and uncoated Ti (Er=22.6±2.7 GPa and H=918±177 MPa). Er: Reduced Elasticity modulus and H:

It can be noticed that the surrounding bone near the uncoated implant have a lower elasticity modulus compared to the bone near the coated implants. Also, the newly formed bone on the top of coated implants presented a reduced elastic modulus lower than the normal surrounding bone which could be accepted for new bone formation. Due to the literature lack of mechanical properties measurment (Er and H) of rabbit mandubilar bone, we have compared our reported results to tibia and cortical rabbit bone measurments that previously published [50,51]. Soares et al., 2014, measured the Er of bone surrounding to long-dental implant insetrted in rabbit tibia diaphysis and reported that the elasticity modulus at the bone-implant interface was Er = 17 ± 2.5 GPa [50]. Also, Isaksson et al., in 2010 reported that the reduced elasticity modulus varies between 24 to 35 GPa and the hardness range between 950 to 1200 MPa in rabbit cortical bone depending on the age of the animal [51]. The Er and H results reported in this study are close to the previously reported data as mentioned above. The reduction in bone elastic modulus and hardness, after implantation, has been correlated to poor integration of the dental implants with surrounding bones [52,53]. Thus, in our study, the reduction of the Er and H values of the surrounding bone to the uncoated implant compared to the surrounding bone to SiONx coated implants could be attributed to the poor bone-implant integration between uncoated implant and surrounding bone. Also, it is known that elastic modulus and hardness of the bone is greatly affected by collagen fibers and hydroxyapatite crystals composite in the bone [54,55]. Thus, the differences in elastic modulus between bones have been speculated to the turnover of bone, i.e., the maturity of the individual osteons [54,56]. In this regard, the reduced elastic modulus of the

newly formed bone in our study can be correlated to the maturity degree of these new bones.

4. CONCLUSIONS

The present study tested the new surface coatings developed by plasma enhanced chemical vapor deposition (PECVD) technique as potential surface coatings for Ti implants. Amorphous SiONx thin film coatings were deposited on silicon wafer and medical grade Ti dental implants and tested *in-vitro* and *in-vivo*. *In-vitro* studied using mesenchymal stem cells revealed that these coatings are biocompatible with no cytotoxic effect and enhanced osteogenesis as confirmed from the elevated alkaline phosphatase activity. Furthermore, antibacterial studies using MRSA bacteria were performed to study the bacterial growth on these coating compared to the commercially pure anodized Ti implants. Antibacterial studies indicated that these coatings have a bacteriostatic effect as indicated by the significant decrease in the number of bacterial on those coatings. SiONx with refractive index n=1.82 and 2.0 presented better results compared to other SiONx coatings. 1000 nm layer of SiONx (n=1.82) was deposited on the anodized Ti dental implants and implanted in critical size defect in rabbit mandibular model. *In-vivo* date indicated faster bone healing with better osseointegration on the coated implants compared to the uncoated Ti. The SiONx coated implants supported bone regeneration and bone growth on the implant surface as confirmed from micro-CT imaging. X-ray imaging and XANES analysis indicated good bone quality with normal mechanical properties on regenerated and surrounding bone near the coated implant. On the other hand, uncoated implants showed slow bone healing with low bone quality as confirmed by soluble phosphate revealed by XANES and less-dense bone as seen

by X-ray, and larger defect size after 8 weeks as seen by micro-CT. The pronounced effect of SiONx coating was attributed to the antioxidant activity of these coating that mitigate the toxic oxidative stress and significantly elevate the osteogenic activity as confirmed from SOD1, 4HNE, and ALP activity in the blood serum studies at 1, 2, 4, and 8 weeks. This study conclude that amorphous SiONx coating deposited by PECVD technique are promising surface modification for Ti implants for rapid bone healing and enhanced bone quality.

Acknowledgements: The authors would like to thank the Varanasi's laboratory members Sara Peper, and Thy Vo at the Bone-Muscle Research Center and Mr. Weike Chen, Chemistry and Biochemistry department, for their assistance towards this manuscript. The authors want to acknowledge Ms. Ayat Omar, Ms. Laureen Abbo Nono, and Ms. Shambhavvi Anand, summer intern students at the Varanasi's laboratory, for their assist during this study. The authors would like to thank Dr. Jiechao Jiang and Mr. David Yan at the Characterization Center for Materials and Biology (CCMB) and engineer Dennis Bueno at the center for Nanotechnology at the University of Texas at Arlington (UTA) for their help during the materials preparation and characterization. The authors want to thank Dr. Tobias Wolfram and Zeke Raiser from KLS Martin for their help and support for this study.

Funding: The authors want to thank the National Institutes of Health (NIH), the Osteo Science Foundation, the University of Texas at Arlington (UTA), and the UTA College of Nursing & Health Innovation Bone-Muscle Research Center (UTA-CONHI-BMRC) for their generous support for this study. The following NIH Grants supported KA and VV: (Grant Number 1R03DE023872-01, 1R56DE027964-01A1-01, NIH S10OD025230).

Also, we thank the UTA-CONHI for their generous support for the first author KA via the CRS Pilot Grant.

REFERENCES

1. Spriano, S., Yamaguchi, S., Baino, F. & Ferraris, S. A critical review of multifunctional titanium surfaces: New frontiers for improving osseointegration and host response, avoiding bacteria contamination. *Acta Biomater.* **79**, 1–22 (2018).
2. Souza, J. G. S. *et al.* Targeting implant-associated infections: titanium surface loaded with antimicrobial. *iScience* **24**, 102008 (2021).
3. Metsemakers, W. J. *et al.* Titanium and steel fracture fixation plates with different surface topographies: Influence on infection rate in a rabbit fracture model. *Injury* **47**, 633–639 (2016).
4. Lindahl, C., Engqvist, H. & Xia, W. Influence of Surface Treatments on the Bioactivity of Ti. *ISRN Biomater.* **2013**, 205601 (2013).
5. Kokubo, T. & Takadama, H. How useful is SBF in predicting in vivo bone bioactivity? *Biomaterials* **27**, 2907–2915 (2006).
6. Sasikumar, Y., Indira, K. & Rajendran, N. Surface Modification Methods for Titanium and Its Alloys and Their Corrosion Behavior in Biological Environment: A Review. *J. Bio- Tribo-Corrosion* **5**, 36 (2019).
7. Schmidt, A. H. & Swiontkowski, M. F. Pathophysiology of Infections After Internal Fixation of Fractures. *JAAOS - J. Am. Acad. Orthop. Surg.* **8**, (2000).
8. Mombelli, A. & Décaillet, F. The characteristics of biofilms in peri-implant disease. *J. Clin. Periodontol.* **38 Suppl 1**, 203–213 (2011).
9. Arciola, C. R., Campoccia, D. & Montanaro, L. Implant infections: adhesion,

biofilm formation and immune evasion. *Nat. Rev. Microbiol.* **16**, 397–409 (2018).

10. Marsh, P. D., Moter, A. & Devine, D. A. Dental plaque biofilms: communities, conflict and control. *Periodontol. 2000* **55**, 16–35 (2011).
11. Flemming, H.-C. & Wingender, J. The biofilm matrix. *Nat. Rev. Microbiol.* **8**, 623–633 (2010).
12. Song, F., Koo, H. & Ren, D. Effects of Material Properties on Bacterial Adhesion and Biofilm Formation. *J. Dent. Res.* **94**, 1027–1034 (2015).
13. Li, D. *et al.* Biomechanical comparison of the sandblasted and acid-etched and the machined and acid-etched titanium surface for dental implants. *J. Biomed. Mater. Res.* **60**, 325–332 (2002).
14. Müller, P., Attin, T. & Herudk, M. W. Polyspecies biofilm formation on implant surfaces with different surface characteristics. *J. Appl. Oral Sci.* **21**, 48–55 (2013).
15. Ferraris, S. & Spriano, S. Antibacterial titanium surfaces for medical implants. *Mater. Sci. Eng. C* **61**, 965–978 (2016).
16. Chang, Y.-Y., Zhang, J.-H. & Huang, H.-L. Effects of Laser Texture Oxidation and High-Temperature Annealing of TiV Alloy Thin Films on Mechanical and Antibacterial Properties and Cytotoxicity. *Materials* vol. 11 (2018).
17. Matos, A. O. *et al.* Three-species biofilm model onto plasma-treated titanium implant surface. *Colloids Surfaces B Biointerfaces* **152**, 354–366 (2017).
18. Ilyas, A. *et al.* Amorphous Silica: A New Antioxidant Role for Rapid Critical-Sized Bone Defect Healing. *Adv. Healthc. Mater.* **5**, 2199–2213 (2016).
19. Ilyas, A. *et al.* Rapid Regeneration of Vascularized Bone by Nanofabricated Amorphous Silicon Oxynitrophosphide (SiONP) Overlays. *J. Biomed.*

Nanotechnol. **15**, 1241–1255 (2019).

20. Ilyas, A., Lavrik, N. V, Kim, H. K. W., Aswath, P. B. & Varanasi, V. G. Enhanced Interfacial Adhesion and Osteogenesis for Rapid “Bone-like” Biomineralization by PECVD-Based Silicon Oxynitride Overlays. *ACS Appl. Mater. Interfaces* **7**, 15368–15379 (2015).
21. Awad, K. *et al.* Ionic Silicon Protects Oxidative Damage and Promotes Skeletal Muscle Cell Regeneration. *International Journal of Molecular Sciences* vol. 22 (2021).
22. Young, S. *et al.* Development and characterization of a rabbit alveolar bone nonhealing defect model. *J. Biomed. Mater. Res. Part A* **86A**, 182–194 (2008).
23. Oliver, W. C. & Pharr, G. M. An improved technique for determining hardness and elastic modulus using load and displacement sensing indentation experiments. *J. Mater. Res.* **7**, 1564–1583 (1992).
24. Aruwajoye, O. O. *et al.* Microcrack density and nanomechanical properties in the subchondral region of the immature piglet femoral head following ischemic osteonecrosis. *Bone* **52**, 632–639 (2013).
25. Varanasi, V. G. *et al.* Role of Hydrogen and Nitrogen on the Surface Chemical Structure of Bioactive Amorphous Silicon Oxynitride Films. *J. Phys. Chem. B* **121**, 8991–9005 (2017).
26. Shi, Y. *et al.* Mesenchymal stem cells: a new strategy for immunosuppression and tissue repair. *Cell Res.* **20**, 510–518 (2010).
27. Prockop, D. J. Marrow Stromal Cells as Stem Cells for Nonhematopoietic Tissues. *Science (80-.).* **276**, 71 LP – 74 (1997).

28. Haynesworth, S. E., Goshima, J., Goldberg, V. M. & Caplan, A. I. Characterization of cells with osteogenic potential from human marrow. *Bone* **13**, 81–88 (1992).

29. Altman, G. H. *et al.* Cell differentiation by mechanical stress. *FASEB J.* **16**, 1–13 (2002).

30. Beresford, J. N., Bennett, J. H., Devlin, C. & Owen, M. E. Evidence for an inverse relationship between the differentiation of adipocytic and osteogenic cells. *Bone Miner.* **17**, 198 (1992).

31. Wakitani, S. *et al.* Mesenchymal cell-based repair of large, full-thickness defects of articular cartilage. *JBJS* **76**, (1994).

32. Johnstone, B., Hering, T. M., Caplan, A. I., Goldberg, V. M. & Yoo, J. U. In VitroChondrogenesis of Bone Marrow-Derived Mesenchymal Progenitor Cells. *Exp. Cell Res.* **238**, 265–272 (1998).

33. Wakitani, S., Saito, T. & Caplan, A. I. Myogenic cells derived from rat bone marrow mesenchymal stem cells exposed to 5-azacytidine. *Muscle Nerve* **18**, 1417–1426 (1995).

34. Kundu, K., Katti, D. R. & Katti, K. S. Tissue-Engineered Interlocking Scaffold Blocks for the Regeneration of Bone. *JOM* **72**, 1443–1457 (2020).

35. Petite, H. *et al.* Tissue-engineered bone regeneration. *Nat. Biotechnol.* **18**, 959–963 (2000).

36. Kon, E. *et al.* Autologous bone marrow stromal cells loaded onto porous hydroxyapatite ceramic accelerate bone repair in critical-size defects of sheep long bones. *J. Biomed. Mater. Res.* **49**, 328–337 (2000).

37. Yamaguchi, M., Shimizu, N., Shibata, Y. & Abiko, Y. Effects of Different

Magnitudes of Tension-force on Alkaline Phosphatase Activity in Periodontal Ligament Cells. *J. Dent. Res.* **75**, 889–894 (1996).

38. Westhauser, F. *et al.* Osteogenic differentiation of mesenchymal stem cells is enhanced in a 45S5-supplemented β-TCP composite scaffold: an in-vitro comparison of Vitoss and Vitoss BA. *PLoS One* **14**, e0212799 (2019).
39. Jo, S. *et al.* Regulation of osteoblasts by alkaline phosphatase in ankylosing spondylitis. *Int. J. Rheum. Dis.* **22**, 252–261 (2019).
40. Neddermann, K. & Nausch, M. Effects of organic and inorganic nitrogen compounds on the activity of bacterial alkaline phosphatase. *Aquat. Ecol.* **38**, 475–484 (2004).
41. Nausch, M. Experimental evidence for interactions between bacterial peptidase and alkaline phosphatase activity in the Baltic Sea. *Aquat. Ecol.* **34**, 331–343 (2000).
42. Turner, N. A. *et al.* Methicillin-resistant Staphylococcus aureus: an overview of basic and clinical research. *Nat. Rev. Microbiol.* **17**, 203–218 (2019).
43. Park, B. & Liu, G. Y. Immune-Based Anti-Staphylococcal Therapeutic Approaches. *Microorganisms* vol. 9 (2021).
44. Fubini, B., Bolis, V., Giamello, E. & Volante, M. Chemical Functionalities at the Broken Fibre Surface Relatable to Free Radicals Production. in *Mechanisms in Fibre Carcinogenesis* 415–432 (Springer US, 1991). doi:10.1007/978-1-4684-1363-2_35.
45. Pezzotti, G. *et al.* Silicon Nitride Bioceramics Induce Chemically Driven Lysis in Porphyromonas gingivalis. *Langmuir* **32**, 3024–3035 (2016).

46. do Monte, F. A. *et al.* Silicon Oxynitrophosphide Nanoscale-Coating Enhances Antioxidant Marker -Induced Angiogenesis During In Vivo Cranial Bone Defect Healing. *JBMR Plus* **n/a**, e10425 (2020).

47. Brazier, M. W., Wedd, A. G. & Collins, S. J. Antioxidant and Metal Chelation-Based Therapies in the Treatment of Prion Disease. *Antioxidants (Basel, Switzerland)* **3**, 288–308 (2014).

48. Kurutas, E. B. The importance of antioxidants which play the role in cellular response against oxidative/nitrosative stress: current state. *Nutr. J.* **15**, 71 (2016).

49. Mouthuy, P. A. *et al.* Biocompatibility of implantable materials: An oxidative stress viewpoint. *Biomaterials* vol. 109 55–68 (2016).

50. Soares, P. B. F. *et al.* Measurement of elastic modulus and Vickers hardness of surround bone implant using dynamic microindentation--parameters definition. *Braz. Dent. J.* **25**, 385–390 (2014).

51. Isaksson, H., Malkiewicz, M., Nowak, R., Helminen, H. J. & Jurvelin, J. S. Rabbit cortical bone tissue increases its elastic stiffness but becomes less viscoelastic with age. *Bone* **47**, 1030–1038 (2010).

52. Baker, M. I., Eberhardt, A. W., Martin, D. M., McGwin, G. & Lemons, J. E. Bone properties surrounding hydroxyapatite-coated custom osseous integrated dental implants. *J. Biomed. Mater. Res. Part B Appl. Biomater.* **95B**, 218–224 (2010).

53. Seong, W.-J., Grami, S., Jeong, S. C., Conrad, H. J. & Hodges, J. S. Comparison of push-in versus pull-out tests on bone-implant interfaces of rabbit tibia dental implant healing model. *Clin. Implant Dent. Relat. Res.* **15**, 460–469 (2013).

54. Rho, J.-Y., Kuhn-Spearing, L. & Zioupos, P. Mechanical properties and the

hierarchical structure of bone. *Med. Eng. Phys.* **20**, 92–102 (1998).

55. Leng, H., Reyes, M. J., Dong, X. N. & Wang, X. Effect of age on mechanical properties of the collagen phase in different orientations of human cortical bone. *Bone* **55**, 288–291 (2013).

56. Balooch, M., Habelitz, S., Kinney, J. H., Marshall, S. J. & Marshall, G. W. Mechanical properties of mineralized collagen fibrils as influenced by demineralization. *J. Struct. Biol.* **162**, 404–410 (2008).

CHAPTER 6: IONIC SILICON PROTECTS OXIDATIVE DAMAGE AND PROMOTES SKELETAL MUSCLE CELL REGENERATION

Kamal Awad[1, 2], Neelam Ahuja[2], Matthew Fiedler[2], Sara Peper[2, 3], Zhiying Wang[2], Pranesh Aswath[1], Marco Brotto[2], * and Venu Varanasi[1, 2, *]

1 Department of Materials Science and Engineering, College of Engineering, University of Texas at Arlington, Texas 76019, USA

2 Bone-Muscle Research Center, College of Nursing & Health Innovation, University of Texas at Arlington, Texas 76019, USA

3 Department of Bioengineering, College of Engineering, University of Texas at Arlington, Texas 76019, USA

*Corresponding Authors,

Dr. Marco Brotto, (marco.brotto@uta.edu) and

Dr. Venu Varanasi, (Venu.varanasi@uta.edu)

Phone: 817-272-1743

Associate Professor, Bone Muscle Research Center

College of Nursing and Health Innovation

University of Texas at Arlington

Address: 655 W. Mitchell St.,

Box 19410, Arlington,

TX 76019

ABSTRACT

Volumetric muscle loss injuries overwhelm the endogenous regenerative capacity of skeletal muscle, and the associated oxidative damage can delay regeneration and prolong recovery. This study aimed to investigate the effect of silicon-ions on C2C12 skeletal muscle cells under normal and excessive oxidative stress conditions to gain insights into its role on myogenesis during the early stages of muscle regeneration. In vitro studies indicated that 0.1 mM Si-ions into cell culture media significantly increased cell viability, proliferation, migration, and myotube formation compared to control. Also, MyoG, MyoD, Neurturin, and GABA expression were significantly increased with addition of 0.1, 0.5, and 1.0 mM of Si-ion for 1 and 5 days of C2C12 myoblast differentiation. Furthermore, 0.1-2.0 mM Si-ions attenuated the toxic effects of H2O2 within 24 hours resulting in increased cell viability and differentiation. Addition of 1.0 mM of Si-ions significantly aid cell recovery and protected from the toxic effect of 0.4 mM H2O2 on cell migration. These results suggest that ionic silicon may have a potential effect in unfavorable situations where reactive oxygen species is predominant affecting cell viability, proliferation, migration, and differentiation. Furthermore, this study provides a guide for designing Si-containing biomaterials with desirable Si-ion release for skeletal muscle regeneration.

Keywords: Muscle Injury; Reactive Oxygen Species; Antioxidant; Silicon; Biomaterials; Volumetric Muscle Loss; Tissue Regeneration.

1. INTRODUCTION

Skeletal muscle constitutes about 40-50% of total body mass and is responsible for movement of the human body [1]. Although skeletal muscle has remarkable endogenous regenerative capacity, severe traumatic tissue loss greater than 20% of specific muscle mass, will overwhelm this capacity [2,3] that is known as volumetric muscle loss (VML). The limitations of skeletal muscle to self-repair following severe injuries and the failure to regenerate healthy and functional muscle tissue has opened the door to the investigation of novel alternative approaches for skeletal muscle regeneration. Thus, many tissue engineering approaches have been investigated for VML repair such as autologous minced muscle grafts [4–7], decellularized extracellular matrix materials (ECM) [8,9], ECMs supplemented with stem or progenitor cells [10,11], and recently inhibition of fibrotic pathways [12]. Furthermore, bioactive scaffolds and cell laden biomaterials [13–15] have been proposed to stimulate functional muscle regeneration. These strategies aim to deliver the native ECM with the required cell types (stem or progenitor cells) and growth factors to the injury site, a key step in the regenerative process [16,17]. This process is initiated by the activation of satellite cells, or mononucleated muscle precursor cells, that undergo several proliferative cycles to finally differentiate to form multinucleated myotubes [18–20]. Various myogenic transcription factors are expressed within hours of satellite cell activation and regulate the myogenic differentiation process. These factors include myogenic determination protein (MyoD), myogenin (MyoG), and myogenic factor-5 (Myf-5) for cell cycle regulation, and muscle regulatory factor-4 (MRF4) for terminal differentiation. MyoD is a vital gene for myoblast progression and regulation during differentiation to form skeletal

muscles [20,21]. Further, there is evidence that increased MyoD acts as a regulator for oxidative metabolism and skeletal muscle biogenesis [21]. The expression of the myogenic marker MyoG is an early indicator of myoblast commitment and differentiation [18,22]. Myokines are molecules released by skeletal muscle and are thought to function as hormone like-molecules, exerting endocrine and paracrine effects on other associated organs and muscle metabolic signaling pathways [23]. Three important myokines include; Neurturin (NRTN) which is a PGC-1α-controlled myokine involved in motor nerve recruitment and neuromuscular junction remodeling, Ɣ-aminobutyric acid (GABA) which is the chief inhibitory neurotransmitter in the central nervous system and very important for muscle tonus, and β-aminoisobutyric acid BAIBA, a muscle-derived osteocyte survival factor also implicated in the reduction of insulin resistance and skeletal muscle inflammation [24,25]. NRTN acts via retrograde signaling from muscle to motor neurons, reducing muscle-mass loss, and maintains muscle fiber volume [26]. PGC-1α proteins also have important roles in the biology of skeletal muscle [26]. BAIBA is a known myokine that can protect osteocytes from toxic reactive oxygen species (ROS) and prevent both bone and muscle loss in vivo due to unloading [25]. These myokines are thought to be released following activation of the PGC-1a receptor due to stressors, nutrient scarcity, degeneration due to age, injury, and disease and act via retrograde signaling [23,24].

ROS levels at the site of muscle injury critically effects the muscle regeneration process [27–29]. At low to moderate levels, ROS stimulates several signaling pathways that significantly impact cell cycle, cell migration, survival, apoptosis, and differentiation for tissue healing and muscle repair [28,30]. However, high levels of ROS are often

associated with severe traumatic injury, aging, and inherited dystrophy of the skeletal muscles, causing oxidative damage to the skeletal muscle cells, inducing degeneration. This high level of ROS also obstructs the activation of satellite cells affecting natural tissue repair, and ultimately compromise the entire regenerative process [28,31]. Oxidative stress occurs when ROS levels exceed the endogenous cellular antioxidant capacity [32], and as such, exogenous antioxidants are needed to compensate for the excess ROS. Although, experimental evidence has shown that antioxidant supplementations have no effect on muscle function during and after exercise [33], dietary antioxidants have been demonstrated to improve antioxidant enzyme expression and subsequent muscle repair and function in muscle injuries [34,35]. Other investigations have explored administering low doses of antioxidants, leading to reduced oxidative stress, cell cycle and migration stimulation, and enhanced myogenesis [28,36].

Muscle regeneration is a multistep process that starts with the activation of satellite cells, followed by myoblast proliferation and migration, and finally myoblasts fusion and differentiation to produce multinucleated myotubes to replace damaged fibers [28,37]. An ideal muscle treatment or graft should enhance cell functionalities without any adverse effects – complementing endogenous processes rather than bypassing them. In recent years, many bioactive materials have been introduced for musculoskeletal tissue engineering including silicon (Si) and Si-based biomaterials [38,39]. Si-based biomaterials have been shown to promote osteoblast differentiation, extracellular matrix deposition, and bone regeneration [40–42]. Silicon carbide has been successfully used as an antithrombogenic coating on vascular stents [43]. Additionally, recent studies have indicated that bioactive silicon nitride, an FDA approved material for

spinal intervertebral arthrodesis devices, enhances osteogenic activity and promotes bone ongrowth and ingrowth [44,45]. More recently, bioactive amorphous silicon oxynitride and silicon oxynitrophosphide coatings have induced rapid regeneration of vascularized bone from the antioxidant activity of sustained release silicon-ions [42,46,47]. Furthermore, amorphous silicon oxynitrophosphide coatings enhanced the angiogenic activity of endothelial cells and ionic silicon improved endothelial cell survival under toxic ROS conditions via enhanced angiogenic marker expression and antioxidant activity [40,42,48]. Additionally, research conducted by Monte et al suggests that Si ions at a concentration of 0.5mM mitigate the toxic effects of ROS by catalyzing the conversion of superoxide to peroxide [21]. The addition of laponite nanosilicates to 3D printed hydrogels supported osteoblast function and enhanced mechanical strength [39,49]. Recent evidence indicates that C2C12 myoblasts cells cultured on a silicon substrate maintained normal biological activities [50]. Research has shown that silica nanoparticles have a beneficial effect on myoblast fusion in C2C12 skeletal muscle cells [18]. Additionally, our preliminary data indicates that micro-patterned silicon oxynitride enhanced adhesion, growth, and myotube and axon alignment of muscle and nerve cells, and that ionic silicon elutes from the material and into solution under physiologic conditions [51–53].

Yet, the effect of Si-ions on skeletal muscle cell activity, such as proliferation, migration, differentiation, and myogenic biomarker expression, has not been explored. Thus, the effect of ionic Si released from Si-based biomaterials needs to be understood in skeletal muscle cells for the optimization of cell-based therapies and tissue engineering applications. In this study, we aim to understand the effect of Si-ions on C2C12 skeletal muscle cells under normal (no added ROS) and toxic ROS conditions to

gain insight into its role on myogenesis during the early stages of muscle regeneration. First, C2C12 cell viability, proliferation, migration, and differentiation were studied following the addition of three different concentrations of Si-ions to cell culture medium to determine the optimal Si-ions dose for C2C12 cells. Second, we studied the effect of Si-ions on myogenic gene expression (i.e., MyoD and MyoG) and myokines (i.e., Neurturin, GABA, and BAIBA) expression. Third, we studied the effects of ROS on C2C12 cell viability by culturing cells in five different concentrations of H_2O_2 to determine the minimum H_2O_2 concentration that induces a significant oxidative damage. Then, four different concentrations of Si-ions were added to culture medium to study the effect of Si-ions on C2C12 cells under toxic oxidative stress condition (0.4 mM H_2O_2).

2. MATERIALS AND METHODS

2.1 Experimental Study Design

To study the effect of Si-ions on C2C12 skeletal muscles under normal and oxidative stress conditions, a series of 2D cell culture experiments were performed. To examine the effects of Si-ions on C2C12 cells under normal conditions, cells were cultured in normal media and in media containing Si-ions at concentrations of 0.1mM, 0.5mM, and 1.0mM. Si ions were obtained using sodium metasilicate powder (Na_2SiO_3) [48,54–56]. Cell viability and proliferation assays were performed on cells cultured in growth media with Si-ions while cell morphology studies were carried out in differentiation media with Si-ions. Cell differentiation media was collected periodically throughout differentiation for biomarker and gene expression analysis. Following cell differentiation, cells were fixed, immunohistochemically stained, and imaged under fluorescence to determine the optimal concentration of Si-ions for myogenic differentiation. Next, cell

viability and proliferation assays were conducted on C2C12s cultured in growth medium (GM) containing different concentrations of hydrogen peroxide to determine the concentration of hydrogen peroxide required to induce oxidative damage (significant cell death). The optimal concentration of Si-ions for mitigating toxic ROS activity was then determined by differentiating C2C12 cells in media containing 0.4mM hydrogen peroxide and Si-ions at concentrations of 0.1mM, 0.5mM, 1.0mM, and 2.0 mM and Si-ions free controls. Following optimization of Si-ions concentration, a final cell culture study was conducted to determine the effects of optimized Si-ions concentrations on cell viability, proliferation, morphology, healing rate, and gene and biomarker expression under the determined concentration of H_2O_2. The cell viability, proliferation, and morphology were determined in the same manner as described above. Media was collected periodically for biomarker and gene expression analysis using qPCR and ELISA. Finally, cell migration was evaluated using a scratch test [48,57] to determine effects on healing rate.

2.2 Materials

Sodium metasilicate powder (Na_2SiO_3, MW: 122.06g/mol, Sigma-Aldrich Co., St. Louis, MO, USA) and hydrogen peroxide (H_2O_2, 30% w/w, Sigma-Aldrich Co., St. Louis, MO, USA) were used as sources of Si-ions and ROS, respectively. Dulbecco's Modified Eagle's Medium ((DMEM-1X) with 4.5 g/L glucose, L-glutamine, and sodium pyruvate), phosphate-buffered saline (PBS-1X), penicillin-streptomycin (P/S) 10,000 U/mL each, and trypsin EDTA-1X solution were purchased from Mediatech Inc. (Manassas, VA, USA). Fetal bovine serum (FBS) and horse serum (HS) were obtained from Thermo Fischer Scientific Inc. (Waltham, MA, USA). C2C12 mouse myoblast skeletal muscle

cell lines were obtained from The American Type Culture Collection (ATCC) (Manassas, VA, USA) after authentication and testing for mycoplasma contamination. CellTiter 96® AQueous One Solution Cell Proliferation Assay (MTS) was obtained from Promega (Madison, WI, USA). Diamidino-2-phenylindole (DAPI), a blue, fluorescent nucleic acid stain, was purchased from Sigma-Aldrich Co., (St. Louis, MO, USA). Human Myosin Heavy Chain (MHC) fluorescein-conjugated antibody was purchased from R&D Systems, Inc. (McKinley Place, MN, USA). Invitrogen™ LIVE/DEAD™ Viability/Cytotoxicity Kit was purchased from Thermo Fischer Scientific Inc. (Waltham, MA, USA). Mouse Neurturin (NRTN) ELISA Kit (Catalog Number. CSB-EL016095MO) was purchased from Biomatik USA, LLC (Wilmington, DE, USA). S)-α-aminobutyric acid (L-AABA) and (R)-α-aminobutyric acid (D-AABA) were purchased from Thermo Fisher Scientific Inc. (Waltham, MA, USA). (S)-β-aminoisobutyric acid (L-BAIBA) and (R)-β-aminoisobutyric acid (D-BAIBA) were purchased from Adipogen Corp. (San Diego, CA, USA), and GABA was purchased from Sigma-Aldrich Co., (St. Louis, MO, USA). For quantitative real-time polymerase chain reaction (qRT-PCR): the RNeasy Mini Kit was obtained from Qiagen (Valencia, CA, USA), the reverse transcription system was obtained from Promega (Madison, WI, USA), and the PCR primers for the targeted genes, MyoD and MyoG, were obtained from Thermo Fischer Scientific Inc. (Waltham, MA, USA).

2.3 Preparation of Si-ions and Hydrogen Peroxide Solutions

Na_2SiO_3 was used as a source of Si-ions. To prepare 100 mM of Si, 610.3 mg of Na2SiO3 was dissolved in 50 mL of sterile DI water then filtered using a nylon syringe filter (33 mm, 0.2 μm,) followed by a serial dilution, the desired concentrations of Si

were obtained (0.1, 0.5, and 1.0 mM) in C2C12 myoblast cell growth media. Hydrogen peroxide is a form of ROS generated when the enzyme superoxide dismutase scavenges superoxide anions 58, thus H2O2 was used as a source of ROS and inducing oxidative damage. 100 mM-H2O2 solution was prepared in 10 mL sterile DI water, filtered, and serially diluted in sterile DI water until the desired concentrations of H2O2 (0.2, 0.4, 0.6, 0.8, and 1.0 mM) were reached in C2C12 cell growth media.

2.4 Cell Culture Studies

C2C12 myoblast is an immortal cell line that are easy to obtain and passage. Typically, C2C12 myoblasts differentiate rapidly under normal, Si-free, conditions, forming contractile myotubes and producing proteins with characteristics similar to endogenous muscle tissue. Using C2C12 myoblasts provides a more stable environment with fewer confounding variables than the normal physiologic environment of human primary cells [59]. Thus, C2C12 myoblasts were cultured using well-established and previously published protocols [60–62]. Briefly, C2C12 cells were cultured in growth medium (GM), GM consisting of DMEM/high glucose + 10% FBS + 100 U/mL P/S, in 75-cm2 Corning cell culture flasks with canted neck and vented caps under normal conditions (37°C, 5% CO2) maintaining cell density at 40-70% confluency. Cells in GM were maintained at 40-70% confluency, allowing them to proliferate but not to differentiate into myotubes. GM was changed every 48 hours. For differentiation studies, after reaching 75% confluency, C2C12 myoblast cells were cultured in differentiation medium (DM), DMEM/high glucose + 2% HS + 100 U/mL P/S, which was changed every 48 hours for 5-7 days until fully developed myotubes were formed.

2.5 Effects of Ionic Si-ions Concentrations on C2C12 Cells Functional Capacity

To study the effect of Si-ions on C2C12 myoblast viability and proliferation, 2.5 x10^4 cells/well were seeded in 24-well plates with 500 µL of GM and incubated as described above. Three different concentrations of Si-ions in GM were tested compared to the normal GM as control. Sample size of n=6 was used for each group; GM, GM + 0.1 mM Si, GM + 0.5 mM Si, and GM + 1.0 mM Si-ions. These different concentrations of Si-ions were added to the media during seeding, then cells were incubated for 6 and 24 hours for cell viability experiments and for 1, 2, and 3 days for cell proliferation studies. After each time point, MTS assays were performed (n=3 for each group) using the CellTiter 96 AQueous One Solution Cell Proliferation Assay kit according to the manufacturer's protocol. Briefly, MTS solution was prepared by adding 40 µL of CellTiter 96 reagent to 200 µL of GM for each sample to be tested. At each time point GM was removed from each sample and 240 µL of the MTS solution was added to each well of the 24-well plate. After 3 hours, 100 µL samples were collected from each well twice and transferred into two separate wells of a new 96 well-plate. The colorimetric absorbance was determined using a microplate reader (SpectraMax® i3, Molecular Devices, CA) at 490 nm. The remaining n=3 for each group each time point was used for the live/dead assay using Invitrogen LIVE/DEAD Viability/Cytotoxicity Kit according to the manufacturer's protocol. Briefly, 200 µL of live/dead solution was added to each well and incubated for 30 minutes. Fluorescent images were then taken using a DMi8 inverted Leica microscope (Leica Microsystems Inc., IL, USA), with green staining for live cells and red staining for dead cells. Three fluorescent images (20× field of view (FOV)) were taken for each well to compare the number of live and dead cells in

samples. The number of live and dead cells in fluorescent images were counted using ImageJ software (NIH).

To study the effect of Si-ion concentration on cell morphology and differentiation capacity, C2C12 cells were cultured for 4 and 7 days in DM containing 3 different concentrations of Si-ions compared to normal DM as control. For all differentiation experiments, 10x104 cells/well were seeded in 6-well plates in GM for 24 hours or until 75% confluency. After reaching 75% confluency, GM was removed, and each well was washed with 2 mL of PBS-1x to remove any unattached cells. Then, 2mL of DM was added to the first group as control and Si-ions at concentrations of 0.1, 0.5, and 1.0mM Si were added to DM for the other three groups (DM + 0.1 mM Si, DM + 0.5 mM Si, and DM + 1.0 mM Si). DM was collected for biomarker expression assays and new DM with the specified Si-ion concentration was added to each well every 48 hours. After each time point, cells were fixed and immunostained following previously published protocols 63,64. Briefly, DM was removed, and cells were washed 3 times with PBS-1x, then fixed with 2 mL of neutral buffered formalin for 7-8 minutes. Cells were washed again and permeabilized with 2 mL of 0.1% triton X-100 in PBS for 10 minutes. Then, cells were stained with 20 µl/mL of conjugated MHC antibody in 1X TBST (PBS with 0.1% Triton and 0.1% Tween) for 45 minutes and counterstained with DAPI (1 ug/µL). Finally, cells were washed with 2mL/well of PBS-1X for 5 minutes, 3 times and fluorescence images were captured at 10X or 20X using the Leica DMi8 Inverted Fluorescence Microscope.

Fusion index [62] (FI), area covered by myotubes (%), and total number of nuclei per fluorescent image were counted to quantify myogenic differentiation of C2C12 cells. FI is defined as: the total number of nuclei within the MHC-expressing multinucleated

myotubes divided by the total number of nuclei in the FOV x 100 [62]. For all experiments, three FOVs in each well were randomly selected for imaging, then ImageJ was used for cell counting and myotube area calculation.

2.6 Different H_2O_2 Concentrations on C2C12 Cell Functional Capacity

To study the C2C12 cell viability under different concentrations of H_2O_2 as a source of ROS, the first experiment was performed to determine the minimal concentration of H_2O_2 that can be used to induce significant cell damage. Five concentrations of H_2O_2 (0.2, 0.4, 0.6, 0.8, and 1.0 mM) were used to compare the effect of H_2O_2 to the normal GM as control. C2C12 cell viability experiment was performed by seeding 2.5 x104 cells/well in a 24-well plate [62,63]. Then, cells were provided with 500 µL of GM as control, and GM + 0.2 mM H_2O_2, GM + 0.4 mM H_2O_2, GM + 0.6 mM H_2O_2, GM + 0.8 mM H_2O_2, and GM + 1.0 mM H_2O_2 as the experimental H_2O_2 groups. Cells were incubated for 6 and 24 hours. At each time point, 12 wells (n=3 each group) were used for the MTS assay and the other 12 wells (n=3 each group) for the live/dead assay, as previously mentioned. Fluorescent images displaying green (live cells) and red (dead cells) were used to count the total number of live cells per FOV using ImageJ.

Based on the above cell viability experiment under ROS conditions, a concentration of 0.4 mM H_2O_2 was used to study the effect of Si-ions on C2C12 cell viability under toxic oxidative stress. This experiment was performed to determine the optimal Si-ions concentration for preserving C2C12 cells under toxic oxidative stress. 2.5 x10^4 cells/well were seeded in a 24-well plate and provided with 500 µL of specified media for each group (n=3). GM was used as the positive control, GM + 0.4 mM H_2O_2 was used as the negative control, and four different Si-ion concentrations were used as

following: GM + 0.4 mM H_2O_2 + 0.1 mM Si, GM + 0.4 mM H_2O_2 + 0.5 mM Si, GM + 0.4 mM H_2O_2 + 1.0 mM Si, and GM + 0.4 mM H_2O_2 + 2.0 mM Si. All plates were incubated for 6 and 24 hours. After each time point MTS and live/dead assays were performed as previously mentioned. Fluorescence images (10×FOV) of stained C2C12 cells were taken to observe the cells after exposure to H_2O_2 and H_2O_2 + Si for 6 and 24 hours.

After determining the optimal Si-ions concentration that can mitigate the effect of oxidative damage on C2C12 cells from the previous experiment, cells were cultured in media with the effective H_2O_2 and optimal Si-ion concentrations. In a 6-well plate, 10x104 cells/well were cultured for 24 hours or until 75% confluency. After reaching 75% confluency, GM was removed, and each well was washed with 2 mL of PBS-1x to remove any unattached cells. Then, normal DM was used as a positive control compared to 0.5 mM Si, 0.4 mM H_2O_2, and 0.4 mM H_2O_2 + 0.5 mM Si-ions. Every 48 hours DM was collected from each well for biomarker expression assays and new DM was added to each well as specified. After 4 days of differentiation, cells were fixed and immunostained and counterstained using MHC and DAPI and fluorescent images were captured at 10X using a Leica DMi8 inverted fluorescence microscope. FI and area covered by myotubes were determined using ImageJ as follows. First, cell count was determined using microscope software and the cell batch counter plug in to count any clustered nuclei. The cell batch counter plug in was then used to count nuclei found within myotubes to determine the FI. The image was then converted to 8-bit, made binary, and converted to mask before determining the area covered by myotubes. The image threshold was converted to black and white, with green fluorescence set to display as black. Finally, the black regions of the image were measured to determine

the percent area covered by myotubes.

2.7 Scratch-Wound Healing Assay Using Live Imaging Microscopy (LIM)

In this study, we have developed a scratch-wound healing assay to quantify the cells' migration rate using dynamic live imaging microscopy (DLIM) to monitor the cells' migration throughout scratch/wound healing. Briefly, we compared the cell migration under normal conditions using GM, oxidative stress using 0.4, 0.6, and 0.8 mM H2O2, Si supplements using 0.1, 0.5-, and 1.0-mM Si-ions, and 0.4 mM H2O2 + 1.0 mM Si, (n=3 and triplicated tests). The experiments were performed by seeding 5x104 cells/well in a 12-well plate with 1 mL GM for 24 hours until full confluency. Then, a 200 µL sterile pipette tip was used to scratch the cells to introduce a thin wound, the media was removed, and each well was washed twice with PBS-1x. Then, 2mL fresh conditioned media was added according to each group as described above. The plate was placed inside the sterile chamber of a Keyence BZX-710 fluorescence live imaging microscope (Keyence Corporation of America, IL, USA) and provided with 5% CO2 at 37 °C. This microscope allowed for high throughput, fully automated cell imaging at the exact same position on each well. Phase contrast images were captured every 2 minutes over 48 hours at 10X magnification (Resolution 0.7 pixels/µm and Z plane separation= 4µm pitch). All images, around 700 for each sample, were used to measure the wound area using the Wound Healing ImageJ software plugin 48,65 and ImageJ WH_NJ macro [66]. ImageJ software (1.52a: Wayne Rasband, National Institutes of Health, USA) was used for image processing applications, including stack projection and wound healing measurements. Keyence BZ-X Analyzer Software v.1.3.1.1. was used for .avi file generation and pseudo-coloring. Linear plots of wound area verses time were extracted,

and the cells' migration rate (mm2/h) was calculated using the slope function.

2.8 Quantitative Real-Time Polymerase Chain Reaction (qRT-PCR)

QRT-PCR was used to detect changes in myogenic gene expression of C2C12 cells under normal conditions compared to treatment with Si-ions over 5 days. A cell differentiation experiment was performed as mentioned above (Section 2.3.1). Three groups of DM with Si-ions (DM + 0.1 mM Si, DM + 0.5 mM Si, and DM + 1.0 mM Si) were compared to the normal DM as a positive control. Cells were differentiated for 1, 3, and 5 days and GM were collected and stored at -20°C for further evaluation. After each time point, cells were lysed, RNA was extracted using RNeasy Mini Kit (Qiagen, CA, USA) and converted to cDNA (Reverse Transcription System, Promega, Madison, WI, USA) according to manufacturer guidelines and our previously published protocol [67]. All groups were tested for MyoD (accession no. NM-010866.2) and MyoG (accession no. NM-031189.2) gene expression using glyceraldehyde 3-phosphate dehydrogenase (GAPDH, accession no. NM-008084.2) as the internal housekeeping gene (Applied biosystems, CA, USA). Quantification of relative gene expression was performed using the delta−delta CT (Δ−Δ-CT) method and expressed as the fold difference [67].

2.9 Biomarker Expression

DM was collected during the cell differentiation experiment over 5 days and stored at -20 °C. Later, collected media was analyzed for myokine expression. A mouse NRTN ELISA kit (Biomatik, DE, USA) was used to determine the concentration of NRTN secreted during C2C12 differentiation. NRTN is a key component in peroxisome-proliferator-activated receptor gamma coactivator-1α (PGC-1α) mediated neurite recruitment by skeletal muscle. NRTN ELISA kit was used according to manufacturer

guidelines. NRTN-specific antibody was precoated onto the microplate in the kit, and standards and samples were pipetted into the wells to allow any present NRTN to bond with the immobilized antibody. Then, biotin-conjugated antibody specific for NRTN was added after removing any unbound molecules. After washing the plate with a wash buffer solution, avidin conjugated horseradish peroxidase (HRP) was added followed by another wash to remove any unbound avidin reagent. Then TMB substrate solution was added to each well and the plate was incubated for 15-30 minutes as previously described while protected from light. After 20 minutes, the stop solution was added, and optical density was determined within 5 minutes using a microplate reader set to 450 nm. Protein expression was determined based on a polynomial regression of the optical density and protein concentration of the provided standards using OriginPro 8.5 software.

The collected media was further analyzed for any markers of aminobutyric acid expression during C2C12 differentiation. Analysis was performed for all aminobutyric acid isomers, including α-aminobutyric acid (AABA), β-aminobutyric acid (BABA), and GABA. Aminobutyric acid concentrations were determined using LC-MS/MS analysis, performed on a Shimadzu LCMS-8050 triple quadrupole mass spectrometer (Shimadzu Scientific Instruments Inc., Tokyo, Japan) at the Shimadzu Center at the University of Texas at Arlington. Analysis was performed based on a previously published LC-MS/MS method that enables baseline separation with sensitive detection of aminobutyric acid isomers in minimal amounts of biological fluid samples developed by the Brotto Research Laboratory [68].

2.10 Statistical Data Analysis and Reporting

Immunofluorescent images were analyzed for cell number, myotube area, and FI using ImageJ. Wound Healing ImageJ software plugin 48,65 and ImageJ WH-NJ macro 66 were used for cell number, myotube area, and FI analysis. Quantitative qRT-PCR and ELISA data was evaluated using the Δ−Δ-CT method and analyzed using Origin software. The results for qRT-PCR are reported as fold differences relative to a GAPDH control. ELISA results are reported as protein concentration (ng/mL) derived by obtaining the optical densities of a set of predetermined standards then performing a standard curve regression analysis and using the resultant equation to derive the protein concentration of experimental groups from the measured optical density.

OriginPro 8.5 software was used for all graphs and statistical analysis. Statistical data are presented by individual data points and a horizontal line indicating the average of each group. Bar graphs display group means and standard deviations. One-way ANOVA followed by Tukey's post hoc was used between group comparisons. Due to the difference in variance between the groups, following a One-way ANOVA, Tukey's post hoc analysis was conducted to compare differences between individual groups. $P < 0.05$ was considered as statistical significance and * represents $p < 0.05$, ** for $p < 0.01$, and *** for $p < 0.001$. FI calculations were conducted blindly by the operator.

3. RESULTS

3.1 Effects of Si-Ions Dose on C2C12 Myoblasts

3.1.1 Si-ions Enhance C2C12 Cell Viability

The effect of Si-ions on C2C12 myoblast cell viability was tested by using three different concentrations of Si-ions at two time points (6 and 24 hours) as shown in

Figure 6. 1. Under normal conditions, all Si-ions concentrations showed no cytotoxic effects on C2C12 cells. After 6 hours, all Si-ion groups displayed higher cell numbers compared to the positive control (GM), but no significant difference was observed as shown in Figure 6. 1A. After 24 hours, 0.1 mM of Si in GM significantly increased cell

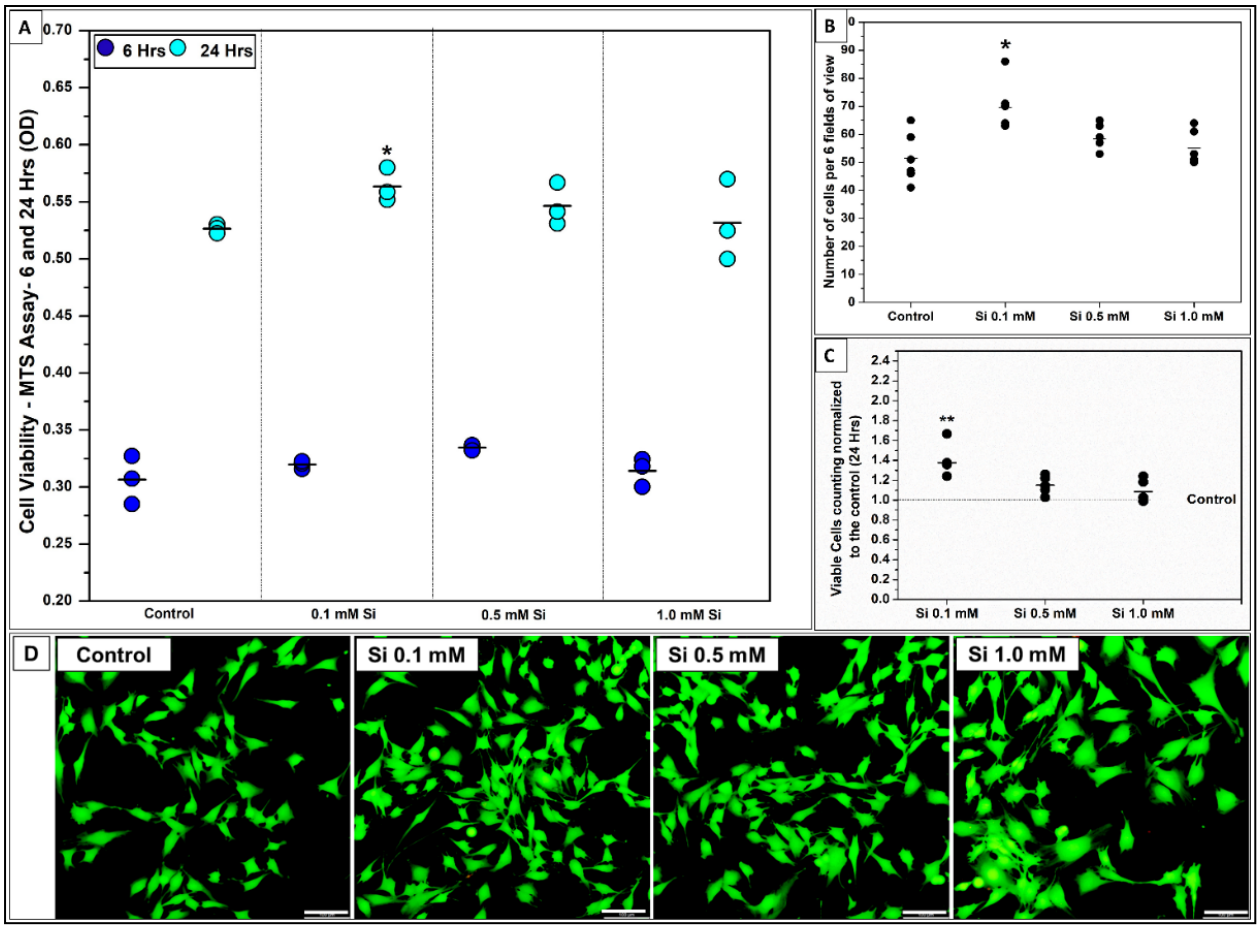

Figure 6. 1: Effect of silicon ions on C2C12 myoblast cell viability. A) Data distribution graph present the cell viability results using MTS-assay after 6 and 24 hrs of C2C12 cell culturing in growth media with three different concentration of Si^{4+} (0.1, 0.5, and 1.0 mM). 0.1 mM of Si4+ into the growth media significantly increases the cell viability after 24 hrs compared to the control (*$p < 0.05$, n=3 per group). B) Data distribution graph presents the number of cells per 6 fields of view confirming that 0.1 mM of Si^{4+} significantly increase the number of cells after 24 hrs. C) Bar graph shows the number of viable cells normalized to the control after 24 hrs. D) Fluorescent pictures (20× view) of C2C12 cells stained with live/dead assay kit shows enhancement on cell viability after being exposed to ionic silicon. (—) in the graphs represents the mean and the scale bar in the fluorescent pictures is 100 µm.

viability compared to the control (*p < 0.05, n=3 per group) as indicated by the MTS-assay results, expressed as optical density (OD) in Figure 6. 1A. Furthermore, live/dead stain confirmed the addition of Si-ions increased cell viability as indicated by the green stain of live cells after 24 hours (Figure 6. 1D). The number of cells counted for each group based on live stain fluorescent images (6 FOVs) confirmed that 0.1 mM of Si-ions significantly increased cell numbers compared to the control (*p < 0.05, n=3 per group), congruent with MTS results. Finally, following normalization of cell counts to the control it was determined that there was a 1.4-fold increase in cell counts with 0.1mM Si.

3.1.2 Si-ions Promote C2C12 Cell Proliferation

Figure 6. 2 presents the effect of Si-ions on C2C12 cell proliferation following 3 days cell culture under normal conditions. Following 1, 2, and 3 days of C2C12 proliferation in Si ions it was determined that cell proliferation increased in all Si-ion groups compared to the control at day 1, and there was a significant increase in cell proliferation in 0.1 mM Si-ion samples following 1 and 3 days (*p<0.05) based on the OD results of the MTS assay. Figure 6. 2B presents the fluorescent images of C2C12 cells stained with live/dead assay kit for live (green) and dead (red) cells following 2 days proliferation. Almost no dead cells were observed for the control and Si-ion groups (p>0.5). An increased number of cells during proliferation were seen in Si ion samples compared to controls was confirmed by counting the 9 FOVs for each well. There was a significant increase in cell number in 0.1 mM Si-ion groups at day 1 (*p<0.05) and day 2 (***p<0.001). Furthermore, the area covered by live C2C12 cells was calculated using the fluorescent images as shown in Figure 6. 2D. Percentage of cell area coverage confirmed that the addition of Si-ions significantly increased the area covered by cells

during proliferation.

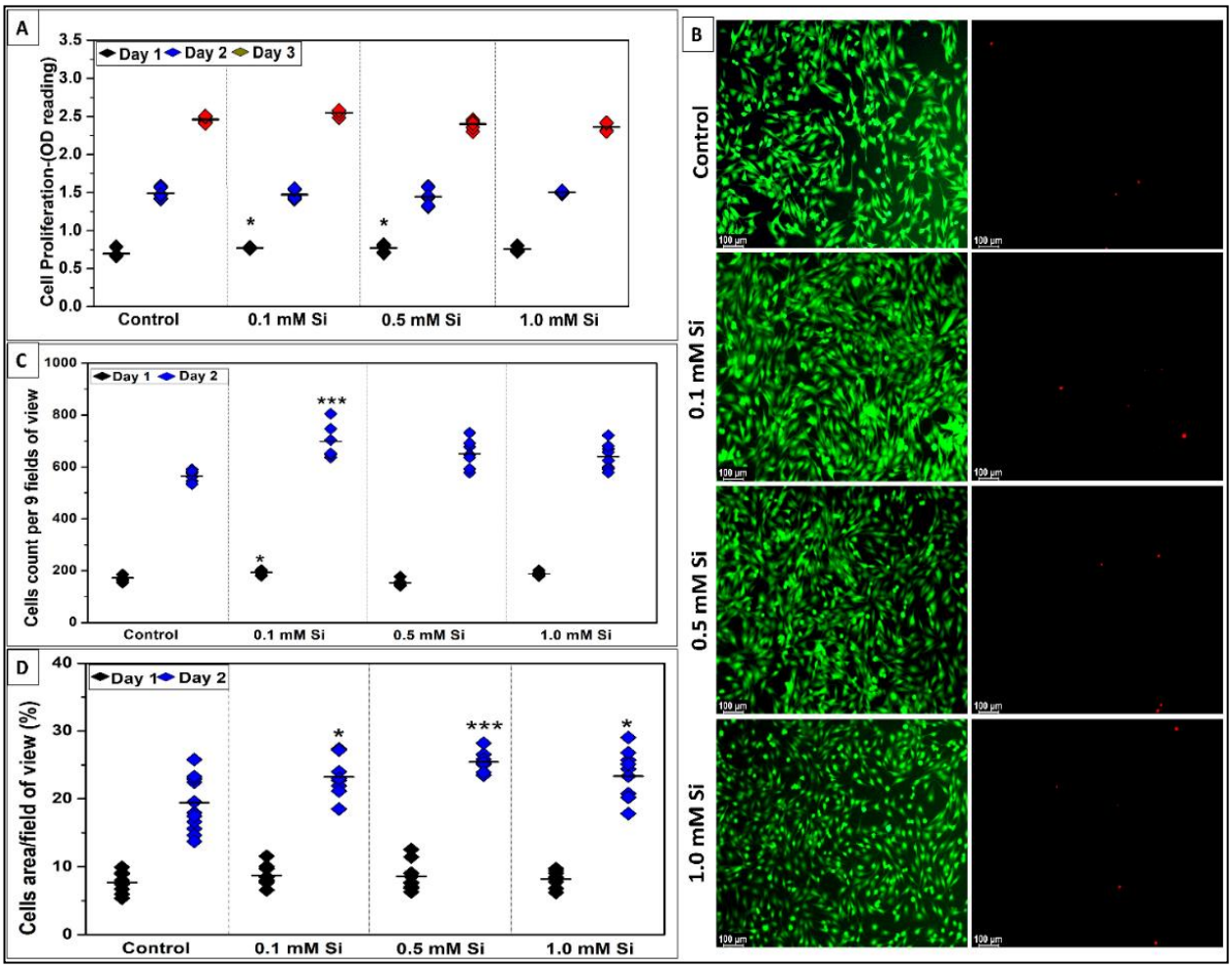

Figure 6.2: Effect of Si-ions concentration on C2C12 cells proliferation for 3 days. A) Data distribution graph shows the MTS-assay results of C2C12 cell proliferation with 3 different concentration of silicon ions for 1, 2, and 3 days. 0.1 mM Si significantly increased the number of cells at day 1 and 3, (*P<0.05). B) Fluorescent pictures (10× view) of C2C12 cells stained with live/dead assay kit shows the live (green) and dead (red) cells after 2 days of proliferation. Almost no dead cells were observed for the control and silicon ions groups. C) Data distribution graph presents the number of cells per 9 fields of view counted from the fluorescent pictures. The cell counts confirmed that 0.1, 0.5, and 1.0mM Si-ions significantly increased the total number of cells by day 2 of proliferation. D) Cell area percentage confirmed that Si-ions significantly increased the area covered by C2C12. (—) in the graphs represents the mean and the scale bar on the pictures is 100 µm, (***p < 0.001, **p < 0.01, n=3 per group).

3.1.3 Si-ions Promote C2C12 Cell Differentiation

To determine the effect of Si-ions on myogenic differentiation, C2C12 cells were cultured with three different concentrations of Si-ions for 4 and 7 days. After each timepoint, the mature myocytes/myotubes were stained with MHC antibody and DAPI counterstain as shown in Figure 6. 3. FI calculations indicated that 0.1 mM Si-ions significantly increased myotube formation compared to the control with FI (%) = 42± 3.3 and 31± 4 at day 4 and FI= 60± 3.2 and 50± 2.4, respectively, at day 7 (***$p<0.001$) as shown in Figure 6. 3A. Also, 0.5 mM and 1.0 mM Si-ions significantly increased the FI compared to the control at day 7, (**$p<0.01$ and *$p<0.05$, respectively). Overall, FI was significantly increased from day 4 to day 7 for all samples including the control (***$p<0.001$). Total number of cells counted from 9 FOVs of DAPI stained nuclei indicated that all Si concentrations significantly increased the total number of cells at day 4 compared to the control with optimal concentration of 0.1 mM Si-ions, ***$p<0.001$ (Figure 6. 3B). Furthermore, area covered by myotubes was calculated based on MHC staining at 4 and 7 days. The calculated myotubes area (%) indicated that all Si concentrations increased the total area of myotubes per FOV compared to the control, however, only 0.1 mM Si-ions presented a significant difference at day 4 (34.3±1.2%) and day 7 (48.9± 2.4%) when compared to the control (25.3± 3.6% and 40.6± 4.8% for day 4 and 7, respectively) as shown in Figure 6. 3C. It is important to mention that there was no significant difference between the total number of cells from day 4 to 7, while the FI and the myotube area % significantly increased from day 4 to day 7 for all groups including the control.

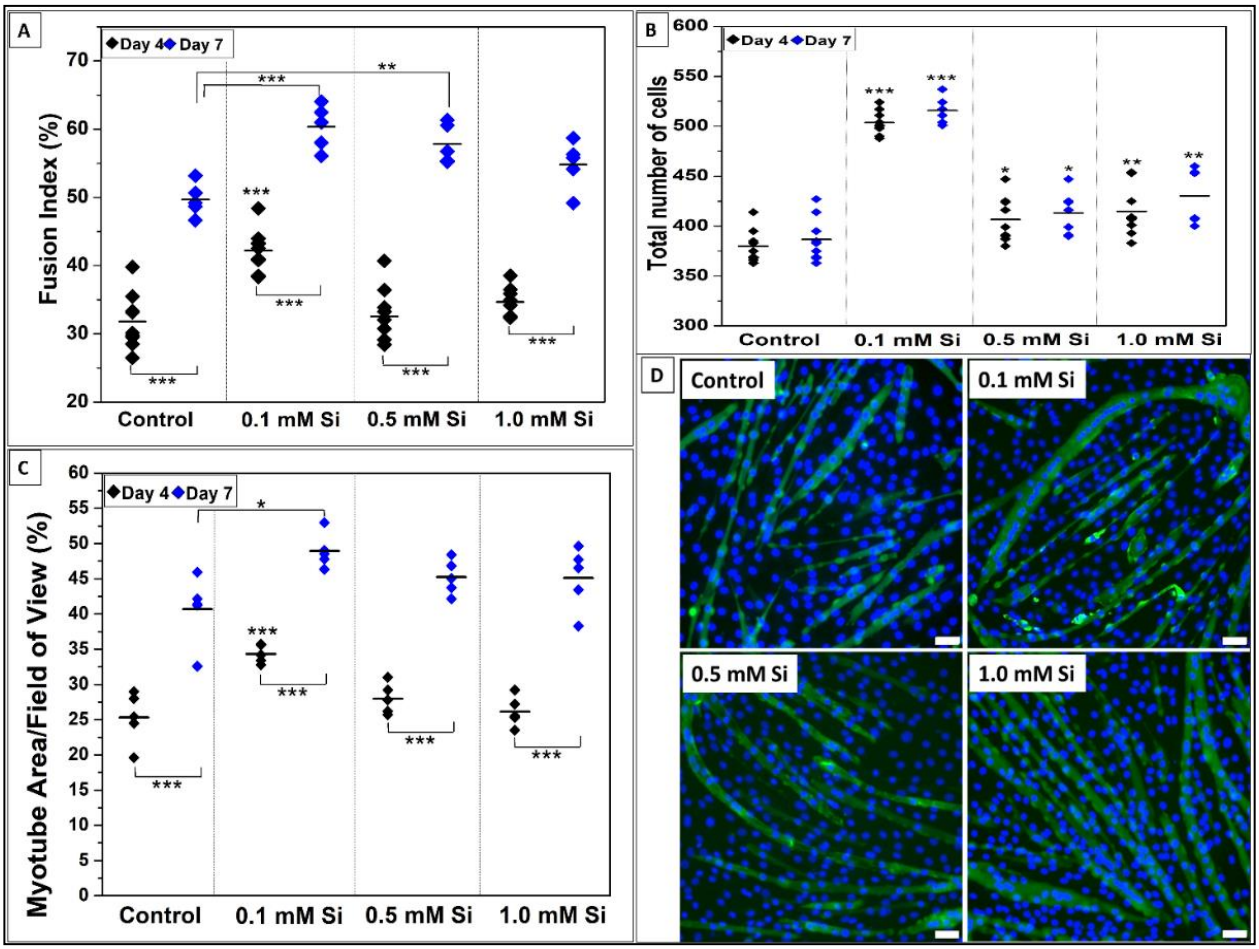

Figure 6.3: Effect of Si-ions concentration on C2C12 cells after 4 and 7 days of differentiation. A) Fusion index (FI) indicates that 0.1 mM of silicon significantly increases the FI compared to the control after 4 days. Also, 0.1, 0.5, and 1.0 mM of silicon significantly increases the FI compared to the control after 7days (***P<0.001, **P<0.01, *P<0.05). FI was significantly increased from day 4 to day 7 for all samples (***P<0.001). B) Total number of cells counted from 9 fields of view of DAPI stained nuclei, all used silicon concentration significantly increased the total number of cells at day 4 and 7 compared to the control and 0.1 mM was the optimal concentration with ***P<0.001 significance. There was no significant difference between the total number of cells from day 4 to 7. C) Area covered by myotubes (%) also indicated that all used silicon concentrations increase the total area of myotubes per field of view compared to the control and 0.1 mM Si showed high significance at day 4 and 7. Also, the myotube area showed a significant increase from day 4 to 7 for all samples and the control. D) represents fluorescence images of DAPI-stained nuclei (blue) and myosin heavy chain antibody (MHC, green)-stained myocytes/myotubes of C2C12 myoblasts on the tissue culture plate (TCP) as a control and the three different Si-ions concentrations (0.1 mM, 0.5 mM, and 1.0 mM) after 4 days of differentiation. Scale bar is 50 µm and ***P<0.001, **P<0.01, *P<0.05.

3.1.4 Si-ions Enhance MyoG and MyoD Gene Expression

Expression of two key regulatory genes of myogenesis related to C2C12 myoblast differentiation were detected using qRT-PCR analysis following 1 and 5 days of differentiation. MyoG is an important myogenic regulatory factor expressed to mark cell commitment to differentiation 21. MyoD is a vital gene for myoblast progression during differentiation to form skeletal muscles 22. Figure 6. 4 shows relative mRNA expression of MyoG and MyoD following 1 and 5 days of differentiation. Figure 6. 4B presents the mRNA expression of MyoG at day 1 and 5 of C2C12 differentiation. All Si-ion concentrations significantly increased MyoG expression compared to control at day 1 and 5. Following day 1 of differentiation MyoG expression increased ~1.3-fold in both 0.1 mM and 0.5 mM Si-ion groups (**$p<0.01$, *$p<0.05$, respectively) then further increased following 5 days of differentiation to ~1.8-fold difference for 0.1 mM Si-ions and ~1.5-fold difference for 0.5 mM Si-ions (***$p<0.001$, **$p<0.01$, respectively) compared to control. For the high concentration 1.0 mM Si-ion group, there was a significant increase by ~2-fold in MyoG expression at day 1 which decreased to a ~ 1.8-fold difference compared to the control by day 5 of differentiation (***$p<0.001$).

The qRT-PCR results indicated that MyoD expression was significantly increased in 0.1, 0.5 and 1.0 mM of Si-ion samples following 1 and 5 days of C2C12 myoblast differentiation as shown in Figure 6. 4A (***$P<0.001$). A 2.5-fold increase in MyoD expression for 0.1 mM Si-ion samples and a 3-fold increase in 1.0 mM Si-ion samples was observed compared to control at day 1. There was a 3-fold difference in MyoD expression in the 0.1 mM Si-ion group and only a 2.8-fold difference in the 1.0 mM Si-ion group following 5 days of differentiation. Finally, there was a 2.5-fold increase in

MyoD expression in the 0.5 mM Si-ion group following 1 day of differentiation that decreased to a 2-fold difference by day 5.

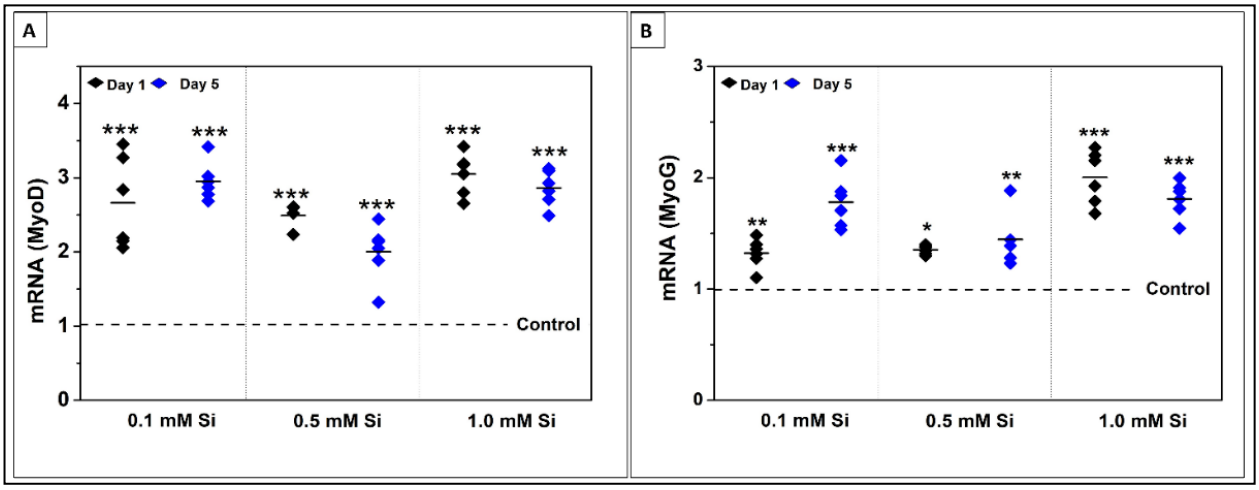

Figure 6.4: Myogenic determination protein (MyoD) and Myogenin (MyoG) genes expression at 1 and 5 days of C2C12 cell differentiation. A) Si-ions increased the expression of MyoD at early stage of differentiation (Day 1); 0.1 and 1.0 mM of Si-ions significantly increased the MyoD expression at day 1 and 5 (*P<0.05). B) MyoG expressed at a later stage marking the commitment to differentiation, 1.0 mM of Si-ions significantly increased the MyoG expression by 2-folds at day 1. By day 5, both 0.1 and 1.0 mM of Si-ions increased the MyoG expression almost 2-fols compared to the control.

3.1.5 Si-ions Enhance Myokines Expression

Collected media were tested to determine the effect of Si-ions on C2C12 biomarker expression following 5 days of differentiation under normal conditions. NRTN expression following 3 and 5 days of differentiation was determined by ELISA assay. NRTN concentration (ng/mL) was increased in Si-ion samples at day 3 compared to the control (Figure 5C). NRTN expression significantly increased in the 0.5 mM Si-ion group compared to the control following 3 days of differentiation (**p<0.01). NRTN expression following 5 days of differentiation indicated that NRTN concentration decreased as differentiation time increased from 3 to 5 days. Although 0.5 mM and 1.0 mM of Si-ions reported the highest NRTN concentration at day 3 of differentiation, 0.5 mM and 1.0 mM Si-ions reported the lowest NRTN concentration by day 5 of differentiation. The initial

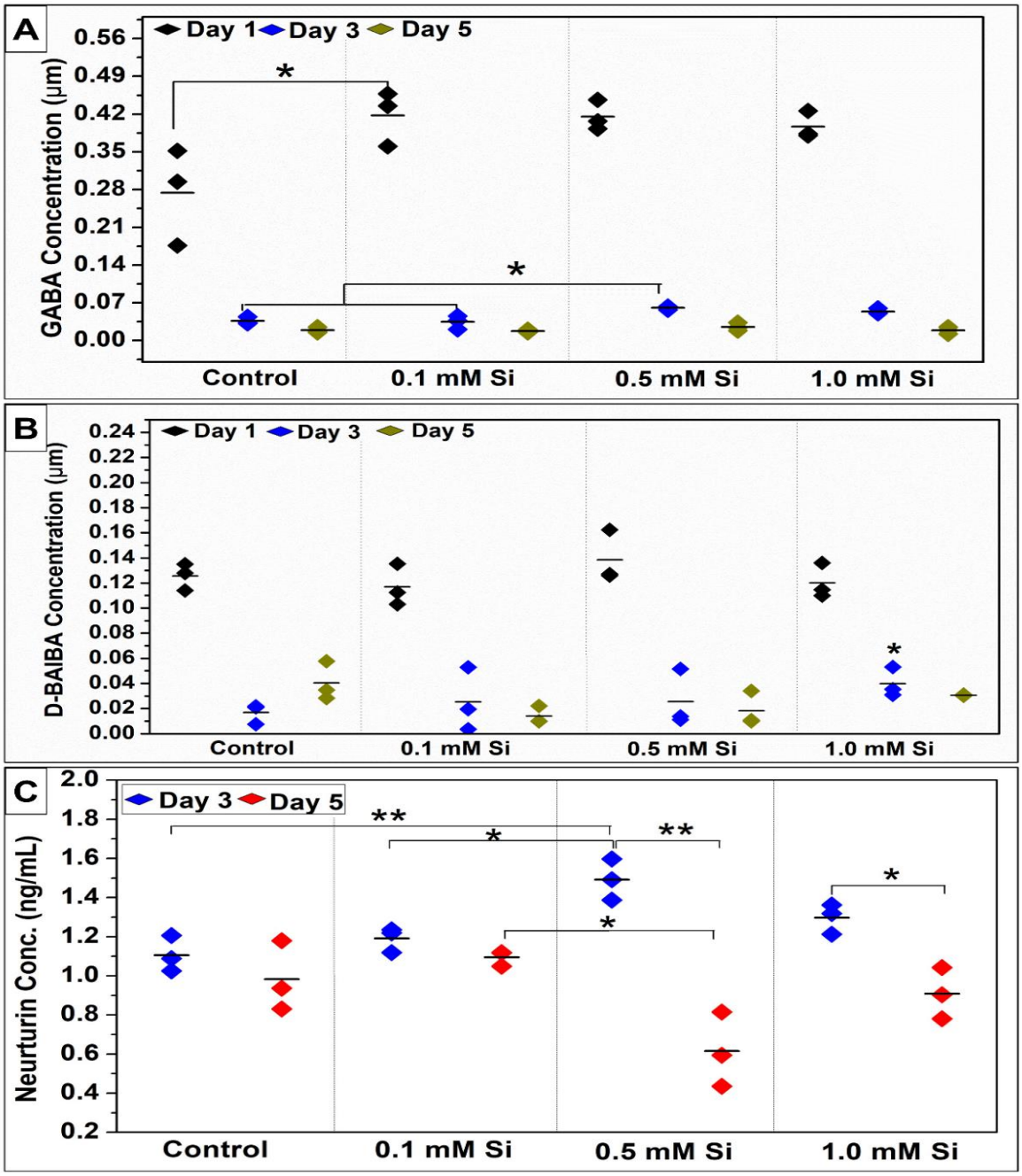

Figure 6. 5: Effect of Silicon-ions on Y-aminobutyric acid (GABA), D-Beta aminoisobutyric acid (D-BAIBA) concentration in µM, and Neurturin (ng/ml) expressed by C2C12 during 5 days of differentiation. A) GABA concentration increased by adding Si-ions to the differentiation media. B) The concentration of D-BAIBA increased by adding 0.5 mM of Si to the differentiation media at day 1, but no significant difference was observed compared to the control. C) Neurturin expression in media (ng/mL) during C2C12 myoblast cell differentiation for 3 and 5 days. All silicon-ion concentrations increased the neurturin expression, but the 0.5 mM of silicon-ions significantly increased the neurturin expression compared to the control at day 3 of differentiation.

increase followed by reduction in NRTN levels may indicate that NRTN secretion was increased, however, the inability to recruit motor neurites via retrograde signaling in vitro resulted in a quick reduction in NRTN concentration.

The collected media was also tested to study the effect of Si-ions on aminobutyric acid expression during C2C12 differentiation. Although the analysis was performed for all isomers of aminobutyric acid (AABA, BABA, and GABA), only GABA and β-aminoisobutyric acid (D-BAIBA) were detected in DM as indicated in Figure 5. At day 1 of differentiation, GABA expression was increased for all Si-ion groups as compared to the control but there was only a significant increase in GABA ~ 0.42± 0.02 μM in the 0.1 mM Si-ion group (*$p<0.05$). At 3 and 5 days of differentiation, GABA concentration was significantly reduced for all Si-ions groups and the control compared to day 1 concentrations. GABA concentration was higher in the 0.5 mM Si-ion group compared to the other groups at day 3. Overall, the GABA concentration reduced dramatically after the first day of differentiation indicating that GABA expression decreases as differentiation time increases. Also, there was no significant difference between the control and Si-ions-media on GABA expression at day 5. D-BAIBA concentration was increased in the 0.5 mM Si-ion group (~0.14± 0.02 μM) compared to the control (~0.12± 0.01 μM) at day 1 of differentiation but no significant difference was observed (Figure 5B). While the D-BAIBA concentration was higher for all Si-ions groups compared to the control on day 3, only the 1.0 mM Si-ion group was significantly different (*$p<0.05$). D-BAIBA concentrations reduced dramatically at day 3 and 5 compared to day 1 of differentiation, indicating that D-BAIBA concentration decreases as differentiation time increases. The initial increase followed by reduction in both GABA and D-BAIBA levels

again suggest that myokine secretion was increased, however, the lack of retrograde signaling in vitro resulted in a quick reduction in myokine concentration.

3.2 Effects of Different H2O2 Concentrations and Si-ions on C2C12 cells

3.2.1 H_2O_2 Impairs C2C12 Myoblast Cell Viability

The effect of H_2O_2 on C2C12 myoblast cell viability was tested using five different concentrations (0.2, 0.4, 0.6, 0.8, and 1.0 mM H_2O_2) compared to the normal GM as a positive control as shown in Figure 6. MTS and live/dead assays were used to determine cell viability at 6 and 24 hours following the addition of H_2O_2. All H_2O_2 concentrations significantly decreased cell viability at 6 and 24 hours compared to the control (***p<0.001, **p<0.01, n=4 per group) as shown in Figure 6A. Live/dead staining confirmed the results obtained from the MTS assay by showing the gradual decrease in the total number of live cells (green) and the increase in dead cells (red) as the H_2O_2 concentration increased from 0.2 to 0.6 mM as shown in Figure 6D. No live cells were observed for 0.8 and 1.0 mM H_2O_2 while the number of dead cells increased. The fluorescent images were further used to count the number of live cells per 6 FOVs for each group (Figure 6B) and the cell number was normalized to the control as shown in Figure 6C. The cell number was significantly reduced in all H_2O_2 groups compared to the control, while 0.4 mM H_2O_2 was the minimum concentration for inducing a high significant difference in cell number (***p<0.001). The normalized cell number indicated that 0.2 mM H_2O_2 decreased the number of viable cells by 37% (**p<0.01) while 0.4 mM H_2O_2 decreased viable cells by 70% at 24 hours (***p<0.001). These results confirmed the results obtained by the MTS assay.

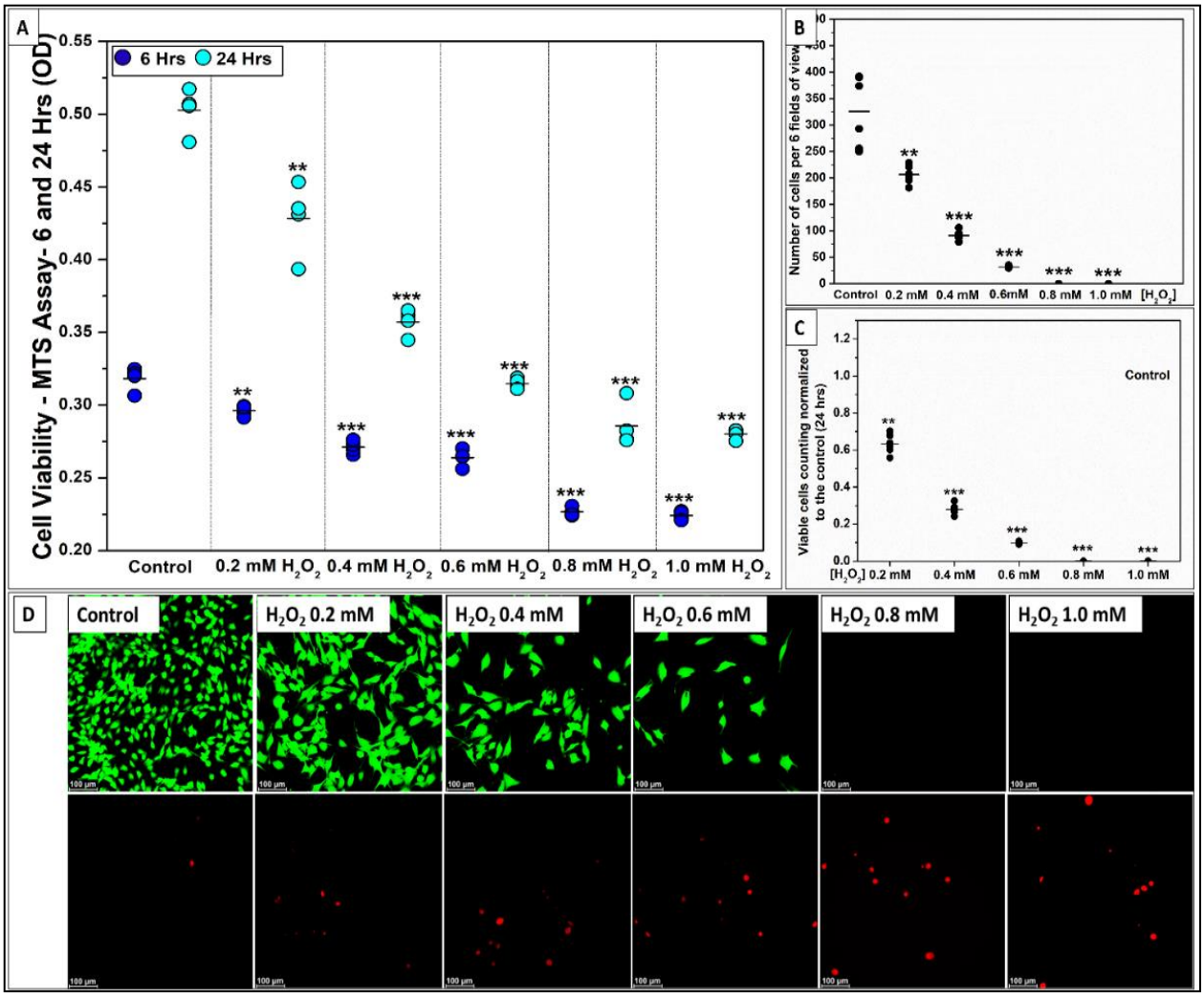

Figure 6. 6: Effect of Hydrogen peroxide (H2O2, ROS-source) on C2C12 myoblast cell viability. A) Data distribution graph presents the cell viability results using MTS assay after 6 and 24 hrs of C2C12 cell culturing in growth media with five different concentration of H2O2 (0.2, 0.4, 0.6, 0.8, and 1.0 mM). 0.4 mM of H2O2 into the growth media significantly decreases the cell viability after 6 and 24 hrs compared to the control (***p < 0.001, **p < 0.01, n=4 per group). B) Data distribution graph presents the number of cells per 6 fields of view confirming the same results from the MTS-assay. C) Bar graph shows the number of viable cells normalized to the control after 24 hrs, 0.2 mM of H2O2 decreased the number of viable cells to 63% and the 0.4 mM H2O2 to ~30% viable cells compared to the control 100% (0 mM H2O2). D) Fluorescent pictures (20× view) of C2C12 cells stained with live/dead assay kit shows the live (green) and dead (red) cells after being exposed to H2O2 for 24 hrs. No viable cells were observed with 0.8 and 1.0 mM of H2O2. (—) in the graphs represents the mean and the scale bar on the fluorescent pictures is 100 µm.

3.2.2 Si-ions Protect C2C12 Myoblast Cells Against Oxidative Damage

As presented above, 0.4 mM H_2O_2 was the minimum concentration to induce a significant effect (***p<0.001, R2=0.99) on C2C12 cell viability. To study the effect of Si-ions on C2C12 under toxic oxidative stress conditions, 0.4 mM H_2O_2 was added to GM to induce ROS related damage, then four different concentrations of Si-ions were added to determine the optimal concentration that attenuated the effect of toxic oxidative stress. Cell viability was measured by MTS assay at 6 and 24 hours as shown in Figure 7A, and the five groups were compared to the control. The 0.4 mM H_2O_2 group (i.e., 0.0 mM Si) presented a significant decrease in cell viability at 6 and 24 hours compared to the control. At 6 hours, there was no significant difference in cell viability for low concentrations of Si-ions (0.1 and 0.5 mM), while higher concentrations of Si-ions (1.0 and 2.0 mM) attenuated the effect of toxic H_2O_2 as indicated by a significant increase in cell viability (***p<0.001, R2=0.98) compared to the 0.4 mM H_2O_2 group. At 24 hours, all Si-ion concentrations attenuated the toxic effects of H_2O_2 resulting in increased cell viability compared to the 0.4 mM H_2O_2 group (***p<0.001, R2=0.99).

Figure 7C presents the fluorescent images after 24 hours for all groups. The number of live cells (green) increased in all Si-ions groups compared to the 0.4 mM H_2O_2 group which presented a higher number of dead cells (red). The fluorescent images were used to count the number of live cells per 6 FOVs for each group, then cell number was normalized to the 0.4 mM H_2O_2 group as shown in Figure 7B. The normalized cell counts indicated that live cell number was significantly increased in all Si-ion groups, congruent with the results obtained from the MTS assay. Importantly, 0.5 mM Si-ions was the optimal concentration of Si-ions that could attenuate the effect of

toxic H_2O_2 as indicated by a significant increase in cell viability (***p<0.001).

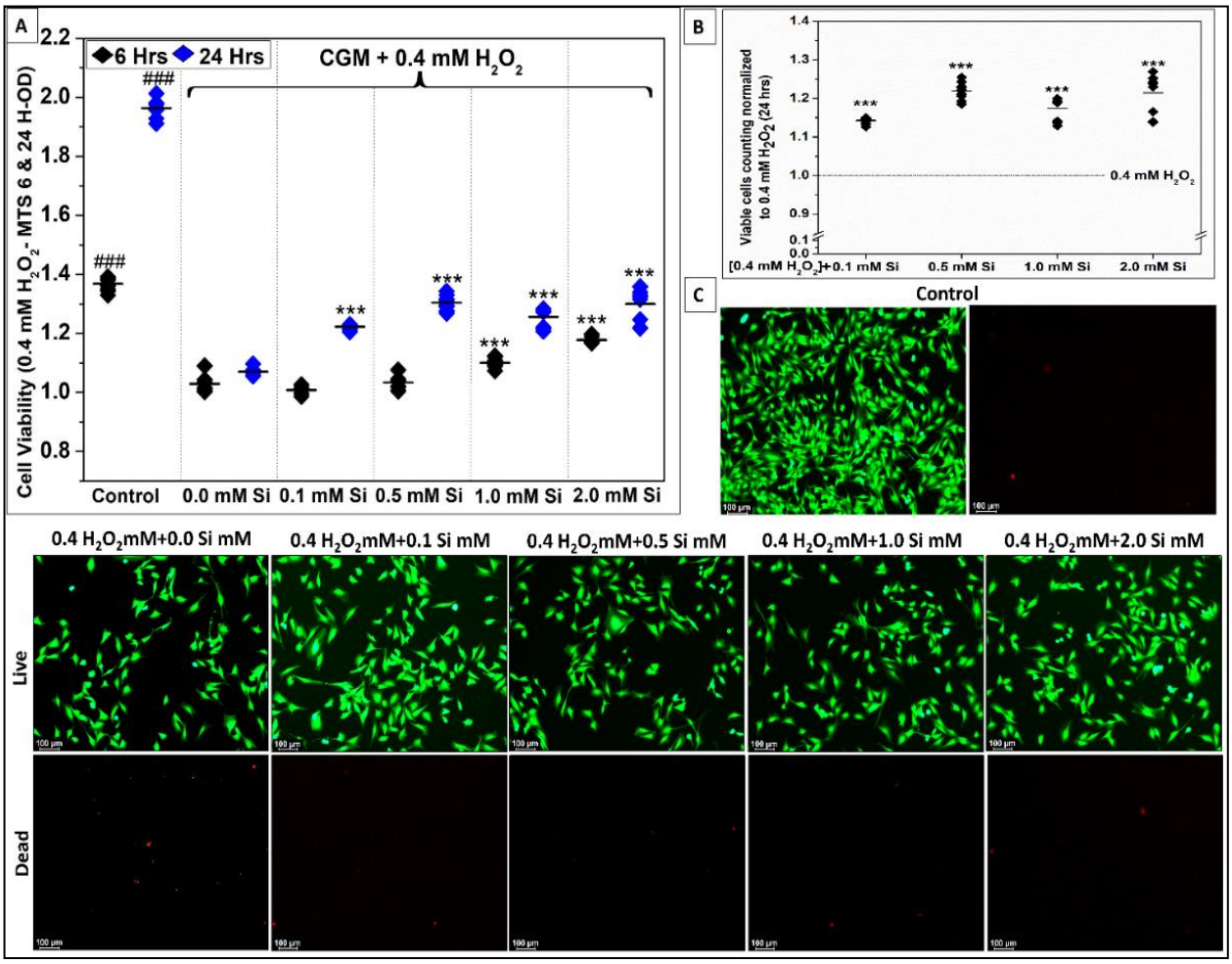

Figure 6. 7: Silicon ions attenuate the effect of toxic oxidative stress (0.4 mM H_2O_2) on C2C12 myoblast cells. A) Data distribution graph presents the cell viability results using MTS assay after 6 and 24 hrs of C2C12 cell culturing in complete growth media (CGM, Control), supplied with 0.4 mM H_2O_2, (test groups) with 0.0, 0.1, 0.5, 1.0 mM Si-ions. 0.0 mM Si indicates that 0.4 mM of H_2O_2 into the growth media significantly decreases the cell viability after 6 and 24 hrs compared to the control (***p < 0.001, n=4 per group), addition of 0.5-1.0 mM of Si into the growth media under ROS significantly enhances the cell viability compared to 0.4 mM H_2O_2 without Si (*p < 0.05, n=4 per group). C) Data distribution graph presents the number of cells per 6 fields of view confirming the same results from the MTS-assay. C) Bar graph shows the number of viable cells normalized to the control after 24 hrs, the control was significantly higher compared to all other groups, 0.5 and 1.0 mM of Si significantly increased the number of viable cells compared to0.4 mM H_2O_2 without Si. D) Fluorescent pictures (10× view) of C2C12 cells stained with calcine Am stain showing cells after being exposed to H_2O_2 for 24 hrs. (___) in the graphs represents the mean and the scale bar on the fluorescent pictures is 100 µm.

3.2.3 Si-ions Enhance Cell Differentiation Under Toxic Oxidative Stress

After determining the optimal concentration of Si-ions for attenuating the toxic effects of oxidative stress on C2C12 myoblast cells, a cell differentiation experiment was performed to study the effect of Si-ions on cell differentiation under toxic H_2O_2. DM was used as a control to compare 0.5 mM Si-ions, 0.4 mM H_2O_2, and 0.4 mM H_2O_2+0.5 mM Si-ion groups as shown in Figure 8. The fluorescent images of DAPI-stained nuclei (blue) and myosin heavy chain antibody (MHC, green)-stained myocytes/myotubes after 4 days of differentiation are presented in Figure 8C. FI for control and 0.5 mM Si-ions groups was significantly higher than the other groups (***p<0.001). FI was increased (22± 5) in the 0.5 mM Si-ion group under oxidative stress compared to 0.4 mM H_2O_2 (18± 6), but no significant difference was observed. Based on the MHC-stained myotubes, the myotube area coverage (%) was calculated per 9 FOVs as shown in Figure 8B. Addition of 0.5 mM of Si-ions resulted in a significant increase in myotube coverage area from 9.5± 2.4% for the 0.4 mM H2O2 group to 12.2± 1.6% for the 0.4 mM H_2O_2+ 0.5 mM Si group (**p<0.01). Figure 8 (D, E) shows the relative mRNA expression of MyoG and MyoD following 1 and 5 days of differentiation under ROS condition. It is clear that 0.4 mM H_2O_2 significantly decreases the MyoG (###p<0.001) and MyoD (#p<0.05) expression at day 1 of differentiation. Although the combined group (0.4 mM H_2O_2 + 0.5 mM Si) presented a significant decrease in MyoG (###p<0.001) expression, no significant change was observed for MyoD expression at day 1. Furthermore, comparing 0.4 mM H_2O_2 group to the Si treated group (0.4 mM H_2O_2 + 0.5 mM Si) revealed that Si addition significantly increased the MyoD and MyoG expression (*p<0.05) under ROS condition at day with no difference at day 5.

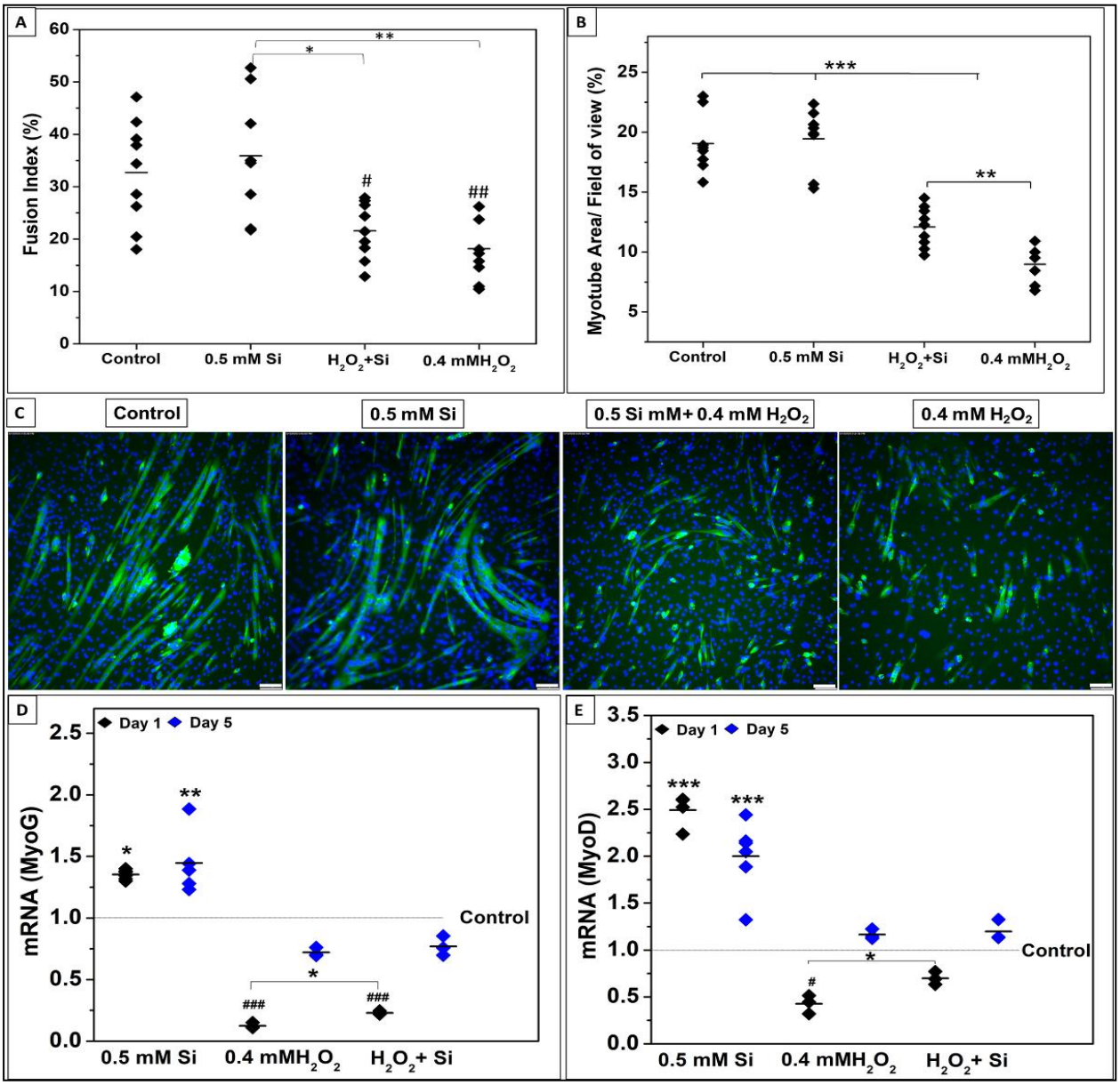

Figure 6.8: Effects of Si-ions concentration on C2C12 myoblast cells after 4 days of differentiation under oxidative stress (0.4 mM H2O2). A) Data distribution graph shows the Fusion index (FI) after 4 days of differentiation comparing the differentiation under 0.4 mM H2O2 to 0.4 mM H2O2 + 0.5 mM Si and the control. Adding 0.5 mM Si increases the FI compared to 0.4 mM H2O2, but no significance deference was observed. B) Area covered by myotubes (%) indicated that addition of 0.5 mM Si increase (*P<0.05) the total area of myotubes compared to 0.4 mM H2O2 by reliving the cells from the toxic oxidative stress. C) Fluorescence images of DAPI-stained nuclei (blue) and myosin heavy chain antibody (MHC, green)-stained myocytes/myotubes of C2C12 myoblasts on the tissue culture plate (TCP) as a control, 0.5 mM Si-ions, 0.4 mM H2O2 + 0.5 mM Si, and 0.4 mM H2O2 after 4 days of differentiation, Scale bar is 100 µm, 10-X magnification. D-E) Myogenic determination protein (MyoD) and Myogenin (MyoG) genes expression at 1 and 5 days of C2C12 cell differentiation under ROS.

3.2.4 Si-ions Enhance Antioxidant Marker Expression Under ROS

To determine the effects of Si-ions on antioxidant activity in the presence of toxic oxidative stress, C2C12 cells were differentiated in media containing 0.5mM Si-ions only, 0.4mM H_2O_2 only, 0.5mM Si + 0.4mM H_2O_2, and no treatment group as a control. After 1 and 5 days of differentiation, real time qRT-PCR was used to quantify the relative concentrations of NRF-2 and SOD-1 mRNA in all 4 groups (Figure 9). At normal condition, Si treatment did not show any significant effect on NRF-2 or SOD-1 expression compared to the control, while 0.4 mM H_2O_2 has increased the SOD-1 and NRF-2 expression with a significant increase only in NRF-2 expression at day 1 and 5 (Figure 9A). For the combined group (0.5mM Si + 0.4mM H_2O_2), there was a significant increase in NRF-2 (1.7±0.1, p=0.00002) and SOD-1 (1.35±0.06, p=0.04) at day 5.

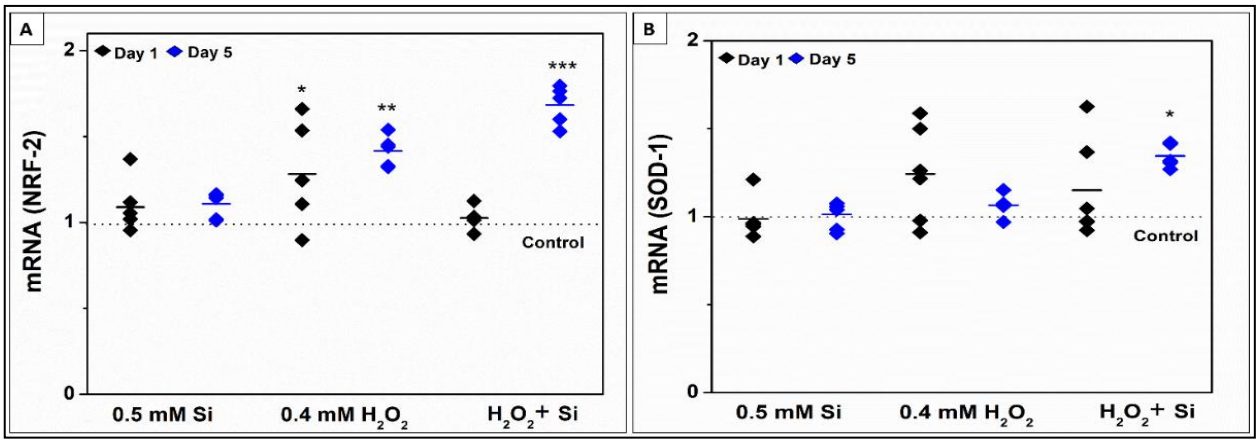

Figure 6.9: Si ions enhance antioxidant marker expression in the presence of toxic oxidative stress. A) Relative concentration of NRF-2 mRNA expressed by C2C12 skeletal muscle cells differentiated in media containing 0.5mM silicon ions only, 0.4mM H_2O_2 only, and media containing 0.5mM Si Ions+0.4mM H_2O_2 for 1 and 5 days. NRF-2 expression was significantly upregulated in the 0.4mM H2O2 group at days 1 (1.28, p=0.03) and 5 (1.41, p=0.008) compared to the control, and in the H_2O_2+Si group at day 5 (1.7, p=0.00002). B) Relative concentration of SOD-1 mRNA expressed by C2C12 skeletal muscle cells differentiated in media containing 0.5mM silicon ions only, 0.4mM H2O2 only, and media containing 0.5mM Si Ions+0.4mM H_2O_2 for 1 and 5 days. SOD-1 expression was significantly upregulated in the H_2O_2+Si group compared to the control at day 5 (1.35, p=0.04).

3.2.5 Si-ions Enhance Wound Healing and Cell Migration Rate under ROS

Scratch-wound healing assay was performed to compare cell migration parameters under different conditions. It is commonly used to measure cells' migration parameters such as speed, persistence, and polarity 69. In this study, we compared myoblast cells' migration rate, referred to as the wound healing rate, under four different conditions: 0.1-1.0 mM Si-ions, 0.4-0.8 mM H_2O_2, 0.4 mM H_2O_2 + 1.0 mM Si-ions, and the control as shown in Figure 10. The cells' migration rate under Si-ions compared to the control is shown in Figure 10A. It is noted that 0.5-1.0 mM Si-ions slightly increased the migration rate, but no significant difference was observed. Figure 10B shows the migration rate under three toxic H_2O_2 concentrations (0.4, 0.6, and 0.8 mM). All used H_2O_2 concentrations significantly decreased the migration rate (***$p<0.001$) compared to the control group as shown in Figure 10B. Addition of 1.0 mM Si-ions to the 0.4 mM H_2O_2 conditioned media attenuated the toxic effect of H_2O_2 and significantly increased the cells' migration rate compared to the non-Si-ions treatment (**$p<0.01$) as shown in Figure 10C. Furthermore, no significant difference was observed between the control group (rate= 0.033± 0.001 mm2/h) and the H_2O_2 + Si group (rate= 0.031± 0.002 mm2/h), while the H_2O_2 alone presented a significant decrease in the migration rate (rate=0.025± 0.001 mm2/h) compared to the control (***$p<0.001$). Figure 10D shows the phase contrast images (10X, scale bar=100 μm) of wound/scratch area at different time points (0, 12, 24, and 28 hours). Migration rate of each group is reported in the inserted table in Figure 10.

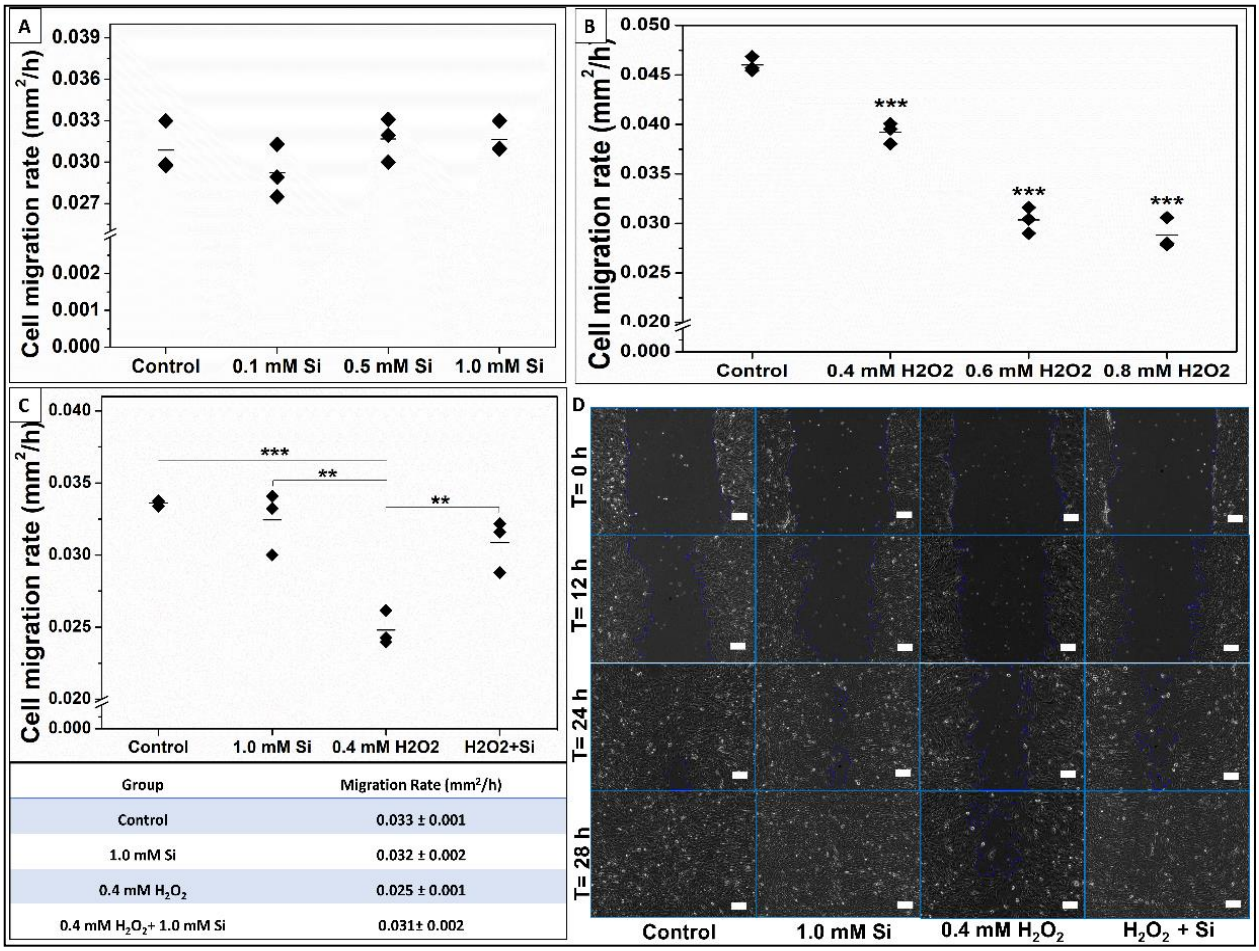

Group	Migration Rate (mm²/h)
Control	0.033 ± 0.001
1.0 mM Si	0.032 ± 0.002
0.4 mM H_2O_2	0.025 ± 0.001
0.4 mM H_2O_2+ 1.0 mM Si	0.031± 0.002

Figure 6.10: Si-ions significantly enhance muscle wound healing by increasing the cells' migration rate under toxic oxidative stress condition. A) Data presents the cell migration rate (mm2 /h) of C2C12 myoblast cells under normal control and three concentrations of Si-ions. Growth media with 0.5-1.0 mM Si-ions enhances the cells' migration rate. B) H2O2 significantly decreases the cells' migration rate under the used concentrations (0.4, 0.6, and 0.8 mM H2O2) (***P<0.001). C) Si-ions attenuate the toxic effect of H2O2 and significantly increase the cells' migration rate under toxic oxidative stress condition. D) Bright field images (10X, scale bar=100 µm) show the wound/scratch area at different time points (0, 12, 24, and 28 hours).

4. DISCUSSION

Our analyses revealed the novel effect of ionic Si-ions on C2C12 myoblasts under normal and toxic oxidative stress conditions. After confirming the positive effect of Si on myoblast functionalities, we studied its effect on C2C12 myoblasts under toxic oxidative

stress conditions produced by H_2O_2 as a source of ROS. Our key results were that ionic Si enhanced the C2C12 viability, proliferation, differentiation, and myogenic gene and marker expression. Importantly, our results indicate that Si-ions at a concentration of 1.0 mM accelerate muscle wound healing by increasing the cell migration rate protecting it from the toxic oxidative damage compared to a positive control. Previous studies had indicated that antioxidants can improve muscle mass recovery [36], enhance viability by reducing muscle cell death [70], and promote the early stages of differentiation by inducing the expression of differentiation markers [28,71,72]. In line with this, our results indicate that Si-ions at a concentration of 0.1 mM can enhance C2C12 cell viability, proliferation, differentiation, and myogenic marker expression, such as MyoG and MyoD, analogous to the antioxidant effect of Si-ions on osteogenesis [41,47,48].

Cell viability and proliferation experiments confirmed that Si-ions at concentrations of 0.1-1.0 mM supports myoblast cell growth, and 0.1 mM Si-ions is the optimal concentration to enhance C2C12 cell viability and proliferation. At early timepoints, all Si-ion concentrations resulted in higher cell numbers compared to the positive control. After 24 hours, 0.1 mM of Si ions in GM significantly increased cell viability compared to the control, congruent with the results of MTS, live/dead assay, and the fluorescent image cell counting. Furthermore, all Si-ion concentrations significantly enhanced C2C12 fusion at an early stage of differentiation (day 4) compared to the control. Specifically, 0.1mM Si-ions significantly increased myoblast fusion as indicated by FI calculations. Also, the size and length of the formed myotubes were more pronounced for the Si-ions groups compared to the control, determined by calculating the area of formed myotubes. It is important to note that the increase of FI and myotube area from

day 4 to day 7 of differentiation occurred despite no change in the total number of cells, counted from DAPI stain, from day 4 to 7 indicating the successful differentiation of C2C12 myoblasts.

This enhancement of C2C12 differentiation can be attributed to the early expression of myogenic markers such as MyoD, which was overexpressed almost 3-fold at day 1 of differentiation compared to control. The effect of Si-ions can be clearly seen from MyoD and MyoG overexpression compared to the Si-free control. MyoG was expressed at a later stage by day 5 to mark the commitment to differentiation. While MyoG expression was significantly increased by 2-fold in the high concentration (1.0 mM) Si-ion group at day 1, an almost 2-fold increase in MyoG expression was observed in both high and low concentration (0.1- and 1.0-mM Si-ions) groups compared to the control at day 5. The early expression of MyoG at day 1 can be attributed to the high dose of Si-ions. Overall, the enhancement in C2C12 cell functionalities such as proliferation and differentiation can be attributed to the antioxidant effect of Si-ions that promotes the early stage of differentiation as indicated by the myogenic marker's expression. The results of this study indicate that certain concentrations of ionic Si promote maximal expression of myogenic biomarkers.

Our results indicated that addition of Si-ions to the differentiation media can increase NRTN, BAIBA, and GABA expression at day 1 of differentiation as compared to the control without Si-ions. Although all Si-ion concentrations increased myokine expression at day 1, myokine expression was drastically reduced as differentiation time increased from day 1 to day 5 for all samples including the control. The initial increase in GABA and D-BAIBA levels followed by reduction in both suggest that myokine

secretion increased, however, the lack of retrograde signaling in vitro resulted in a quick reduction in myokine concentration. On the other hand, it has been well established that ROS has a dose-dependent effect on assisting or hindering tissue regeneration. Low to moderate levels of ROS can enhance regeneration by inducing cell migration and differentiation [29,30]. While high levels of ROS can delay the regeneration process and prolong hospital stays, a common scenario in severe muscle injuries [31,73,74]. Thus, antioxidant supplements have been used to attenuate the harmful effects of high level of ROS in severe injuries [28,73,75].

Excessive oxidative stress is a major contributor for various skeletal muscle tissue pathologies including prolonged severe traumatic injuries, sarcopenia, degenerative diseases and also other muscular atrophies [76]. Severe traumatic injuries and degenerative muscle loss can be due to the presence of additional reactive species and the reduction of the cells capacity to remove it obstructs the cellular repair process along with obstruction in activation of the satellite cells to induce muscle regeneration. Oxidative stresses at higher amounts also creates an imbalance impairing the functionality of proteins and cellular structures, also high concentration of myoglobin in skeletal muscles making it more sensitive to free radical induced oxidative damage especially in chronic degenerative cases [76,77].

Thus, our second aim was to study the effect of Si-ions on C2C12 activity under toxic oxidative stress. Our objectives were to determine the minimal concentration of H_2O_2 needed to induce oxidative damage on C2C12 cells, then determine the optimal Si-ion concentration to counteract or attenuate the effect of H_2O_2. We performed cell viability studies with five different concentrations of H_2O_2 to determine the minimal

concentration of ROS for inducing significant cell death. All used H_2O_2 concentrations had a negative impact on cell viability, but 0.4 mM was the minimum concentration for inducing a strong significant difference (***$p<0.001$). Results of MTS assay and cell counting indicated that 0.2 mM H_2O_2 decreased the number of viable cells by 37%, while 0.4 mM H_2O_2 decreased the number of live cells by 70% at 24 hours. Then, 0.4 mM H_2O_2 was used to study the effect of Si-ions in a toxic oxidative stress environment, and four different concentrations of Si-ions were tested. The results indicated that high concentrations of Si-ions (1.0-2.0 mM) can attenuate the effect of toxic ROS after only 6 hours, while the low concentrations of Si-ions induced significant enhancement of cell viability after 24 hours compared to control. Thus, we concluded that 0.5 mM Si-ions is the optimal concentration of Si-ions for attenuating the effect of toxic H_2O_2 based on a significant increase in cell viability. Furthermore, after determining the effective concentration of H_2O_2 (0.4 mM) and the effective concentration of Si-ions (0.5 mM), a cell differentiation study was performed to investigate if Si-ions have any effect on fusion. FI was increased in the 0.5 mM Si-ion group (22± 5) under oxidative stress conditions compared to 0.4 mM H_2O_2 (18± 6), but no significant difference was observed. Previous studies indicated that antioxidants reduce the deleterious effects of H_2O_2 on cell migration but not cell fusion [28]. Although the FI results are in agreement with this previously reported effect, here we found that 0.5 mM of Si-ions significantly increased the myotube coverage area from 9.5± 2.4% for the 0.4 mM H_2O_2 group to 12.2± 1.6% for the 0.4 mM H_2O_2 + 0.5 mM Si group. This indicates that measuring the myotubes area combined with FI calculations is a more accurate method to assess cell differentiation. This enhancement in cell differentiation under ROS condition with Si

treatment was further confirmed by MyoD and MyoG gene expression analysis.

Our last observation was that 0.5-0.1 mM Si-ions increased the cell's migration rate under normal conditions compared to the control. Furthermore, 1.0 mM Si-ions significantly enhanced muscle wound healing by increasing the cells' migration rate under toxic oxidative stress condition. In a previous study, 0.1 mM H_2O_2 increased C2C12 cell migration rate while the high concentration of 0.5-1mM hindered cell mobility [28]. In line with this, our data indicated that 0.4-0.8 mM H_2O_2 significantly decrease the cells' migration rate that usually results in poor wound healing and prolonged healing time under severe muscle injuries. Adding 1.0 mM Si to the media with H_2O_2 attenuated the toxic effect and enhanced the healing rate under these conditions. It is important to mention the advantages of using the live dynamic imaging technique in such wound-healing assays (see cell migration video, S1). Firstly, it allows to capture cells' migration images at the same exact position over long periods of time until complete wound/scratch healing. Secondly and as, we noted, the scratches closed in 27, 27.8, 35, and 28.7 hours, respectively, a small interval between completion times that may have been overlooked with less frequent imaging. Also, the healing rates based on 6-hour readings were slightly different than the obtained healing rates based on the live dynamic imaging technique. Overall, we can conclude that 1.0 mM Si-ions attenuate the effect of H_2O_2 and enhance cells' migration rate compared to the control.

Additionally, the results of qRT-PCR assays suggest that Si may upregulate the expression of SOD-1 when in the presence of oxidative stress, however, the same effect was not observed under normal conditions or oxidative stress conditions in the absence of Si-ions. Although 0.4 mM H_2O_2 group presented a significant increase in

NRF-2 expression (1.4 fold change), the expression was more pronounced under Si treatment with 1.7 fold change. This suggests that Si-ions may play a role in mitigating the effects of excessive reactive oxidative species by upregulating antioxidant markers. H_2O_2 can react with metal ions in the cells to produce hydroxyl radical which is one of the most reactive species in the biological systems [78]. High levels of ROS with imbalanced antioxidants expression usually generates an oxidative stress that leads to degenerative changes to muscle with all of the characteristics of a muscular dystrophy [76–79]. In this regard, Si treatment could be a beneficial approach for upregulation of SOD-1 in some muscle dystrophies related SOD deficiencies. Furthermore, the cells' migration results combined with cell viability and differentiation indicate that ionic Si may have a potential role in unfavorable situations where ROS are predominant, to protect from oxidative damage and inducing muscle cell regeneration in case of traumatic muscle injury and delaying the degenerative process of the muscle improving the life expectancy in degenerative muscle diseases.

5. CONCLUSIONS

In this study, we explored the effect of Si-ions on C2C12 skeletal muscle cell myogenesis, such as proliferation, migration, differentiation, and myogenic biomarker expression to gain insight into its role on myogenesis during the early stages of muscle regeneration. In vitro studies indicated the addition of 0.1 mM Si-ions to media significantly increased cells' viability, proliferation, migration, and myotube formation compared to control. Also, Si-ions significantly increased MyoG and MyoD gene expression within 5 days of C2C12 myoblast differentiation. Si-ions attenuated the toxic effects of H2O2 within 24 hours resulting in increased cells' viability and differentiation

compared to the 0.4 mM H_2O_2 group. Also, 1.0 mM Si-ions increased the cells' migration rate with a significant decrease in the scratch healing time to achieve faster healing under oxidative stress conditions. The observed upregulation of NRF-2 and SOD-1 in the 0.5mM Si + 0.4mM H_2O_2 group combined with the lack of a significant difference in expression for groups containing only Si-ions or only H_2O_2 suggest that Si-ions at optimal concentrations may enhance ROS metabolism and clearance in C2C12 cells under oxidative stress. These results indicate that ionic Si may have antioxidant and stimulatory effects on muscle tissue to promote skeletal muscle repair. Thus, this study provides novel evidence of the potential role of Si-ions that influence the cellular response during the myogenesis process and pave the way for designing Si-containing biomaterials with desirable Si-ions release for muscle tissue regeneration applications along with muscle drug delivery systems for degenerative disease conditions.

Supplementary Materials: can be found at www.mdpi.com/xxx/s1.

Author Contributions: Conceptualization, V.V. and K.A.; methodology, K.A.; software, K.A. and M.F; validation, K.A., N.A. and M.F.; formal analysis, K.A.; investigation, K.A. S.P., and Z. W.; resources, V.V.; data curation, K.A.; writing—original draft preparation, K.A.; writing—review and editing, K.A. and M. F; visualization, K.A.; supervision, V.V., P.A., and M.B; project administration, V.V, and M.B.; funding acquisition, V.V. All authors have read and agreed to the published version of the manuscript.

Funding: This research was funded by the University of Texas STARS award and the National Institutes of Health (Grant Number 1R03DE023872-01, 1R56DE027964-01A1-01, NIH S10OD025230). Also, CRS Pilot Grant from the College of Nursing and Health Innovation at UTA.

Acknowledgments: The authors would like to thank Dr. Jian Huang, Dr. Chenglin Mo, and Dr. Leticia Brotto, for their assistance and the helpful discussion. We would also like to acknowledge our other lab members, Thy Than Vo and Yan Chang for their time and contribution towards this manuscript.

Conflicts of Interest: The authors declare no conflict of interest.

REFERENCES

1. Nakayama, K. H. et al. Treatment of volumetric muscle loss in mice using nanofibrillar scaffolds enhances vascular organization and integration. Commun. Biol. 2, 170 (2019).
2. Goldman, S. M., Henderson, B. E. P., Walters, T. J. & Corona, B. T. Co-delivery of a laminin-111 supplemented hyaluronic acid based hydrogel with minced muscle graft in the treatment of volumetric muscle loss injury. PLoS One 13, e0191245 (2018).
3. Kasukonis, B. et al. Codelivery of Infusion Decellularized Skeletal Muscle with Minced Muscle Autografts Improved Recovery from Volumetric Muscle Loss Injury in a Rat Model. Tissue Eng. Part A 22, 1151–1163 (2016).
4. Corona, B. T. et al. Autologous minced muscle grafts: a tissue engineering therapy for the volumetric loss of skeletal muscle. Am. J. Physiol. Physiol. 305, C761–C775 (2013).
5. Hurtgen, B. J. et al. Autologous minced muscle grafts improve endogenous fracture healing and muscle strength after musculoskeletal trauma. Physiol. Rep. 5, e13362 (2017).
6. Corona, B. T., Rivera, J. C., Wenke, J. C. & Greising, S. M. Tacrolimus as an

adjunct to autologous minced muscle grafts for the repair of a volumetric muscle loss injury. J. Exp. Orthop. 4, 36 (2017).

7. Corona, B. T., Henderson, B. E. P., Ward, C. L. & Greising, S. M. Contribution of minced muscle graft progenitor cells to muscle fiber formation after volumetric muscle loss injury in wild-type and immune deficient mice. Physiol. Rep. 5, e13249 (2017).
8. Turner, N. J. et al. Xenogeneic Extracellular Matrix as an Inductive Scaffold for Regeneration of a Functioning Musculotendinous Junction. Tissue Eng. Part A 16, 3309–3317 (2010).
9. Valentin, J. E., Turner, N. J., Gilbert, T. W. & Badylak, S. F. Functional skeletal muscle formation with a biologic scaffold. Biomaterials 31, 7475–7484 (2010).
10. Corona, B. T. et al. Further development of a tissue engineered muscle repair construct in vitro for enhanced functional recovery following implantation in vivo in a murine model of volumetric muscle loss injury. Tissue Eng. Part A 18, 1213–1228 (2012).
11. Merritt, E. K. et al. Repair of traumatic skeletal muscle injury with bone-marrow-derived mesenchymal stem cells seeded on extracellular matrix. Tissue Eng. Part A 16, 2871–2881 (2010).
12. Corona, B. T., Rivera, J. C., Dalske, K. A., Wenke, J. C. & Greising, S. M. Pharmacological Mitigation of Fibrosis in a Porcine Model of Volumetric Muscle Loss Injury. Tissue Eng. Part A 26, 636–646 (2019).
13. Quintero, A. J., Wright, V. J., Fu, F. H. & Huard, J. Stem cells for the treatment of skeletal muscle injury. Clin. Sports Med. 28, 1–11 (2009).

14. Stilhano, R. S., Martins, L., Ingham, S. J. M., Pesquero, J. B. & Huard, J. Gene and cell therapy for muscle regeneration. Curr. Rev. Musculoskelet. Med. 8, 182–187 (2015).

15. Rizzi, R. et al. Tissue engineering for skeletal muscle regeneration. Muscles. Ligaments Tendons J. 2, 230–234 (2012).

16. Patel, A. et al. Carbon-based hierarchical scaffolds for myoblast differentiation: Synergy between nano-functionalization and alignment. Acta Biomater. 32, 77–88 (2016).

17. Greising, S. M., Corona, B. T., McGann, C., Frankum, J. K. & Warren, G. L. Therapeutic Approaches for Volumetric Muscle Loss Injury: A Systematic Review and Meta-Analysis. Tissue Eng. - Part B Rev. 25, 510–525 (2019).

18. Poussard, S. et al. Internalization and fate of silica nanoparticles in C2C12 skeletal muscle cells: Evidence of a beneficial effect on myoblast fusion. Int. J. Nanomedicine 10, 1479–1492 (2015).

19. Quiroga, H. P. O., Goto, K. & Zammit, P. S. Skeletal Muscle Regeneration in the Mouse. Methods Mol. Biol. 1460, 85–100 (2016).

20. Gurevich, D., Siegel, A. & Currie, P. D. Vertebrate Myogenesis. Results Probl. Cell Differ. 56, 191–213 (2015).

21. Shintaku, J. et al. MyoD Regulates Skeletal Muscle Oxidative Metabolism Cooperatively with Alternative NF-κB. Cell Rep. 17, 514–526 (2016).

22. Han, X. H., Jin, Y.-R., Seto, M. & Yoon, J. K. A WNT/beta-catenin signaling activator, R-spondin, plays positive regulatory roles during skeletal myogenesis. J. Biol. Chem. 286, 10649–10659 (2011).

23. Pedersen, B. K. Muscles and their myokines. J. Exp. Biol. 214, 337–346 (2011).
24. Rai, M. & Demontis, F. Systemic Nutrient and Stress Signaling via Myokines and Myometabolites. Annu. Rev. Physiol. 78, 85–107 (2016).
25. Kitase, Y. et al. β-aminoisobutyric Acid, L-BAIBA, Is a Muscle-Derived Osteocyte Survival Factor. Cell Rep. 22, 1531–1544 (2018).
26. Mills, R. et al. Neurturin is a PGC-1α1-controlled myokine that promotes motor neuron recruitment and neuromuscular junction formation. Mol. Metab. 7, 12–22 (2018).
27. Ji, L. L. Exercise at Old Age: Does It Increase or Alleviate Oxidative Stress? Ann. N. Y. Acad. Sci. 928, 236–247 (2001).
28. Bosutti, A. & Degens, H. The impact of resveratrol and hydrogen peroxide on muscle cell plasticity shows a dose-dependent interaction. Sci. Rep. 5, (2015).
29. Powers, S. K., Talbert, E. E. & Adhihetty, P. J. Reactive oxygen and nitrogen species as intracellular signals in skeletal muscle. J. Physiol. 589, 2129–2138 (2011).
30. Bae, Y. S., Oh, H., Rhee, S. G. & Yoo, Y. Do. Regulation of reactive oxygen species generation in cell signaling. Mol. Cells 32, 491–509 (2011).
31. Siu, P. M., Wang, Y. & Alway, S. E. Apoptotic signaling induced by H2O2-mediated oxidative stress in differentiated C2C12 myotubes. Life Sci. 84, 468–481 (2009).
32. Harrison, D. G. Basic science: Pathophysiology: oxidative stress. J. Am. Soc. Hypertens. 8, 601–603 (2014).
33. Hernández, A., Cheng, A. & Westerblad, H. Antioxidants and Skeletal Muscle

Performance: ‘Common Knowledge’ vs. Experimental Evidence. Front. Physiol. 3, 46 (2012).

34. Leelayuwat, N. Chapter 19 - Update of Nutritional Antioxidants and Antinociceptives on Improving Exercise-Induced Muscle Soreness. in (ed. Watson, R. R. B. T.-P. A. and the A. B.) 199–208 (Academic Press, 2017). doi:https://doi.org/10.1016/B978-0-12-805094-1.00019-8.

35. Drowley, L. et al. Cellular antioxidant levels influence muscle stem cell therapy. Mol. Ther. 18, 1865–1873 (2010).

36. Bennett, B. T., Mohamed, J. S. & Alway, S. E. Effects of resveratrol on the recovery of muscle mass following disuse in the plantaris muscle of aged rats. PLoS One 8, e83518–e83518 (2013).

37. Pallafacchina, G., Blaauw, B. & Schiaffino, S. Role of satellite cells in muscle growth and maintenance of muscle mass. Nutr. Metab. Cardiovasc. Dis. 23, S12–S18 (2013).

38. Henstock, J. R., Canham, L. T. & Anderson, S. I. Silicon: The evolution of its use in biomaterials. Acta Biomater. 11, 17–26 (2015).

39. Gaharwar, A. K. et al. Bioactive silicate nanoplatelets for osteogenic differentiation of human mesenchymal stem cells. Adv. Mater. 25, 3329–3336 (2013).

40. do Monte, F. A. et al. Silicon Oxynitrophosphide Nanoscale-Coating Enhances Antioxidant Marker -Induced Angiogenesis During In Vivo Cranial Bone Defect Healing. JBMR Plus n/a, e10425 (2020).

41. Ilyas, A., Lavrik, N. V, Kim, H. K. W., Aswath, P. B. & Varanasi, V. G. Enhanced Interfacial Adhesion and Osteogenesis for Rapid “Bone-like” Biomineralization by

PECVD-Based Silicon Oxynitride Overlays. ACS Appl. Mater. Interfaces 7, 15368–15379 (2015).

42. Monte, F. A. do et al. Amorphous Silicon Oxynitrophosphide-Coated Implants Boost Angiogenic Activity of Endothelial Cells. Tissue Eng. Part A 26, 15–27 (2019).

43. Heublein, B., Ozbek, C. & Pethig, K. Silicon carbide-coated stents: clinical experience in coronary lesions with increased thrombotic risk. J. Endovasc. Surg. 5, 32—36 (1998).

44. Awad, K. R. et al. Silicon nitride enhances osteoprogenitor cell growth and differentiation via increased surface energy and formation of amide and nanocrystalline HA for craniofacial reconstruction. Med. DEVICES SENSORS 2, e10032 (2019).

45. McEntire, B. J. & Lakshminarayanan, R. Processing and Characterization of Silicon Nitride Bioceramics. Bioceram. Dev. Appl. 6, 1–9 (2016).

46. Varanasi, V. G. et al. Role of Hydrogen and Nitrogen on the Surface Chemical Structure of Bioactive Amorphous Silicon Oxynitride Films. J. Phys. Chem. B 121, 8991–9005 (2017).

47. Ilyas, A. et al. Rapid Regeneration of Vascularized Bone by Nanofabricated Amorphous Silicon Oxynitrophosphide (SiONP) Overlays. J. Biomed. Nanotechnol. 15, 1241–1255 (2019).

48. Monte, F. et al. Ionic silicon improves endothelial cells' survival under toxic oxidative stress by overexpressing angiogenic markers and antioxidant enzymes. J. Tissue Eng. Regen. Med. 12, 2203–2220 (2018).

49. Cebe, T. et al. Novel 3D-printed methacrylated chitosan-laponite nanosilicate composite scaffolds enhance cell growth and biomineral formation in MC3T3 pre-osteoblasts. J. Mater. Res. 35, 58–75 (2020).

50. Bhuyan, M. K., Rodriguez-Devora, J. I., Fraser, K. & Tseng, T. L. B. Silicon substrate as a novel cell culture device for myoblast cells. J. Biomed. Sci. 21, 4–8 (2014).

51. AWAD, K. R. et al. Micro-patterned Bioactive Amorphous Silicon Oxynitride Enhances Adhesion, Growth, and Myotubes and Axon Alignment in Muscle and Nerve Cells. FASEB J. 34, 1 (2020).

52. Ahuja, N. et al. Preliminary study of in-situ 3D bioprinted nano-silicate biopolymer scaffolds for muscle repair in VML defects. FASEB J. 34, 1 (2020).

53. Awad, K. R. et al. Patterned Silicon Oxynitride (SiONx) Scaffolds Enhance Alignment and Myogenic Differentiation of C2C12 Muscle Cells. FASEB J. 33, 539.5-539.5 (2019).

54. Perry, C. C. An Overview of Silica in Biology: Its Chemistry and Recent Technological Advances BT - Biosilica in Evolution, Morphogenesis, and Nanobiotechnology: Case Study Lake Baikal. in (eds. Müller, W. E. G. & Grachev, M. A.) 295–313 (Springer Berlin Heidelberg, 2009). doi:10.1007/978-3-540-88552-8_13.

55. Han, P., Wu, C. & Xiao, Y. The effect of silicate ions on proliferation, osteogenic differentiation and cell signalling pathways (WNT and SHH) of bone marrow stromal cells. Biomater. Sci. 1, 379–392 (2013).

56. Zou, S., Ireland, D., Brooks, R. A., Rushton, N. & Best, S. The effects of silicate

ions on human osteoblast adhesion, proliferation, and differentiation. J. Biomed. Mater. Res. B. Appl. Biomater. 90, 123–130 (2009).

57. Bobadilla, A. V. P. et al. In vitro cell migration quantification method for scratch assays. J. R. Soc. Interface 16, 20180709 (2019).

58. Simerabet, M. et al. Preconditioning by an in situ administration of hydrogen peroxide: Involvement of reactive oxygen species and mitochondrial ATP-dependent potassium channel in a cerebral ischemia–reperfusion model. Brain Res. 1240, 177–184 (2008).

59. Lin, M., Zhou, S. & Sakamoto, K. Alpha Mangostin promotes myogenic differentiation of C2C12 mouse myoblast cells. Biochem. Biophys. Res. Commun. 528, 193–198 (2020).

60. Jähn, K. et al. Skeletal muscle secreted factors prevent glucocorticoid-induced osteocyte apoptosis through activation of β-catenin. Eur. Cell. Mater. 24, 197–210 (2012).

61. Mo, C., Romero-Suarez, S., Bonewald, L., Johnson, M. & Brotto, M. Prostaglandin E2: from clinical applications to its potential role in bone- muscle crosstalk and myogenic differentiation. Recent Pat. Biotechnol. 6, 223–229 (2012).

62. Huang, J. et al. Fibroblast growth factor 9 (FGF9) inhibits myogenic differentiation of C2C12 and human muscle cells. Cell Cycle 18, 3562–3580 (2019).

63. Huang, J. et al. Crosstalk between MLO-Y4 osteocytes and C2C12 muscle cells is mediated by the Wnt/β-catenin pathway. JBMR plus 1, 86–100 (2017).

64. Huang, J. et al. METTL21C is a potential pleiotropic gene for osteoporosis and

sarcopenia acting through the modulation of the NF-κB signaling pathway. J. Bone Miner. Res. 29, 1531–1540 (2014).

65. Rasband, W. ~S. ImageJ: Image processing and analysis in Java. ascl:1206.013 (2012).

66. Silva Nunes, J. P. & Martins Dias, A. A. ImageJ macros for the user-friendly analysis of soft-agar and wound-healing assays. Biotechniques 62, 175–179 (2017).

67. Varanasi, V. G. et al. Enhanced osteocalcin expression by osteoblast-like cells (MC3T3-E1) exposed to bioactive coating glass (SiO2–CaO–P2O5–MgO–K2O–Na2O system) ions. Acta Biomater. 5, 3536–3547 (2009).

68. Wang, Z. et al. Quantification of aminobutyric acids and their clinical applications as biomarkers for osteoporosis. Commun. Biol. 3, 39 (2020).

69. Cory, G. Scratch-wound assay. Methods Mol. Biol. 769, 25–30 (2011).

70. Dirks Naylor, A. J. Cellular effects of resveratrol in skeletal muscle. Life Sci. 84, 637–640 (2009).

71. Montesano, A., Luzi, L., Senesi, P., Mazzocchi, N. & Terruzzi, I. Resveratrol promotes myogenesis and hypertrophy in murine myoblasts. J. Transl. Med. 11, 310 (2013).

72. Kaminski, J. et al. Resveratrol initiates differentiation of mouse skeletal muscle-derived C2C12 myoblasts. Biochem. Pharmacol. 84, 1251–1259 (2012).

73. Valko, M. et al. Free radicals and antioxidants in normal physiological functions and human disease. Int. J. Biochem. Cell Biol. 39, 44–84 (2007).

74. Gilliver, S. F., Jones, D. A., Rittweger, J. & Degens, H. Effects of oxidation on the

power of chemically skinned rat soleus fibres. J. Musculoskelet. Neuronal Interact. 10, 267–273 (2010).

75. Jackson, J. R., Ryan, M. J. & Alway, S. E. Long-term supplementation with resveratrol alleviates oxidative stress but does not attenuate sarcopenia in aged mice. J. Gerontol. A. Biol. Sci. Med. Sci. 66, 751–764 (2011).

76. Rando, T. A. Oxidative Stress and the Pathogenesis of Muscular Dystrophies. Am. J. Phys. Med. Rehabil. 81, (2002).

77. Murphy, M. E. & Kehrer, J. P. Oxidative stress and muscular dystrophy. Chem. Biol. Interact. 69, 101–173 (1989).

78. Halliwell, B. & Gutteridge, J. M. Role of free radicals and catalytic metal ions in human disease: an overview. Methods Enzymol. 186, 1–85 (1990).

79. Rando TA, Crowley RS, Carlson EJ, Epstein CJ, M. P. Overexpression of copper/zinc superoxide dismutase: A novel cause of murine muscular dystrophy. Annals of Neurology vol. 44 381–386.

CHAPTER 7: FACILE APPROACH FOR AMORPHOUS SILICA BASED NANOPARTICLES SYNTHESIS

Kamal Awad[1, 2, 3], Pranesh Aswath[1], and Venu Varanasi[1, 2, *]

[1]Department of Materials Science and Engineering, College of Engineering, University of Texas at Arlington, Texas 76019, USA

[2]Bone-Muscle Research Center, College of Nursing & Health Innovation, University of Texas at Arlington, Texas 76019, USA

[3]Department of Ceramics and Building materials, National Research Center, Dokki, Cairo, Egypt, 12622.

*Corresponding Authors,

Dr. Venu Varanasi, (Venu.varanasi@uta.edu)

Phone: 817-272-1743

Associate Professor, Bone Muscle Research Center

College of Nursing and Health Innovation

University of Texas at Arlington

Address: 655 W. Mitchell St.,

Box 19410, Arlington,

TX 76019

ABSTRACT

Bioactive amorphous silica nanoparticles and surface modified silica nanoparticles with different surface chemistry are promising nanomaterials for drug delivery and biomodulation applications. In this study, novel approaches were introduced and tested towards synthesis of pure amorphous silica nanoparticles and surface modified silica nanoparticles with SiONx and SiONPx-based structures. Facile and novel approach based on the natural silicification process was tested to rapid hydrolysis and condensation of TEOS, Si-precursor, via imidazole and glucose assistance as catalysts. Another approach utilized APTES, Si-precursor with terminal amine group, to synthesize silica nanoparticles with SiONx-based structure. Phosphoric acid was utilized to modify these two approaches to synthesize amorphous silica nanoparticles containing phosphorus with SiONPx-based structure. Our results indicated the viability of these approaches to synthesize nanosilica and successful nitrogen and phosphorus incorporation in the silica network. The synthesized pure silica and SiONx-based nanoparticles indicated mono-dispersion of spherical shaped nanoparticles as seen by HR-SEM, with amorphous nature as indicated from the XRD and TEM analysis. SiONPx approaches yield nanoscale silica with nitrogen and phosphorus incorporated. Furthermore, hydrolysis of TEOS-H_3PO_4 in presence of imidazole and glucose lead to spherical-corona shape “virus-like” nanoparticles formation that could be potential in drug delivery systems and biomodulation applications. This study concluded that the proposed approaches are successful in synthesis and in-situ surface functional modification of amorphous silica nanoparticles.

Keywords: Amorphous nanosilica; Bioactive, Biomodulation; Surface modification.

1. INTRODUCTION

Silica nanoparticles (Si-NPs) are one of the most extensively explored nanomaterial in the field of nanotechnology and nanobiotechnology due to their unique characteristics such as high surface area, excellent biocompatibility, capability for drug's load and release, and tunable surface chemistry [1–3]. Furthermore, Si-NPs have been granted great attention in diverse fields and applications due to the possibility to control the particle size, shape, porosity, crystallinity, and the easiness to synthesize it in different forms such as solid particles, mesoporous, hollow or core-shell, rod shaped particles, and virus-form silica [4–6]. Thus, Si-NPs have been widely used in agricultural field, food industry, drug delivery, and industrial applications [1,2,5,7]. On top of that, Si-NPs have been emerged in various investigations as a promising platform for constructing drug delivery systems, diagnostic, and medical imaging [1,8,9]. In this regard, recently the silica-based drug Cornell Dots has been approved by the United States Food and Drug Administration (FDA) for molecular imaging of cancer for first-in-human clinical trials [10]. In addition, ciprofloxacin loaded amorphous Si-NPs exhibited a sustained release of the ciprofloxacin good bacterial inhibition against E. coli and S. aureus as reported by Araichimani et. al., 2020 [11]. Most recent, Si-NPs have reached the field of 3D printing for targeted and specific hydrogels modifications. Si-NPs loaded into alginate–gelatin composite hydrogels have increased the scaffolds printability, significantly improved the compressive modulus, inhibited the swelling and degradation properties, and significantly increased the biocompatibility and osteogenic activity [12].

On the other hand, the inert nature of the bare silica allowed it to have a double-edged sword role that was reflected on Si-NPs applications over the last decades. The

inert nature minimizes the negative impact of Si-NPs on biological systems and ensures good biocompatibility, while it largely restricted the functionalities of Si-NPs and its application as biomodulators. Yet, knowledge of controlling the Si-NPs surface functionality and taking advantages of the silica chemistry to shift Si-NPs from nanocarriers to biomodulation is still rare. In this regard, Yang et al., in 2020, targeted novel Si-NPs designed as biomodulators to regulate intracellular microenvironment and cell signaling, such as the oxidative stress and antioxidants levels for improving the anticancer efficacy of therapeutics and mRNA transfection in specific cell lines [8]. They concluded that diversified functionality of the Si-NPs could bring unpredictable risks in biosystems, thus one specific function for one specific target is recommended. Also, Varanasi et al., provided promising knowledge on amorphous silica-based thin film coatings with different surface chemistry (e.g., silicon nitride SiONx, and silicon oxynitrophosphide SiONPx) that targeted specific cell signaling such as antioxidant and osteogenic activity [13–19]. These amorphous silica-based coatings indicated a sustained release of ionic silicon that enhances osteogenesis [20], antioxidant activity [16,20], surface hydroxyapatite formation [14,21], improves endothelia cells survival by mitigating oxidative stress [13,14,22,23], and recently enhances myogenesis in skeletal muscle cells via myogenic and antioxidant expression [15]. However, the availability of these amorphous silica-based bioactive materials only as thin-films coatings on metal substrates, by plasma enhanced chemical vapor deposition, restrict their applications in soft tissue regeneration applications and 3D printing technologies.

In this study, we targeted specific facile and reproducible synthesis approach to create amorphous Si-NPs with different surface functionality. This approach is based on

mimicking the role of the active sites (i.e., histidine and silicatein) during the natural silicification process in sponges by using structurally similar chemicals such as imidazole and glucose in the presence of Si-precursors. Synthesis of SiO_x/SiONx/SiONPx-nanoparticles were targeted based on the hydrolysis of Tetraethyl Orthosilicates (TEOS, Si-precursor) and 3-Aminopropyl triethoxysilane (APTES, Si-precursor) in the presence of phosphoric acid (H_3PO_4) as the source of phosphorus and the use of glucose and imidazole as catalysts. The synthesized bio-inspired nanoparticles were characterized using different techniques and the proposed mechanism for each reaction was discussed.

2. MATERIALS AND METHODS:

2.1 Materials

The chemicals and materials required for the synthesis of Si-NPs in this study are as follows. Tetraethyl orthosilicate (TEOS, MW= 208.33 g/mol, Purity 98%, d= 0.0.933 g/ml) and 3-Aminopropyl triethoxysilane (APTES, MW=221.37 g/mol, Purity 99%, d= 0.949 g/ml) as Si-precursors were purchased from Sigma-Aldrich, USA. Phosphoric acid powder (H_3PO_4, MW= 98 g/mol, Purity 99%) was purchased from Fluka analytical, Munich, and used as source of phosphorus. Pure ethyl alcohol (Ethanol, MW= 46.07 g/mol, d= 0.797 g/ml) was purchased from Sigma-Aldrich, USA.

2.2 Synthesis of Amorphous SiO_x Nanoparticles (Rxn 1):

Firstly, imidazole and glucose were grinded to fine powders to facilitate their solubility, and then the two powders were sufficiently mixed (powder mix). TEOS solution was added to the powder mix and mixed using touch mixer (vortex) for 5 minutes until all powders are dissolved or slightly dissolved. The ratio of TEOS to

imidazole and glucose was 1:2 mole ratio. Then, water was added to the mixture with 2:1 mole ratio to TEOS, and then mixed using touch mixer for 30 seconds or clear solution was observed, then allowed to react for 10, 30, 60, 120, 180, and 360 minutes. White precipitate can be seen in the mixture within 10 minutes of the reaction, this precipitate is formed in a solution of water and ethanol, which is released as by product of the above reactions. After each time point, 90% ethanol (≥99.5%) was added to stop the reaction, and the solution was mixed for 2 minutes. Then, solution was centrifuged for 15 minutes at 4000 rpm, to settle down the stable precipitate at the bottom. The precipitate was collected by removing the supernatant, the precipitate was washed 3 times with DI water and ethanol to dissolve and remove any unreacted glucose or imidazole. Finally, the white precipitate was suspended in ethanol and allowed to dry in oven at 37 °C overnight. The schematic of the synthesis process is as shown in Figure 7-1A. The particles generated from this mechanism are termed as amorphous silica (SiO_x) nanoparticles.

2.3 Synthesis of Amorphous $SiON_x$ Nanoparticles (Rxn 2):

For amorphous $SiON_x$, 15 mL of pure ethanol was added to a beaker and ultrasonicated. TEOS and APTES were added simultaneously to the ethanol while continuously being sonicated. The mixture was then left at room temperature for 10 minutes. After 10 minutes, 0.5 mL of DI water was titrated at a rate of 12 mL/1 hr. The mixture was then allowed to react for 3 hours while continuously being ultrasonicated, over time, the mixture was observed to be cloudier and whiter over time. After 3 hours, pure ethanol (≥99.5%) was added to stop the reaction, and the solution was mixed for 2 minutes. Then, solution was centrifuged for 15 minutes at 4000 rpm, the precipitate was

collected by removing the supernatant and washed 3 times with DI water. Then, the white precipitate was washed in ethanol and allowed to dry in 37 °C oven overnight. The schematic of the synthesis process is as shown in Figure 7-1B. The particles synthesized from this mechanism are termed as amorphous silica ($SiON_x$).

2.4 Synthesis of Amorphous $SiONP_x$ Nanoparticles

For amorphous $SiONP_x$, two approaches were tested based on the SiOx and SiONx synthesis mechanisms that were mentioned above.

***(1) In the first approach (Rxn 3)*:** powder mix of imidazole and glucose was disolved in 2.5 mL of Ethanol. In a separate container, 2.5 ml of TEOS solution was mixed with 1.178 ml of phosphoric acid (H_3PO_4). The first mixture of glucose and imidazole in ethanol was added to the second mixture of TEOS and H_3PO_4 using touch mixer for 5 minutes untill all powders are dissolved or slightly dissolved. 1.5 mL of water was added to the mixture, and then mixed using touch mixer for 30 seconds or clear solution was observed, the mixture was allowed to react for 30 minutes. After 30 minutes, 90% ethanol was added to stop the reaction and the same procedure was continued as in SiO_X nanoparticles in section 2.2. The nanoparticles obtained from this reaction labeled as SiONPx1. The schematic of the synthesis process is as shown in Figure (1-C).

(2) *In the second approach* (Rxn 4): 2.5 ml of TEOS solution was mixed with 1.178 ml of phosphoric acid (H_3PO_4) and allowed to react for 3 minutes. Then, TEOS-H_3PO_4 mixture and APTES were added simultaneously to the beaker containing 15 ml of absolute ethanol while continuously being sonicated. Then, the procedure was

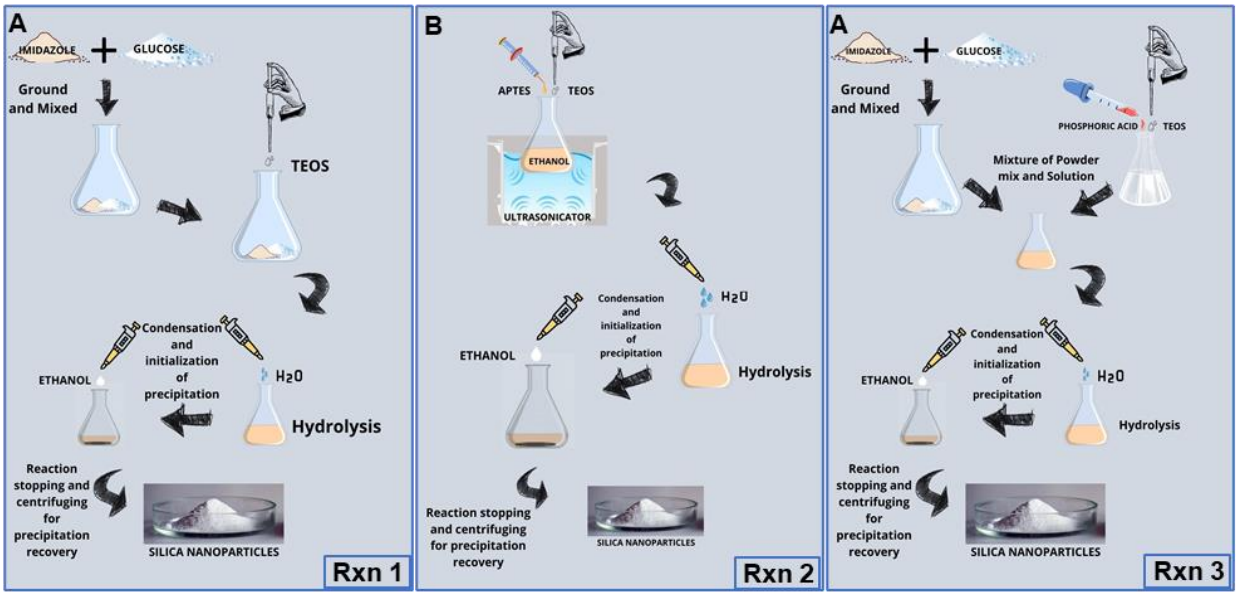

Figure 7.1: Schematic diagram of the proposed SiOx, SiONx, and SiONPx nanoparticles reactions.

continued as in Rxn 2 (Section 2.3: synthesis of amorphous $SiON_x$ nanoparticles). The nanoparticles obtained from this reaction labeled as $SiONP_{x2}$.

2.5 Nanoparticles characterization

After drying the nanoparticles obtaining from each reaction, the yield-weight of each reaction was recorded. The morphology and particles size were investigated using ultra–High-Resolution Scanning Electron Microscope (HR-SEM, Hitachi S-4800 II FE SEM, Hitachi). For HR-SEM imaging, samples were prepared as follows; 1.0 mg of the nanoparticles was suspended in 1.0 ml of absolute ethanol and ultrasonicated for 20 minutes to allow the dispersion of the Si-NPs. Then, one drop was seeded on a clean silicon wafer and allowed to dry in 37 °C oven to be used for imaging. For compositional analysis of the prepared nanoparticles, nanoparticles powders were compressed into a small disk shape and characterized using energy dispersive X-ray (EDX) coupled with SEM (S-3000N, Hitachi, Japan), X-ray diffraction analysis (Bruker D8 Advance X-ray diffractometer), raman spectroscopy (DXR Raman Microscope), and high-resolution transmission electron microscopy (TEM, Hitachi H-9500, Japan).

3. RESULTS:

Morphology and particles size of the synthesized Si-NPs were characterized using ultra-HR-SEM. Figure 2 shows the amorphous SiOx nanoparticles obtained from

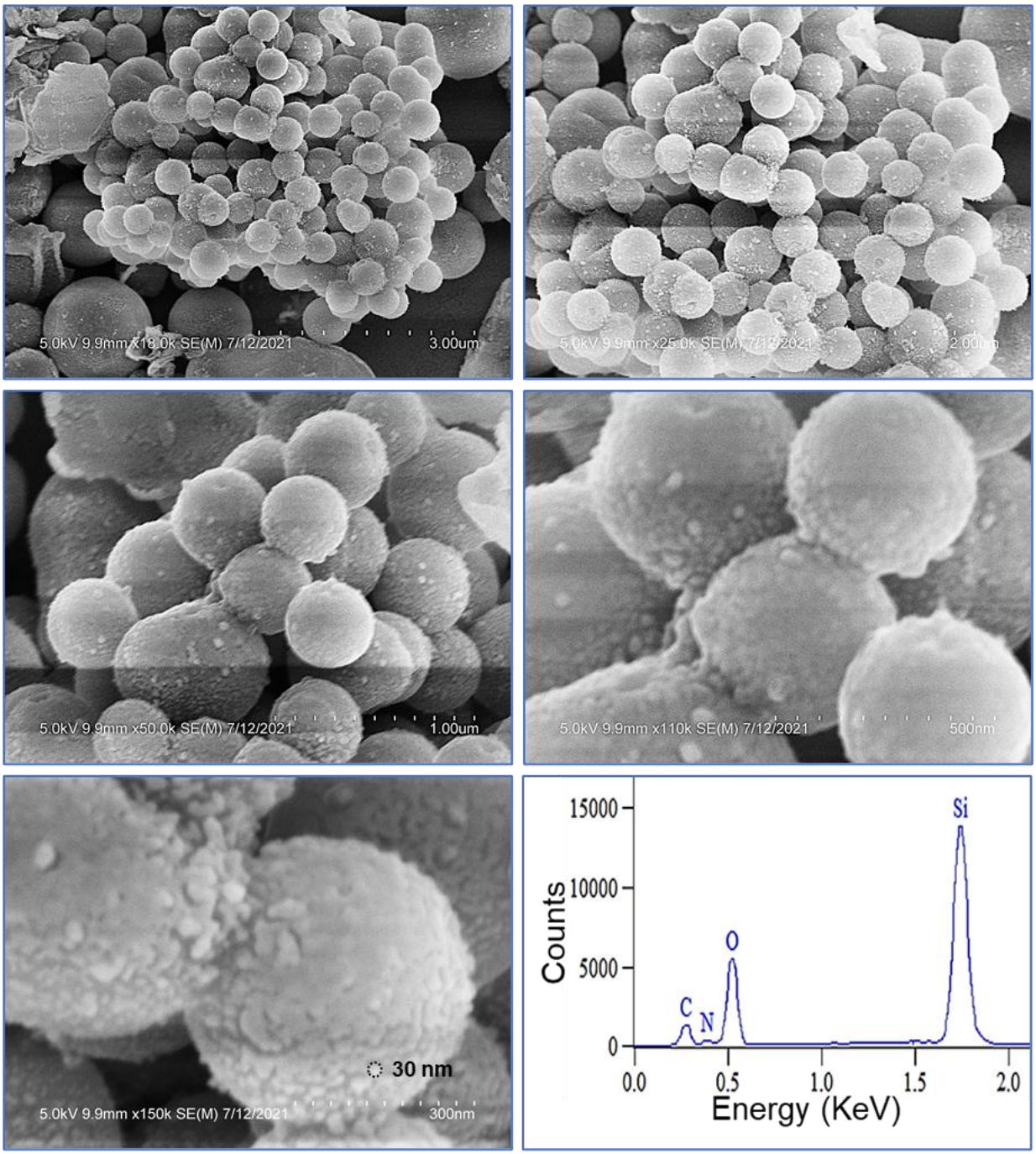

Figure 7.2: HR-SEM images of the amorphous SiOx nanoparticles and the EDX spectra showing the compositional analysis. Images are at different magnifications 18k, 25k, 50k, 110k, and 150k.

Rxn 1 (TEOS hydrolysis and condensation within glucose and imidazole presence) that presented complete spherical shape and monodispersed nanosized particles with low aggregation degree. The high magnification (150 K) revealed that the particles size is approximately 30 nm. The EDX spectra indicated the presence of silicon (Si = 28.1±0.06 at%), oxygen (O = 60.57±0.85 at%) as well as small amount of carbon (c = 10.13±0.63 at%) and nitrogen (N = 1.18±0.15 at%). According to SiO_x synthesis reaction (Rxn 1), white precipitate was observed at 10 minutes indicating rapid hydrolysis and condensation. Thus, different reaction-times were tested to determine the optimal reaction-time for TEOS hydrolysis and condensation utilizing glucose and imidazole as catalysts. Series of reactions were performed at time range from 10 minutes to 360 minutes and the yield-weight was measure after obtaining the dried nanoparticles. Figure 7.3 presents the SiO_x NPs yield in mg versus the reaction time.

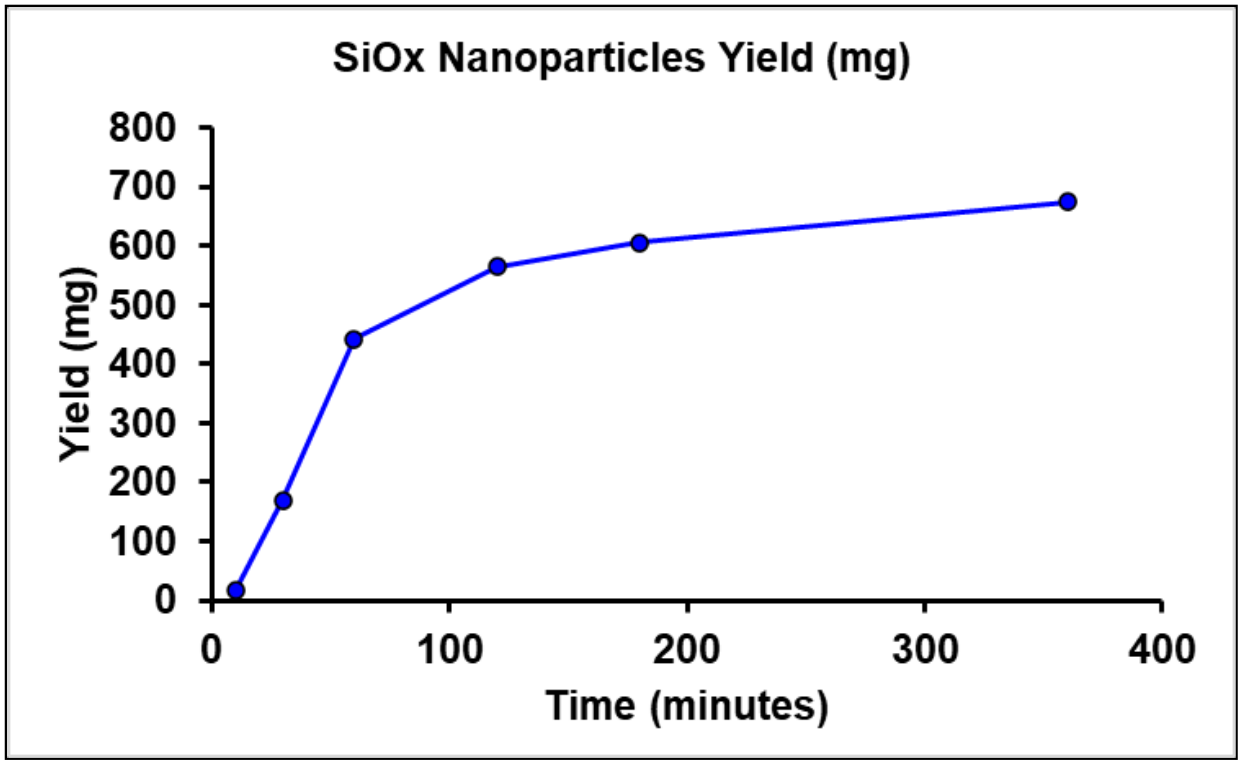

Figure 7.3: Amorphous SiO_x nanoparticles yield versus the reaction time.

At 10 minutes, the yield of SiOx nanoparticles was 16 mg which increased over time until 675 mg after 6 hours of TEOS reaction. It was noticed that there is no significant change in the yield after 3 hours (yield = 605 mg) of reaction time as seen by the plateau stage in Figure 7.3.

Figure 7.4 shows the HR-SEM images of the synthesized nanoparticles obtained from Rxn 2, co-condensation of APTES and TEOS. The amorphous $SiON_x$ nanoparticles presented incomplete spherical shape of monodispersed nanosized particles with high aggregation degree. The high magnification (180 K) SEM images revealed that the particles size is in the range of 30-35 nm as measured using ImageJ software. The EDX spectra (Figure 7.4) indicated the presence of silicon (Si = 16.2±1.6 at%), oxygen (O = 56.75±1.2 at%), as well as high amount of carbon (C = 21.74±1.7 at%) and nitrogen (N = 5.33±0.25 at%).

The nanoparticles obtained from Rxn3 (TEOS hydrolysis and condensation within presence of phosphoric acid and glucose and imidazole catalysts) are shown in Figure 7.5. HR-SEM images indicated that these SiONPx1 nanoparticles are close to virus-like silica nanoparticles as can be seen from Figure 7.5-A & D. The particles sized are in the range of 20-25 nm with epitaxial growth of perpendicular silica nanotubes of 113±6 nm length. The EDX spectra (Figure 7.5-F) indicated the presence of silicon (Si = 23.7±7 at%), oxygen (O = 57.6±8 at%), as well as high amount of carbon (C = 13.2±3 at%), nitrogen (N = 2.8±1 at%), and phosphorous (P = 2.7±0.6 at%).

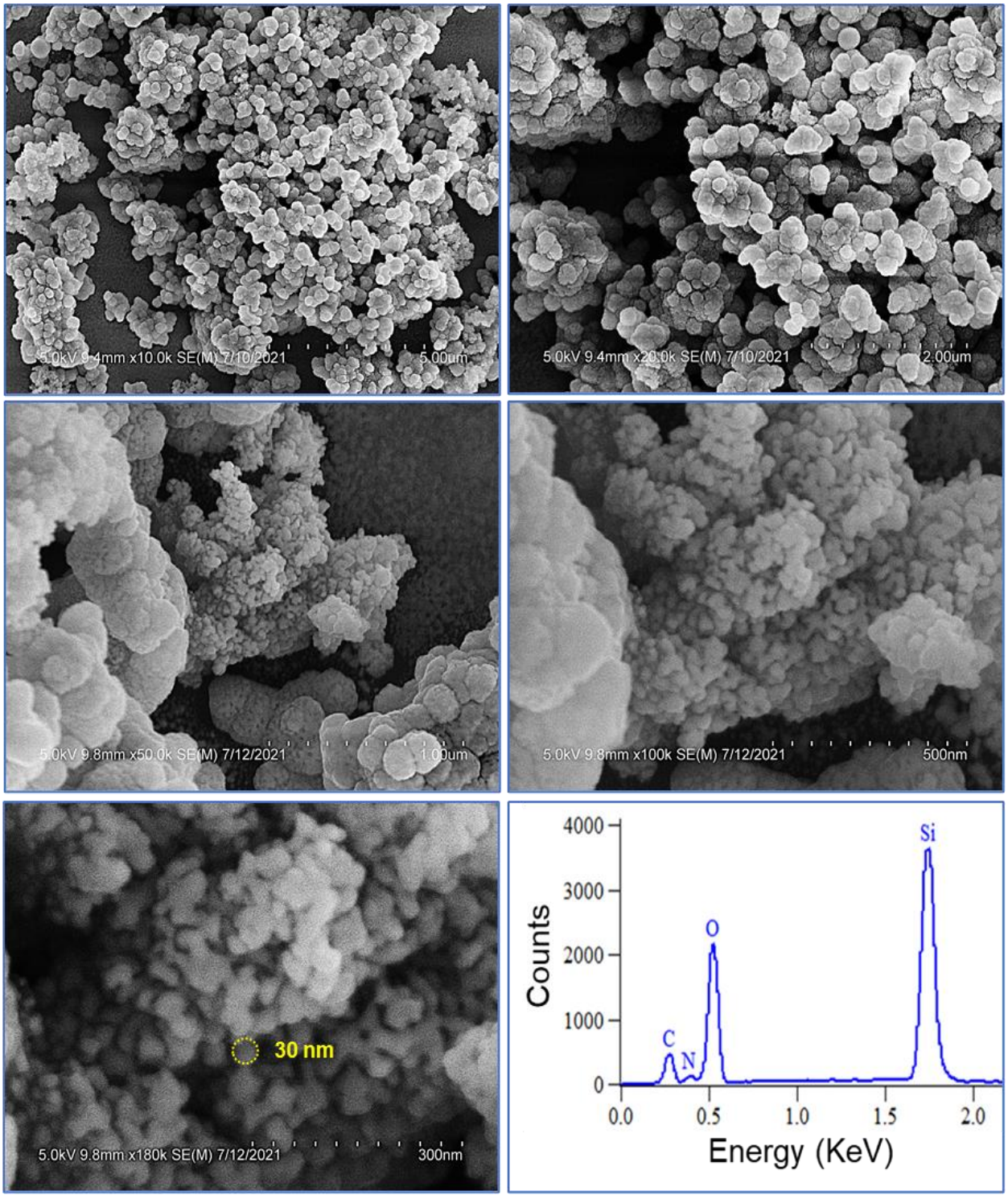

Figure 7.4: HR-SEM images of the amorphous SiONx nanoparticles and the EDX spectra showing the compositional analysis. Images are at different magnifications 10k, 20k, 50k, 100k, and 180k.

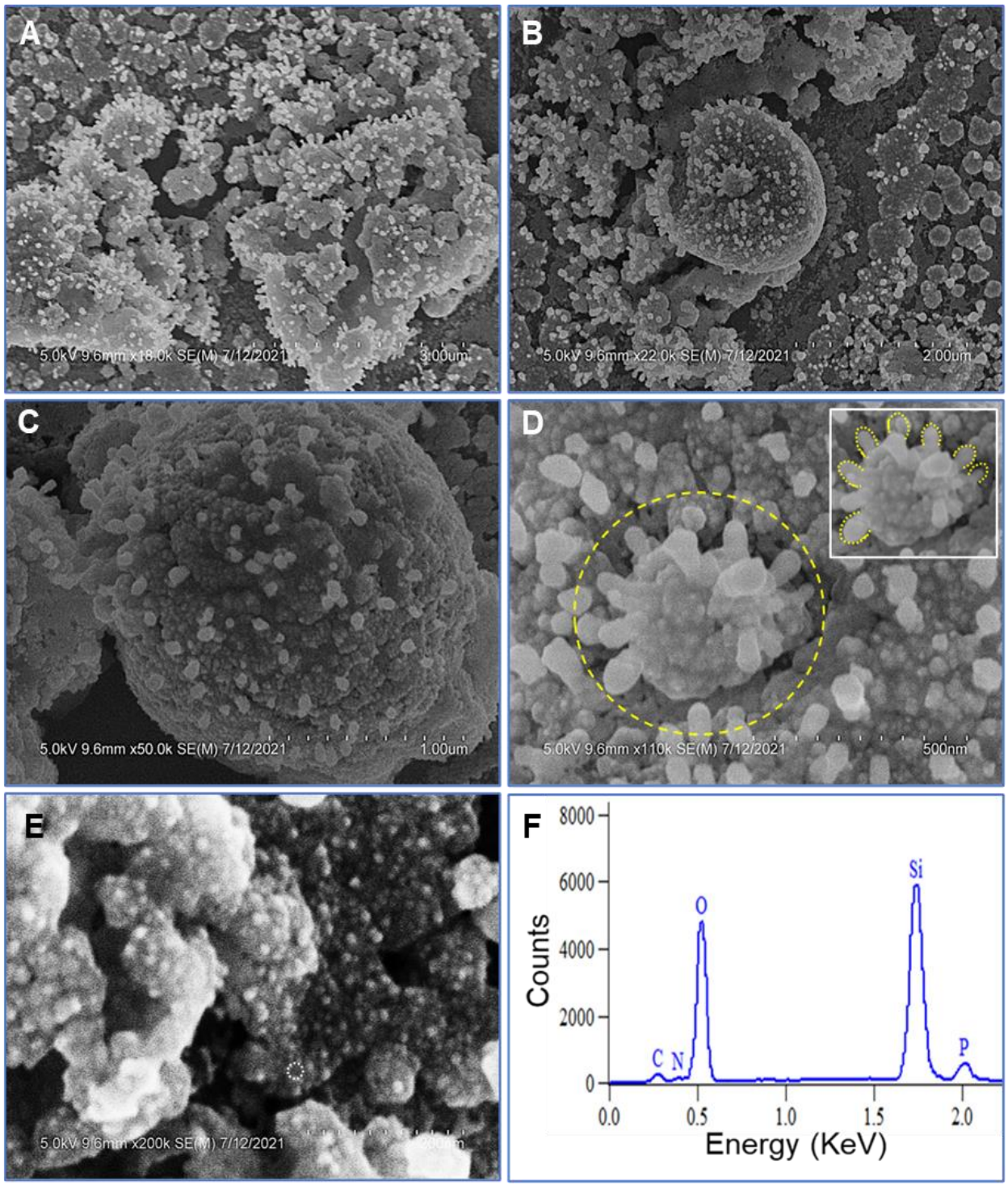

Figure 7.5: HR-SEM images of the amorphous SiONPx1 nanoparticles and the EDX spectra showing the compositional analysis. Images are at different magnifications 18k, 22k, 50k, 110k, and 200k.

HR-TEM and XRD analysis were employed to investigate the crystalline/amorphous nature of the obtained nanoparticles. Figure 7.6 shows the X-ray scattering of SiOx (A), SiONx (B), and SiONPx (C) nanoparticles. XRD scans were acquired at small θ-2θ angle (10-50°). The obtained spectra from all tested nanoparticles indicated the formation of amorphous silica structure as seen from the broad single peak ranged from 15-30°. This was further confirmed from the HR-TEM

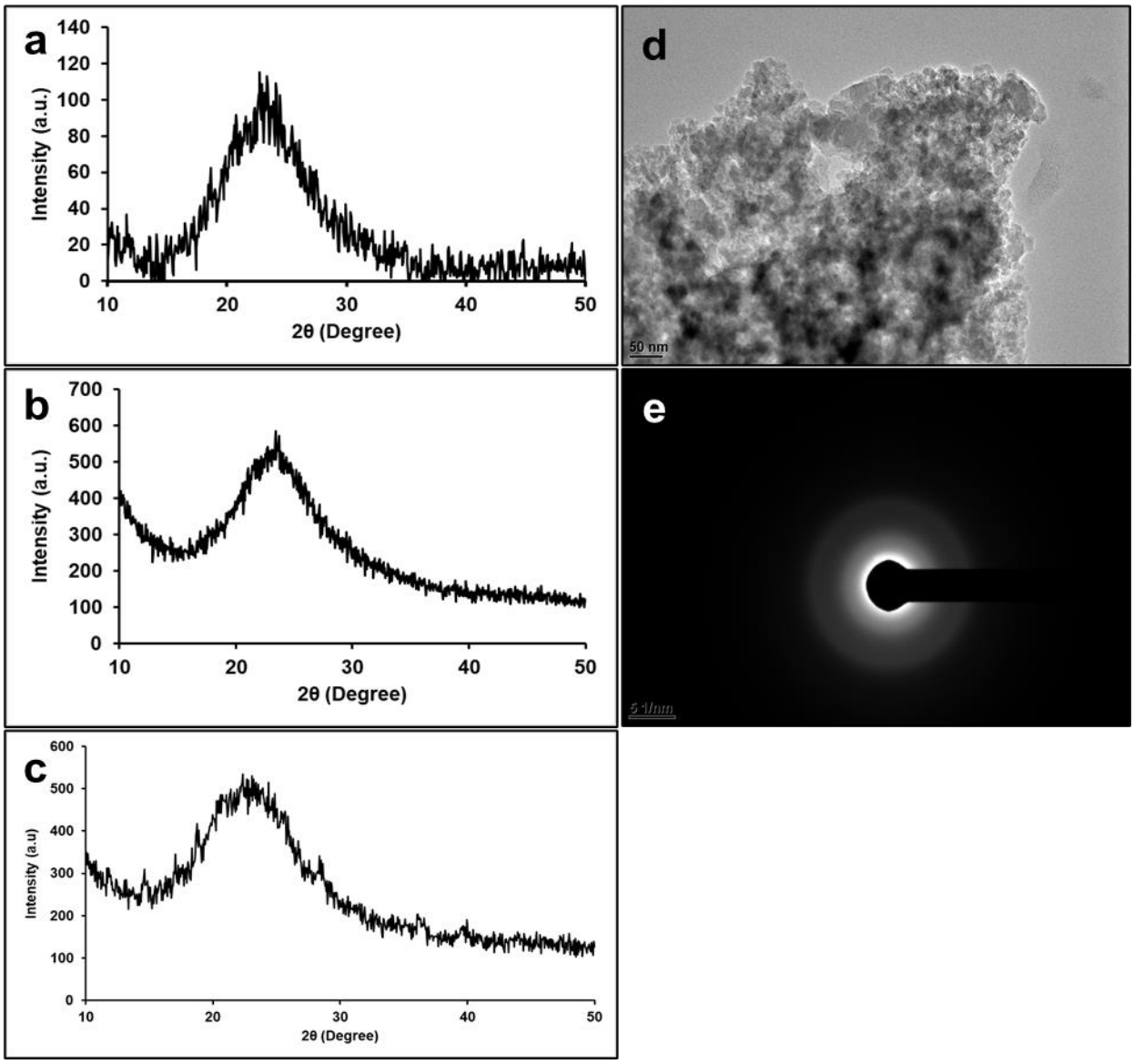

Figure 7.6: XRD and TEM analysis confirming the amorphous nature of the synthesized SiOx (a), SiONx (b), and SiONPx (c) nanoparticles.

micrographs at different magnifications and the Selected Area Electron Diffraction (SAED) pattern that showed dispersion of nanosized particles with amorphous nature.

Chemical composition and surface functionality of the synthesized nanoparticles were analyzed using raman spectroscopy. The raman spectra of all tested samples and starting materials were stacked as shown in Figure 7.7. Spectra of the different synthesized nanoparticles confirmed the presence of amorphous silica nanoparticles that can be characterized in three unique regions; strong polarized band ranged from 250-550 cm^{-1} and centered at 446 cm^{-1}, broad weak band at 795 cm^{-1}, and medium intensity with some weak bands at 1050 cm^{-1} and 1200 cm^{-1}. These bands are attributed to the Si-O-Si bonds and the broadening in the peaks indicates the amorphous nature of the nanoparticles. Sharp bands were observed at 492 cm^{-1} for all nanoparticles. Strong band appeared at 945-1010 cm^{-1} is attributed to the Si-OH band in amorphous silica. Spectra of the amorphous SiOx obtained from Rxn 1 indicated the presence of fingerprint peaks of imidazole observed at 1100 cm^{-1} to 1550 cm^{-1} region with a slight shift to higher wavenumber, indicating its bonding affected due to incorporation in the silica structure.

Raman spectra of SiONx nanoparticles from Rxn 2 revealed the presence of amorphous silica bands as well as CH_2-NH_2 at 1456 cm^{-1}, N-CH_2 at 2820 cm^{-1}, and strong bands of O-CH2 and CH=CH at range 2845-3050 cm^{-1}. Presence of these bands confirms the incorporation of the APTES in the silica network leading to organo surfcae functionality. $SiONP_{x2}$ nanoparticles (Rxn 4, which was synthesized following the same Rxn 2 mechanism but in presence of phosphoric acid) presented raman spectra that exactly matche the SiONx but with the presence of PO_4^{3-} peaks appered at 900 cm^{-1}.

Finally, raman spectra of SiONPx1 (Rxn3, TEOS hydrolysis and condensation in presence of phosphoric acid, imidazole, and glucose) indicated the presence of phosphate group PO_4^{3-} peaks appered at 900 cm^{-1} as well as NH and CH_2 bands at 1456 cm^{-1} indicating the incorporation of phosphorus and nitrogen in the $SiONP_{x2}$ nanoparticles.

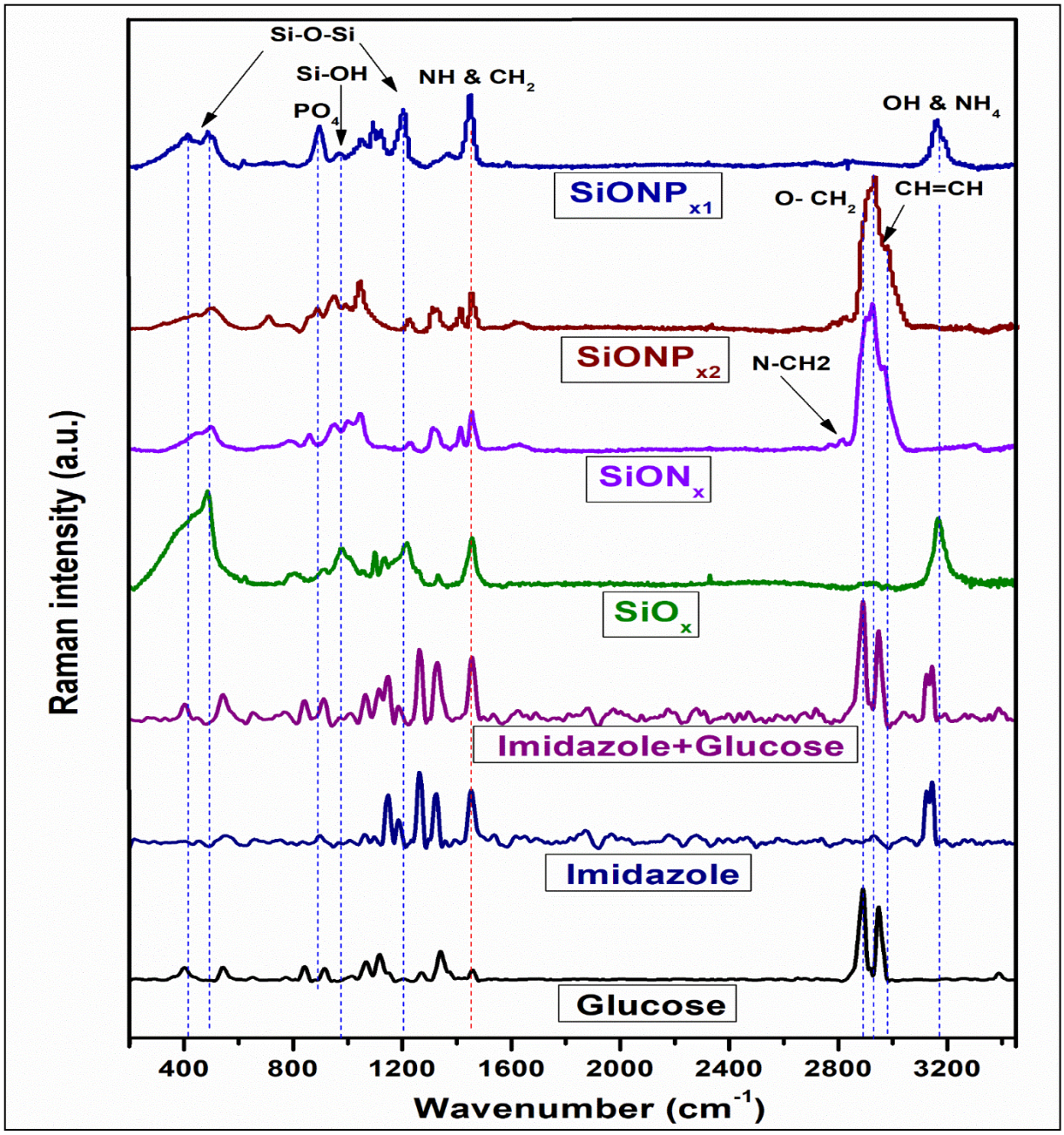

Figure 7.7: Raman spectra of the synthesized nanoparticles.

4. DISCUSSION

Intricate and highly repeatable biosilica structures are observed in marine organisms like sponges and diatoms. They synthesis such elaborate structures at ambient pressure and temperature conditions in neutral or near neutral pH. It was discovered that proteins like silaffins and silicatein acted enzymatically in the formation of silica in diatoms and sponges, respectively [24]. A site directed mutagenesis study of silicatein showed that Ser-26 and His-165 moieties were active sites involved in hydrolysis of TEOS, used as a Si precursor in-vitro [25]. Cha et al found that the hydroxyl bond from the Ser-26 site initiates a nucleophilic attack on the Si-ion in the precursor, causing hydrolysis of TEOS, leading to condensation of TEOS and formation of Si-O-Si bond [25]. Later, M-K. Liang et al., reported that imidazole group from poly-histidine can catalyze silicic acid condensation through its dual features that form hydrogen bonds with silicic acid and electrostatic attraction toward oligomeric silicic acid species [26].

In this study, novel approaches were investigated to synthesis pure amorphous nanosilica and Si-NPs with modified surface functionality. Amorphous spherical SiO_x-nanoparticles were synthesized using facile and reproducible approach based on mimicking the natural silicification process in marine sponge. As mentioned above, natural silicification process of TEOS is catalyzed due to combinatorial presence of charged nitrogen presence and dangling OH bonds. The silicification process involves first hydrolysis of the precursor to form silicic acids and condensation reaction to form siloxane (Si-O-Si) linkages. The condensation/polymerization process of silica sols is a three-step process, polymerization of monomers to form particles, particle growth and particle linkage to form network forming aqueous silica gels. It is found from this study,

to achieve successful synthesis of nanoparticles from the TEOS precursor system changes at two steps is required, catalysis during hydrolysis step of TEOS and condensation processes interrupted to prevent particle linkage to form gels and instead precipitate out. The reaction condition and the proposed mechanism of reaction (Rxn1) is presented as follows:

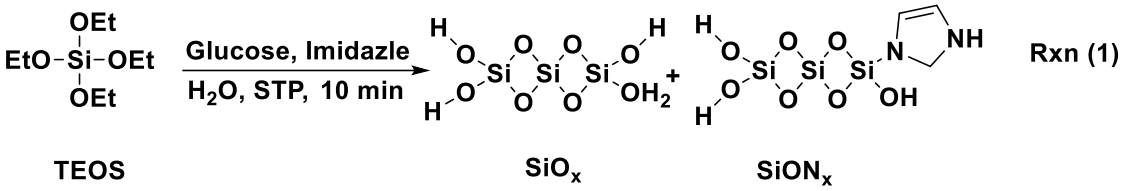

Based on the mechanism below (Figure 7.8), it is seen that imidazole moiety forms a hydrogen bond from its N3 (pyridine like site) with OH dangling bond of glucose, rendering the O atom to initiate a nucleophilic attack on Si atom of TEOS. Further imidazole moiety also interacts with silicic acids to catalyze condensation process and forms interactions with particles to produce precipitates instead of gelation, possibly from its cationic ally charged basic site N3. The particles precipitated are mainly amorphous in nature as observed from the XRD and broad raman spectra. SEM analysis shows spherical agglomerates of about 400 nm in size which are further made up of 30-40 nm in diameter of individual particles. The complete spherical morphology of the SiOx nanoparticles can be attributed to that particles network is predominantly formed from $Si(OEt)_4$ and then condenses onto this network in three-dimensional network leads to complete spherical shape [27]. EDX and raman indicated the presence of nitrogen and NH group, respectively, in the SiOx nanoparticles which can be attributed to the incorporation of imidazole in the silica network during the condensation step. This can be explained according to the proposed reaction mechanism as

mentioned below in Figure 7.8. Thus, we concluded that hydrolysis of TEOS in presence of imidazole and glucose could form SiONx structure with very small nitrogen content (N = 1.18±0.15 at%) and the exact modified silica structure is proposed as SiO_2-O-N_2-$(CH)_3$. The TEOS hydrolysis reaction Rxn 1 was repeated several times under different reaction times and the optimal yield was obtained after 3 hours.

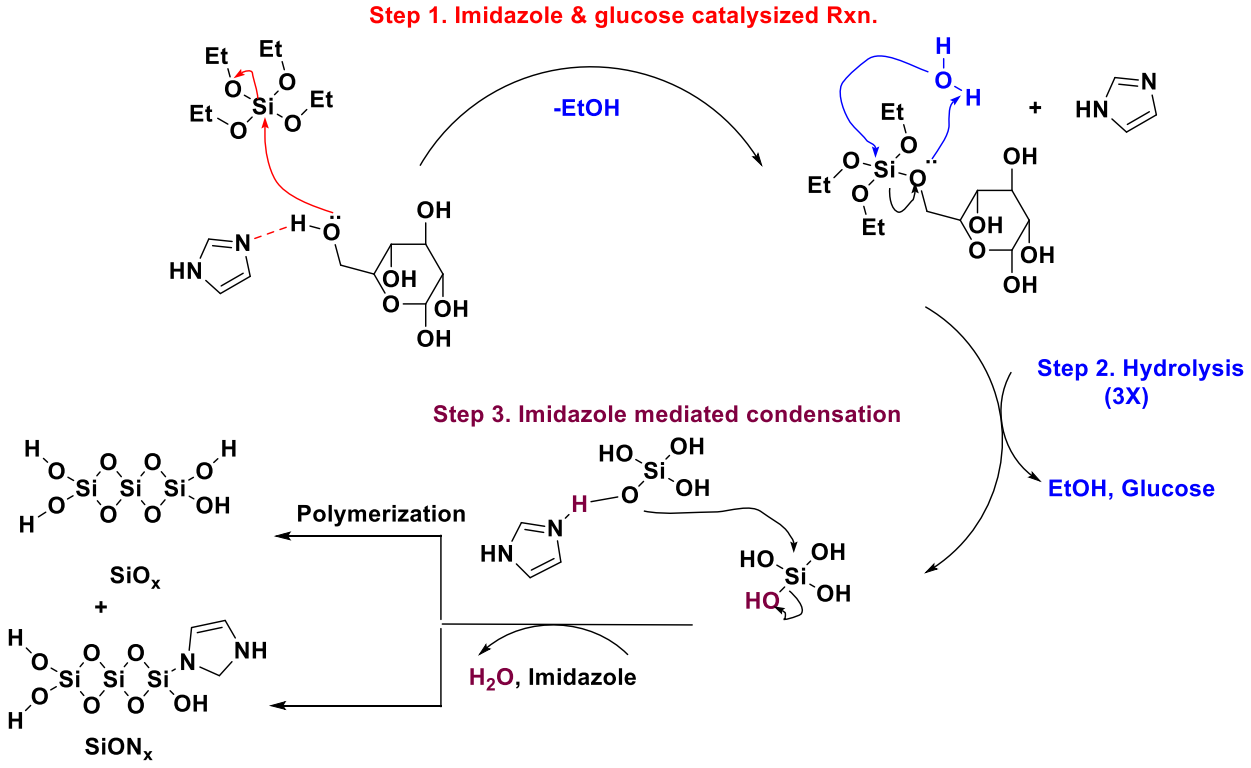

Figure 7.8: Proposed synthesized mechanism for amorphous SiO_2 and imidazole modified SiO_2.

Surface modification of amorphous Si-NPs will enhance their bioactivity due to the amorphous nature and the presence of surface multi-functional groups (i.e., Si-OH, Si-NH, Si-H, Si-O-P-OH, and N-H) that are partially soluble under physiological conditions through immediate dissolution/degradation *in-vivo.* In this regard, we aimed to synthesize SiONx and SiONPx as amorphous Si-NPs. For $SiON_x$, co-condensation approach was utilized to synthesize organo-functionalized amorphous silica

nanoparticles as describe in proposed mechanism at Figure 7.9 and summarized in Rxn 2 as follows:

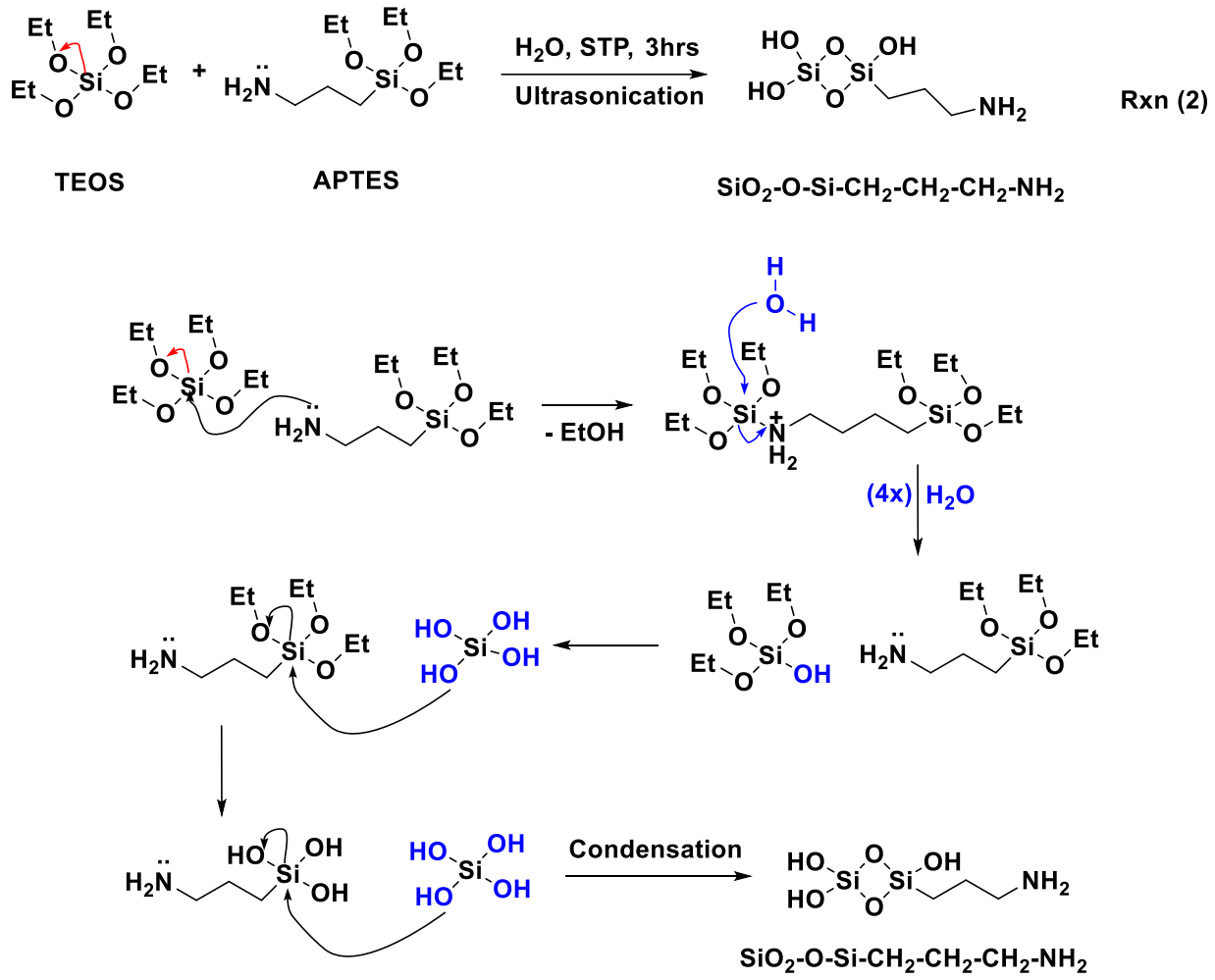

Figure 7.9: Proposed synthesized mechanism for amorphous SiONx nanoparticles.

It is important to mention that this approach was successful in obtaining organo functionalized nanosilica (SiO_2-O-Si-CH_2-CH_2-CH_2-NH_2) with 30 nm diameter particle size. This approach was previously reported by I.A. Rahman et al., in 2009 and used to synthesize nanosilica with partcle size of ~ 60 nm and organo-functional groups at the silica particles surface [27]. The nitrogen incorporation in this silica structure was higher (N = 5.33±0.25 at%) than Si-NPs obtained by Rxn 1. The nitrogen percentage can be

controlled by the amount of APTES used in the reaction. The incomplete spherical shape of SiONx particles obtained from Rxn 2 can be explained due to the presence of organic groups on the silica surface. This lower the cross-linking density formation on the silica network in three dimentional due to the preesence of trialkoxysilane (R-Si-$(OEt)_3$) from APTES against tetraalkoxysilane (Si-$(OEt)_4$) of TEOS .

For $SiONP_x$ nanoparticles, two novel approaches were tested based on the above mentioned reactions (Rxn 1 and Rxn 2). As a first step, phosphoric acid was allowed to react with TEOS for 10 minutes and the resultant mixture was utilized to form $SiONP_x$ via two different pathways (Rxn 3 and Rxn 4). Rxn 3 investigated the TEOS-H_3PO_4 hydrolysis within glucose/imidazole presence similar to Rxn 1, while Rxn 4 investigated the hydrolysis via the self-catalyzed reaction by the amine group of ATPES, similar to Rxn 2. The obtained SiONPx1 are amorphous in nature and the particle size range ~ 20-25 nm. The proposed reactions and mechanisms for Rxn3 and Rxn 4 are as follws:

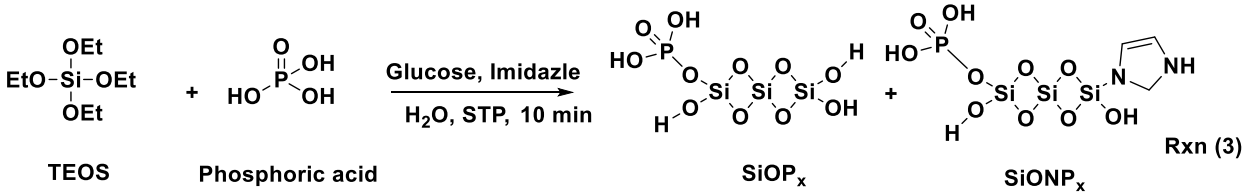

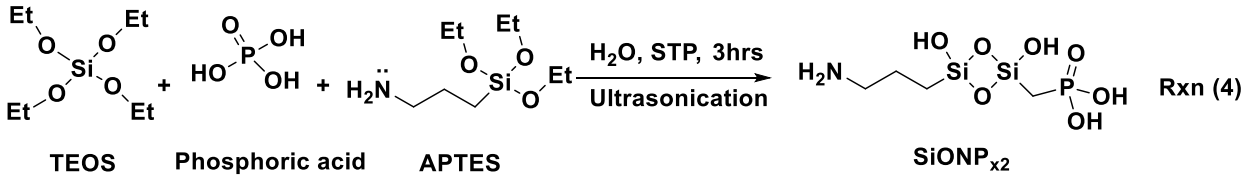

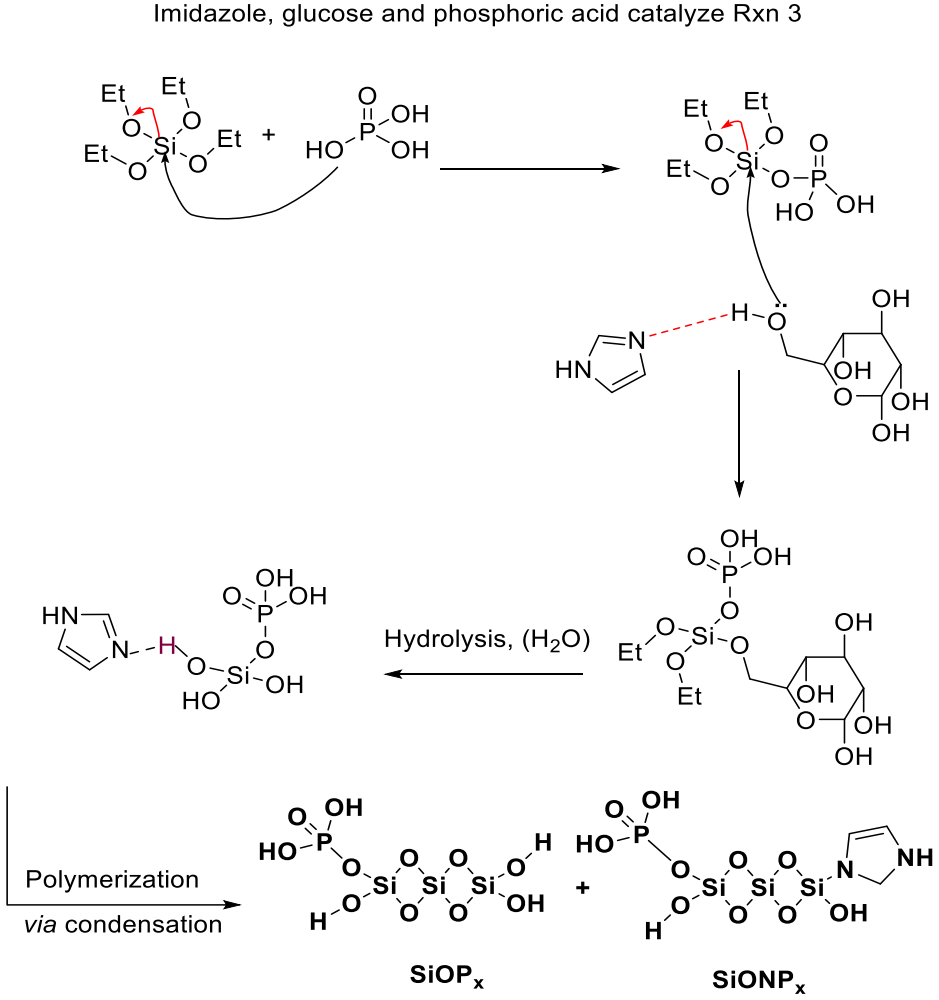

Figure 7.10: Proposed synthesized mechanism for amorphous SiONPx1 nanoparticles.

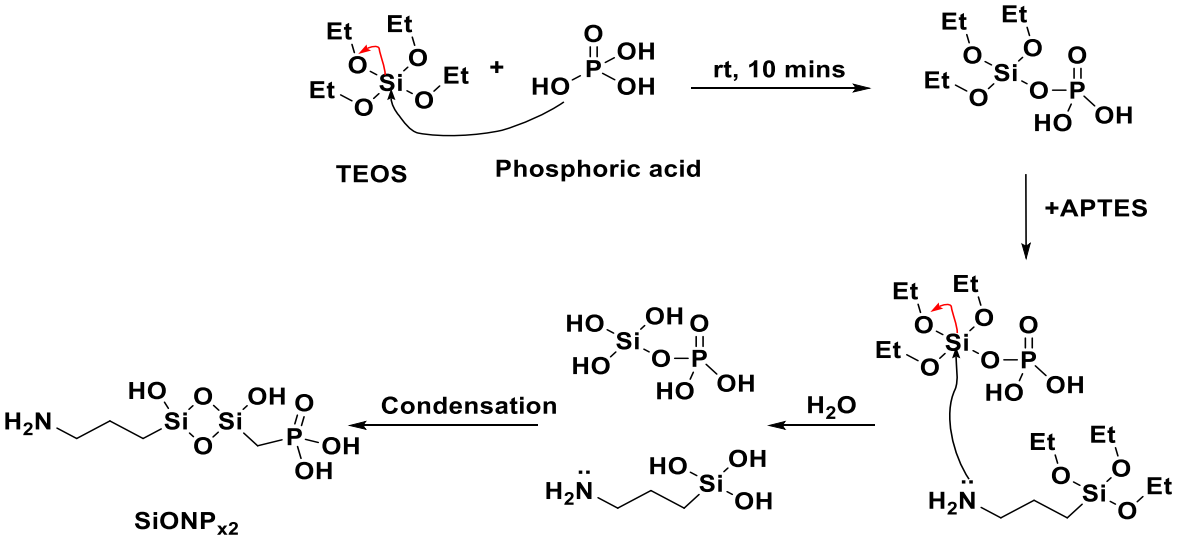

Figure 7.11: Proposed synthesized mechanism for amorphous $SiONP_{x2}$ nanoparticles.

HR-SEM images indicated that Rxn 3 can yield SiONPx1 nanoparticles with shape close to virus-like silica [4] nanoparticles of 20-25 nm particle size with epitaxial growth of perpendicular silica nanotubes of 113±6 nm length. The EDX and raman data confirmed the presence of N and P in the SiONPx1 as can be seen in Figure 7.5 & 7.7.

Raman spectra provided valuable knowledge on the chemical structure and the surface functionality of the obtained nanoparticles. Presence of sharp peak at 492 cm^{-1} confirms the formation of four membered ring of silicon and oxygen (siloxane rings) in the silica network [28,29]. This also can be attributed to the structural defects associated with the broken Si-O-Si bonds in silica network [28,29] which confirms the modifications introduced to the silica structure. Furthermore, two distinct features in the raman spectra were observed, that usually used to confirm and distinguish the amorphous silica from the crystalline structure [30,31]. First is the presence of sharp peak at 975 cm^{-1} that can be attributed to the Si-O stretching associated with the silanol group in the amorphous silica network. Second, is the presence of -OH bonds at ~3100-3300 cm^{-1} which is one of the distinguishing characteristics of amorphous silica [30,31]. Finally, the amorphous nature of all synthesized nanoparticles were confirmed by the broad single peak of XRD and the TEM-SAED analysis as shown in Figure 7.6.

5. CONCLUSION

This study investigates novel approaches for synthesis and surface modification of amorphous silica nanoparticles. The proposed approach for amorphous nanosilica indicated the possibility of TEOS hydrolysis and condensation under ambient conditions to synthesis nanoscale silica (40 nm) within 10 minutes utilizing imidazole and glucose to mimic the natural silicification process. Presence of low content nitrogen in the silica

structure suggested the incorporation of imidazole in the silica structure leading to SiONx like structure. Another approach was utilized to synthesis SiONx with higher nitrogen content utilizing APTES that self-catalyze the TEOS hydrolysis and condensation leading to spherical nanoparticles of amine-modified silica structure. Third approach was introduced to synthesize SiONPx like structure through the initial interaction of phosphoric acid with TEOS, then hydrolysis of TEOS-H_3PO_4 via glucose and imidazole approach or APTES approach. Both SiONPx approaches yield nanoscale silica with nitrogen and phosphorus incorporated. Furthermore, hydrolysis of TEOS-H_3PO_4 in presence of imidazole and glucose lead to virus-like nanoparticles formation that could be potential in drug delivery systems and biomodulation applications. This study concluded that the proposed approaches are successful in synthesis and surface functional modification of amorphous silica nanoparticles.

ACKNOWLEDGEMENTS:

The authors want to greatly thank Ms. Ayat Omar, and Ms. Laureen Abbo Nono, summer intern students at the Varanasi's laboratory, for their assist in repeating some of the reactions for validation during this study. The authors would like to thank Dr. Jiechao Jiang and Mr. David Yan at the Characterization Center for Materials and Biology (CCMB) at the University of Texas at Arlington (UTA) for their help during the materials characterization.

Funding:

The authors want to thank the National Institutes of Health (NIH), the Osteo Science Foundation, the University of Texas at Arlington (UTA), and the UTA College of Nursing & Health Innovation Bone-Muscle Research Center (UTA-CONHI-BMRC) for their generous support for this study. The following NIH Grants supported KA and VV: (Grant Number 1R03DE023872-01, 1R56DE027964-01A1-01, NIH S10OD025230). Also, we thank the UTA-CONHI for their generous support for the first author KA via the CRS Pilot Grant.

6. REFERENCES

1. Wang, Y. *et al.* Mesoporous silica nanoparticles in drug delivery and biomedical applications. *Nanomedicine Nanotechnology, Biol. Med.* **11**, 313–327 (2015).

2. Ha, S.-W., Weiss, D., Weitzmann, M. N. & Beck, G. R. Chapter 4 - Applications of silica-based nanomaterials in dental and skeletal biology. in *Micro and Nano Technologies* (eds. Subramani, K. & Ahmed, W. B. T.-N. in C. D. (Second E.) 77–112 (Elsevier, 2019). doi:https://doi.org/10.1016/B978-0-12-815886-9.00004-8.

3. Niculescu, V.-C. Mesoporous Silica Nanoparticles for Bio-Applications . *Frontiers in Materials* vol. 7 36 (2020).

4. Wang, W. *et al.* Facile Synthesis of Uniform Virus-like Mesoporous Silica Nanoparticles for Enhanced Cellular Internalization. *ACS Cent. Sci.* **3**, 839–846 (2017).

5. Şen Karaman, D. & Kettiger, H. Chapter 1 - Silica-based nanoparticles as drug delivery systems: Chances and challenges. in (ed. Grumezescu, A. M. B. T.-I. F. as S. N.) 1–40 (William Andrew Publishing, 2018). doi:https://doi.org/10.1016/B978-0-12-813661-4.00001-8.

6. Singh, P., Srivastava, S. & Singh, S. K. Nanosilica: Recent Progress in Synthesis, Functionalization, Biocompatibility, and Biomedical Applications. *ACS Biomater. Sci. Eng.* **5**, 4882–4898 (2019).

7. Mamaeva, V., Sahlgren, C. & Lindén, M. Mesoporous silica nanoparticles in medicine--recent advances. *Adv. Drug Deliv. Rev.* **65**, 689–702 (2013).

8. Yang, Y., Zhang, M., Song, H. & Yu, C. Silica-Based Nanoparticles for Biomedical Applications: From Nanocarriers to . *Acc. Chem. Res.* **53**, 1545–1556 (2020).

9. Keshavarz Moraveji, M. *et al.* Application of amorphous silica nanoparticles in improving the rheological properties, filtration and shale stability of glycol-based drilling fluids. *Int. Commun. Heat Mass Transf.* **115**, 104625 (2020).

10. Phillips, E. *et al.* Clinical translation of an ultrasmall inorganic optical-PET imaging nanoparticle probe. *Sci. Transl. Med.* **6**, 260ra149 LP-260ra149 (2014).

11. Araichimani, P. *et al.* Amorphous silica nanoparticles derived from biowaste via microwave combustion for drug delivery. *Int. J. Appl. Ceram. Technol.* **18**, 583–589 (2021).

12. Roopavath, U. K., Soni, R., Mahanta, U., Deshpande, A. S. & Rath, S. N. 3D printable SiO2 nanoparticle ink for patient specific bone regeneration. *RSC Adv.* **9**, 23832–23842 (2019).

13. do Monte, F. A. *et al.* Silicon Oxynitrophosphide Nanoscale-Coating Enhances Antioxidant Marker -Induced Angiogenesis During In Vivo Cranial Bone Defect Healing. *JBMR Plus* **n/a**, e10425 (2020).

14. Ilyas, A. *et al.* Rapid Regeneration of Vascularized Bone by Nanofabricated Amorphous Silicon Oxynitrophosphide (SiONP) Overlays. *J. Biomed. Nanotechnol.* **15**, 1241–1255 (2019).

15. Awad, K. *et al.* Ionic Silicon Protects Oxidative Damage and Promotes Skeletal Muscle Cell Regeneration. *International Journal of Molecular Sciences* vol. 22

(2021).

16. Varanasi, V. G. *et al.* Role of Hydrogen and Nitrogen on the Surface Chemical Structure of Bioactive Amorphous Silicon Oxynitride Films. *J. Phys. Chem. B* **121**, 8991–9005 (2017).

17. Varanasi, V. G. *et al.* Chapter 9 - Surface Modifications and Surface Characterization of Biomaterials Used in Bone Healing. in (eds. Bose, S. & Bandyopadhyay, A. B. T.-M. for B. D.) 405–452 (Academic Press, 2017). doi:https://doi.org/10.1016/B978-0-12-802792-9.00009-4.

18. Varanasi, V. G. *et al.* Enhanced osteocalcin expression by osteoblast-like cells (MC3T3-E1) exposed to bioactive coating glass (SiO2–CaO–P2O5–MgO–K2O–Na2O system) ions. *Acta Biomater.* **5**, 3536–3547 (2009).

19. Awad, K. R. *et al.* Patterned Silicon Oxynitride (SiONx) Scaffolds Enhance Alignment and Myogenic Differentiation of C2C12 Muscle Cells. *FASEB J.* **33**, 539.5-539.5 (2019).

20. Ilyas, A. *et al.* Amorphous Silica: A New Antioxidant Role for Rapid Critical-Sized Bone Defect Healing. *Adv. Healthc. Mater.* **5**, 2199–2213 (2016).

21. Ilyas, A., Lavrik, N. V, Kim, H. K. W., Aswath, P. B. & Varanasi, V. G. Enhanced Interfacial Adhesion and Osteogenesis for Rapid “Bone-like” Biomineralization by PECVD-Based Silicon Oxynitride Overlays. *ACS Appl. Mater. Interfaces* **7**, 15368–15379 (2015).

22. Monte, F. *et al.* Ionic silicon improves endothelial cells’ survival under toxic

oxidative stress by overexpressing angiogenic markers and antioxidant enzymes. *J. Tissue Eng. Regen. Med.* **12**, 2203–2220 (2018).

23. Monte, F. A. do *et al.* Amorphous Silicon Oxynitrophosphide-Coated Implants Boost Angiogenic Activity of Endothelial Cells. *Tissue Eng. Part A* **26**, 15–27 (2019).

24. Kröger, N., Deutzmann, R. & Sumper, M. Polycationic Peptides from Diatom Biosilica That Direct Silica Nanosphere Formation. *Science (80-.).* **286**, 1129 LP – 1132 (1999).

25. Cha, J. N. *et al.* Silicatein filaments and subunits from a marine sponge direct the polymerization of silica and silicones in vitro. *Proc. Natl. Acad. Sci. U. S. A.* **96**, 361–365 (1999).

26. Liang, M.-K., Patwardhan, S. V, Danilovtseva, E. N., Annenkov, V. V & Perrya, C. C. Imidazole catalyzed silica synthesis: Progress toward understanding the role of histidine in (bio)silicification. *J. Mater. Res.* **24**, 1700–1708 (2009).

27. Rahman, I. A., Jafarzadeh, M. & Sipaut, C. S. Synthesis of organo-functionalized nanosilica via a co-condensation modification using γ-aminopropyltriethoxysilane (APTES). *Ceram. Int.* **35**, 1883–1888 (2009).

28. Biswas, R. K. *et al.* Study of short range structure of amorphous Silica from PDF using Ag radiation in laboratory XRD system, RAMAN and NEXAFS. *J. Non. Cryst. Solids* **488**, 1–9 (2018).

29. Mikkelsen, J. C. & Galeener, F. L. Thermal equilibration of raman active defects in

vitreous silica. *J. Non. Cryst. Solids* **37**, 71–84 (1980).

30. De Tommasi, E. *et al.* UV-shielding and wavelength conversion by centric diatom nanopatterned frustules. *Sci. Rep.* **8**, 16285 (2018).

31. Akse, S. P., Middelburg, J. J., King, H. E. & Polerecky, L. Rapid post-mortem oxygen isotope exchange in biogenic silica. *Geochim. Cosmochim. Acta* **284**, 61–74 (2020).

CHAPTER 8: GENERAL CONCLUSION

Silica based biomaterials and the sustained release of ionic silicon from these materials seemed to be an effective approach in managing oxidative stress via antioxidant activation to promote musculoskeletal tissue healing and regeneration. In this dissertation, the author investigated novel materials, approaches, and characterization techniques to test this hypothesis. The knowledge gained from this study concluded that silica-based biomaterials and especially amorphous silicon oxynitride and oxynitrophosphide are promising bioactive materials for musculoskeletal tissue regeneration applications. Release of Si-ions with higher valance state (+4) increases the charge transfer to antioxidant and enhances the overall antioxidant production (e.g., SOD1 and NRF-2) that mitigates the oxidative stress and improves the overall cellular behavior and rapid tissue regeneration.

As initial step, the author utilized X-ray absorption near edge structure (XANES) spectroscopy technique to study changes in bone chemical structure. This part of the study assessed local calcium (Ca) and phosphorus (P) coordination of various bone samples. Results indicated that XANES is a sensitive technique that can be used to detect soluble phosphates in the bone structure, which can provide insights on the bone remodeling and quality. The presence of soluble Ca and P, products of bone resorption, suggests unbalanced bone resorption and formation. This knowledge was further used to study and evaluate the extracted rabbit mandibular bone after critical size defect and Ti implantation to compare the effect of bare Ti to SiONx coated Ti implants.

Then, we aimed to enhance the Ti surface bioactivity via strongly adherent bioactive thin film coatings of SiONx or SiONPx deposited by low temperature (< 400

^{0}C) plasma enhanced chemical vapor deposition (PECVD) technique on nanopore anodized Ti surface. Commercially pure Ti (CP-Ti) implants were coated with SiONx or SiONPx and tested in-vitro and in-vivo to reveal the effect of the silica-based coating on the bone healing. Knowledge gained from the in-vitro studies indicated that the proposed silica-based coatings coating significantly enhanced the Ti surface bioactivity that presented the highest surface coverage of carbonated hydroxyapatite (HCA, ~ 40%) with a Ca/P ratio (~ 1.65) close to the stoichiometric hydroxyapatite (~ 1.67) found in bone biomineral. Furthermore, our results indicated that a strongly adherent thin film coatings can be successfully deposited on any medical device or implantable material that can fit in the PECVD reactor geometry. The chemical bonding between the Ti-O surface and the deposited amorphous silica films indicated strong inter-connection at the interface explained by the following reactions:

$$O\text{-}Ti\text{-}O + wSiH_4 + xN_2O \rightarrow O\text{-}Ti\text{-}O\text{-}Si_wO_x + 2wH_2 + xN_2 \quad \textit{(Rxn. 1)}$$

$$O\text{-}Ti\text{-}O + wSiH_4 + xN_2O + yNH_3 \rightarrow O\text{-}Ti\text{-}O\text{-}Si_wO_xN_y + (2w+1.5y)\,H_2 + xN_2 \quad \textit{(Rxn. 2)}$$

$$O\text{-}Ti\text{-}O + wSiH_4 + xN_2O + yNH_3 + zPH_3 \rightarrow O\text{-}Ti\text{-}O\text{-}Si_wO_xN_yP_z + (2w+1.5y+1.5z)\,H_2 + xN_2 \quad \textit{(Rxn. 3)}$$

This section concluded that the surface bioactivity of the SiON and SiONP amorphous silica-based PECVD coatings that are strongly adherent to CP-Ti implants are potential coatings for rapid HA formation and enhanced bone healing.

After that, the modified Ti-implants were tested in-vitro using mesenchymal stem cells and MRSA bacteria, and in-vivo using rabbit mandibular bone defect compared to bare Ti implants. The *in-vitro* study using mesenchymal stem cells revealed that these coatings are biocompatible with no cytotoxic effect and enhanced osteogenesis as confirmed from the elevated alkaline phosphatase activity. Antibacterial studies indicated that these coatings have a bacteriostatic effect as indicated by the significant

decrease in the number of bacteria on those coatings. SiONx with refractive index n=1.82 and 2.0 presented better results compared to other SiONx coatings. Thus, SiONx with n=1.82 was further used for the in-vivo testing. *In-vivo* data indicated faster bone healing with better osseointegration on the coated implants compared to the uncoated Ti. The SiONx coated implants supported bone regeneration and bone growth on the implant surface as confirmed from micro-CT imaging. X-ray imaging and XANES analysis indicated good bone quality with normal mechanical properties on regenerated and surrounding bone near the coated implant. The pronounced effect of SiONx coating was attributed to the antioxidant activity of these coating that mitigate the toxic oxidative stress and significantly elevate the osteogenic activity as confirmed from SOD1, 4HNE, and ALP activity in the blood serum studies at 1, 2, 4, and 8 weeks. These data align perfectly with the proposed hypothesis that silica-based biomaterials and the sustained release of ionic silicon play a significant role in managing oxidative stress via antioxidant activation.

On the other hand, we investigated the effect of silicon-ions on C2C12 skeletal muscle cells under normal and excessive oxidative stress conditions to gain insights into its role on myogenesis during the early stages of muscle regeneration. This section revealed that ionic silicon played an important role in the skeletal muscle cell activity under normal and oxidative stress conditions. Si-ions addition into the cell culture media significantly increased cell viability, proliferation, migration, and myotube formation compared to the control. Also, MyoG, MyoD, Neurturin, and GABA expression were significantly increased with addition of 0.1, 0.5, and 1.0 mM of Si-ion for 1 and 5 days of C2C12 myoblast differentiation. These results suggest that ionic silicon may have a

potential effect in unfavorable situations where reactive oxygen species is predominant affecting cell viability, proliferation, migration, and differentiation. Furthermore, this part provides a guide for designing Si-containing biomaterials with desirable Si-ion release for skeletal muscle regeneration.

Based on the presented knowledge above, the author aimed to synthesize these silica-based bioactive coatings in nanoparticles form to allow their application in soft tissue applications via three-dimentional (3D) printing technology. The investigator proposed novel approaches to syjthesize SiOx, SiONx, SiONPx in amorphous nature. Facile and novel approach based on the natural silicification process was tested to rapid hydrolysis and condensation of TEOS, Si-precursor, via imidazole and glucose assistance as catalysts. Another approach utilized APTES, Si-precursor with terminal amine group, to synthesize silica nanoparticles with SiONx-based structure. Phosphoric acid was utilized to modify these two approaches to synthesize amorphous silica nanoparticles containing phosphorus with SiONPx-based structure. The provided results indicated the viability of these approaches to synthesize nanosilica and successful nitrogen and phosphorus incorporation in the silica network. These silica and in-situ modified silica nanoparticles are promising nanomaterials for drug delivery, biomodulation applications, and hydrogel modification for soft tissue regeneration.

As a recommendation and future work approach, the author strongly recommend conduction of comprehensive chemical analysis for the novel synthesized nanoparticles to better quantify their chemical structure. Then, ion release studies to understand their potential use as nanoparticles for soft tissue applications. After obtaining this knowledge, 3D printed scaffolds loaded with these nanoparticles are strongly

recommended to be tested for muscle and bone regeneration applications. On the other hand, application of micro-patterned amorphous silica based thin film coatings in muscle and nerve regeneration applications are highly recommended to yield aligned myotubes and axons for enhanced tissue regeneration.

In conclusion, these findings strongly support the use of the amorphous silica-based biomaterials as promising bioactive materials for musculoskeletal tissue regeneration. We believe that the presented evidence is an initial step that could lead to a significant progress in this field.